2014

Pulmonary Gas Transport and Drug Delivery in a Patient Specific Lung Model During Invasive High Frequency Oscillatory Ventilation

Mohammed Sabty Alzahrany
Lehigh University

PULMONARY GAS TRANSPORT AND DRUG DELIVERY IN A PATIENT SPECIFIC LUNG MODEL DURING INVASIVE HIGH FREQUENCY OSCILLATORY VENTILATION

By

Mohammed Sabty Alzahrany

A DISSERTATION

Presented to the Graduate and Research Committee
of Lehigh University
in Candidacy for the Degree of
Doctor of Philosophy

in

Mechanical Engineering

Lehigh University

(January 2015)

Approved and recommended for acceptance as a dissertation in partial fulfillment of the requirements for the degree of Doctor of Philosophy.

_____

DATE

_____

Professor Arindam Banerjee, Advisor

_____

Accepted DATE

Committee Members:

_____

Professor Donald O. Rockwell, MEM

_____

Professor Edmund Webb III, MEM

_____

Professor Bryan Berger, ChE

ACKNOWLEDGEMENTS

All praise to ALLAH for the strength and his blessing in completing this work. My sincere and deepest gratitude goes to my advisor, Professor Arindam Banerjee. This work would not have been possible but for his patience and faith in me and most importantly providing me with financial support during the last year of my dissertation studies. The motivation and guidance he gave throughout my research were invaluable. The publications arising from this work would never have been accepted without his limitless effort and perseverance. Not only did he help shape my research, but also he was a source of inspiration as my spirit waned during the doctoral study. I would like to thank Dr. Gary Salzman, M.D. at the University of Missouri, Kansas City for providing us with the CT-scans that were used to generate the lung model. I would like to express gratitude to my thesis committee members, Professor Donald O. Rockwell, Professor Edmund Web III, and Professor Bryan Berger for their support and cooperation. I would also like to thank my colleagues from Prof. Banerjee's research group for their patience, sharing their valuable skills, and, overall, sharing unforgettable moments in the same lab: Timothy van Rhein, Nitin Kolekar, Ashwin Vinod, Denis Aslangil, Rinosh Polavarapu, Rahul Raghavendra, Aaron Haley, Varun Lobo and Pamela Roach. I would like to give thanks to my brothers and friends; their support, encouragement, and inspiration offered to me throughout my studies have been invaluable. Finally, I would like to thank my wife and children, who are my world - the purpose of all of this work and without whom, none of this would have been possible.

TABLE OF CONTENTS

LIST OF TABLES

LIST OF FIGURES

NOMENCLATURE

Symbols

A	Cross-sectional area, m^2
A^*	Amplitude of pulsation
A_{ETT}	Area of the ETT inlet, m^2
A_k	Equivalent area of outlet k, m^2
$A_{t,i}$	Total of the equivalent areas of the outlets that are supplied by the branch corresponding to the i^{th} branch, m^2
a	Radius, m
C	Compliance, $l/cm\ H_2O$
C_c	Cunningham correction factor
C_D	Drag coefficient
C_L	Compliance of the left lung, $l/cm\ H_2O$
C_o	Total compliance, $l/cm\ H_2O$
C_{outk_j}	Compliance at each k^{th} outlet in each Gj, $l/cm\ H_2O$
C_R	Compliance of the right lung, $l/cm\ H_2O$
C_s	Smagorinsky model constant
C_v	Vreman model constant
C_w	WALE model constant
D	Tube diameter, m
$\tilde{D}$	Brownian diffusivity, m^2/s
D_d	The daughters diameter, m
D_h	Hydraulic diameter
D_p	Parent's tube diameter, m
$D_{T_{ave}}$	Average diameter of the trachea, m
d	Diameter of each Weibel airway, m
d_p	Particle diameters, μm
F_P	Force acting on the particle, N
f	Frequency, Hz
Gi	Generation number i
$\bar{g}_{ij}$	Velocity gradient tensor
h_p	Distance from the wall to the particle, m
i	Imaginary number, $\sqrt{-1}$
J_o	Zeroth Bessel function of the first kind
k_B	Boltzman constant, $(m^2\ kg)/(s^2 K)$
L	Length of each Weibel segment, m
m_p	Mass of the particle, kg
$\hat{n}$	Unit wall normal vector
P	Pressure applied by the ventilator, Pa
P_{am}	Pressure Amplitude, $cm\ H_2O$

$P_{H,i}$	Mass fraction obtained from Horsfield model for branch *i*
p_k	Mass flow rate fraction at outlet *k*
P_{mus}	Pressure due to the respiratory muscles, *Pa*
$p(t)_{outk_j}\Big\|_{\Delta p-resist}$	Total pressure loss from the outlet k^{th} outlet of the CT model (in G*j*) to the alveoli due to resistance, *Pa*
$p(t)_{outk_j}\Big\|_{\Delta p-comp}$	Total Pressure loss due to compliance at outlet k^{th} outlet of the CT model (in G*j*), *Pa*
Q	Inlet Flow rate, m^3/s
$Q_{\max}$	Peak flow rate , m^3/s
Q_u	Flow rate in the mother tube, m^3/s
Q_1	Flow rate in the daughter tube 1 (branches 1), m^3/s
Q_2	Flow rate in the daughter tube 2 (branches 2), m^3/s
$q_b(t)\Big\|_i$	Flow rate in each branch of G*i* of Weibel model, m^3/s
$q_{inlet}(t)$	Instantaneous flow rate at ETT inlet, m^3/s
$q_k(t)$	Instantaneous flow rate at k^{th} outlet, m^3/s
$q(t)_{outk_j}$	Instantaneous flow rate at outlet number *k* (in G *j*), m^3/s
R	Resistance, $H_2O/(l/s)$
R_{ETT}	Radius of the endotracheal tube, *m*
R_L	Poiseuille (laminar) resistance, $H_2O/(l/s)$
R_{TB}	Global tracheobronchial resistance, $H_2O/(l/s)$
R_τ	Relaxation time ratio
r	Radial distance, *m*
$\bar{S}_{ij}$	Strain rate tensor.
S_{ij}^d	Traceless symmetric part of the square of the velocity gradient tensor
T	Total cycle time, *s*
T_f	Absolute temperature of the fluid, *K*
TKE	Turbulent kinetic energy, m^2/s^2
t	Time, *s*
$\hat{t}$	Unit wall-tangent vector
U	Velocity, *m/s*
$U(t)$	Sinusoidal velocity, $U(t) = u_{amp}\sin(2\pi ft)$, *m/s*
U_{ave}	Averaged velocity, *m/s*
U_{mean}	Mean velocity, *m/s*
$U_{T\max}$	Maximum velocity at the trachea, *m/s*
u_{amp}	Amplitude velocity, $u_{amp} = fV_t / R_{ETT}^2$, *m/s*
$\bar{u}_i$	Filtered (resolved) i^{th} velocity, *m/s*

$u_i^{'}$	Fluctuation velocity, *m/s*
$u_m(t)$	Mean velocity obtained from HFOV waveform, *m/s*
u_P	Particle velocity, *m/s*
u''	Unresolved velocity component, *m/s*
u_τ	Frictional velocity, *m/s*
$u(r,t)$	Inlet velocity profile, *m/s*
V	Volume, *ml*
V_r	Radial component of velocity, *m/s*
V_p	Particle volume, m^3
V_T	Tidal volume, *ml*
V_{T1}	Volume exchanged between the daughter branches (branch 1 at EnIn), *ml*
V_{T2}	Volume exchanged between the daughter branches (branch 2 at EnEx), *ml*
V_u	Volume delivered to the unit , *ml*
WP	Wetted perimeter, *m*
x_i	i^{th} position component, *m*
x_p	Position of the particle, *m*

Greek Symbols

α_{ETT}	Womersley number based on the ETT diameter
α_τ	Womersley number based on the trachea diameter
β	Angle between the main bronchi
γ_p	Mean x-ray attenuation coefficient of the pixel
γ_w	Mean x-ray attenuation coefficient of water
$\dot{\gamma}$	Shear rate, *1/s*
Δ	Filter cutoff width, *m*
δ	Stokes layer thickness, $\delta = \sqrt{\upsilon / \pi f}$, *m*
ε	Turbulence dissipation rate, m^2/s^3
ζ	Random number
η	Kolmogorov length scale, $\eta = (\upsilon^3 / \varepsilon)^{1/4}$, *m*
λ	Mean free path, *nm*
μ	Fluid dynamic viscosity, *kg*/(*s m*)
ν	Kinematic viscosity, m^2/s
υ_{sgs}	Subgrid eddy viscosity, m^2/s
ρ	Fluid density, kg/m^3
ρ_p	Particle density, kg/m^3
τ	Time constant, *s*
τ_{ij}	Subgrid-scale stress
ω	Angular velocity, *rad/s*

Dimensionless Numbers

$\mathrm{Re} = DU/\nu$	Reynolds number
$\mathrm{Re}_{ETT} = 4fV_T/\nu D_{ETT}$	Reynolds number based on ETT inlet
$\mathrm{Re}_T = D_{T_{ave}} U_{T\max}/\nu$	Peak Reynolds number based on trachea mean diameter and maximum velocity
$\mathrm{Re}_\tau = D_{T\,ave} U_{mean}/\nu$	Reynolds number based on trachea mean diameter and mean velocity
$\mathrm{Re}_\delta = U\delta/\upsilon$	Stokes layer Reynolds number
$y^+ = u_\tau y/\nu$	Dimensionless wall distance
$Kn = 2\lambda/d_p$	Knudsen number
$St = \rho_p d_p^2 u/18\mu L$	The Stokes number
$\alpha = a\sqrt{\omega/\nu}$	Womersley number

Acronyms

ALI	Diseases such as acute lung injury
ARDS	Acute respiratory distress syndrome
BCs	Boundary conditions
CFD	Computational fluid dynamics
CFL	Courant–Friedrichs–Lewy
CMV	Conventional mechanical ventilation
COPD	Chronic obstructive pulmonary disease
CR	Compliance ratio
CR_{Local}	Local compliance ratio variation
CT	Computed tomography
DF_G	Global deposition fraction
DF_L	Local deposition fraction
DF_t	Transient particle deposition fraction
DICOM	Digital Imaging and Communications in Medicine
DNS	Direct numerical simulation
EaEx	Early expiration phase
EaIn	Early inspiration phase
EnEx	End expiration phase
EnIn	End inspiration phase
ERV	Expiratory reserve volume
ETT	Endotracheal tube
FR	Flow distribution ratio
FRC	Functional residual capacity
f_{P}	Pendelluft time percent
f_{PI}	Percent of the lead and lag time to the inspiratory time
HFOV	High frequency oscillatory ventilation
HU	Hounsfield units
IC	Inspiratory capacity
ICU	Intensive care units

IRV	Inspiratory reserve volume
LDA	Laser Doppler anemometry
LES	Large eddy simulation
LL	Left lung
LLL	Left lower lobe
LUL	Left upper lobe
MB	Main bronchi
MF	Mass Fraction
MRI	Magnetic resonance imaging
RANS	Reynolds Averaged Navier Stokes
R&C	Resistance and Compliance
RL	Right lung
RLL	Right lower lobe
RML	Right middle lobe
RMS	Root mean square
RUL	Right upper lobe
RV	Residual volume
SFS	Secondary flow strength
SGS	Subgrid scale stress
STL	Stereolithography
TB	Tracheobronchial tree
TLC	Total lung capacity
T_P	Elapsed time during the pendelluft flow
VC	Vital capacity
VILI	Ventilator-induced lung injury
V_p	Pendelluft volume percent
VR	Air volume ratio
WALE	Wall-adopting local eddy viscosity
WSS	Wall shear stress

ABSTRACT

The objective of this dissertation research was to investigate gas transport, mixing and aerosol-drug delivery during high frequency oscillatory ventilation (HFOV) for various ventilator specific conditions that are vital to critical care clinicians. A large eddy simulation based computational fluid dynamics approach was used in a patient specific human lung model to analyze the effect of invasive HFOV on patient management. Different HFOV waveform shapes and frequencies was investigated and the square waveform was found to be most efficient for gas mixing; resulting in the least wall shear stress on the lung epithelium layer thereby reducing the risk of barotrauma to both airways and the alveoli for patients undergoing therapy. Traditional (outlet) boundary conditions based on mass fraction or outlet pressures were found to be inadequate in describing the complex flow physics that occurs during HFOV. Physiological boundary conditions that used the time-dependent pressure coupled with the airways resistance and compliance (R&C) were derived and used for the first time to investigate the lung lobar ventilation and gas exchange for accurate HFOV modeling.

A Lagrangian approach was then used to model gas-solid two-phase flow that allowed investigation of the potential of aerosol-drug delivery under HFOV treatment. We report, for the first time, computational fluid dynamics studies to investigate the possibilities of aerosol drug delivery under HFOV. Understanding the role of different carrier gases on the gas exchange and particle deposition, which may allow for optimum drug delivery and ventilation strategy during HFOV. Increasing the operating frequency resulted in a significant change in the global and local deposition indicating strong dependency on the frequency, which could be beneficial for the targeted drug delivery.

The global deposition as a fraction of the total injected particles at the endotracheal tube inlet was equivalent to the cases of normal breathing and conventional mechanical ventilation signifying a potential for efficient drug delivery during HFOV. In addition, HFOV had a unique characterization of the local particle deposition due to the rapid ventilation process and a strong influence of the endotracheal tube jet.

Very often during ventilation therapy, a clinician uses a cocktail of various gases to enhance targeted therapy. To quantify this process for a futuristic HFOV based patient management, we undertook detailed studies to understand the role of carrier gas properties in gas exchange and particle transport during HFOV. A substantial amplification of the pendelluft flow was achieved by utilizing a low-density carrier gas instead of air, which resulted in gas exchange improvement. Reducing the carrier gas density was found to significantly alter the aerosol-drug delivery under HFOV management. As the density decreased, the deposition fraction in the upper tracheobronchial tree decreased, indicating enhancement of the lung periphery delivery. Furthermore, the filtered aerosol-drug in the ventilator circuit could be significantly reduced by using Heliox, and further reduction could be achieved by reducing the operating frequency. In general, high-frequency oscillatory ventilation therapy could be improved under Heliox with greater content of Helium, thereby reducing the lung hyperinflation risk.

CHAPTER 1

INTRODUCTION AND OVERVIEW

1.1.Respiratory Function

Natural inhalation is driven by the generation of a negative force, which is controlled by muscles and the lung compliance. The contraction of the diaphragm expands the thorax, creating a negative pressure inside the airways, which is below the atmospheric pressure at the nasal/mouth opening [1, 2], see Figure 1.1. The pressure difference drives the airflow from outside (ambient) throughout the extrathoracic passages all the way to the gas exchange zone in the lungs (i.e. alveoli). The exhalation process is passive; the diaphragm expands allowing the lung to recoil due to lung elasticity and return to its normal size creating higher pressure inside the airways relative to the ambient environment. Consequently, the pressure difference drives the gas in the opposite direction out of the lungs, see Figure 1.1. The process of inhalation/exhalation could be entirely collapsed during respiratory failure, which is life threatening if suitable support is not provided quickly enough.

Respiratory failure is a syndrome in which the respiratory system fails to achieve adequate gas exchange [1-3]. Mortality rates associated with respiratory failure due to various pulmonary diseases is at par with mortality figures due to breast cancer or HIV [3-6]. Respiratory failure is classified as hypoxemic or hypercapnic, the former is a condition in which there is a deficiency of oxygen in the arterial blood; while the later occurs due to elevated levels of carbon dioxide elimination occurs, respectively. The failure of respiratory function is not considered a disease *per se* but a byproduct of other diseases or conditions [1, 2]. These are summarized in Table 1.1 below.

Table 1.1 Common diseases cause respiratory failure.

Disease	**Cause and condition**
Chronic obstructive pulmonary disease (COPD)	Airway damage resulting in pathological changes and limiting of the airflow in and out of the airways
Acute respiratory distress syndrome (ARDS)	Acute lung injury causing serious airway abnormality and shortness of breath
Chest injury	Damage to the tissues and ribs around the lungs due to chest injury, which causes inability to breath
Toxic inhalation	Inhalation of harmful and toxic agents such as smoke and fumes, resulting in lung injury
Asthma	Infections and allergies cause airway inflammation, in turn causing wheezing and shortness of breath
Chronic bronchitis	Inflammation of the bronchial airways resulting in sputum that could narrow or cause airway closure
Emphysema	Air trapped due to airway damage leading to difficult breathing.
Acute bronchitis	Viral or bacterial infection of the lungs resulting in shortness of breath
Cystic fibrosis	A genetic condition causing poor clearance of mucus from the bronchi; the accumulated mucus results in repeated lung infections

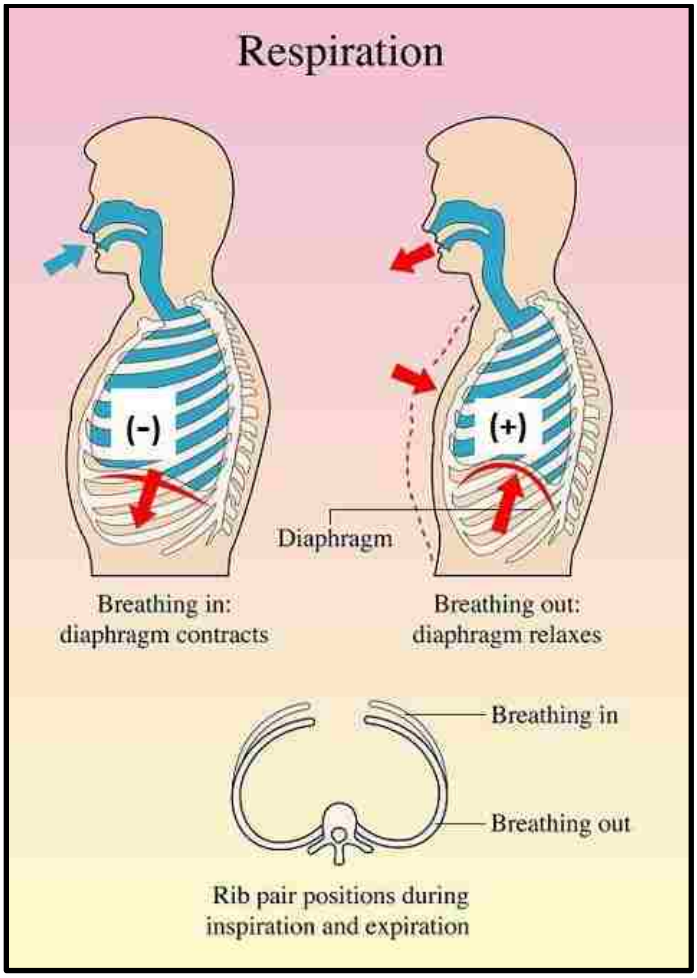

Figure 1.1 Representation diagram of the inhalation and exhalation process under normal breathing [7].

1.2. Mechanical Ventilation

Mechanical ventilation intervention to substitute spontaneous breathing and maintain adequate gas exchange is mandatory for patient support during respiratory failure. The mechanics of inhalation in supported breathing fundamentally differs from normal breathing. The mechanical ventilator creates differential pressure by applying a positive pressure above atmospheric, either at the nasal/mouth opening (in the case of

noninvasive ventilation) or at the endotracheal tube opening (in the case of invasive ventilation); thereby driving air or a mixture of various gases into the lungs. This type is known as positive pressure ventilation [1, 2, 8].

1.2.1. Conventional Mechanical Ventilation

Conventional mechanical ventilation (CMV) is used to replace the patient's spontaneous breathing and delivers a tidal volume of 6-10 ml/kg [2, 9, 10] at a breathing rate (frequency) ranging from 12- 40 breaths/minutes (0.2 – 0.67 Hz). The tidal volume is defined as the total air volume inhaled during a single breath. It is greater than the anatomical dead space in the conducting airways and allows the gas to transport by a bulk convection mechanism. The use of CMV is, however, not always a safe intervention in many cases.

1.2.2. Ventilator-Induced Lung Injury

CMV is associated with several risks that leads to complications in the patient. In many critical situations, it exacerbates the illness conditions and leads to lung injury, a condition referred to as ventilator induced lung injury (VILI). A common cause of VILI during CMV is the large tidal volume which results in lung over-distention (volutrauma) or lung damage due to excessive pressures (barotrauma) [1, 2, 11]. Airway and alveoli damages due to abnormal mechanical stress (i.e. shear stress) exerted at the airways walls is also a common cause of lung injury. The wall shear stress could be amplified due to phenomena variety of factors. The presence of intubation is seen to cause high-speed jet impingement at the trachea-carina ridge, which leads to high wall shear stress at the upper airways [12]. The airways obstructions and asymmetry in compliance between lung

units could produce higher velocity and velocity gradient along small airways, which is a mechanism that may increase the wall shear stress [13]. Lung injury and damage of the airways epithelium cells could be initiated as a consequence of the shear stress. Airway collapse and reopening applies additional stress at the alveoli, leading to an injury known as Atelectrauma [14-16]. Table 1.2 summarizes the common VILI causes and their mechanisms. An alternate form of ventilation that involves high frequency oscillatory flow, commonly known as HFOV is used to avoid complications arising from CMV while maintaining adequate gas exchange [1, 2, 17] .

Table 1.2 Forms of VILI and mechanism of occurrence.

Type of VILI	Mechanism
Volutrauma [1, 2]	Lung over-distention associated with high tidal volume under CMV.
Barotrauma [1, 2]	Lung injury due to excessive pressure under CMV.
Atelectrauma [14-16]	Abnormal mechanical stress that is applied to the alveoli and small airways due to fluid occlusion during airways collapse and reopening.
Biotrauma [16, 18-20]	Alveoli damage and inflammatory response to shear stress injuries secondary to atelectrauma.
Shearing injury [12, 13, 16, 20-22]	Airways epithelium cell rupture and inflammation due to high wall shear stress.
Oxygen toxicity [23, 24]	Toxicity by oxygen overexposure leading to surfactant impairment.

1.2.3. High Frequency Oscillatory Ventilation

Different mechanical ventilation modes were developed to reduce or avoid the lung injury associated with CMV. Lung ventilation by high frequency oscillation has become an alternative way to maintain adequate gas exchange while at the same time protecting against lung injury. This mode has been utilized for decades. It was first described in 1952 but not clinically used until early 1970s. Originally used only for infants and children, it was not approved for adults until recently (2001) [17]. The principles of ventilation strategy during high frequency oscillatory ventilation (HFOV) are different from CMV and normal breathing (Table 1.2). A very small tidal volume of ~1-2 ml/kg is delivered at high operating frequencies of 1 - 30 Hz [2, 17, 25, 26]. Furthermore, in CMV the lung is set to expire the air from the lung naturally, i.e. passive expiration; during HFOV, however, expiration is active.

Table 1.3 Comparison between CVM and HFOV.

characteristics	CMV	HFOV
Frequency	12- 40 bpm (0.2-0.67 Hz)	60-3000 bpm (1- 50 Hz)
Tidal volume	6-10 ml/kg	1-2 ml/kg
Inspiration	Active	Active
Expiration	Passive	Active

To achieve gas exchange in the lung, the delivered tidal volume must exceed dead space volume [27]. The delivered tidal volume during HFOV is less than the anatomical dead space volume, which disputes the principal of gas exchange occurrence [27]. It is

therefore believed that gas transport under HFOV strategy cannot be achieved by only a bulk convention mechanism and there are other mechanisms contributing to the process. Previous studies [28-31] have identified several complex flow mechanisms that play a role in gas transport and mixing during HFOV. However, those complex mechanisms are not fully understood [28, 30]. A schematic diagram of the mechanisms of gas transport during HFOV is presented in Figure 1.2. These mechanisms have been classified and defined as follows:

1) **Bulk convection** which contributes to the ventilation; however, unlike the CMV, it only impacts the proximal alveoli.
2) **Taylor-dispersion** (or augmented diffusion) that is defined as the interaction between the axial velocity and radial concentration gradient.
3) **Pendelluft mechanism** which is defined as the asynchrony of the time constant due to variation of respiratory units resistance (R) or compliance (C). This causes gas exchange between the adjacent lung units [32].
4) **Coaxial counter flow** which occurs when the flow switches between inspiration and expiration phases (and vice versa). The flow with higher momentum through the middle of the airways lags behind while the gas at the vicinity of the walls respond on time and flow in phase. Consequently, a net convective mixing occurs.
5) **Cardiogenic gas mixing** that occurs due to the cyclic movement of the heart.
6) **Molecular diffusion** that plays an important role in gas exchange at the alveolus.

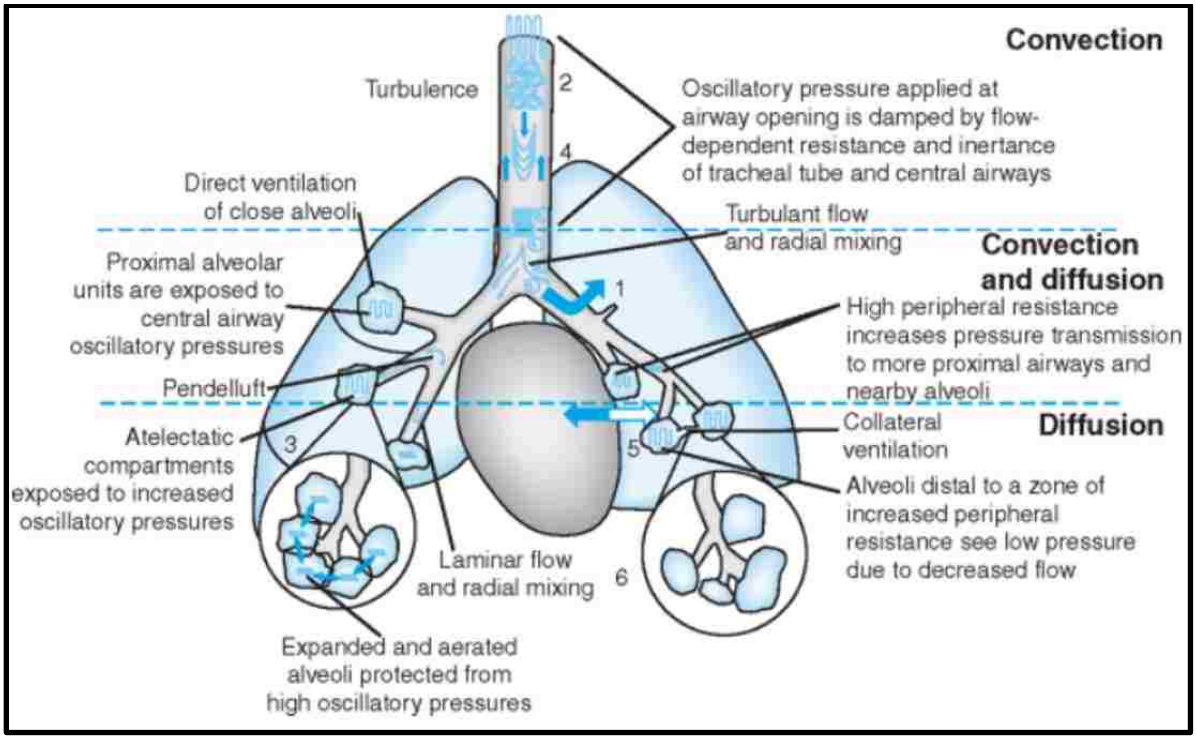

Figure 1.2 Mechanisms of gas transport during HFOV management. 1) bulk convection, 2) Taylor-dispersion, 3) pendelluft flow, 4) coaxial counter flow, 5) cardiogenic mixing, and 6) molecular diffusion [2, 33].

1.3. Aerosolized Drug Delivery

The respiratory tract has recently become an attractive route for drug delivery, as the lung has the capability for absorbing pharmaceuticals either for local or systemic delivery [34]. Although mechanical ventilation is used to facilitate the patient's breathing [35], in many situations, especially in long-term administration, aerosol drug delivery is inevitable during the ventilation process [36, 37]. The aerosolized form of the drug is delivered for local treatment, such as ephedrine for nasal decongestion, beta-2 agonists for bronchodilation, and to combat inflammation in diseased airways such as from asthma and COPD [38]. It has also become a preferred route for systemic delivery: insulin for diabetes therapy, pain management, cancer therapy, and nano-therapeutics.

This preference is due to many advantages that the lung route offers for health care. It avoids the traditional invasive methods of delivering drugs into the bloodstream (injection), avoids gastrointestinal tract problems (oral delivery), and lessens side effects because there is no exposure to the drug for the rest of the body. One of the most attractive factors is that the lung has a large surface area ~ 70-140 m^2, which allows for excellent absorption and exchange with the bloodstream [38]. Pulmonary drug delivery, however, is still a challenging task [34, 39]. For example, to achieve optimum drug delivery (i.e. result in efficient treatment, reduce side effects and be cost-effective), the drug should be directed from the release point to a predetermined site. This process of targeted drug delivery, however, needs to optimize many factors that affect aerosol transport, such as drug-particle characteristics (size), inhalation waveform, and particle release point [39]. Furthermore, drug delivery to a mechanically ventilated patient is very complex, and a very low amount of aerosols successfully reach the lower lung sites due to the many complications that arise during therapy management procedures [37, 40, 41]. This complexity increases during invasive HFOV because of very rapid ventilation and low tidal volume [42]. Efficacy of aerosol deposition relies on various parameters [37, 41]:

(a) **Ventilator related**: these include ventilation mode, tidal volume, respiratory rate, duty cycle, inspiration waveform, and the breath-triggering mechanism.

(b) **Circuit related**: endotracheal tube size, humidity and density of inhaled gas.

(c) **Device related**: the type of device (nebulizer, metered dose inhaler, or dry powder inhaler), fill-volume, gas flow, cycling (inspiration vs. continuous), duration, and timing of actuation.

(d) **Drug related**: dosage, formulations, particle size, targeted site for delivery, and duration.

(e) **Patient related**: age, ethnicity, severity of airway obstruction, mechanism of obstruction, presence of dynamic hyperinflation, and patient ventilator synchrony.

Due to a lack of specific knowledge regarding the role of these factors, producers of ventilator machines currently recommend disconnecting the patient from a HFOV and applying manual ventilation during inhaled drug administration [42]. This, however, could possibly be harmful to the patient [42].

1.4. Motivation and Objective

1.4.1. Research Motivation

The dissertation research was motivated by several unresolved issues associated with understanding pulmonary fluid dynamics and aerosol-drug delivery during HFOV. Although HFOV has become a common therapy, its outcomes are, however, still unclear and is the topic of much debate amongst clinicians [43, 44]. Pulmonary flow physics based on HFOV management strategy is very complex and is not yet fully understood. The variation in the frequency and shape of the HFOV waveform plays an important role in gas transport and exchange [21, 45]. Little attention is given to the shape of the HFOV waveform, as the majority of the earlier work used a sinusoidal approximation [21, 45]. This gap should be bridged to understand HFOV fluid dynamics for clinically relevant conditions. It is well documented in the literature that the shape of the HFOV waveform is machine/manufacturer-specific and is characterized by different acceleration /deceleration patterns [45]. Moreover, the presence of intubation has a strong effect on

the flow structure during HFOV and is critical for understanding flow conditions that can lead VILI.

For CFD modeling of pulmonary gas dynamics, traditional boundary conditions are used at the domain outlets. It is classified as follows: Type-I boundary condition where a flow rate, or velocity at each outlet is specified, Type-II boundary condition where uniform pressure is used, and Type-III boundary condition where the mass fraction (MF) at each outlet of the statistical lung models is imposed. These boundary conditions, however, do not account for non-uniformity of the lung ventilation [46]. Furthermore, gas exchange between adjacent units cannot be captured due to the absence of consideration of asymmetry in compliance and resistance of these units. Various CFD studies have modeled HFOV with these types of outlets' boundary conditions [47, 48]. However, the pendelluft flow was either not observed [47] or observed merely due to geometry asymmetry at the main bronchi [48]. Physiologically relevant boundary conditions will accurately predict lung lobar ventilation and are vital to fully capture all the dominant flow mechanisms that occur during HFOV. The pendelluft flow between lung units and the existence of asymmetric units compliance significantly contribute to wall shear stress in the small pathway, which could play a vital role in lung injuries.

The feasibility of drug delivery during high frequency ventilation management has long been dubious due to the numerous challenges associated with this ventilation mode, and is not sufficiently understood. However, the potential of drug delivery during HFOV is a current topic of debate in the medical community [42, 49]. Due to insufficient knowledge regarding the role of the ventilator parameters and patient-related factors,

ventilator machines producers currently recommend disconnecting the patient from HFOV and applying manual ventilation during inhaled drug administration [42], a recombination that could potentially be harmful to the patient [42]. In addition, there are only limited *in vitro* and *in vivo* studies of flow and aerosol transport in the lung during HFOV [42, 50]. Despite the great contribution of these studies, they entail many flaws, such as the lack of predicting the regional deposition of aerosols. In addition, patient-related parameters such as airway geometry, pulmonary disease, and exhaled aerosols were not considered. Further and extensive investigations are therefore required in order to understand and optimize aerosols transport during HFOV [37, 42]. Detailed and validated CFD could be an alternative route to study and understand drug delivery during HFOV. The realistic model and physiological boundary conditions would allow, for the first time, to quantify aerosolized drug delivery to the lungs under HFOV conditions, which could be efficient depending on the ventilation strategy. The developed drug delivery model under HFOV conditions will provide an opportunity to investigate the effect of different carrier gases on the particle transport during HFOV. The carrier gas properties will have a strong impact on the gas and particle transport, which may drastically change the flow field and particle motion allowing optimum HFOV therapy.

1.4.2. Research Objectives

The main objective of the dissertation is to develop an accurate computational fluid dynamic model using a high order turbulence model to investigate the following unresolved problems of gas and particle transport in the patient specific human lung under invasive HFOV therapy and various lung conditions:

i. Investigate various (ventilator) device-specific conditions that are vital to critical care clinicians.

ii. Study the effects of the presence of intubation (ETT) on the gas transport and lung injury.

iii. Test the efficacy of traditional boundary conditions on gas exchange and particle transport under HFOV and develop a physiologically relevant boundary condition that is capable to predict the lung lobar flow redistribution and capture the crucial gas transport mechanisms.

iv. Analyze the potential of the aerosol-drug delivery under HFOV using physiologically relevant boundary conditions and demonstrate the important mechanisms that influence the particle dynamics under rapid ventilation process. In addition, enhance HFOV therapy by investigating the role of the carrier gas on the gas exchange and particle deposition.

The dissertation aims to provide deeper insight into the fundamental mechanisms of gas transport and mixing in a transient turbulent flow that occurs in a branched complex system like the human respiratory tract. A systematic study would allow for: (i) advancement in the current understanding of the flow mechanisms during HFOV; (ii) enhance the accuracy of CFD modeling of gas and aerosol transport under HFOV; (iii) provide guidelines that may lead to optimizing ventilator management protocols and treatment under HFOV and assess particle deposition rates and patterns for clinically relevant conditions; and, (iv) provide a systematic pathway for diagnosing lung diseases and severity.

1.4.3. Procedures

To achieve the objectives of the dissertation, the present study was conducted as follows:

i. Reconstructed a large-scale patient-specific human lung model using medical computed tomography (CT) scans for a mechanically ventilated patient.

ii. CFD simulations using a high order turbulent model to properly capture impotent flow physics were conducted. Large eddy simulation was implemented.

iii. The equation of motion (pressure as a function of the flow rate and lung resistance and compliance) that governs the flow during mechanical ventilation was used to create various commonly used ventilator pressure-controlled waveform shapes and applied at the model inlet. Intubation was represented by invasive endotracheal tube (ETT).

iv. Developed, validated and implemented boundary conditions based on physiological properties. Time-dependent pressure boundary conditions were developed and applied to the realistic lung model based on airways' coupled resistance-compliance.

v. FORTRAN subroutines were used to implement Lagrangian approach to model the aerosol-drug transport under HFOV parameters and different lung conditions. Detailed analysis and quantification of the global and local deposition fraction of the particles in a realistic large-scale lung model were presented.

vi. Gas exchange and particle transport under various carrier gases with a wide range of density and kinematic viscosity under rapid ventilation process were tested.

1.5. DISSERTATION OVERVIEW

The dissertation is divided into eight chapters. Following chapter 1, the respiratory tract descriptions and a literature review of the classical lung models are presented in chapter 2. Details of the procedures and methods for reconstructing the present patient specific lung model are discussed and demonstrated. In chapter 3, the procedures of meshing the obtained complex geometry are discussed. In addition, detailed descriptions of the numerical techniques along with the grid independence studies and validation exercises with available experimental data from the literature are provided. We review existing numerical and experimental studies of flow transport under HFOV in chapter 4. The specifics of ventilator waveform shapes and implementation as relates to our CFD study are presented. In addition, a convergence study—depending on the number of ventilation cycles—is conducted and discussed. It is followed by details of the outlet boundary conditions application based on the classical model of Horsfield *et al* [51]. The results are presented and discussed in terms of the coaxial counter flow patterns, existence of the pendelluft mechanism, and flow structures. The lung injury due to wall shear stress and conclusion of the best and safest HFOV setting are discussed. Chapter 5 discusses the derivation, validation and employment of physiological outlet time-dependent pressure boundary conditions. In addition, a review of the traditional boundary conditions and their capability of resolving flow mechanisms under HFOV is presented. The role of airways coupled resistance-compliance during HFOV is discussed; the results are presented in terms of airflow redistribution in the lung lobes under different ventilator parameters and lung conditions. The captured pendelluft flow throughout the lung model is characterized. The use of coupled resistance-compliance

boundary conditions is also compared to the traditional boundary conditions. Chapter 6 is devoted to exploring the drug delivery during HFOV. A Lagrangian approach to model particle transport under HFOV conditions is validated and discussed. Detailed quantification of the total and regional particle deposition is demonstrated. The discussion of the potential of drug delivery during ventilation by high oscillation frequency is given. Last, the efficacy of HFOV therapy is investigated in light of the comparison with drug delivery under normal breathing and conventional mechanical ventilation. Chapter 7 addresses the role of carrier gas properties on the gas exchange and aerosol-drug delivery during HFOV management. The effects of gas density and kinematic viscosity on the turbulence, airways resistance, gas transport, and particle deposition are presented. The enhancement of HFOV therapy is discussed. Chapter 8 presents conclusions and limitations of the current research and several future directions are discussed.

CHAPTER 2

PATIENT-SPECIFIC MODEL RECONSTRUCTION

2.1. Pulmonary Anatomy and Physiology

The human respiratory tract is a system of gas passages with complex and dynamic structures [1, 2, 34, 39, 52, 53]. It is divided into three regions based on anatomy: (a) the extrathoracic region, which includes the oral cavity, the nasal cavity, the pharynx, the larynx, and the upper part of the trachea; (b) the upper bronchial region, which includes the main bronchi; and (c) the lower bronchial region, comprised of the bronchioles and the alveolar region [1, 2, 34, 39]. Figure 2.1 presents detailed information and illustrations for the respiratory tract anatomy [54].

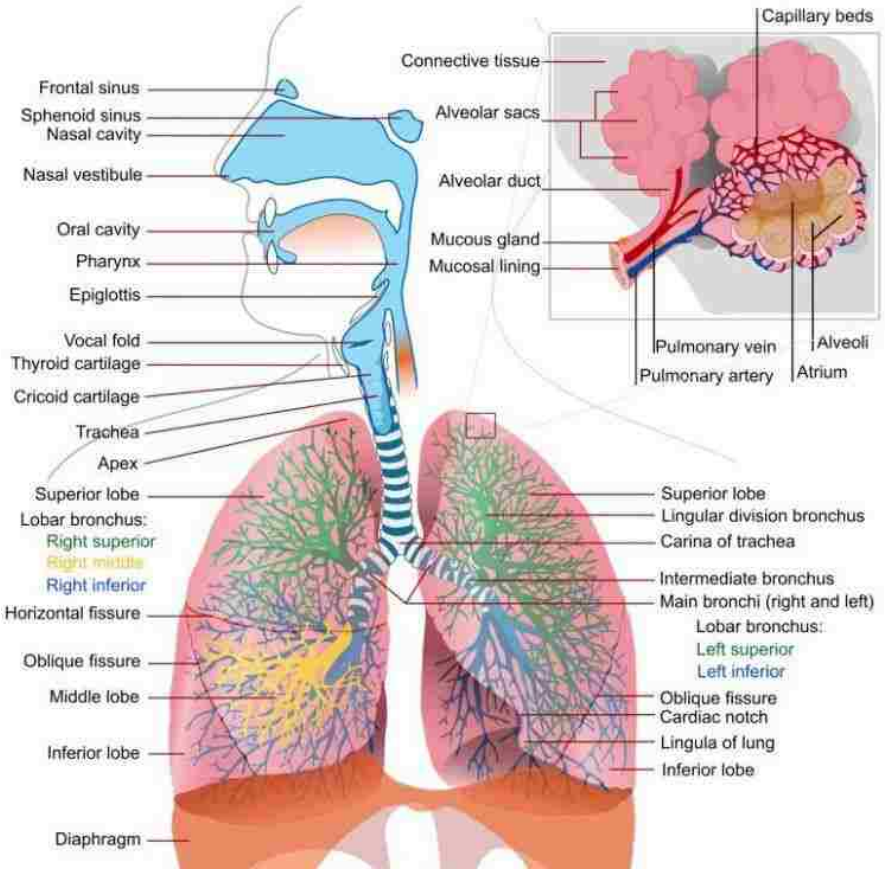

Figure 2.1 Schematic for human respiratory tract [54].

The present study focuses on invasive mechanical ventilation. In this type of ventilation, an endotracheal tube is inserted through either nose or mouth to a certain level in the trachea [55-58]. The extrathoracic region therefore has no role on the gas and aerosol transport under invasive ventilation strategy. For this reason, the segmentation processes and model configurations include only the upper tracheobronchial tree along with intubation.

2.1.1 Tracheobronchial Tree

The regions from the trachea and the bronchi, and bronchioles is termed the tracheobronchial tree (TB) [34, 39, 59], primarily due to the fact that at the end of the trachea, the tracheobronchial tree bifurcates or branches into right and left lungs constituting tree-like structures [39]. The two lungs are asymmetric and constitute a network of hollow tubes. Each tube, which is called a "mother" or "parent" branch, bifurcates into two branches called "daughter" branches. Figure 2.2 displays a single representative bifurcation tube and the most popular terminologies for the bifurcated

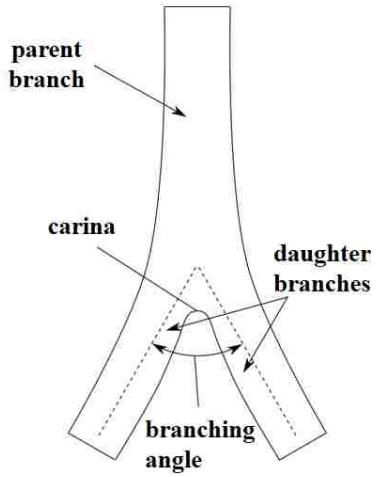

Figure 2.2 Bifurcation terminologies.

airways segment. The branch angle is the angle between the two daughter branches of a bifurcation. The ridge-like area that divides the flow between the daughter tubes is called a carina. The airways network are then progressively bifurcated into smaller airways without overlapping, which decreases in diameter and length at each branching [39, 53]. The airways after each bifurcation are considered to be in a new generation; and each bronchial generation is assigned a number starting—at the trachea—from zero (i.e. generation zero, G0), progressing to G1 at the main bronchi and so forth up to generation (G23) at the end of the TB, see Figure 2.3 [39, 53].

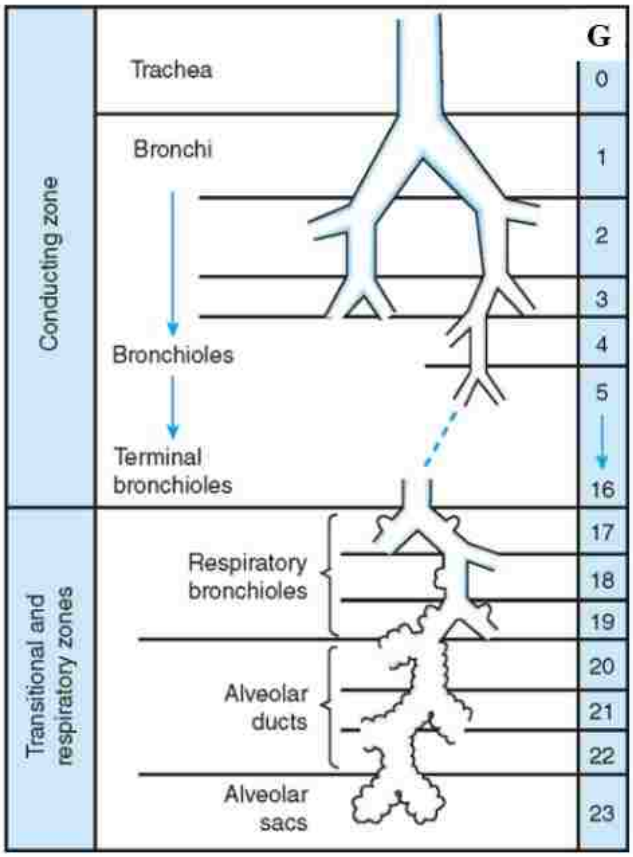

Figure 2.3 Schematic diagram of the human tracheobronchial tree, its division and airways generations [39, 59, 60]. Adopted with permission from Elsevier publishing.

The number of airways in each generation is approximately double that of the previous generation. Since the airways consist of 23 generations, the total tracheobronchial tree encompasses a total of 2^{23} airways in addition to millions of alveoli [34, 61]. Cartilaginous rings exist around the upper airway segments. The main functions of the cartilages are to maintain stiffness and prevent all of these airways from collapsing. The trachea has about 16 – 20 cartilaginous C-shaped rings , which continue to the subsequent airways, the shape and size gradually changing and decreasing as the generation number increases [39].

The tracheobronchial tree is functionally separated into different regions. With a focus on respiratory function, the respiratory tract is divided into a conducting zone and respiratory zone [34]. The conducting zone extends from G0 at the trachea up to G16. The function of the conducting zone is to convect the gas from the larger airways to the small airways; therefore, the gas exchange does not occur in this zone. Between the conducting and respiratory zones, there is a transitional zone constituted by respiratory bronchioles, where the gas continues through, moving to lower airways while some gas exchange starts taking place. The respiratory zone consists of alveolar ducts and sacs where the primary function is gas exchange [62]. Schematic diagrams for the tracheobronchial tree division based on function and generations are presented in Figure 2.3.

The lung is anatomically further subdivided into five major lobes (Figure 2.4). The left lung encompasses two major lobes: the left upper lobe (LUL) and left lower lobe (LLL). The right lung is divided into three major lobes: right upper lobe (RUL), right middle lobe (RML) and right lower lobe (RLL). The airways wall is lined with

epithelium cells [63, 64]. The airway epithelium has a major role in heating and conditioning the inhaled gas [39, 65]. Furthermore, it is a primary line of defense against pathogens and particulates inhaled from the environment [66]. The epithelium contains several cell types: ciliated, goblet, brush, and basal cells [67, 68]. In a diseased lung, the function of the airway epithelium is affected by local inflammation. This causes hypersecretion of mucus resulting in airway closure problems [69-72].

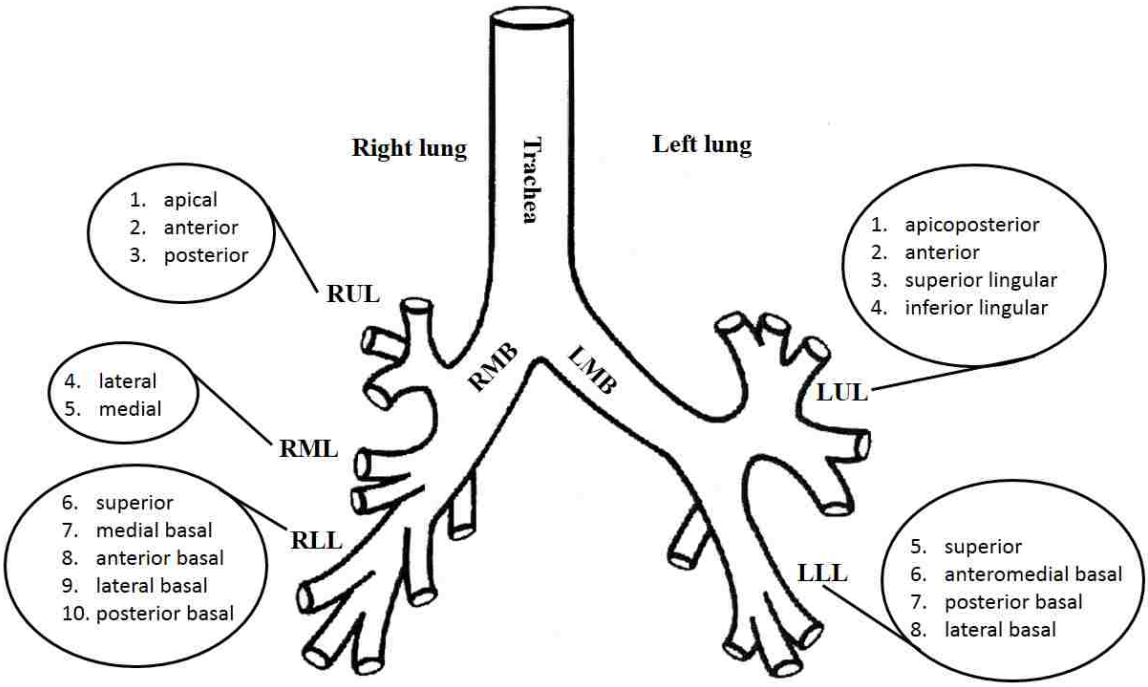

Figure 2.4 Lung major lobes and subdivisions. **RMB**: right main bronchus. **LMB**: left main bronchus. **RUL**: right upper lobe. **RML**: right middle lobe. **RLL**: right lower lobe. **LUL**: left upper lobe. **LLL**: left lower lobe.

2.1.2. Lung Volume and Capacity

The amount of the air in the lung can be subdivided into different volumes and capacities. Figure 2.5 explains the terms and divisions of the lung volumes [2, 39, 73]. Approximately 1/10 of the total lung capacity is used during normal breathing at rest

whereas higher amounts are delivered when exercising [2, 39]. The tidal volume is defined as the volume of gas that is inhaled and exhaled in a single normal inspiration or expiration. The volume of air existing in the lungs after a deep inhaled breath is called the

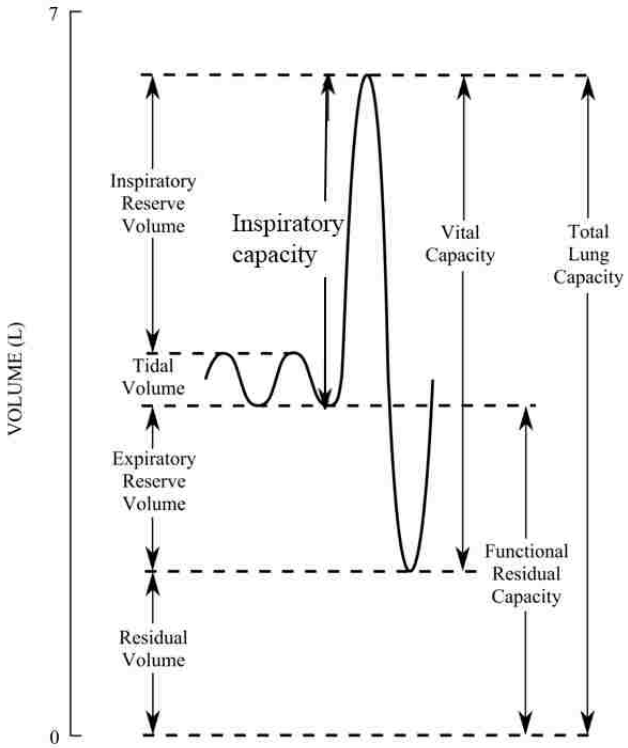

Figure 2.5 Lung volume definitions and capacities [73].

total lung capacity (TLC). Even with maximum effort to fully expire all the air occupying the lung, a residual volume (RV) exists. The result of the difference between the residual volume and the total lung capacity constitutes the vital capacity (VC). The inspiratory reserve volume (IRV) is the maximum volume of air that can be inspired above a normal tidal inspiration, and the expiratory reserve volume (ERV) is the maximum volume of air that can be exhaled after expiration of a normal tidal volume. The volume of maximum inhalation is the sum of the inspiratory reserve volume and the tidal volume, which is

known as the inspiratory capacity (IC). The sum of the expiratory reserve volume and the residual volume results in the functional residual capacity (FRC), which constitutes the volume of air that remains in the lungs after a normal tidal expiration. Table 2.1 summarizes all the lung volumes and capacities and the relationship to the total lung capacity and tidal volume [2, 39].

Table 2.1 Lung volumes and capacities.

Volume and capacity	**Definition**	**Volume* (mL)**
Total lung capacity (TLC)	The maximum volume in the lung	6000
Tidal volume (V_T)	Inspired and exhaled volume	500
Inspiratory reserve volume (IRV)	Max. volume can be inhaled above V_T	3000
Expiratory reserve volume (ERV)	Max. volume can be exhaled above V_T	1200
Vital capacity (VC)	IRV+ERV+V_T	4700
Inspiratory capacity (IC)	IRV+ V_T	3500
Functional residual capacity (FRC)	ERV+RV	2500
Residual volume (RV)	TLC-VC or FRC-ERV	1300

* The values are for average volume in a 70-kg young adult based on Pierce [2].

2.2. Intubation

Tracheal intubation is an unavoidable procedure in the intensive care unit during invasive mechanical ventilation [57]. A compliant tube is connected to the ventilator circuit to serve as a gas passageway from the ventilator to the trachea inside the lung. There are several types of intubations [74-77]. A flexible endotracheal tube can be inserted through the nasal or oral passages. The oral passage is the most frequently used

pathway for intubation [2, 77]. In this type of intubation, the tube is inserted through the mouth passing through the pharynx to a distance above the carina inside the trachea. Tracheotomy is another type of intubation, in which the tube is inserted through a surgical incision that is made at the anterior portion of the neck [2]. Tracheotomy intubation is done when there is a need for prolonged mechanical ventilation or given the impracticality of using the nasal or oral passages for the tube—often in critical situations such as head and neck cancers, severe facial trauma, large congenital tumors of the head and neck, and inflammation of the head and neck [2]. The common endotracheal tube size for adult females is 7 or 7.5 mm (inner diameter) while for adult males it is 8 or 8.5 mm [2, 55]. Figure 2.6 shows the different types of intubation.

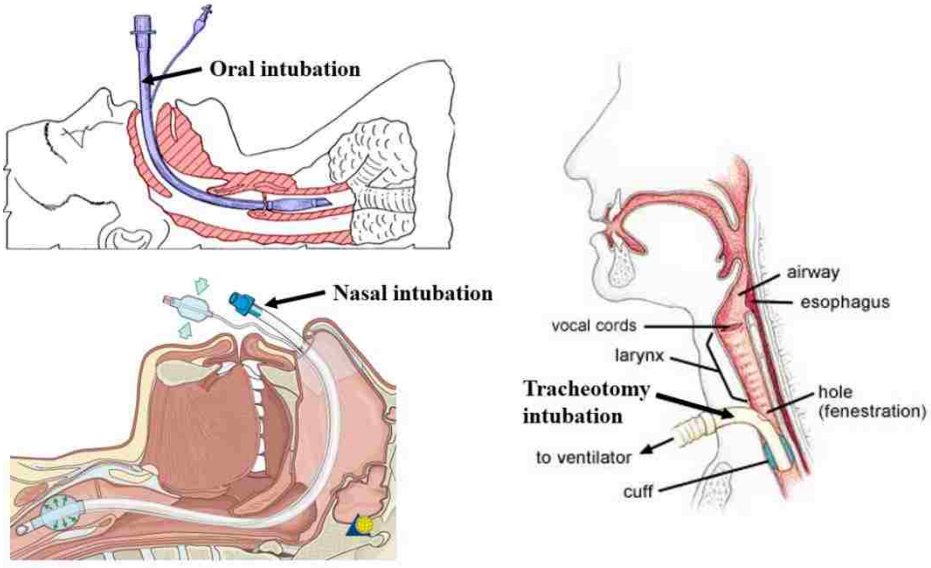

Figure 2.6 Illustration of different types of intubation.

The presence of endotracheal tubes is seen to be one of the most crucial features in gas transport [78, 79]. It is therefore important to be included in the model. Several past

studies have been devoted to studying the role of the endotracheal tube [75, 80-83]. The emphasis of these studies, however, has merely been on assessing the influence of the ETT tube on airways resistance and work of breathing, or on hospital practices to prevent tracheal damage. Esteban *et al* [74] reported that an endotracheal tube or a tracheotomy is used for ~99 % of the mechanically ventilated patients in America, which emphasizes that understanding the effects of the endotracheal tube is critical for clinical applications.

2.3. Classical Lung Model

The most important component of modeling the pulmonary fluid dynamic and particle transport is the human lung geometry. There are many computational and experimental studies that have been conducted to investigate the flow and particle deposition inside the respiratory tract [48, 84-91]. However, traditionally, all of these studies used classical models for the sake of simplicity. The most popular classical lung models are the Weibel model [59] and Horsfield model [51]. These are based on a statistical description of the lung, which are not realistic and physiologically non-representative. These models do not represent a real effective diameter and length of each individual branch. Furthermore, they are composed of a network of cylindrical tubes with uniform cross-sectional and symmetric branches (the Horsfield model does have a slight virtue of accounting for asymmetry). Although there is much to be learnt from the study of a simplified bifurcation, a greater degree of detail is needed to gain more useful insight into the problems of airflow and particle transport throughout the respiratory system.

2.4. Patient Specific Model Reconstruction

The recent advancements in medical imaging technology and image processing techniques have facilitated a way to reconstruct anatomically realistic lung models [39, 53, 92]. Data-set images of a patient can be obtained using CT-scans or magnetic resonance imaging (MRI). These scans describe the anatomical shape of the lung and can be used to reconstruct the lung model, thus allowing the traditional use of simplified models to be replaced by more realistic ones in pursuit of patient-specific modeling. Several studies have begun to use realistic geometries based on CT scans of patients, including nasal, oral, and the tracheobronchial tree [34, 39, 46, 47, 93-97]. The particular geometry features have shown to have a significant role in altering the flow fields and particle transport throughout the airways domain. It is therefore essential to use a model that resolves the important anatomical characteristics of the lung geometry [34, 39, 53, 98-100].

In the current study, the tracheobronchial tree was reconstructed for a mechanically ventilated female patient using CT-scans. The reconstruction procedures involve several operations starting with CT-scans acquisition from our collaborator Dr. Gary Salzman at the university hospital and University of Missouri, Kansas City; converting 2D images of interested regions to 3D geometry; a segmentation process; and finally using a suitable modeling software to prepare the model for meshing and computational modeling. Figure 2.7 shows a flow chart of the reconstruction and segmentation process. Details of the process are discussed in the subsequent sections.

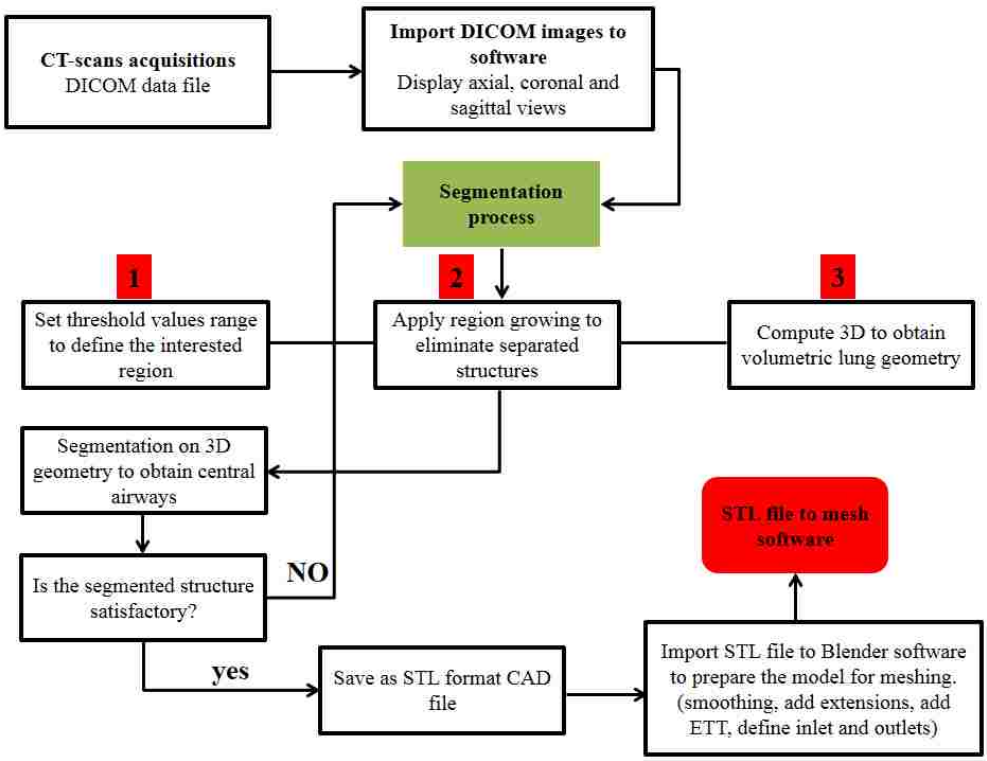

Figure 2.7 Illustration of geometry reconstruction and the segmentation process.

2.4.1. CT-Scans

Computed tomography is a medical imaging system that employs an x-ray emitter and detector to generate a series of planar cross-sectional images along an axis [39, 101-104]. During the imaging acquisition, the patient lies on a table that moves into the CT scanner. The x-ray tube emits a beam that rotates around the patient, taking multiple x-rays in cross-sections along the desired region of the body. The x-ray details are collected by the detector and directed to the computer, which creates separate images of the organ in order to form slices. Figure 2.8 shows representative slices of the lung from the trachea entrance to the lobar bronchus. Unlike the conventional x-ray where a single 2D slice is obtained, CT-scans consist of a set of 2D images that can be grouped in a stack of images

(see Figure 2.9), which can be stored using a DICOM (Digital Imaging and Communications in Medicine) format.

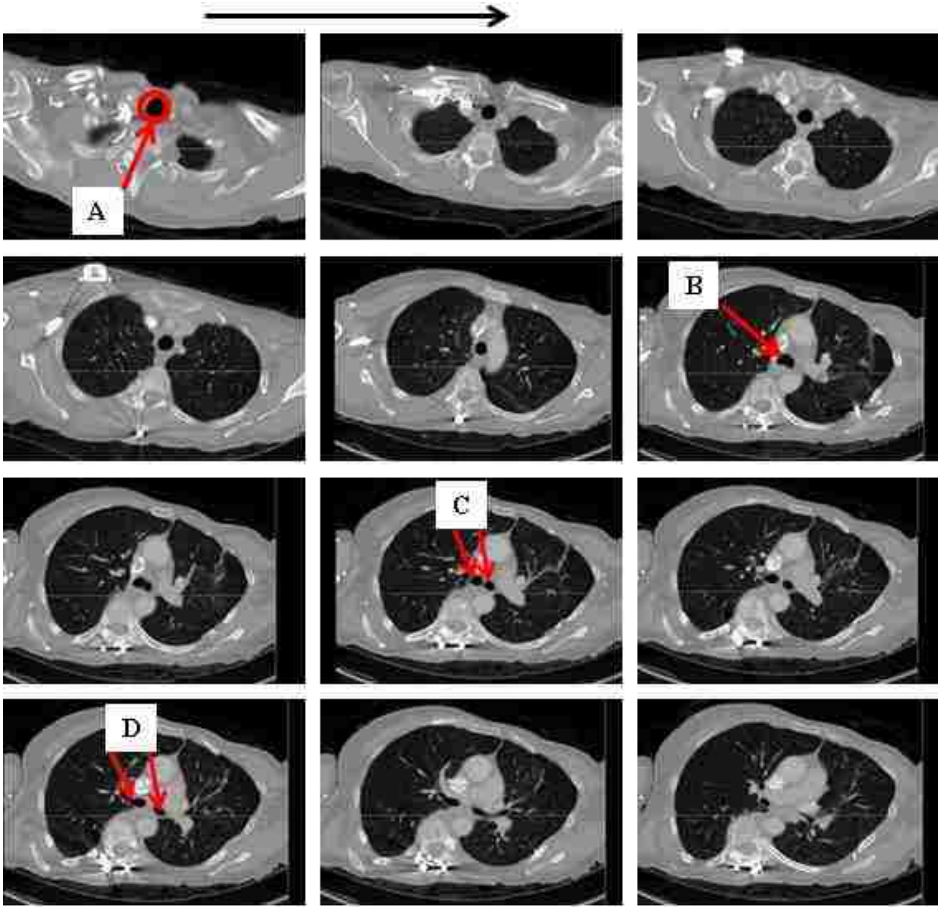

Figure 2.8 randomly selected 2D slices (in axial sections) from the trachea to lobar bronchus. **A**: inlet of trachea, **B**: the point where the trachea splits into the main bronchi. **C**: the entrances of right and left main bronchi, and **D**: the right and left bronchi segments.

Thus, the CT-scans can be viewed in different planes via a DICOM viewer or converted to a 3D model using suitable image processing software by stacking the slices together, see Figure 2.9. The three planes of the CT-scans and the definitions of the positions are illustrated in Figure 2.10. Each structure of the organs (i.e. lung, in current study) has a

different degree of absorption or reduction of the x-ray beam [39, 103-105], which subsequently attenuates the strength of the x-ray accordingly. Any slice is a set of a matrix of pixels and each pixel has a grayscale value corresponding to the degree of attenuation caused by each structure or tissue [39, 103-105].

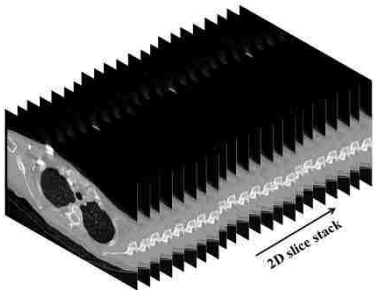

Figure 2.9 Two-dimensional slice stack of CT-scans constituting a 3D lung geometry.

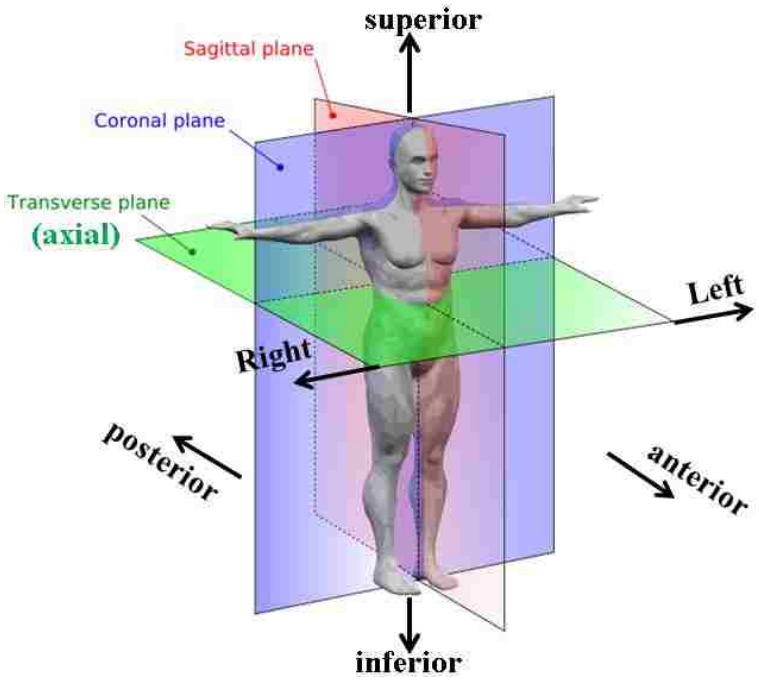

Figure 2.10 Anatomical planes and positions definition.

The grayscale values are measured in Hounsfield units (HU) and are defined as [39, 103-105]:

$$HU = \frac{\gamma_p - \gamma_w}{\gamma_w} \times 1000 \qquad (2.1)$$

where γ_p is the mean x-ray attenuation coefficient of the pixel, and γ_w is the mean x-ray attenuation coefficient of water [39, 103, 104]. Figure 2.11a presents the HU values for different structures (with air clearly having the minimum attenuation coefficient while bone has the highest). The distance between each slice is known as a slice thickness, which takes the 2D pixel into a 3D volume element called a voxel, see Figure 2.11b.

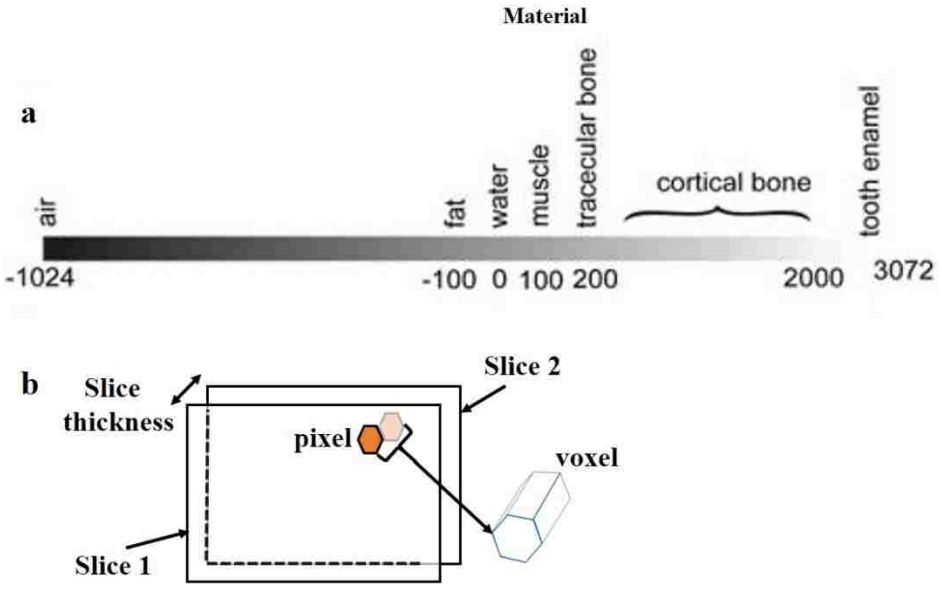

Figure 2.11 (a) Grayscale and Hounsfield unit value for different material and (b) illustration of the pixel and voxel elements [39].

The voxel dimension is represented by pixel size × pixel size × slice increment. The CT-scans for the current study were acquired for a 60-year-old female patient undergoing

mechanical ventilation treatment at the University of Missouri at Kansas City (UMKC) hospital. A Siemens SOMATOM Definition AS+ (140 KV and 74 mAs) CT scanner was used. A total of 260 slices were obtained and stored as a DICOM format file. The quality of a CT scan is determined by several metrics, such as: field of view, resolution, pixel size, slice increment, and pixel depth [101]. The field of view was approximately 34 cm and covered the entire lung. The resolution of each scan was 512×512 pixels, with a pixel size of about 0.602×0.602 mm and a slice increment of 3 mm. Images were taken at a pixel depth of 12-bit grayscale. Table 2 summarizes the important scan parameters.

Table 2.2 Details of Computed Tomography scans.

Metric	Value
Field of view	34.4 cm
Slice thickness	3 mm
Resolution (Width × Length)	512 mm × 512 mm
Pixel size	0.671 mm
Total images	260

2.4.2. Model Reconstitution

The obtained CT-scans images were used to reconstruct the current tracheobronchial tree. The 3D reconstruction was performed using Mimics® software (Materialize Inc., Belgium) in which the imported DICOM file of the CT raw images (260 slices) was converted to appear in axial or transverse, sagittal and coronal planes, see Figure 2.12.

Figure 2.12 The tree views of the images as they appear in MIMICS interface.

The reconstruction operations begin by performing a thresholding process [39, 106]. This is achieved by setting a range of HU values that represents the region of interest and then extracting the set of voxels with grayscale values in the selected range. The green mask in Figure 2.13a is the initial thresholding region. A region growing process was then executed on the set of voxels that was undergoing the threshold process to attain a continuous set of voxels, which eliminated all separated structures [39, 106]. The created mask (yellow) after the region growing maneuver is presented in Figure 2.13b.

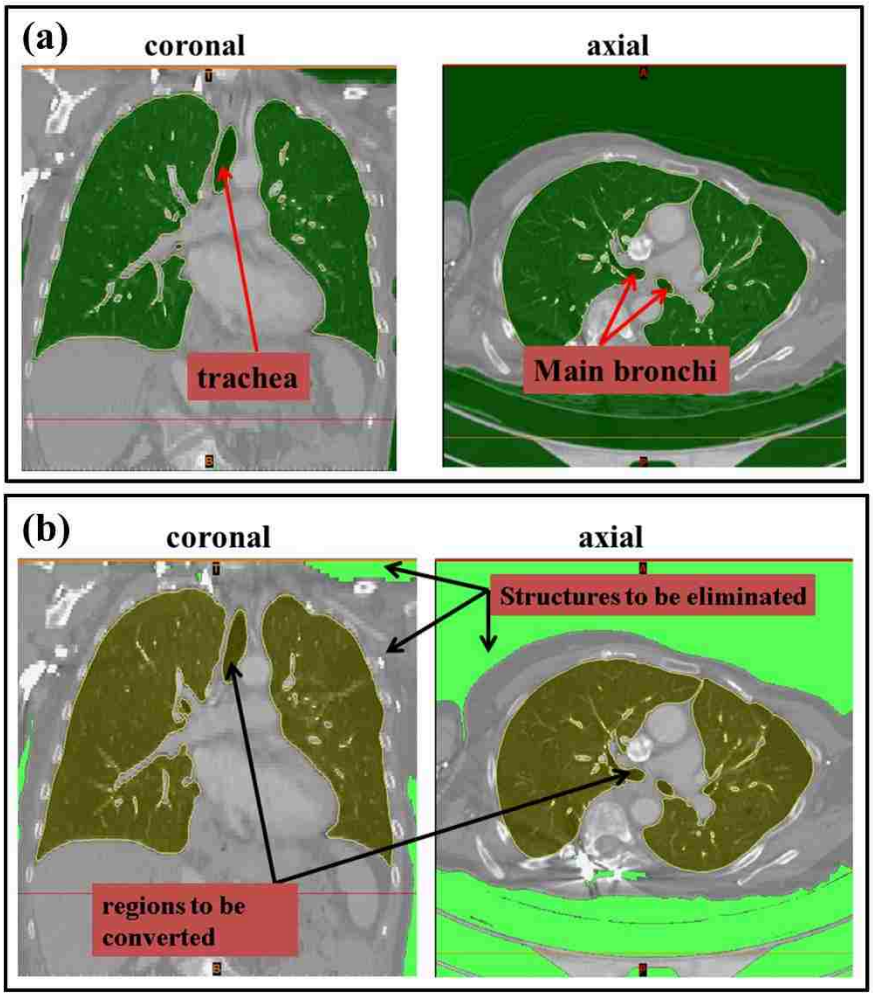

Figure 2.13 (a) The thresholding process and (b) The region growing process.

To reconstruct the volumetric geometry of the lungs, the *Calculate 3D operation* in Mimics was implemented. Figure 2.14 shows the obtained 3D lung model. Segmentation process was subsequently performed on the reconstructed volumetric lung to remove under-resolved branches and extract the final upper trachea-bronchial geometry. The under-resolved regions were eliminated by removing voxels from the mask of the 3D volumetric model. The region growing process was performed again to extract the airways of the tracheobronchial area. The raw extracted 3D airways model is presented in

Figure 2.15. After the segmentation process, the set of voxels constitutes the upper airways of the respiratory system, and the volume represents space that gas would flow

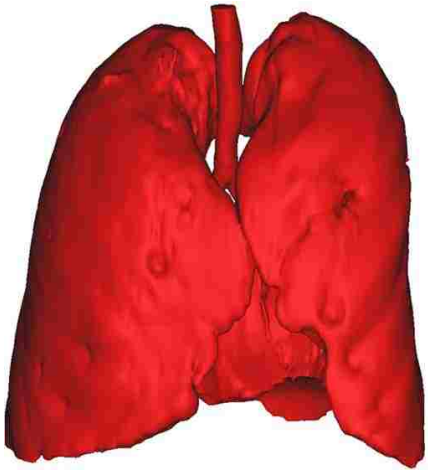

Figure 2.144 3D volumetric lung geometry.

through in the lungs. The extracted airways should be later manipulated and cleaned up to create a smooth surface and to create inlets and outlets for air to flow through [107, 108]. This is a necessary operation, which prepares the airways model for setting boundary conditions during computational fluid dynamics simulations. The model preparations were made using the open-source modeler software, Blender 2.5. The segmented airways were exported as STL (stereolithography) using *available STL+ module* command in Mimics. The STL file of the geometry was imported into Blender 2.5. Then the smoothing process was carefully performed. At each outlet of peripheral branches, a set of faces were grouped and were projected onto a plane (at the end of the branch) perpendicular to the branch the outlet belonged to. Extensions were added to each outlet to avoid any back flow and ensure fully developed flow [94, 109, 110]. To create the

extension, the projected faces parallel to the branch segment were extruded while gradually transitioning the outlet shape to a circle.

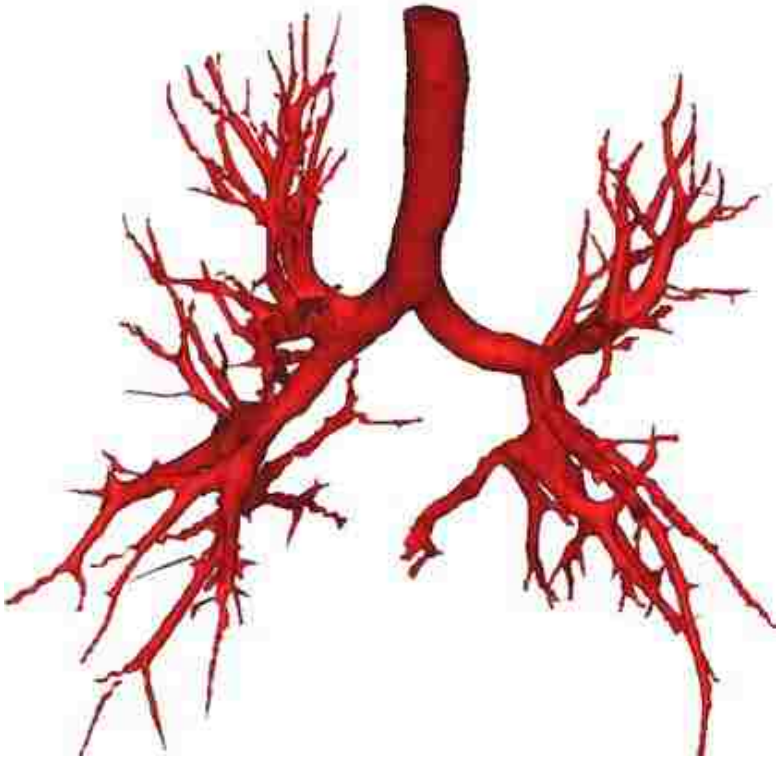

Figure 2.155 Segmented airways.

In the clinical practice, the patient is ventilated through a tube, which results in altering the inhaled gas conditions. Previous studies to predict flow phenomenon during HFOV have concluded that invasive devices like the endotracheal tube must be accounted for in order to capture the complicated flow physics [111]. As a result, an 8 mm interior diameter ETT was chosen and added to the model to complete the lung geometry [2, 55]. For meshing purpose, the completed geometry was exported from

Blender in STL format file to be used by a mesh generator software. The prepared geometry in Blender is shown in Figure 2.16.

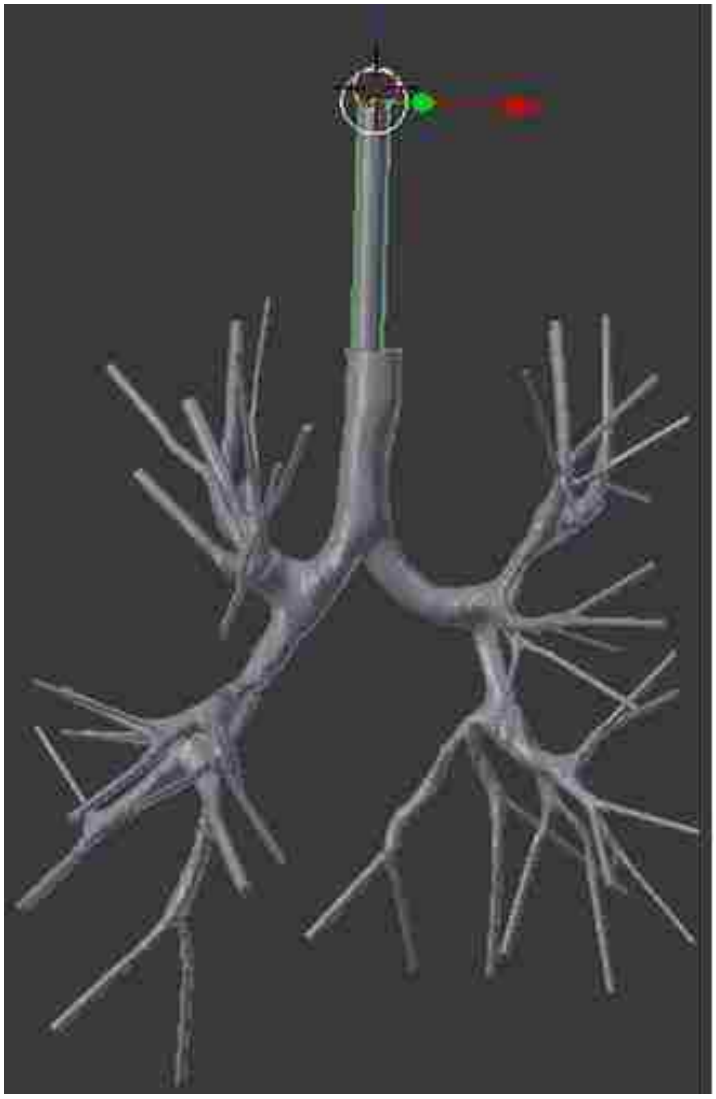

Figure 2.166 Cleaned up model with extensions and ETT.

2.5. Final Upper Tracheobronchial Tree Model

The finial realistic human airways geometry under consideration is shown in Figure2.17. The upper tracheobronchial model consists of the endotracheal tube (ETT),

which was inserted into the trachea, and seven generations beyond the trachea, i.e. G0 to G7. The final model encompasses fifty-three small, peripheral airways. To identify the outlets in the left and right lung, each outlet was assigned a number from 1 to 53, consecutively. The model was identified by the major lung lobes as: main bronchi (MB),

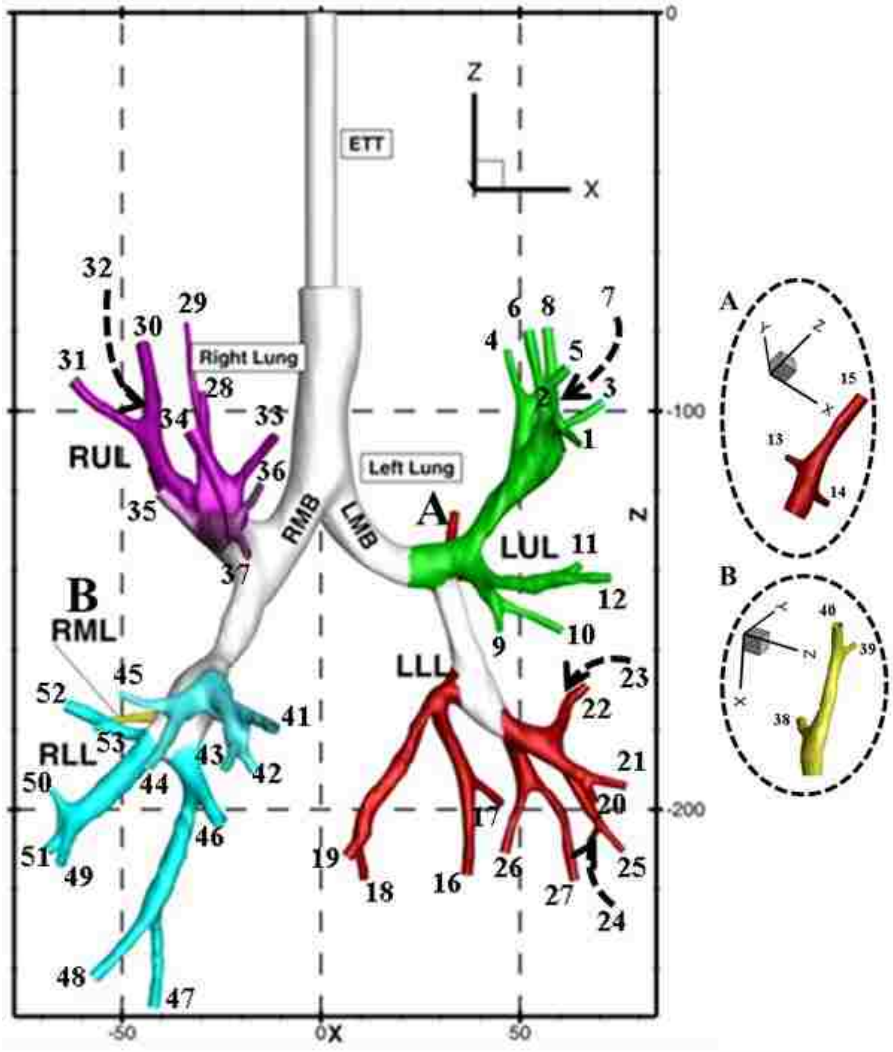

Figure 2.177 Final tracheobronchial tree with endotracheal tube. Left upper lobe (LUL). Left lower lobe (LLL). Right upper lobe (RUL). Right middle lobe (RML). Right lower lobe (RLL). The outlets numbered consecutively from 1 up to 53. The inset represents a magnified plot of point A for superior part of LLL and point B for RML, where outlet numbers are not evident in the original plot.

left upper lobe (LUL), left lower lobe (LLL), right upper lobe (RUL), right middle lobe (RLM), and right lower lobe (RLL). Detailed descriptions of the model outlets dimensions, generation, and the anatomical parts the outlet belongs to were present in appendix A.

The current geometry major features were compared to the two most common statistical models (i.e. the Weibel [59] and Horsfield [51] models) and to selected realistic models existing in the literature in Table 2.3. It is not feasible to compare airway size directly with the statistical models or other realistic models because of human airways intra- and intersubject variabilities, which depend on many elements such as: height, weight, physical activity, age, gender and sundry physiological factors [93, 112]. Therefore, the major sizes of the current model were compared to other models in terms of a diameter ratio of the first two generations, i.e. the trachea and main bronchi bifurcations. The diameter ratio presented in Table 2.3 is defined as the daughter branch diameter (main bronchus) divided by the parent branch diameter (trachea). The minor diameter ratio is the smaller diameter ratio of the bifurcation while the larger ratio is the major diameter ratio. The current model exhibits a similar major diameter ratio as that of the asymmetric Horsfield [51] and realistic large scale model of Choi [47]. In addition, the minor diameter ratio was similar to the idealized model used by Heraty [98]. In general, the current features of the model are consistent with those described in the literature for both classical and image-based models. The current realistic model has many important points of advantage concerning lung geometry over the classical models that have previously been used intensively. These points include the shape and orientation of the airways, which includes the realistic direction the branching occurs, the

branching angles, and airways' curvature. Therefore, the modeling of gas and particle transport in the current model would capture more realistic physics of the fluid flow due to resolving the geometry crucial features. Moreover, the coupled computational fluid dynamics–image based geometry is a more accurate representation of a patient's airway size, shape, position, curvature, and diameter variations. Image based modeling also provides patient-specific characteristics such as airway constrictions due to lung disease. Although some important features of the geometry through medical imaging techniques have been resolved, the current geometry still lacks some details such as cartilaginous rings and deeper airways generation (beyond G7). This is because of the limitations of the resolution and data acquisition techniques of current CT-scans [34, 39].

Table 2.3 Comparison of the major dimensions of the geometry of the current study to the statistical (idealized) and realistic models in the literature.

Study	D_d/D_p*	
	Minor Diameter Ratio	Major Diameter Ratio
Present study	0.64	0.75
Horsfield model [51]	0.69	0.75
Weibel model [59]	0.68	0.68
Heraty - Realistic Model [98]	0.64	0.68
Heraty - Idealized Model [98]	0.84	
Choi - Idealized Model [47]	0.70	
Choi - Large-scale model [47]	0.75	

*D_p is the parent (G0) diameter; D_d is the daughters (G1) diameter of the main bronchi.

CHAPTER 3

NUMERICAL METHODS AND VALIDATION

3.1. Mesh Generation

The geometry mesh is one of the fundamental aspects in computational fluid dynamics as the mesh quality plays a major role in accurate modeling and in resolving real physics of the flow field [39]. The grid represents a discrete of the geometry domain where a discretized set of mathematical partial differential equations are solved.

There are two categorizes of mesh type, structured and unstructured. Typically, a mesh is considered structured when the cells have a regular (uniform) pattern, which consists of hexahedral elements in 3D (quads in 2D). On the other hand, an unstructured mesh is defined as a mesh with cells of irregular pattern, usually comprised of triangles in 2D or tetrahedral elements in 3D. Different mesh elements types can be seen in Figure 3.1. The selection of mesh type and style is very crucial; however, the complexity of the

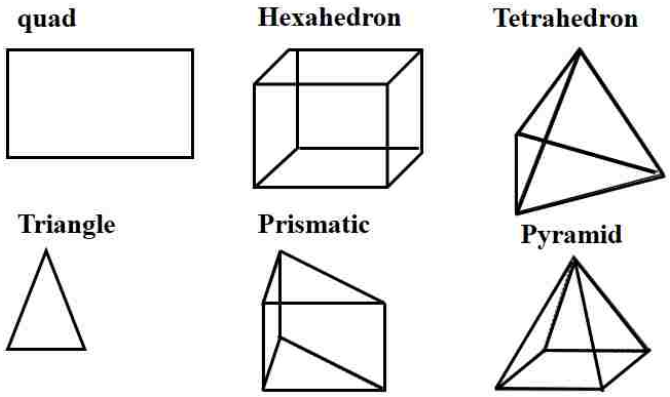

Figure 3.1 2D and 3D mesh elements types.

computational model plays the pivotal role in determining suitable mesh [39, 113, 114]. Structured hexahedral elements are always preferred over other mesh types due to their alignment with the flow direction. However, in spite of this preference, the structured hexahedral meshes are prohibitively expensive in terms of time [1-3]. In addition, complex geometries like the realistic network of human airways do not fit exactly in the Cartesian coordinate, which is required for application of structured mesh [39]. Table 3.1 summarizes the most used mesh styles in the literature for problems and geometries relevant to the current study. In general, image–based models and some of the simplified geometries have always employed pure tetrahedral mesh elements [47, 97, 107, 115-120]. The hexahedral or tetrahedral with prism layers were used only for simplified geometry with single or few generations, especially when performing RANS (Reynolds-averaged Navier–Stokes) turbulence model [95, 121, 122]. In the current study, the computational geometry was reconstructed based on a set of CT-scans, which led to a very complex tracheobronchial tree model as described in Chapter 2 and appendix A. The computational mesh used in this research was generated using unstructured tetrahedral elements, which is considered appropriate for complex geometries like present CT-scan based lung models [4-12]. To properly resolve the boundary layer, a very fine mesh was created near the wall.

ANSYS ICEM 14 CFD® was used to generate the computational mesh. Due to the large variation of the airways size from trachea to the peripheral segments (see Table A.1and A.2 in appendix A), the geometry was broken into different parts to enable mesh element size specifications locally. Figure 3.2 shows the flow chart for mesh creation procedures. The STL file of the broken geometry was then fed into ICEM and then a

"build topology operation" was applied to create the curves and points that define the geometry parts and to inspect the geometry walls for any holes. To increase the mesh quality, all points and

Table 3.1 Literature review of geometries, mesh styles and turbulence models used in studies relevant to respiratory flow dynamic.

Author (year)	Flow Modeling	Geometry	Mesh type
Isaacs *et al* (2006) [123]	Laminar	Simplified: G0-G1	Hexa
Lin *et al* (2007) [124]	DNS	CT-scan: M -G7	Tetra
Farkas *et al* (2007) [116]	Laminar	Simplified: G0 - G2	Tetra
De Backer *et al* (2007) [97]	RANS	CT-scan: G0 - ~G7	Tetra
Xi *et al* (2008) [121]	k-ω	CT-scan: M-G0 Simplified:G3-G4	Tetra P Hexa
Xi *et al* (2008) [125]	k-ω	CT-scan: larynx - G5	Tetra P
Zhang *et al* (2008) [126]	k-ω	Simplified: G0-G15	Hexa
Gemci *et al* (2008) [117]	Laminar	Simplified: G0 - G17	Tetra
De Backer *et al* (2010) [107]	k-ω	CT-scan: M - ~G7	Tetra
Xia *et al* (2010) [118]	LES	CT-scan: M- G7	Tetra
Choi *et al* (2010) [127]	LES	CT-scan: M -G7	Tetra
Lambert *et al* (2011) [119]	LES	CT-scan: M -G7	Tetra
Dehbi (2011) [122]	LES	Simplified: M – G0	Tetra P
Katz *et al* (2014) [120]	Laminar	CT-scan: G0 ~ G6	Tetra

Abbreviations: M: mouth. **Hexa:** Hexahedral. **Tetra:** pure tetrahedral. **Tetra P:** tetrahedral with prism layer. **Simplified:** idealized model based on Weibel [59] or Horsfield [51].

unnecessary curves were removed to avoid needless constraints for the mesh; and only those guide curves where the mesh should be split were kept (e.g. at inlet, outlets). The maximum size of each part of the geometry was set and Octree method mesh in the domain [128] was selected to create the domain of a primary mesh. After computing the mesh, the volume mesh was deleted and only the surface mesh was kept. This step was necessary to later improve mesh quality by creating the volume mesh with an operation that extrudes mesh inward from higher quality surface mesh. Meanwhile, the surface mesh was then smoothed using the Laplace smoothing method, which is an iterative process resulting in a more uniform spacing of nodes.

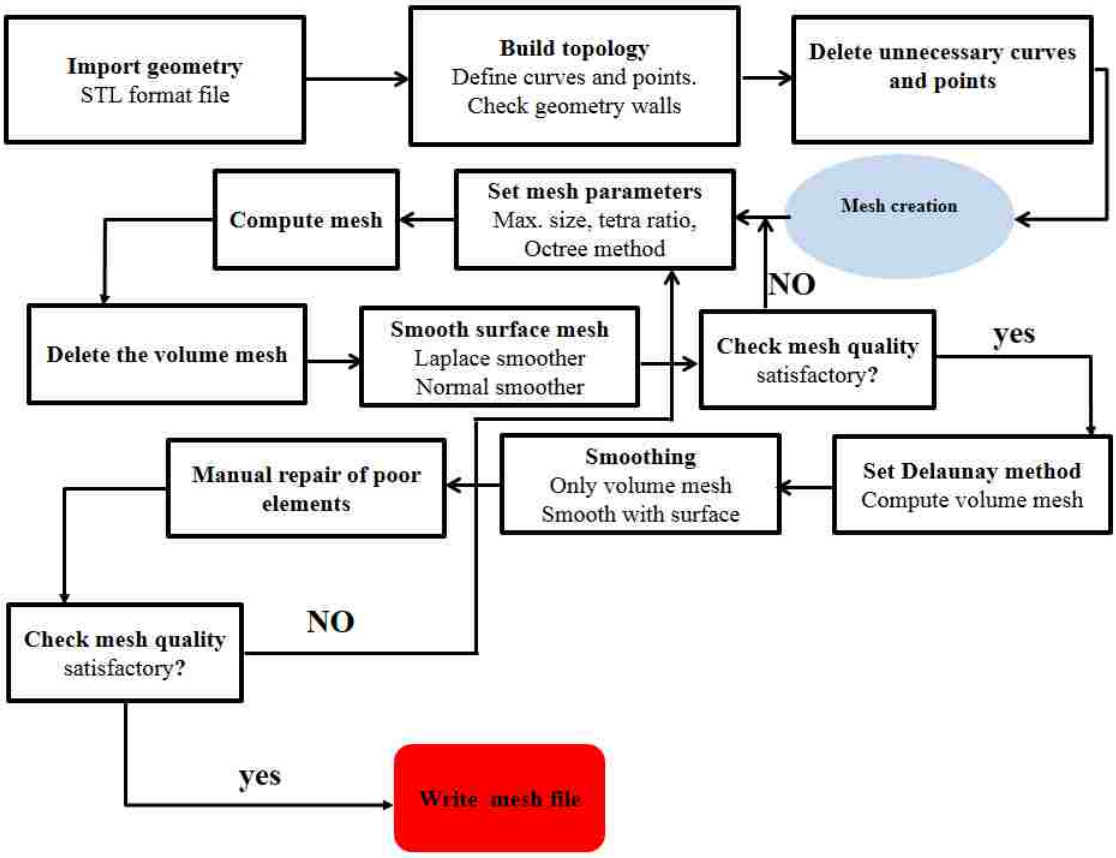

Figure 3.2 Mesh generation procedures used in the current work.

The surface mesh was further smoothed using a normal smoothing algorithm available in ICEM, also an iterative method, which works by moving nodes to improve the quality of the surface elements. Subsequently, a surface mesh with higher quality was achieved. The quality of a surface element (triangle) is defined as the minimum ratio of the height of the triangle to its corresponding base length, normalized so that an equilateral triangle would have the highest quality of 1, while zero is the lowest and worst quality [16]. For the current surface mesh, after manual manipulation of poor elements by splitiing ediges or merging nodes, a minimum quality of 0.45 and average of ~0.85 was attained, which is considered high-quality mesh [16]. The smoothing process does not change the geometry features and size due to constriction of the nodes to the surface specified in the imported STL file. The front Delaunay method, which is the most common operation used in mesh generation [129, 130], was then applied to create the volume mesh [128]. In this operation, a Delaunay triangulation is used to create the tetrahedral elements. To refine the mesh near the wall, a value of 1.25 for the growth ratio was applied to control the expansion of the volume elements as the distance from the wall increased [16]. The smoothing process was later reapplied to the created volume mesh. The quality of a tetrahedral volume element is defined as the ratio of the radius of an inscribed sphere to the radius of a circumscribed sphere, normalized so that a regular tetrahedron would have a quality of unity [16]. The process employed in the present study led to a mesh with minimum mesh average quality of ~0.75, with a minimum quality of any volume element of 0.40. Figure 3.3 shows the adopted mesh for all simulations in the present study. The final mesh consisted of 2.42×10^{6} total elements. The justification of this choice is discussed in details in the section of the mesh convergence study of this chapter.

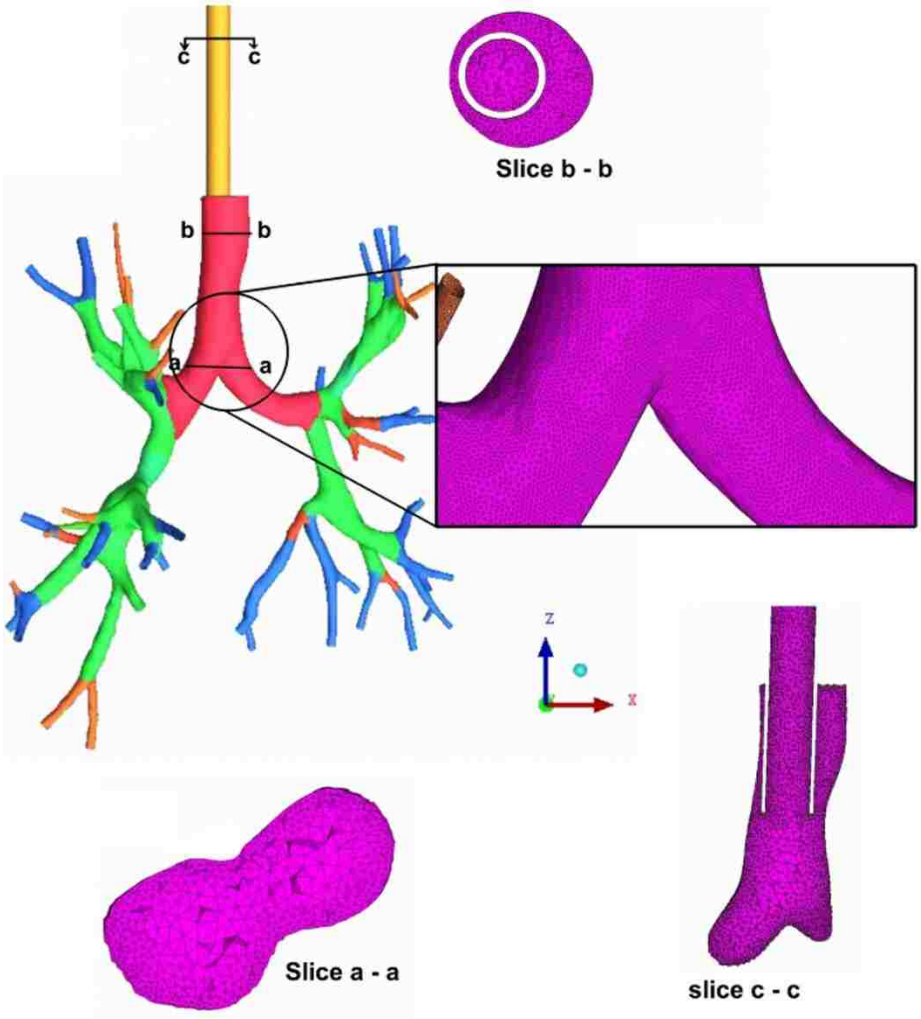

Figure 3.3 Final mesh. The expanded view displays the surface mesh. Slice a-a shows the volume mesh in a cut plane through the transition between parent and daughter branches in the first bifurcation. Slice b-b show the volume mesh in a cut plane through the trachea and the endotracheal tube. Slice c-c show the volume mesh in a vertical cut plane through the endotracheal tube, trachea and main bronchi.

3.2. Computational Method and Turbulence Modeling

The set of governing equations were solved for the flow field variables CFD approach. CFD uses the discrete domain (i.e. discretized into a finite set of control volumes) to replace the continuous domain, where the transport equations for mass and

momentum are discretized into algebraic equations to solve for the flow variables at the grid points [39, 131-133]. The dimensionless Reynolds number is a criterion used to characterize the flow regimes pattern in internal flow [134]. It is defined as the ratio of the flow inertial force to the viscous force: $\mathrm{Re} = \frac{UD}{\nu}$, where U is the velocity, D is the tube diameter, and ν is the kinematic viscosity, $\nu = \mu / \rho$ where μ is the fluid dynamic viscosity and ρ is the fluid density. For the flow in a perfect circular tube, the flow is characterized as laminar when $Re < 2300$, transient when $2300 < Re < 4000$, and turbulent when $Re > 4000$ [134]. The jet caused by flow through the endotracheal tube and complex features of the geometry (like curvatures, asymmetry, successive branching angle and non-uniform cross-sections) contributes additional disturbances to the flow. Consequently, the critical values of Re, where the transition to turbulence is initiated, become lower in bifurcated tubes [135, 136]. Therefore, the turbulence was modeled in the current study using a high order turbulence model.

Traditionally, CFD modeling flow in the airways uses two equation RANS models like k-ε and k-ω (k: turbulence kinetic energy, ε: turbulence dissipation rate, ω: specific dissipation) [34, 39]. A list of different models used can be found in Table 3.1. However, such low order models are not able to capture anisotropic turbulence, which is significant near the wall boundaries of the upper airway regions. Additionally, they involve model constants, which should be experimentally calibrated [39]. Furthermore, in the case of modeling particle transport while using RANS to model continuous phase, an additional model is needed to account for the influence of the velocity fluctuation on the particle transport, which could reduce the modeling accuracy [39, 53]. The flow field can

be fully resolved using direct numerical simulation (DNS); an approach where a solution of the discretized governing

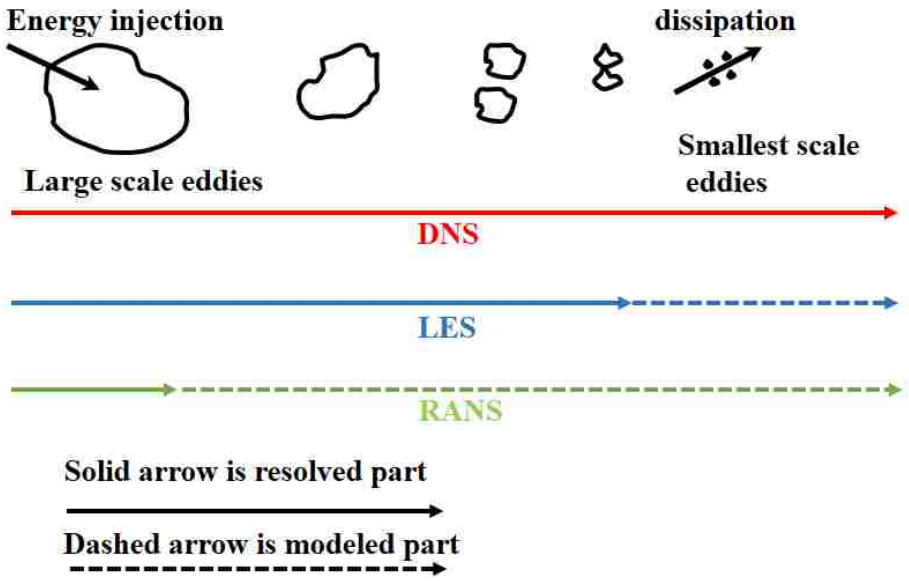

Figure 3.4 Comparison of the LES model to RANS and DNS.

equations is obtained using higher order methods and are completely independent of modeling application, though this entails application of a very fine mesh to resolve the smallest scales of the motion, i.e. the Kolmogorov length scale: $\eta = (\nu^3 / \varepsilon)^{1/4}$. DNS of three-dimensional problems therefore requires a computing mesh with a total number of grid points of order ~$Re^{9/4}$ with overall computational cost related to ~Re^3 [132, 137, 138]. For these reasons, DNS is limited to flows with a very low Reynolds number and simple computational domains. High order LES has recently become an alternative approach for modeling flow inside the lungs, see Table 3.1. In contrast to RANS, where all turbulence scales are modeled, LES has a unique feature that the large scale eddies are

resolved and the effect of small scales are modeled using a subgrid scale model [34, 39, 137-140]. LES is therefore considered as a middle ground between RANS and DNS in terms of the accuracy and computational cost, see Figure 3.4. Moreover, Another distinct advantage of LES over RANS is its ability to resolve large scale turbulence eddies, specifically in regard to accurately modeling particle transport [141]. Since particle, motion is influenced more by the larger scales, the subgrid scales effect is diminished for particles with higher inertia [142]. Therefore, in the present study, LES was used to model the 3D transient oscillatory flow during HFOV.

3.2.1. Filtering Operation

The principle behind LES is the application of a spatial filtering to separate the large from small scale eddies instead of using time-averaging techniques. Subsequently, the larger scale eddies are directly resolved while the smaller scales are modeled [132, 139, 140]. The spatial filtering operation is applied using a filtered variable defined as [132, 138, 140]:

$$\overline{f}(x,t) = \iiint_{\Omega} G(x,x',\Delta)\, f(x',t)\, dx_1' dx_2' dx_3' \tag{3.1}$$

where Ω is the entire domain, $\overline{f}(x,t)$ is the filtered variable, $f(x',t)$ is the unfiltered variable, and $G(x,x',\Delta)$ is the filter function. Δ is the filter cutoff width. The overbar indicates spatial filtering. There are three commonly used filter functions *G* [132, 138, 140] are listed below in Table 3.2.

Table 3.2 Common filter functions.

Filter type	Filter function
Box filter	$G(x,x',\Delta)=\begin{cases}1/\Delta^3, & \lvert x-x'\rvert \le \Delta/2\\ 0 & , \lvert x-x'\rvert > \Delta/2\end{cases}$
Gaussian filter	$G(x,x',\Delta)=\left(\frac{6}{\pi\Delta^2}\right)^{3/2}\exp\left(-6\frac{\lvert x-x'\rvert^2}{\Delta^2}\right)$
Spectral cutoff	$G(x,x',\Delta)=\prod_{i=1}^{3}\frac{\sin[(x_i-x_i^{'})/\Delta]}{(x_i-x_i^{'})}$

Figure 3.5 illustrates the energy cascade decomposition during LES using the filter width Δ to separate the energy-containing eddies and energy-dissipating eddies. The commonest filter width used for the filtering operation is the grid size, for 3D computations $\Delta=\sqrt[3]{\Delta x\Delta y\Delta z}$, where Δx, Δy and Δz are the grid size in in x, y and z directions, respectively [132, 140].

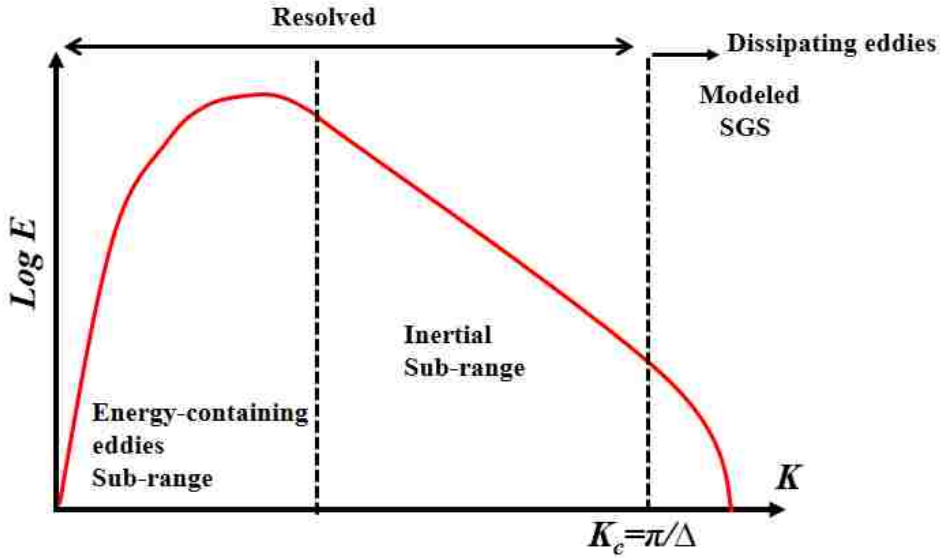

Figure 3.5 Energy cascade decomposition during LES. K_c is the cutoff wavenumber computed using cutoff width Δ.

3.2.2. Filtered Navier-Stokes Equations

Applying the spatial filtering operation to the Navier-Stokes equations, all eddies whose scales are smaller than the filter width Δ are filtered out. The filtered conservation of mass equation for incompressible flow is:

$$\frac{\partial \overline{u}_i}{\partial x_i} = 0 \tag{3.2}$$

where $\overline{u}_i$ is the filtered i^{th} velocity component with an overbar denoting filtering. The filtered momentum equation for incompressible flow is [139, 140]:

$$\frac{\partial \overline{u}_i}{\partial t} + \frac{\partial}{\partial x_j}(\overline{u}_i \overline{u}_j) = -\frac{1}{\rho}\frac{\partial \overline{p}}{\partial x_i} + \frac{\partial}{\partial x_j}\left[\upsilon\left(\frac{\partial \overline{u}_i}{\partial x_j} + \frac{\partial \overline{u}_j}{\partial x_i}\right)\right] - \frac{\partial \tau_{ij}}{\partial x_i} \tag{3.3}$$

where x_i is the i^{th} position component, ρ was set 1.185 kg/m^3, and p is the pressure. The filtering process leads to the subgrid-scale stress τ_{ij}, defined as [139, 140]

$$\tau_{ij} = \overline{u_i u_j} - \overline{u}_i \overline{u}_j \tag{3.4}$$

The total field velocity is defined as $u = \overline{u} + u''$, where $\overline{u}$ is the resolved velocity and u'' is unresolved velocity component. To account for the effect of the unresolved small scale eddies, the subgrid scale stress (SGS) must be modeled [132, 138, 140].

3.2.3. Subgrid Scale Model

Several subgrid scale models used for LES modeling. The most classical model is the Smagorinsky model [143] where the eddy-viscosity is modeled in terms of strain rate tensor as: $\upsilon_{sgs} = (C_s \Delta)^2 \sqrt{2\overline{S}_{ij}\overline{S}_{ij}}$, where C_s is constant. However, it is well known that Smagorinsky's model entails many defects [144, 145]: the model constant has to be

adjusted for each flow, the model has near wall limiting behavior of $\sim O(y^0)$ which is not correct, and for laminar flow the model does not diminish and is highly dissipative in transition region. The developed version of the Smagorinsky model was also introduced by Germano [146], which is known as the dynamic model. While the dynamic model has a feature of adjusting the model constant automatically to the flow type, several other limitations have not been resolved [33, 34]. An advanced SGS model was developed and introduced by Nicoud and Ducros [147]. It is known as the wall-adopting local eddy viscosity (WALE) and is based on the square of the velocity gradient tensor. The WALE-SGS model has the ability to reproduce laminar to turbulent transitions and to return the correct wall-asymptotic $\sim O(y^{+3})$ variation of the SGS viscosity [33, 34]. Furthermore, the WALE model is invariant to coordinate translation or rotation and only local information are needed, which makes the LES appropriate in complex geometry [33, 34]. In general, the SGS model should satisfy several flow properties for accurate modeling such as: correct wall-behavior and produce zero eddy viscosity in the case of a pure shear. Table 3.3 summarizes the capability of different well-known models in terms of several important properties.

Table 3.3 Comparison of different well-known models in terms of several important properties [145]

Property	Smagorinsky [143] C_s	Vreman [148] C_v	WALE [147] C_w
Asymptotic	$\sim O(y^0)$ (NS)	$\sim O(y)$ (NS)	$\sim O(y^{+3})$ (S)
Pure shear	1 (NS)	0 (S)	0 (S)
Isotropic	2.45 (NS)	1 (NS)	0 (S)

Abbreviations: S: satisfy; **NS:** not satisfied

For its many advantages, the WALE model was adopted for the subgrid-scale eddy viscosity model. The relationship between the SGS and the large-scale strain rate tensor $\bar{S}_{ij}$ is expressed in Equation 3.5 [139, 140]:

$$(\tau_{ij} - \frac{\delta_{ij}}{3}\tau_{kk}) = 2\upsilon_{sgs}\bar{S}_{ij} \tag{3.5}$$

The strain rate tensor, $\bar{S}_{ij}$ is defined as [139, 140]:

$$\bar{S}_{ij} = \frac{1}{2}\left(\frac{\partial \bar{u}_i}{\partial x_j} + \frac{\partial \bar{u}_j}{\partial x_i}\right) \tag{3.6}$$

The subgrid scale viscosity v_{sgs} for the LES WALE model is modeled as [140, 147]

$$\upsilon_{sgs} = (c_w\Delta)^2 \frac{(S_{ij}^d S_{ij}^d)^{3/2}}{(\bar{S}_{ij}\bar{S}_{ij})^{5/2} + (S_{ij}^d S_{ij}^d)^{3/4}} \tag{3.7}$$

In Equation 3.7 S_{ij}^d is the traceless symmetric part of the square of the velocity gradient tensor [139, 140]:

$$S_{ij}^d = \frac{1}{2}(\bar{g}_{ij}^2 + \bar{g}_{ji}^2) - \frac{1}{3}\delta_{ij}\bar{g}_{kk}^2 \tag{3.8}$$

where $\bar{g}_{ij}$ is the velocity gradient tensor [139, 140]:

$$\bar{g}_{ij} = \frac{\partial \bar{u}_i}{\partial x_j} \tag{3.9}$$

3.2.4. Numerical procedures

The computational investigations were carried out using an implicit finite volume based solver, ANSYS® CFX14. The advection term was solved using a second order central differencing scheme. For LES, a central differencing scheme is necessary for accurate modeling. The artificial numerical diffusion, arising due to discretization that

presents itself in different schemes such as upwind, is eliminated [16]. A second order backwards Euler scheme was used for the transient term. Convergence criteria was set such that the root mean square (RMS) residual for mass and momentum equations was less than 10^{-4} [48, 117]. The time step was set such that the low Courant–Friedrichs–Lewy (CFL) was satisfied. More details of numerical procedures, time step specification, particle-tracking modeling, and user-enhanced programs are presented in the subsequent chapters. The transient simulation was run on an 8-processor (2.4 GHz) Dell precision workstation T7500 with 24 GB of RAM.

3.3. Mesh Independence study

The predicted solution must be independent of the grid resolution [39, 131-133]. Prior to CFD modeling, the mesh independence can be achieved by examining the important flow variables on different mesh sizes at equivalent flow conditions. In the present study, a grid convergence analysis was performed over eight different meshes with the total number of mesh elements ranging from 1.182×10^5 to 6.535×10^6. Average velocity and turbulent kinetic energy $(TKE = 0.5\overline{u_i' u_i'})$, where u_i' is the fluctuation velocity, were used as the convergence criteria. The average velocity and TKE were evaluated for slices at the left (L-L) and right (R-R) main bronchi. The percentage difference of the results from each of the two successive meshes is presented in Table 3.4. The inset plot shows the locations of the slices L-L and R-R where the variables were evaluated. Clearly, for all variables at all locations, the solution is converged for mesh size > 8.47×10^5 elements with maximum difference of ~4.4%. Therefore, a mesh of size 2.42×10^6 elements was used for all simulations.

Table 3.4 Details of grid independence study.

Mesh size	**Percent Difference%***			
	U_{ave} L-L	U_{ave} R-R	TKE L-L	TKE R-R
1.18×10^5	-	-	-	-
4.6×10^5	14.73	6.02	17.82	18.92
8.5×10^5	10.19	6.77	23.46	13.54
1.6×10^6	4.03	3.33	4.44	1.85
2.4×10^6	3.13	1.09	3.48	2.12
3.5×10^6	3.59	2.92	4.22	1.04
4.1×10^6	3.21	3.69	2.55	1.31
6.5×10^6	2.21	3.93	2.00	2.86

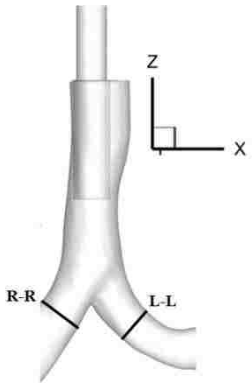

*Percent Difference% is define as $\frac{M1-M2}{M1}\times100$

Abbreviations: M1 is U or TKE value of mesh 1, M2 is U or TKE of mesh 2, Mesh1 and mesh2 are each two successive meshes.

3.4. LES VALIDATION

LES modeling was validated against available experimental data of the oscillatory flow inside a bifurcation model by Lieber and Zhao [87]. This experimental study is usually used to validate the numerical modeling procedures of oscillatory flow in bifurcated tubes [47, 85, 149-151]. A single idealized model was used in the experimental study. A glycerin-water solution ($\nu = 6.3\times10^{-6}\, m^2/s$) was used as a working fluid and was pumped through the test section by a reciprocating pump, see Figure 3.6. Velocity measurements were taken at key points in the domain using laser Doppler anemometry (LDA). The

Reynolds number based on the peak flow rates was 2077. The Womersley number α =4.2 ($\alpha = a\sqrt{\omega/\nu}$, where a is the tube radius and the angular frequency $\omega = 2\pi f$, where f is the frequency). The computational model was created following the description provided by Zhao and Lieber [88]. It was a single idealized bifurcation based on the Weibel model [59], see Figure 3.7a. The numerical simulation was set to match the experimental procedures. Similar working fluid properties were used. To mimic the experiment outlet conditions setup, mass flow rate in left and right branches were employed as a fraction of the instantaneous inlet mass flow rate. The measured flow rates in the left and right branches were 48% and 52% of the inlet flow rate, respectively. The walls were assumed rigid, with a no slip condition. The Womersley velocity profile along with a sinusoidal flow waveform were imposed at the inlet of the parent tube [47].

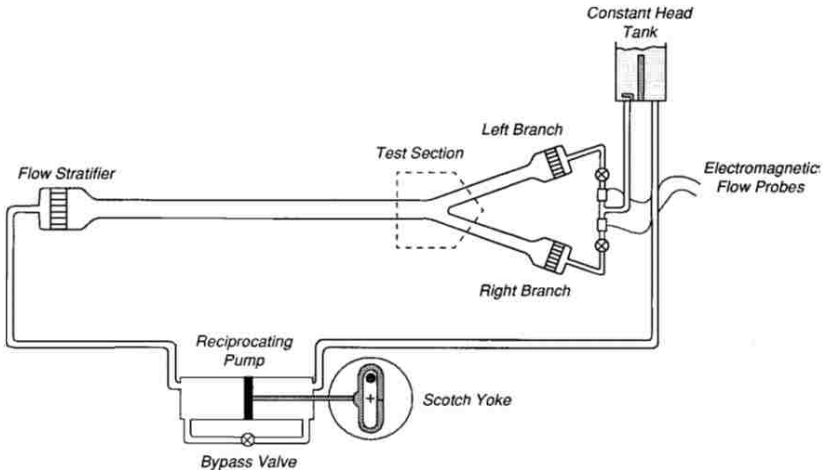

Figure 3.6 Experimental apparatus from [152]. Adopted with permission from (ASME).

$$u(r,t) = \mathrm{Re}\,al\left[\frac{1}{i\rho\omega}\left(1-\frac{J_0(\alpha r i^{3/2})}{J_0(\alpha i^{3/2})}\right)A^* e^{i\omega t}\right] \tag{3.10}$$

where i is $\sqrt{-1}$, r is the non-dimensional radial distance such that r =0 in the center of the tube and r =1 at the wall, and, J_o is the zeroth Bessel function of the first kind. The pressure gradient driving the flow is represented by the real part of $A^* e^{i\omega t}$. The peak flow rate of $Q_{\max} = \mathrm{Re}\,\pi\nu\, D/4$ is used to determine the parameter A^*. A user-enhanced FORTRAN subroutine was used to implement the Womersley velocity profile in CFX solver. The LES–WALE turbulence model, along with the numerical solver procedures described in the previous sections, was implemented to simulate transient oscillatory flow matching the experimental investigation. Figure 3.7b compares the velocity profile results from the CFD simulation to experimental measurements at different locations along the bifurcation. The axial velocity obtained by the current numerical code, at both inspiration and expiration phases, agreed with the LDA measurements. These concordances indicate that the present code and LES model are sufficiently accurate to model oscillatory flow in the human tracheobronchial tree model.

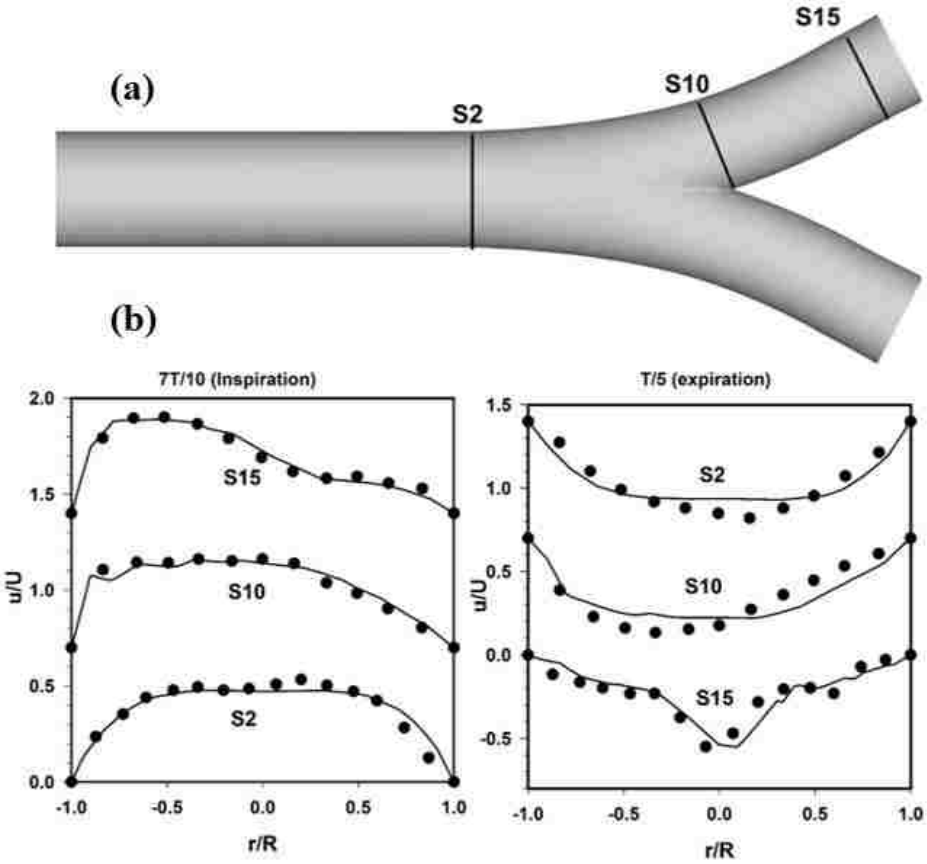

Figure 3.7 (a) The replicated bifurcation model matches the experimental model. (b) Results from experimental validation. Circles represent LDA measurements of velocity from Lieber and Zhao [152]; lines represent velocity profiles obtained by simulation. Data are for two different cycle times 0.7T (inspiration phase) and 0.2T (expiration phase).

CHAPTER 4[1]

FLOW TRANSPORT AND GAS MIXING DURING INVASIVE HIGH FREQUENCY OSCILLATORY VENTILATION

[1] *This chapter was based on the following published paper with permission from Elsevier publishing:*

Alzahrany M., Banerjee A., Salzman G. Flow Transport and Gas Mixing During Invasive High Frequency Oscillatory Ventilation. Medical Engineering and Physics. 36 (6), P647–658

4.1. Introduction

A mechanical ventilator is commonly used in intensive care units to facilitate and support patient breathing during acute respiratory failure [1, 2, 25]. As reviewed in Chapter 1, in many critical situations, as in acute lung injury and acute respiratory distress syndrome, usage of CMV based therapy could lead to lung injury due to high tidal volumes of 6-10 ml/kg [2, 9, 10]. High Frequency Oscillatory Ventilation is then considered a useful ventilation mode as it allows for adequate gas exchange and prevents lung injury due to the usage of small tidal volumes of ~1-2 ml/kg [9], albeit at higher frequencies of 1 - 30 Hz [2, 25, 153]. Unlike CMV where the primary mechanism of flow transport is bulk convection, flow transport during HFOV is complicated and not fully understood [28, 30]. Previous work [28-31] has identified several physical mechanisms that play a role in gas transport and mixing during HFOV: (a) bulk convection; (b) gas exchange between respiratory units or pendelluft; (c) counter flow; (d) longitudinal mixing; and, (e) gas exchange by molecular diffusion. A detailed understanding of these mechanisms is essential for optimizing ventilation management strategies during HFOV and is the focus of this work.

Oscillatory flow and convective mixing through human lungs have been numerically investigated by Choi *et al* [47] in a computed tomography (CT) based human airway model. The inlet condition was imposed at the mouthpiece of the model. There different flow conditions were modeled. Normal breathing case (NORM, V_T = 500 mL and f = 0.2 Hz), a high frequency- normal-Re case (HFNR, V_T = 16.58 mL and f = 6.28 Hz), HFOV (V_T = 47 mL and f = 6.28 Hz). While the coaxial counter flow was totally absent in case of NORM, it was found more evident in case of HFNR. The contribution

of the counter flow to the mixing was ~20% during HFOV. Nagels and Cater [48] carried out a numerical simulation of HFOV in a simplified double bifurcation model. Sinusoidal velocity was impost at the trachea inlet with operating frequency of 25 Hz. Large eddy simulation along with Smagorinsky SGS was implemented. They observed flow reversal near the wall due to residual motion of the fluid at different times of the ventilation cycle. Flow transport between main bronchus was by pendelluft mechanism due to geometry asymmetry, a feature also reported by Adler and Brucker in their experimental study [111]. Bauer and Brucker [78] studied, in vitro, airway reopening and observed that the collapsed airway can be recruited at a high Womersley number. Oscillatory flow of HFV in a symmetric 3-generation Weibel model was numerical investigated under by Zhang and Kleinstreuer [150]. Differences between the oscillatory flow and the equivalent steady state was found even at peak flow. Tanaka *et al* [154] used laser Doppler anemometer to study the fluid dynamic in side idealized 3 generation Horsfield [51] based model. The spatial and temporal secondary flow intensities and its influence on gas mixing in HFOV was examined. Secondary velocity was found to be highly dependent on geometry features like the branching angle and curvature ratio of each bifurcation. Heraty *et al*. [98] conducted in vitro investigation of gas exchange during HFOV in a single idealized and realistic bifurcation geometry and reported that bifurcated geometry features influence the flow leading to secondary flow structures. Hatcher *et al*. [45] studied mechanical performance of five clinically available neonate HFOVs and reported that ventilator performance varied widely for the models chosen even though the devices had similar operating parameters (the difference attributed to different waveform shapes). The presence of intubation during ventilation therapy causes

a high speed-jet, which is released at the carina-trachea environment and induces shear stress at the airways walls. The wall shear stress (WSS) is seen to cause airways inflammation and epithelial erosion [12, 22]. Green [22] studied WSS in an idealized model and found that the high flow rate at the peak expiration due to coughing caused a high wall shear stress, which subsequently leads to airways inflammation. Muller *et al* [12] investigated experimentally the wall shear stress in a neonatal tracheal scaled model under high frequency jet ventilation (HFJV) by varying the location of the jets inside the ETT. High values of WSS were measured and it was observed that it doubled itself when the jet was moved closer to the wall from the center of the ETT.

The majority of *in vitro* and computational studies have looked at the effect of ventilation frequency or ventilation mode during HFOV. It is well-known that the HFOV waveform varies between clinically available models, and it is hypothesized that this variation in the shape of ventilator waveform coupled with the frequency of the device and presence of intubation plays an important role in gas transport and mixing and lung injury. The current work is motivated by the need to study the effect of frequency (15, 10 and 6 Hz) and waveform shapes (sinusoidal, exponential, and square) for three commercially available high frequency ventilators. The following problems have been addressed:

- The ventilator-related parameters effects on gas transport during HFOV: ventilation waveform shapes and operating frequency
- Effects of presence of intubation on the flow structure and ventilator-induced lung injury.

- Influence of waveform shape and the rapid change in acceleration/deceleration of flow and pressure on lung injury during HFOV.

4.2. Method

4.2.1. Numerical Method

Transient three-dimensional high frequency oscillatory flow was solved using an implicit finite volume CFD solver (ANSYS® CFX13). Turbulence is modeled using the LES based WALE model described in Chapter 3 [147]. The advection term was solved using a second order central differencing scheme while a second order backwards Euler scheme was used for the transient term. Convergence criteria was set such that the RMS residual for mass and momentum equations was less than 10^{-4} [48, 117]. Courant–Friedrichs–Lewy was constrained to unity during the whole breathing cycle by using adaptive time step with upper and lower limit of 10^{-3} s and 10^{-6} s respectively. Figure 1 shows the geometry with the locations of all slices used in this chapter to compute different variables.

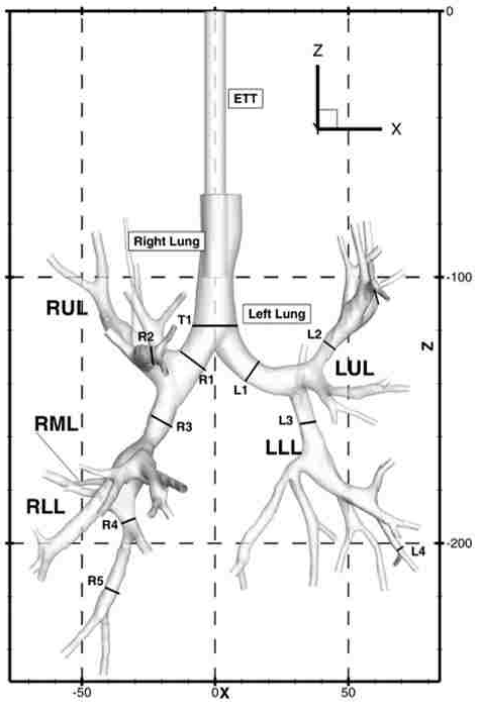

Figure 4.1 Illustration of the slices locations on the tracheobronchial tree model.

Inlet boundary condition: A blunt turbulent velocity profile [95] was imposed at the inlet of ETT; the mean velocity $u_m(t)$ was based on the corresponding pressure-controlled ventilator waveform and its creation is discussed in the subsequent section of breathing conditions and waveforms. The velocity profile was defined as:

$$u(r,t) = 1.224\, u_m(t)\left(1-\frac{r}{R_{ETT}}\right)^{\frac{1}{7}} \tag{4.1}$$

where R_{ETT} is radius of the endotracheal tube. A similar blunt velocity profile was reported by Martonen *et al* [90] based on velocity measurements near the bifurcation site for *Re* = 1225. Xi and Longest [95] found a similar velocity profile just upstream of the larynx for *Re* range of 1211 to 2421. For current study, Reynolds number ($\mathrm{Re}_{ETT} = 4fV_t/\nu D_{ETT}$, where D_{ETT} is the ETT diameter) ranges from 6960 to 24694

for all cases based on the ETT inlet, and it was considered appropriate to choose a blunt profile.

***Outlet boundary condition*:** The mass flow rate at each outlet was calculated and set as a partial percentage of instantaneous mass flow rate at the inlet and defined as:

$$q_k(t) = P_k \times q_{inlet}(t), \text{ where } P_k = P_{H,i}\,\frac{A_k}{A_{t,i}} \tag{4.2}$$

In equation (3), *k* denotes outlet number; $q_k(t)$ and $q_{inlet}(t)$ are the instantaneous flow rate at both k^{th} outlet and ETT inlet, respectively; P_k is the mass flow rate fraction at outlet *k*; $P_{H,i}$ is the mass fraction obtained from Horsfield *et al* [51] for branch *i*; A_k is the equivalent area of outlet *k*; and, $A_{t,i}$ is the total of the equivalent areas of the outlets that are supplied by the branch corresponding to the i^{th} branch. Similar mass flow rate specifications have been used in past studies [95, 96, 100, 155, 156]. Tables 4.1and 4.2 present the mass flow rate fraction used at each outlet in left and right lung respectively.

Walls condition: The airway walls were considered to be rigid, dry and smooth and a no-slip boundary condition was imposed [34, 39, 53].

4.2.2. Breathing Conditions and Waveforms

The boundary condition at the ETT inlet was specified in terms of a transient velocity $u_m(t)$ associated the blunt profile (i.e. Eqn. 4.1). The equation of motion that governs the flow during mechanical ventilations (Eqn. 4.3) was used to obtain the flow rate curve from a given pressure waveform shape [1, 2]. The flow rate was then used to compute the transient velocity at the inlet. Therefore, the pressure function was not

applied directly to the CFD simulations and was achieved in two separate steps, see Figure 4.2. Prior to the CFD runs, a MATLAB code was used to generate the transient velocity $u_m(t)$. For a defined pressure function (waveform shapes: sinusoidal, exponential and square),

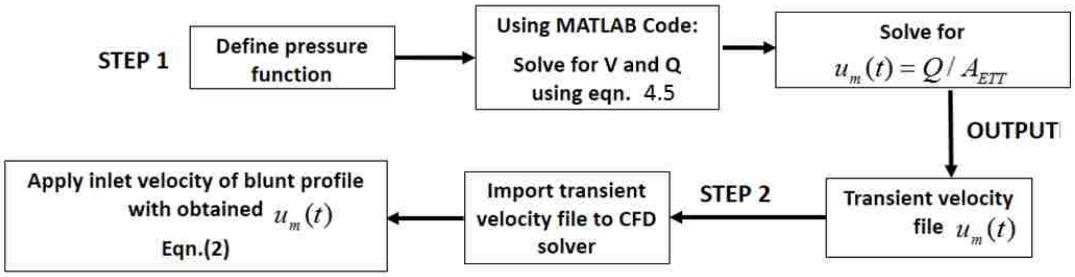

Figure 4.2 Flow chart of the transient velocity generation using the ventilator input pressure waveform.

Eqn. (4.3) was numerically solved using the MATLAB code for the volume and flow rate [1, 2]. Figure 4.3a plots the shape of three given pressure functions. Figs. 4.3b and 4.3c are the computed volume and flow rate curves respectively. From the flow rate curve (Figure4.3c), the transient velocity $u_m(t)$ was obtained as $u_m(t)=Q/A_{ETT}$, where A_{ETT} is the area of the ETT inlet. This transient velocity field was imported to the CFD runs as the inlet velocity profile. The equations of motion states that the pressure applied to the respiratory system for ventilated patient equal to the sum of pressure loss due to the total airways resistance, pressure drop due to the total lung compliance and the positive end-expiratory pressure (PEEP). The pressure applied to the respiratory system is the sum of the pressure applied by the ventilator (P) and the pressure due to the respiratory muscles (P_{mus}). Thus, the equation of motion is described as [1, 157, 158]:

$$P + P_{mus} = RQ + \frac{V}{C} + PEEP \; ; \quad Q = \frac{dV}{dt} \tag{4.3}$$

where Q is flow rate and V is volume. The lung compliance and airway resistance are defined as:

$$C = \frac{\Delta V}{\Delta P} \; ; \; R = \frac{\Delta P}{\Delta Q} \tag{4.4}$$

R and C were taken as 4.33cm H_2O/(L/s) and 0.127 L/cm H_2O respectively, and were based on averaged values for different patients from Grimby [159] and were considered constant in evaluating waveform pattern [160]. The PEEP was assumed zero and for totally supported patient, the contribution of the muscles is zero (P_{mus} is zero) [1, 157, 158]. Consequently, Eqn. (4.3) collapses to:

$$P = RQ + \frac{V}{C} \tag{4.5}$$

HFOV is characterized by a tidal volume that is less than or equal to the dead space volume of the conducting airways [1]. For current geometry, the dead space volume was 60 mL. A tidal volume of 50 mL was chosen such that it satisfies the above constraint and allows us to compare present work with previous studies [47, 79, 98]. The inverse of the active inspiration phase was used to impose the active expiration phase such that inspiration to expiration ratio (I:E) was 1:1. Table 4.3 presents flow parameters for all cases considered in the current study.

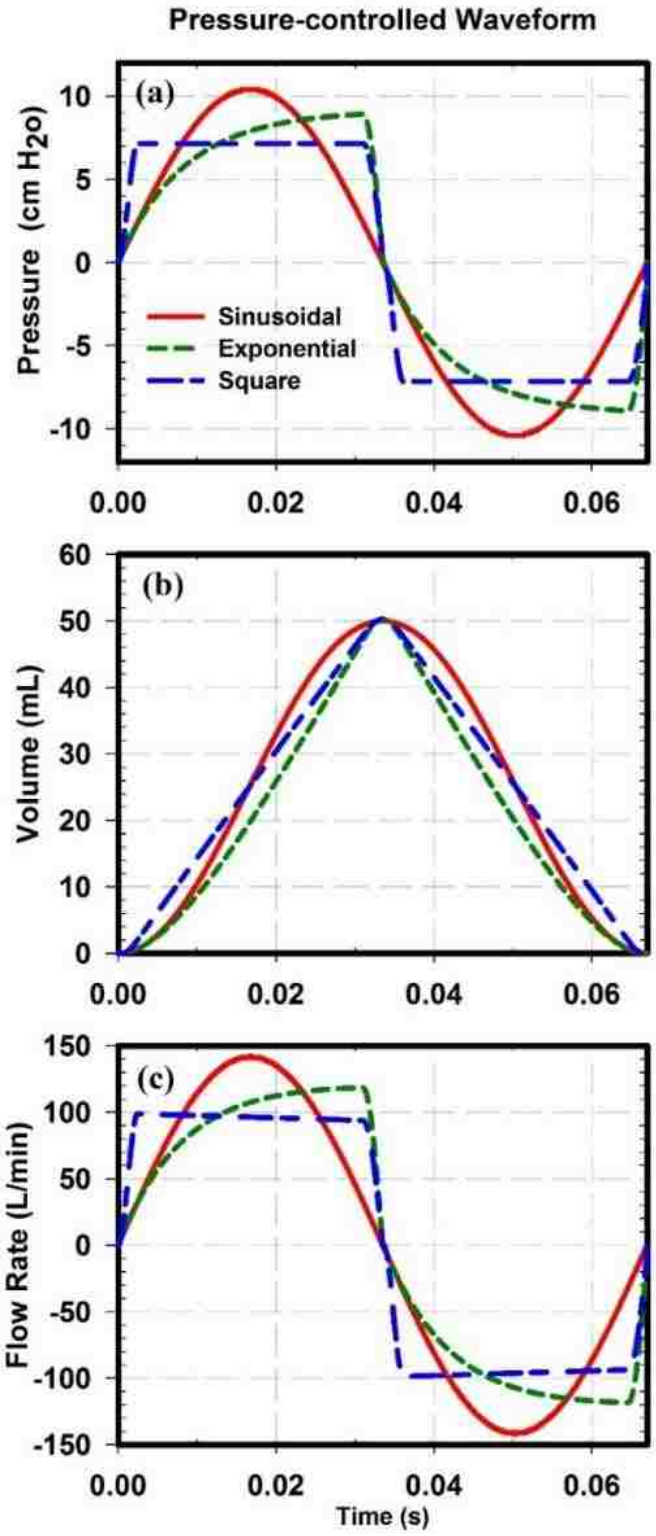

Figure 4.3 Pressure-controlled waveforms and flow rates' curves at f = 15Hz.

Table 4.1 Mass flow rate fraction for each outlet used for boundary conditions in left lung.

Anatomical part	Outlet No.	Generation	Diameter (mm)	Mass flow rate%
Trachea	-	G0	14.82	100%
LUL: Anterior	1	G5	2.01	1.11%
	2	G5	2.3	1.46%
	3	G5	2.2	1.33%
	4	G5	2.98	2.45%
LUL: Posterior	5	G6	2.65	2.64%
	6	G6	1.96	1.44%
	7	G6	1.52	0.87%
	8	G6	2.74	2.82%
LUL: Lingula-Superior	9	G4	1.68	1.10%
	10	G4	2.05	1.64%
LUL: Lingula-Inferior	11	G4	2.42	1.93%
	12	G4	2.27	1.70%
LLL: Superior	13	G4	1.27	0.90%
	14	G4	1.16	0.75%
	15	G4	2.34	3.05%
LLL: Posterior basal	16	G6	2.85	2.16%
	17	G6	2.37	1.50%
	18	G6	2.28	1.38%
	19	G6	3.2	2.73%
LLL: Anterior Basal	20	G7	2.36	1.66%
	21	G7	2.07	1.28%
	22	G7	2.35	1.65%
	23	G7	2.35	1.65%
	24	G7	1.59	0.76%
	25	G7	1.61	0.77%
LLL: Lateral basal	26	G6	2.56	2.41%
	27	G6	2.5	2.29%

Table 4.2 Mass flow rate fraction for each outlet used for boundary conditions in right lung.

Anatomical part	Outlet No.	Generation	Diameter (mm)	Mass flow rate%
RUL: anterior	28	G5	2.35	2.33%
	29	G5	1.44	0.88%
RUL: Posterior	30	G6	3.88	2.53%
	31	G6	3.02	1.53%
	32	G5	4.7	3.71%
RUL: Apical	33	G5	2.59	1.25%
	34	G5	5.01	4.68%
	35	G4	3.77	2.65%
	36	G5	2.02	0.76%
	37	G5	2.72	1.38%
RML: Lateral	38	G4	1.75	0.90%
RML: Medial	39	G5	0.97	0.28%
	40	G5	1.86	1.02%
RLL: Meddle basal	41	G6	3.09	2.81%
	42	G7	2.72	2.17%
	43	G7	2.75	2.22%
	44	G6	3	2.65%
	45	G6	1.78	0.93%
RLL: Posterior basal	46	G6	3.92	4.52%
	47	G7	2.89	2.46%
	48	G7	3.25	3.11%
RLL: Anterior basal	49	G6	2.79	2.29%
	50	G6	1.85	1.01%
	51	G6	3.01	2.66%
RLL: Superior	52	G6	3.12	2.86%
	53	G6	1.81	0.96%

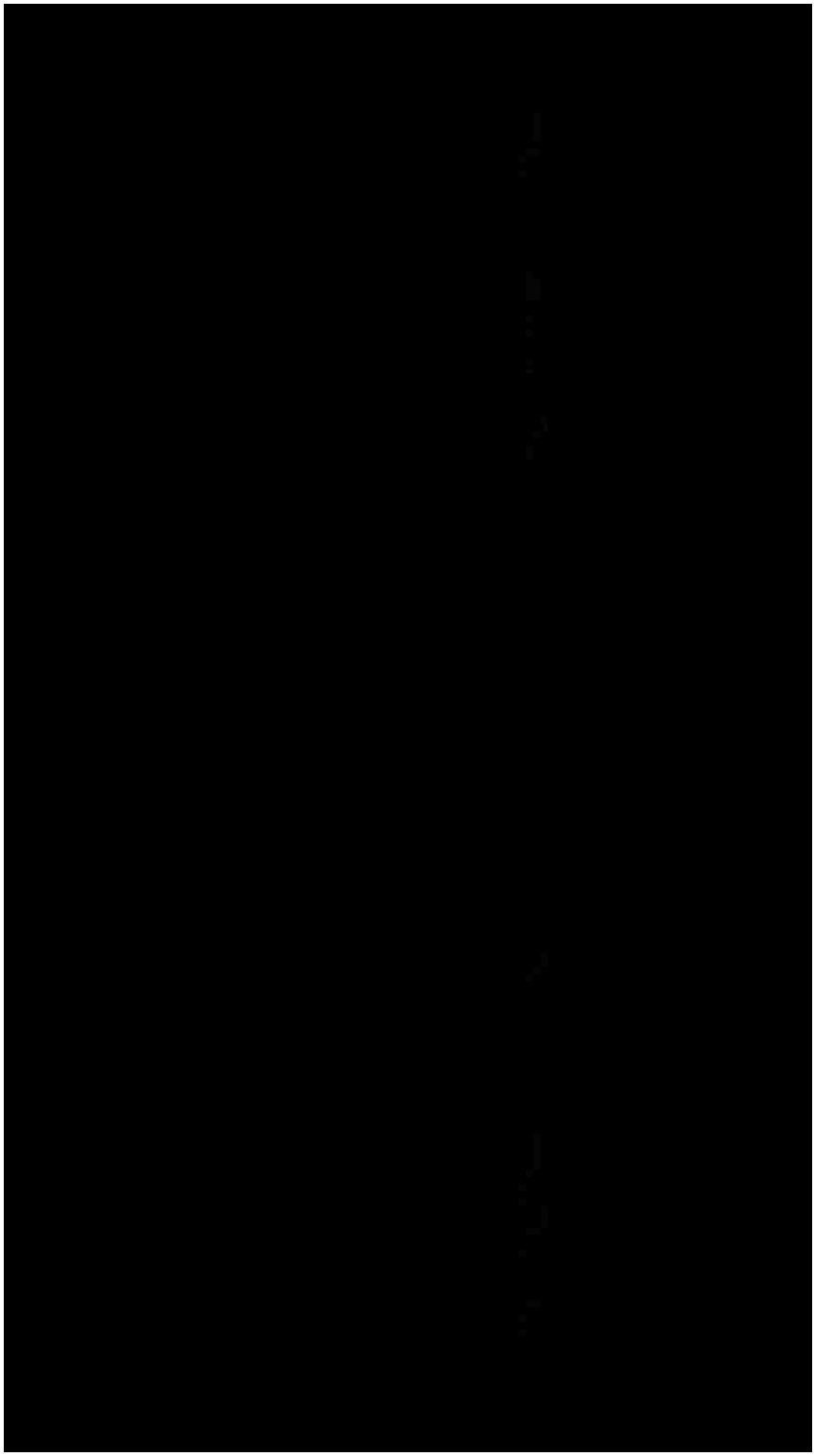

4.2.3. Solution Independent of Cycle's Number

To evaluate the required number of cycles to reach a statistically independent solution, a transient simulation was run up to ten HFOV cycles. Average velocity and turbulent kinetic energy were used as the convergence metric. The average velocity and TKE were evaluated at slices at left L and right R main bronchi; see Figure 4.1 for the locations of the slices. The percent difference of the results from each two successive cycles are presented in Table 4.4. It was observed that flow parameters converged after approximately two cycles with a maximum difference of ~2.5% in TKE and ~4.9% in the average velocity. An oscillatory difference in the root-mean-square velocity of 4% persists during multi-cycles of HFOV was observed by Nagels and Cater [48]. Four HFOV cycles were considered adequate and values reported in this study are for the fourth cycle.

Table 4.4 Solution independent of the cycle number study.

Cycle No.	Percent Difference%*			
	U_{ave} L	U_{ave} R	TKE L	TKE R
1	-	-	-	-
2	1.39	0.79	57.11	33.73
3	1.05	1.85	0.66	16.21
4	2.47	4.90	1.86	2.45
5	2.02	3.46	1.89	0.67
6	0.58	0.32	0.02	1.01
7	4.47	3.08	0.01	0.57
8	4.41	0.97	0.22	0.58
9	4.46	4.75	0.02	0.02
10	2.08	4.06	0.07	0.13

*Percent Difference% is define as $\frac{M1-M2}{M1}*100$

Abbreviation: M1 is U or TKE value of Cycle 1, M2 is U or TKE of Cycle 2
Cycle1 and Cycle2 are each two successive cycles.

4.3. Results

Results from the computations of oscillatory flow in a patient specific lung model under HFOV conditions are described next. Simulations were performed with and without ETT to understand the effect of invasive medical devices. The flow field for all cases was characterized by high turbulence and strong secondary motions due to waveform shapes, complexity of the geometry, presence of invasive devices, and a high Reynolds number due to high frequency.

4.3.1. Effect of Waveform Shape

4.3.1.1. Coaxial Counter Flow

Figure (4.4) plots velocity vectors for the three-waveform shapes at f = 15 Hz on a vertical slice made by a plane which cut through the ETT, trachea, and main bronchi; the inspiratory and expiratory flow is denoted by red and blue arrows, respectively. For clarity, a close-up picture of the near bifurcation site is provided as an inset. The flow structures at end expiration (EnEx) qualitatively resembled that at early inspiration (EaIn); similarly, the flow at end inspiration (EnIn) resembled that at early expiration (EaEx). Variations in coaxial counter flow were observed between the cycle phases (see Figure 4.4) and varied with waveform shape. For example, during the EnEx phase, the flow at the vicinity of the right trachea and outer wall of the right main bronchus was in-phase for sinusoidal and exponential waveforms (zones 1 and 2) but out-of phase for the square waveform (zone 3). These differences were also present during the EnIn phase. The exponential and square waveforms (zones 4 and 5) exhibited a uniform coaxial

counter flow compared to the sinusoidal case (zone 6). For the sinusoidal wave, the flow was mostly in-phase except at the outer wall of right bronchus. For the exponential and square waveforms, the flow had lower momentum at the vicinity of outer walls of the main bronchi and the walls of the trachea and flows ahead of phase.

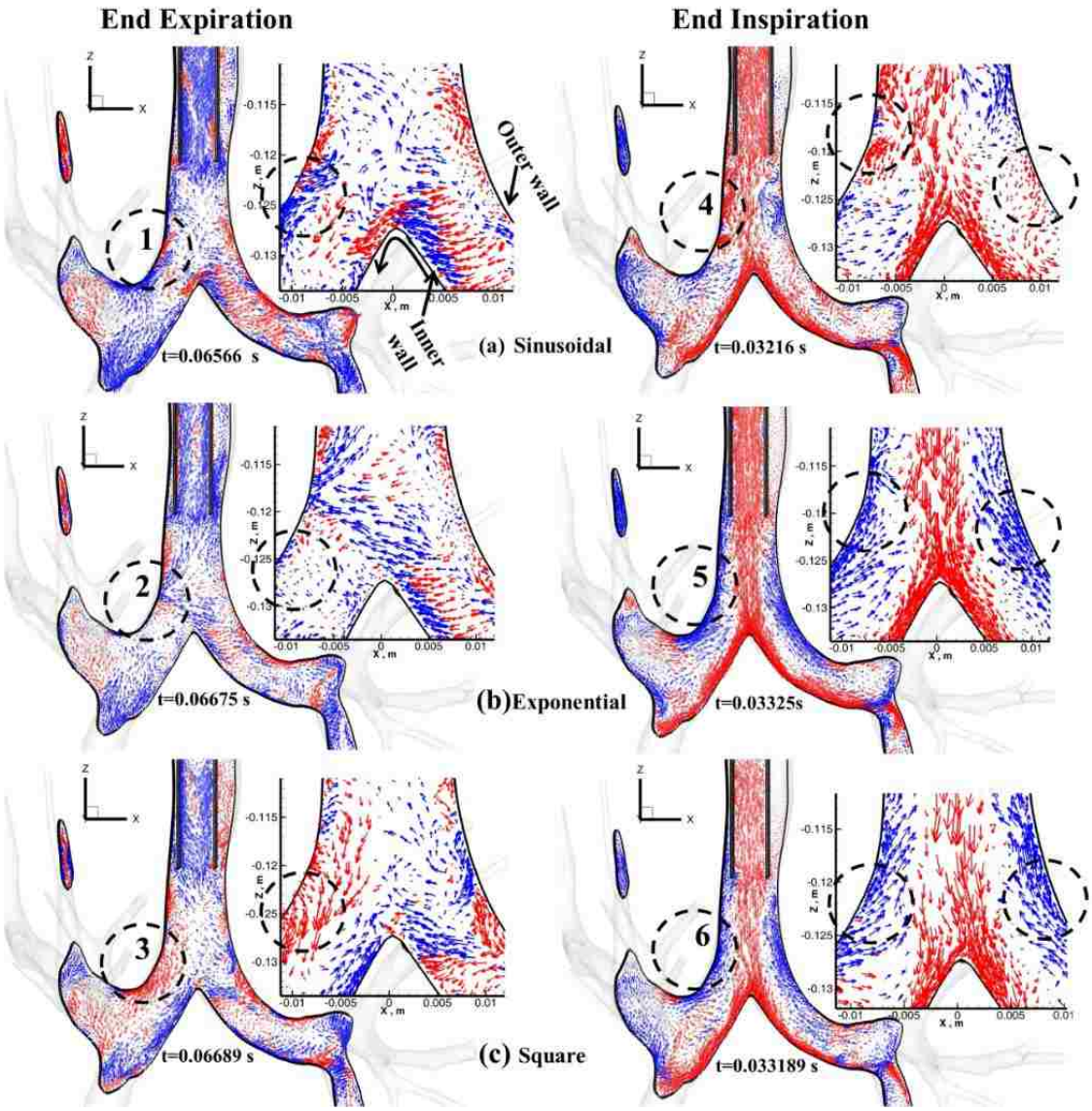

Figure 4.4 Co-axial counter flow for (a) sinusoidal, (b) exponential, and (c) square waveforms at end expiration (EnEx) and end inspiration (EnIn) phases for f =15 Hz and $|Q|$=18.2 L/min. Red arrows represent inflow vectors (inspiration) and blue arrows represent outflow (expiration) vectors

4.3.1.2. Pendelluft Flow

Gas exchange between left and right main bronchi was observed for the sinusoidal waveform in EnEx phase (Figure 4.4a) and was found to persist up to the EaIn phase (see Figure 4.5a). The flow at the left bronchus reversed its motion, moved over the carina ridge to the right bronchus and demonstrated a pendelluft-like gas transport. In the case of the square waveform, pendelluft was observed during the EaIn phase (see Figure 4.5b) but was absent for the other phases. Pendelluft-like features were completely absent at all phases for the exponential waveform.

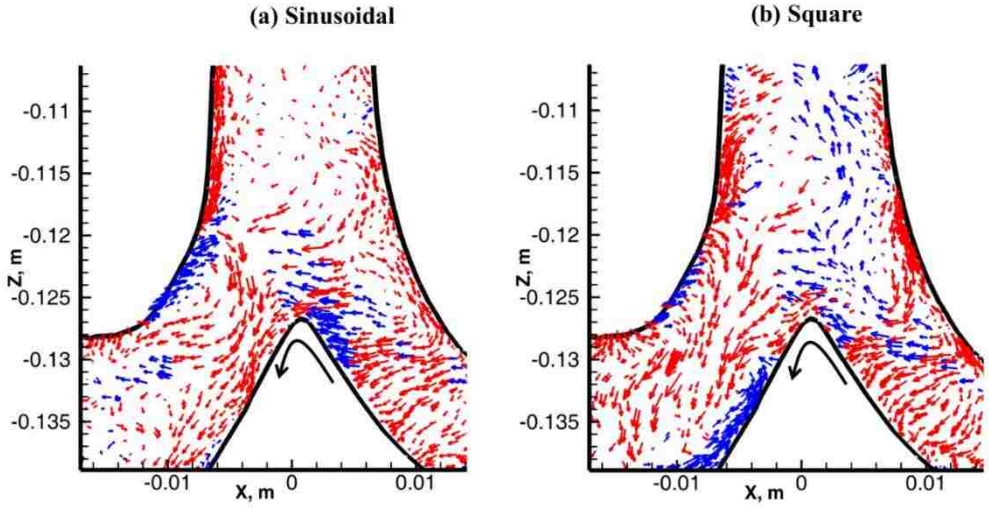

Figure 4.5 Pendelluft-like flow at end inspiration (EaIn) at the main bronchi bifurcation site, and vector plots for 15 Hz HFOV frequency using (a) sinusoidal-waveform, and, (b) square-waveform. Red arrows denote inspiratory flow and blue arrows denote expiratory flow.

4.3.1.3. Secondary Flow

Figure 4.6 presents secondary flow strength (SFS) contours and instantaneous streamlines that are used to analyze secondary flow features at a vertical slice (made by a plane which cuts through the ETT, trachea and main bronchi) and two different cross-sectional planes (TI and T2). Secondary flow strength is defined as the ratio of the radial

(V_r) component of velocity to the mean velocity component at a given location [161]. SFS was characterized as strong when the ratio is greater than 0.6, moderate when $0.3 \leq$ SFS ≤ 0.6, and weak when SFS < 0.3. Contour plots for En-Ex and En-In phases were plotted for three waveform shapes at f = 15 Hz. Flow transport, under current conditions, as characterized by strong secondary flow (i.e. SFS > 0.6) due to the high Reynolds number and presence geometrical complexity such as ETT, successive branching tubes, curvatures and non-uniform cross-sections. The secondary flow behavior differed based on waveform shape and phase. Different vortical structures were associated with the flow field near flow reversal. Small vortical structures existed due to presence of shear layers between coaxial counter flows. Complex, distorted, asymmetric and unstructured vortices formed at the transverse planes at all locations and during all phases. However, the shape and strength of these vortices differed from one station to another. For example, at the EnEx phase of the sinusoidal wave (see Figure 4.6a) a large counter-clockwise swirl motion existed at slice T1 while a pair of asymmetric counter-rotating vortices developed at T2 due to the effects of asymmetric merging of the flow from the main bronchi and effects of curvatures. Additionally, the secondary motion, at any given location, changed appreciably depending on ventilator phase. As illustrated in Figure 4.6a, a single vortex occurred at T1 in the EnEx phase, whereas two counter-rotating vortices formed at the dorsal side of the trachea and a large clockwise vortex at the ventral side at the same location during EnIn phase.

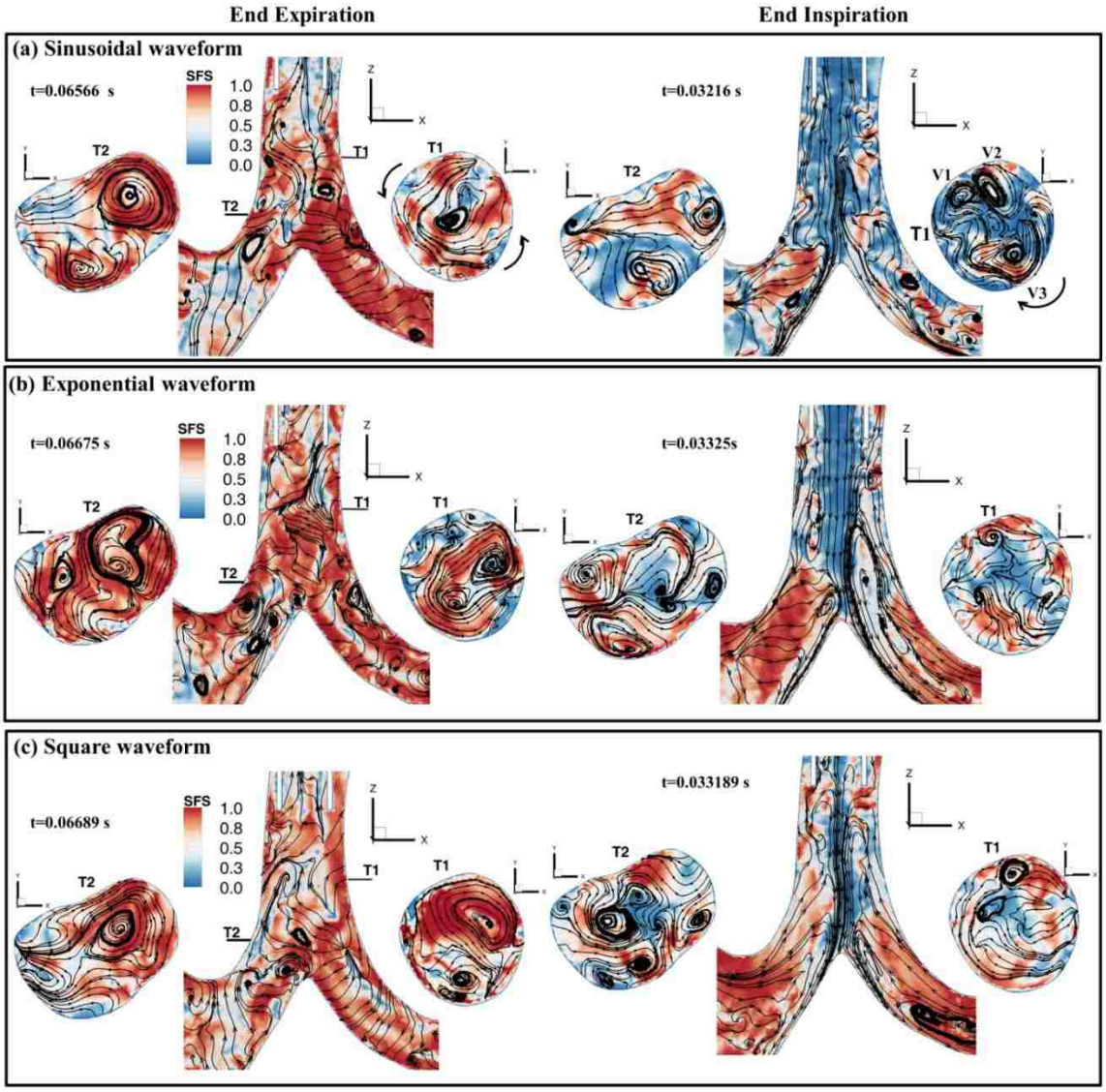

Figure 4.6 Secondary Flow Strength (SFS) contour and streamlines at different planes (vertical slice and two different transverse slices T1&T2) for f = 15 Hz for (a) sinusoidal, (b) exponential, and, (c) square waveforms. Plots presented for end expiration (EnEx) and end inspiration (EnIn) phases.

The secondary flow pattern changed with variation in the waveform shape. A stronger secondary flow with a higher radial velocity occurred at the main bronchi during the EnIn phase of the non-sinusoidal waveforms (Figure 4.6a). This enhancement was

also evident by counting the total number of counter-rotating vortical structures that existed on the transverse slice T2 at the same phase. Upon comparing the streamlines on T2, it was observed that three counter-rotating vortices exist for a sinusoidal waveform (Figure 4.6a). However, upon changing to a non-sinusoidal waveform (exponential or square), the number of vortices increased, depicting a further strengthening of secondary flow which would subsequently lead to enhanced gas mixing at the same plane.

Figure 4.7 plots the averaged SFS for the sinusoidal and square waveforms at different times during the ventilation cycle. SFS was averaged at different locations, cross-sectional planes were considered in the trachea (T1) and main bronchi (L1 and R1, see Figure 4.1). High SFS values were observed over the cycle time for both cases with four distinct peaks that indicates the start and end of inspiration and expiration. The peak value during EaIn occurred approximately ~6% quicker for the square waveform and was followed by a rapid deceleration that led to the occurrence of the second peak for En-In. It was observed, however, that the occurrence of the second peak was delayed for the square waveform due to lower deceleration compared to the sinusoidal case. Similar observations were made for the expiration phase. The square waveform is characterized by a relatively steep gradient of pressure and flow rate and this leads to stronger disturbance, which was characterized by an intermediate peak during the inspiration phase (see L1 and R1 in Figure 4.7b); such a peak was not present for the sinusoidal case. Additionally, at T1, a noticeable difference in SFS magnitude was observed during the EnEx phase. Towards the end of the cycle, the SFS decreased for the case of a sinusoidal waveform as opposed to increasing that of the square waveform. This was attributed to

the flow history along with the presence of a strong merging of the flow from the left and right airways main bronchi.

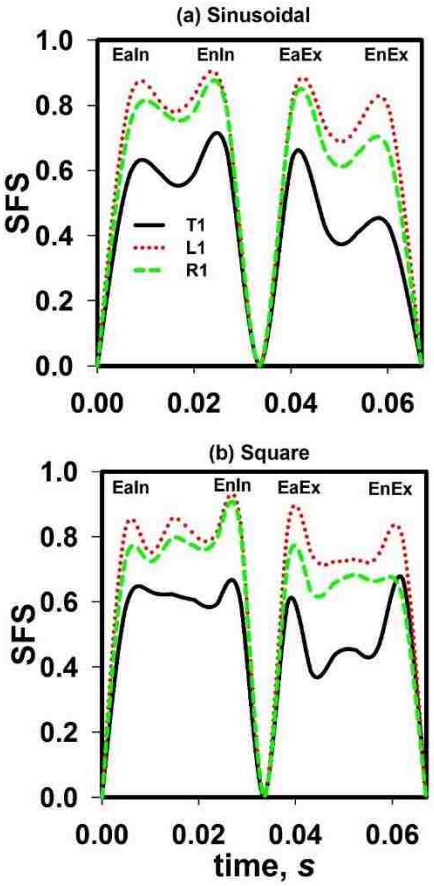

Figure 4.7 Temporal variation of averaged-SFS for *f*= 15 Hz at different locations (cross-sectional slices, T1 at the trachea and L1-R1 at the main bronchi). (a) Sinusoidal waveform. (b) Square waveform.

4.3.1.4. Turbulence

Figure 4.8 displays spatial distribution of normalized TKE from the ETT entrance down to the lower branches (G6-G7) for both the left and right lungs; normalized values are reported at the peak inspiration phase (i.e. maximum TKE) for the sinusoidal and square waveform. TKE increased from the entrance to the end of the ETT before gradually decreasing (~ 40% in value) in the lower regions of the trachea. TKE

dropped abruptly to ~ 44% as the flow passed on to the main bronchi (G1). Downstream of the main bronchi, an increase in TKE was observed at the entrance regions of G2 and G3 in the left and right lungs due to geometrical complexity of successive branching tubes and non-uniform cross sections. A relatively higher magnitude in the left side occurred due to the sharper transition in the geometry. TKE decayed gradually further downstream until it reached the lower region of G5, where the TKE value dropped to < 5% and the flow was deemed to be laminar. During the process of decay in the lower generations, the right lung had a slightly higher TKE compared to the left lung, which was attributed to the asymmetry and local geometrical differences between the left and right airways.

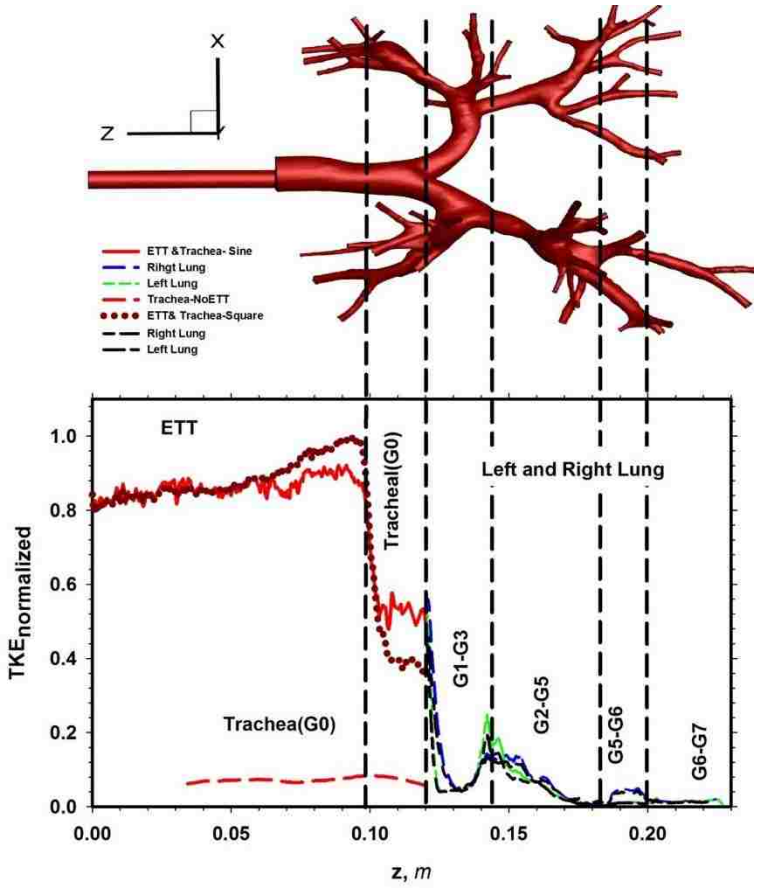

Figure 4.8 Plot of Turbulence Kinetic Energy (TKE) from ETT inlet to lower generations (G7) in both left and right lungs at the peak inspiration phase (f = 15 Hz) and two waveforms and model without ETT. TKE normalized by TKEmax =806 m2/s2.

To quantify the variations in turbulence with changes in HFOV waveforms, temporal variation of normalized TKE was plotted (see Figure 4.9). TKE was averaged at a vertical slice that cuts through the ETT, trachea and main bronchi. Gas transport with the square wave resulted in higher turbulence than the sinusoidal and exponential cases as the square waveform is distinguished by higher deceleration period (i.e. 93% of the inspiration phase) resulting in higher flow disturbance [135] and a resulting high TKE. In contrast, the flow deceleration occupied 50% of the inspiration phase for the sinusoidal waveform and the associated TKE values were lower.

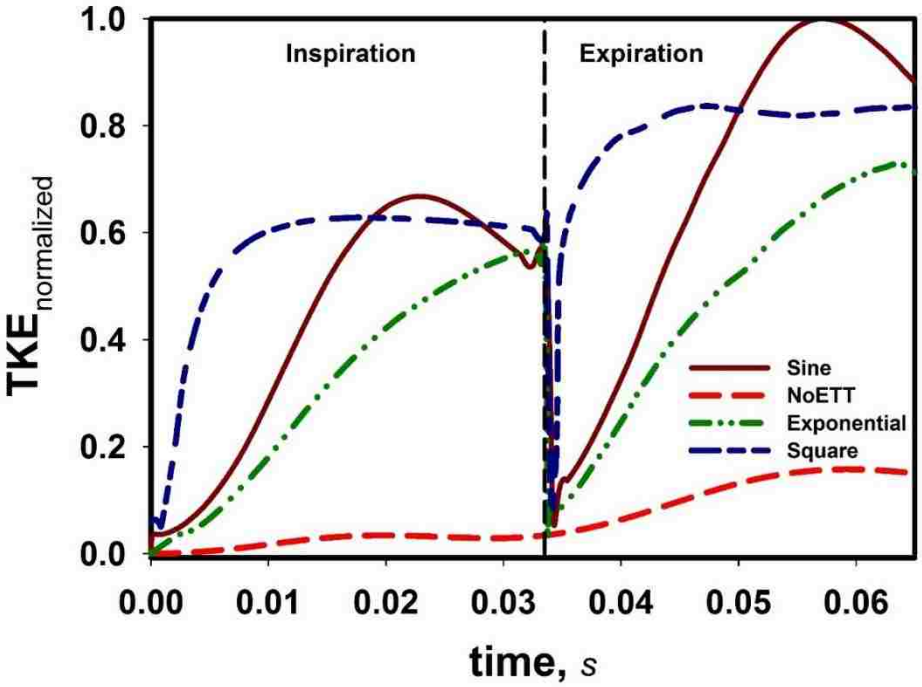

Figure 4.9 Temporal variation of TKE for f = 15 Hz at vertical made by a plane which cut through the ETT, trachea and main bronchi for cases of sinusoidal waveform, exponential waveform, square waveform and sinusoidal waveform for the case without ETT. TKE normalized by the maximum time-averaged TKE =212.73 m^2/s^2.

4.3.1.5. Wall Shear Stress

Figure 4.10a-c compares WSS contours at peak inspiration for the three waveforms at the first bifurcation site; an enlarged back view of the site is presented for the benefit of the reader. Due to the impingement of the ETT-jet at the first carina, high values of wall shear stress were observed and mostly concentrated at the bifurcation site of the main bronchi (see Figure 4.10a) for the sinusoidal waveform. The high shear stress region extended from the lower region of the trachea to the branches that led to the upper and lower lobes of the left lung (see back view) and to first carina ridge of the right lung.

The shear stress was minimal along the top surface of the main bronchi due to a large swirling motion along the outer walls. Beyond these locations, the WSS appeared merely around the carina's ridge in lower generations. However, the magnitude of WSS varied depending on the location of the carina and was ~20% of the value at the main bronchi. A change in the waveform shape to exponential led to more localized patches of the WSS (see Figure 4.10b). Even more reduction of the WSS patches were observed while using square waveform. In the latter case, the patches of local maximum shear stress appeared solely at the inner wall very close to the flow divider of the first bifurcation (see Figure 4.10c). The distribution of WSS was inversely proportional to the level of TKE in the flow. The square form, which had the maximum TKE resulted in more localized patches when compared to the sine waveform where the WSS was more distributed.

The time variation of WSS was also calculated at the carina (denoted by point P) and is shown in figure 4.10d. The point P is located on the inner wall at the entrance to the right main bronchus (see Figure 4.10d); it was susceptible to local maximum shear stress in all cases. It was observed that WSS increased during flow acceleration and decreased during flow deceleration following a pattern similar to the flow rate curve. In addition, a large increase in WSS occurred during inspiration compared to expiration due to the influence of ETT-jet.

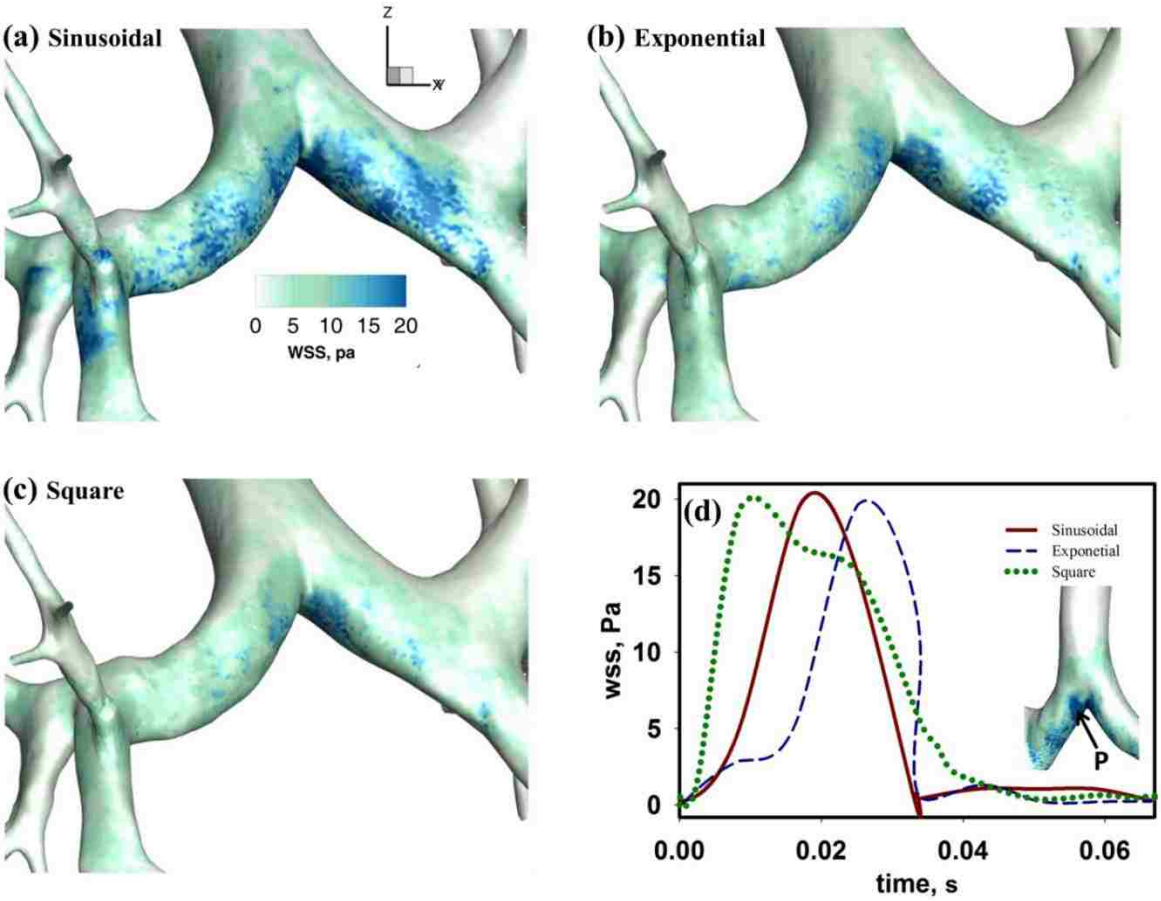

Figure 4.10 (a)-(c) Wall shear stress (WSS) contour at peak inspiration (f = 15 Hz) for the three waveforms. Plots show the back view of the first bifurcation. (d) Temporal variation of the WSS at point P for the three waveforms and f=15 Hz.

4.4. Effect of Frequency

To understand the effect of HFOV frequency, simulations were run at frequencies of 10 Hz and 6 Hz [Womersley number (α) of 14.85 and 11.50 respectively]. Counter-flow patterns for the sinusoidal and square waveforms at EaIn phase are plotted in Figure 10a. Changing oscillatory frequency had a pronounced effect in counter flow pattern. For example, for the sinusoidal case, flow at the right side of trachea was still in phase (zone 1), whereas, at the same location (zone 3) the flow was out of phase. The differences in

the counter flow pattern when using different waveform shape still existed even when changing the frequency. This was clearly observed by comparing the flow at zones 2-4 in the case of 10 Hz and zones 3-5 for the 6 Hz frequency (Figure 4.11a). The pendelluft-like motion was observed at EaIn phases when using a sinusoidal waveform with frequency of 6 Hz (see Figure 4.11a). For non-sinusoidal shapes, pendelluft was not present when HFOV frequency was decreased.

The variation of the wall shear stress along the cycle time had similar profiles for all frequencies. Its magnitude, however, dropped with a decrease in the frequency (see Figure 4.11b). For further illustration, Table 4.4 presents the maximum wall shear stress WSS (at point P in Figure 9d) for the inspiration and expiration phase for all three waveform and frequencies. It was found that the WSS value dropped by ~ 72% when the frequency was reduced from 15 Hz to 6 Hz, indicating a reduction in the risk of alveolar damage and barotrauma at lower frequencies.

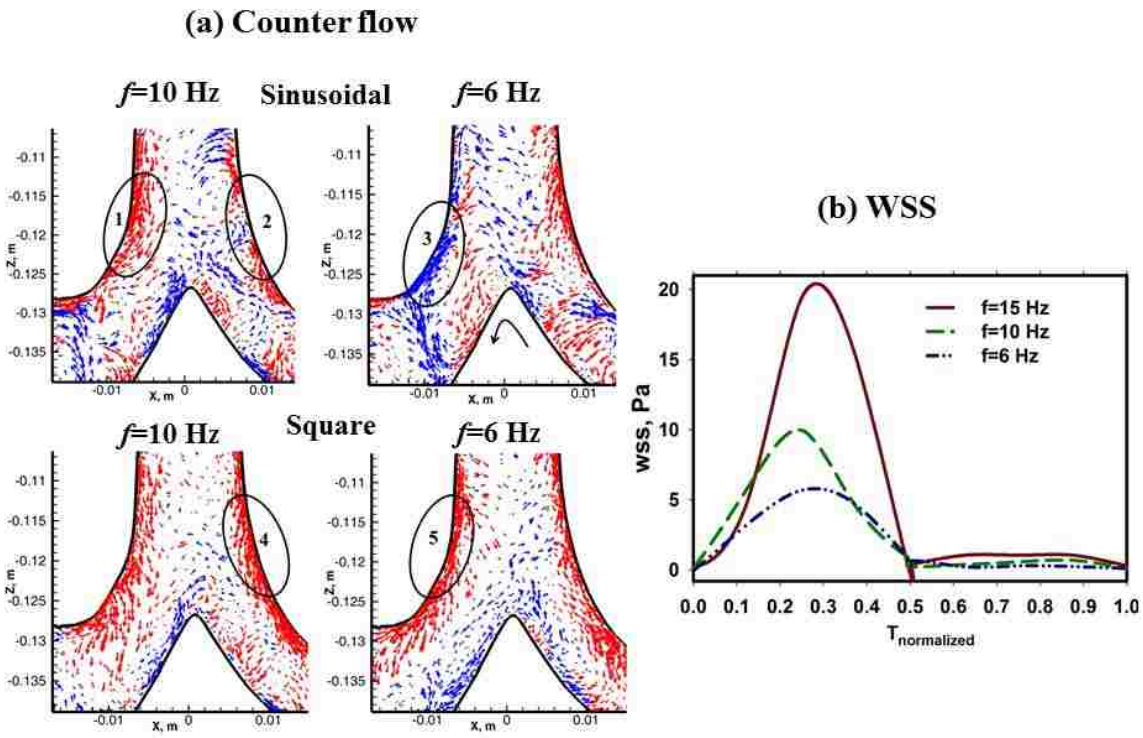

Figure 4.11 (a) Coaxial counter flow at the bifurcation site for the sinusoidal and square waveforms. Data are for HFOV frequencies of 10 and 6 Hz and EaIn. Red arrows denote inspiratory flow and blue arrows denote expiratory flow. (b) WSS versus normalized cycle time ($T_{normalized} = t/T_{cycle}$) at point P (see Figure 9d) for frequencies of 6, 10 and 15 Hz and the case of the sinusoidal waveform.

4.3.1. Effect of Endotracheal Tube

To check the influence of ETT on fluid transport and mixing, simulations were performed without the ETT for the sinusoidal waveform at a frequency of 15 Hz. The results show that the presence of ETT had a significant effect on the flow structure. Figure 4.12a shows the coaxial counter flow at En-In for the cases with and without ETT. The coaxial counter flow had zones of reversal flow in the case of ETT (Figure 4.12a). In the case without ETT, the inspiratory flow moved uniformly in the core region of the

trachea and inner wall of the main bronchi and the expiratory flow transported along the outer wall of the main bronchi and trachea.

Figure 4.12b shows the wall shear stress distribution at the first bifurcation site (back-view) for the case without ETT. The local maximum WSS moved downstream (lower generation) and was present at the carina site between generation G2 and G3 in the left lung (see Figure 4.12b). This was in sharp contrast to the case where the ETT jet was present and resulted in patches of maximum WSS at the bifurcation of the main bronchi.

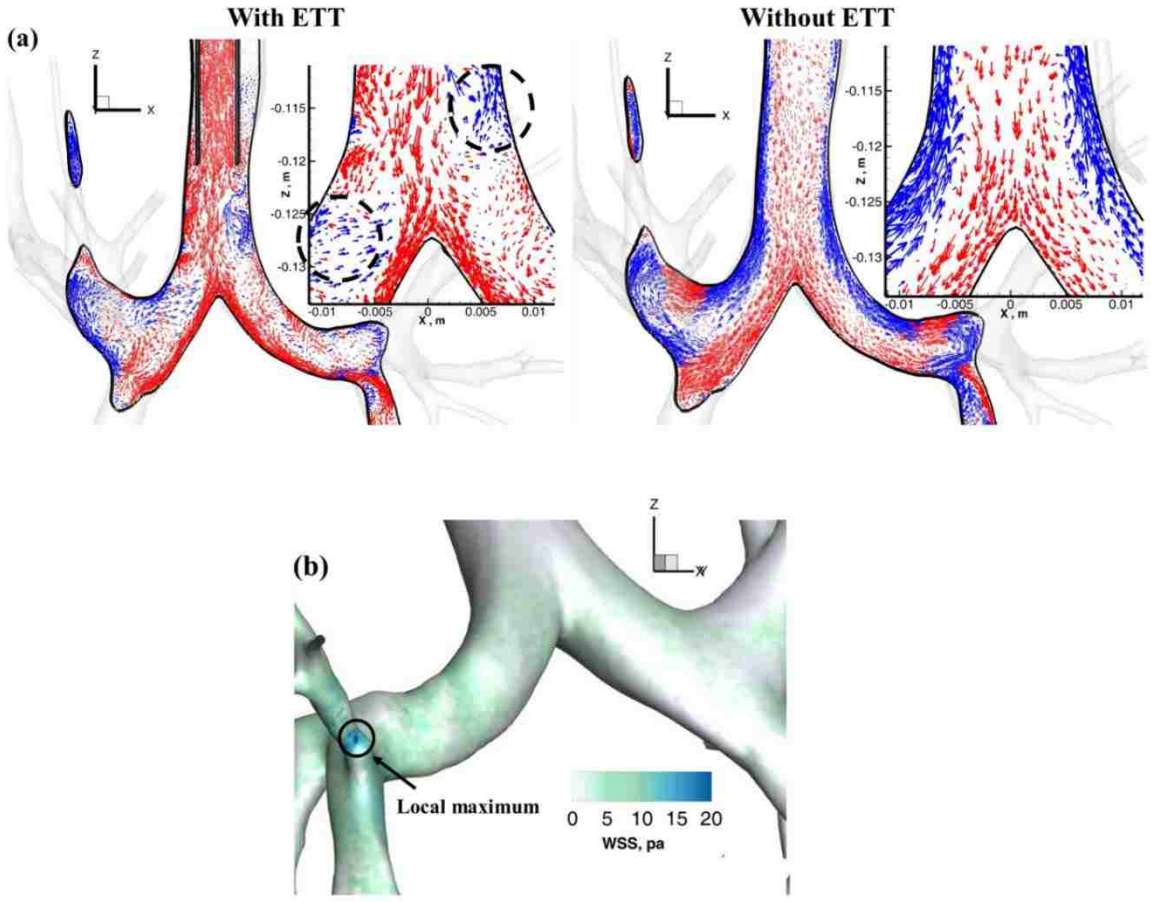

Figure 4.12 Coaxial counter flow at Ea-In for sinusoidal waveform (f=15 Hz) for cases with and without ETT; (b) Wall Shear Stress (WSS) contours at the first bifurcation site (back view) for the case without ETT (sinusoidal wave, f =15 Hz).

To further elaborate the effects of ETT, the maximum WSS at the point P (see Figure 4.10d) during inspiration and expiration, for the cases with and without ETT, are listed in Table 4.4. The maximum WSS during inspiration phase decreased ~87% when the ETT was absent. The absence of ETT was seen to drastically reduce the overall turbulence in the geometry. In the trachea, when ETT was present, the TKE observed to be ~ 20 times higher (see Figure 4.8). Furthermore, the averaged TKE was ~ 94% and ~ 83% lower during inspiration and expiration respectively when intubation was absent.

Table 4.5 Maximum wall shear stress (WSS) at point ***P*** for all cases at inspiration and expiration phases.

Waveform		**Sinusoidal**				**Exponential**			**Square**		
Frequency, Hz		15	10	6	No ETT*	15	10	6	15	10	6
Wall Shear stress Pa	**In**	19.72	9.96	5.66	2.61	19.61	7.21	5.18	19.24	8.98	4.48
	Ex	1.04	0.68	0.28	2.00	1.27	0.44	0.24	2.38	0.41	0.40

*At *f*=15 HZ

4.4. Discussion

The effectiveness of the convective mixing (non-diffusive component due to stretching and folding of material region of fluid) depends on the interaction and activity of the flow structures [47, 162]. The gas mixing occurs in the case of irreversible oscillatory flow and diminishes when the flow is reversible (i.e. the fluid particle returns to its initial location at the end of cycle). Therefore, the radial and axial mixing rate increases when the coaxial counter flow is associated with higher secondary flow and

turbulence [47, 98, 162-164]. On the contrary, even with existence of counter flow, the absence of secondary flow leads to zero net convective mixing [47]. The qualitative results from the present study demonstrated that the coaxial counter flow occurs near flow reversal for all three waveforms with different features. These differences of the flow pattern could lead to a significant impact on the gas mixing. The counter flow was associated with higher turbulence intensity and slightly stronger secondary flow when using square waveform than the other cases. Furthermore, using square waveform led to a high reduction on the WSS distribution due to lower flow rate and the flow structures activity at the vicinity of the lung walls. This implies that using square waveform could be more efficient for gas mixing and less dangerous to the lung epithelium layer, due to the reduction of the WSS [12].

The present results were also compared to existing studies in the literature to examine the effect of the geometry morphology. Heraty *et al* [98] experimentally studied the oscillatory flow in both single idealized and realistic bifurcation models. Choi *et al* [47] numerically studied HFOV in idealized single bifurcations and a large scale realistic lung model. The following differences were observed: for a sinusoidal waveform, the irregular counter flow had a different pattern (highly disturbed) to that in Choi *et al* [47] (idealized model) and Heraty *et al* [98] for all frequencies. It resembled the patchy appearance of the counter flow in case of HFNR (high frequency normal Reynolds number) in the large-scale model [47]. In addition, at the EnIn/EaEx phase, using non-sinusoidal waveform exhibited entirely different patterns of the counter flow to that in Choi *et al* [47] (large-scale model). The counter flow pattern was relatively uniform and resembled that in Heraty *et al* [98]. It was also observed that the pendelluft

flow was absent when using exponential waveform shape. This mechanism was also not reported in previous studies [47, 98]. These variations suggest that the geometry features along with the waveform shape play a major role in the coaxial counter flow pattern and the pendelluft flow. Furthermore, both studies [47, 98] used an idealized geometry and reported existence of Dean-type vortices [165], whereas highly complex and asymmetric vortices were observed in the current geometry. The variation in the geometry morphology and the presence of the ETT-jet had a major role in this difference. The comparison of the major dimensions of the current geometry, Heraty *et al* [98] and Choi *at al* [47] are listed in Table 4.5.

Table 4.6 Comparison of the major dimensions of the geometries of the current study, Heraty *et al* [98] and Choi *et al* [47].

Study	D_d/D_p		**β°**
	Right	Left	
Present study	0.64	0.75	74.33°
Heraty - Realistic Model	0.64	0.68	44°
Heraty - Idealized Model	0.84		63°
Choi - Idealized Model	0.70		70°
Choi - Large-scale model	0.75		70°

Note: D_p is the parent (G0) diameter, D_d is the daughter (G1) diameter, and, β is the angle between the main bronchi.

4.5. Conclusion

A LES-WALE model was used to investigate gas transport and mixing in HFOV for three different waveform shapes and frequencies. The primary focus of this study was to understand how different flow mechanisms were altered as a result of changes to waveform and frequencies. It is concluded from the study that:

1- The coaxial counter flow existed near flow reversal for all three waveforms with different features. The non-sinusoidal waveforms exhibited a uniform coaxial counter flow compared to the sinusoidal case at End-Inspiration/Early Expiration phase.
2- Pendelluft flow was present for the sinusoidal waveform at all frequencies but occurred only at early inspiration for the square waveform at highest frequency, whereas this was absent in the case of using exponential waveform.
3- A square waveform shape resulted in higher secondary flow strength (SFS>0.6) and higher turbulence intensity, which could lead to more efficient mixing.
4- A reduction of ~87% in the wall shear stress occurred during inspiration phase when the intubation was absent. The turbulence kinetic energy in the case of using ETT was found to be 20 times greater than when the ETT was absent.
5- The square waveform resulted in the least wall shear stress on the lung epithelium layer and may be used in patients without the risk of barotrauma to both airways and the alveoli.

CHAPTER 5[2]

THE ROLE OF COUPLED RESISTANCE-COMPLIANCE IN UPPER TRACHEOBRONCHIAL AIRWAYS UNDER HIGH FREQUENCY OSCILLATORY VENTILATION

[2] *This chapter was based on the following published paper with permission from Elsevier publishing:*

Alzahrany M., Banerjee A., Salzman G. The Role of Coupled Resistance-Compliance in Upper Tracheobronchial Airways under High Frequency Oscillatory Ventilation. Medical Engineering and Physics. Published online. September 2014.

5.1. Introduction

The Pulmonary flow based on HFOV is notably complex [32], and several physical mechanisms are thought to play a role in gas transport and mixing. See chapters 1 and 4 for more details. A better understanding of gas transport associated with these mechanisms is vital for the improvement of HFOV management [32]. Detailed CFD studies provide valuable information on flow physics that can be used to formulate the ventilation technique, and boundary conditions are of paramount importance to accurately modeling the flow physics during HFOV. For instance, gas exchange between respiratory units (i.e. pendelluft mechanism) is time constant dependent. The time constant (τ) is the product of the resistance and the compliance of the airways; the asynchrony of the time constant due to variation of the respiratory units resistance or compliance causes the gas exchange between the units [32]. It is therefore essential to model resistance and compliance at the domain outlets properly to capture this movement correctly and to characterize the flow redistributions that occur during HFOV. Traditionally, different types of (flow) outlet BCs are utilized in pulmonary CFD, including: (a) Type-I BCs where uniform flow rate or velocity is prescribed [47]; (b) Type-II BCs where uniform pressure is used [48, 117]; and (c) Type-III where the mass flow rate at each outlet is set as the mass fraction of the instantaneous inlet mass flow rate [96, 166] and is based on statistical model data [51]. However, these BCs do not account for non-uniformities of lung ventilation [46], and gas exchange between adjacent units cannot be captured due to inability of modeling the asymmetry in R&C between adjacent units. Hirahara *et al* [109] have studied air flow in an idealized lower airways

model (G18-20) using the lumped and CFD method. They implemented Type-II BCs based on R&C of the airways and determined that pressure had a phase-delay due to compliance asymmetry, which caused flow transport by pendelluft mechanism.

In the present study, time-dependent pressure BCs as a function of instantaneous flow rate and coupled R&C was imposed at the exits of the image-based lung geometry model. The primary objective is to perform LES modeling to investigate the effect of coupled resistance-compliance BCs on the lung lobar ventilation and gas transport, particularly mass exchange by asynchronous ventilation, under invasive HFOV. To account for healthy and diseased lungs, several scenarios were considered by varying lung compliance either between lungs or locally between units.

5.2. Methods

Figure 5.1a shows the lung model with an endotracheal tube and the units locations. LES is used to model the transient three-dimensional oscillatory flow using a finite volume solver (ANSYS® CFX14). Wall Adapting Local Eddy viscosity sub-grid scale model is adopted to model small-scale eddy effects [167]. The details of the numerical techniques and computational mesh of the current complex lung geometry were described in chapter 3. The time step was set to be 10^{-5} s to ensure a low CFL number [46].

5.2.1. Breathing Cycle and BCs

Inlet boundary condition: A sinusoidal waveform was considered as follows:

$Q(t) = Q_{max} \sin(2\pi ft)$, where the maximum flow rate $Q_{max} = \pi f V_t$ and t is the cycle time. HFOV frequencies of 6, 10 and 15 Hz were selected. A tidal volume of 50

mL was chosen and was appropriate, as it was less than the dead space volume [1, 47]. A blunt velocity profile was imposed at the inlet of ETT as [90, 95]:

$$u(r,t) = 1.224\,U(t)\left(1-\frac{r}{R_{ETT}}\right)^{\frac{1}{7}} \tag{5.1}$$

$U(t) = u_{amp}\sin(2\pi ft)$ is obtained velocity from the HFOV waveform; and $u_{amp} = fV_t / R_{ETT}^2$ is the amplitude velocity.

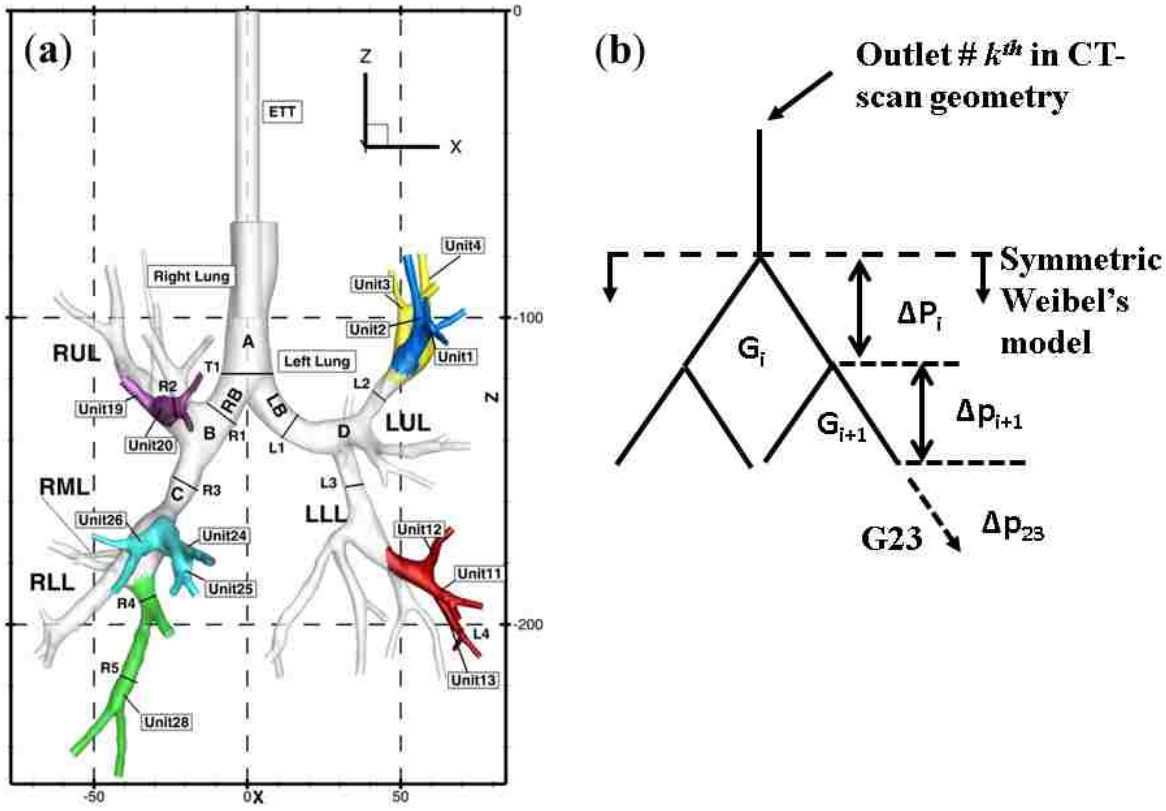

Figure 5.1 (a) Model with descriptions of the locations of all selected units and lung main lobes [RB: right bronchus, LB: left Bronchus. RUL: right upper lobe, RML: right middle lobe, RLL: right lower lobe; LUL: left upper lobe, LLL: left lower lobe]. The letters A to D represent the following: A represents the main bronchi bifurcation (LB and RB), B represents the bifurcation between the RUL and the branch that leads to both RML and RLL, C represents the bifurcation between the RML and RLL, and D represents bifurcation between the LUL and LLL. (b) The dimensions of a symmetric Weibel's Model are used to calculate the pressure at each resolved outlet branch in the CT-scan model.

Outlet boundary conditions: The equation of motion [eqn. (5.2)] was used to compute pressure at each outlet in the CT model as a function of instantaneous flow rate $q(t)_{outk_j}$ at outlet number *k* (generation *j*) of CT model and the R&C of the airways as [109, 166, 168, 169]:

$$p(t) - PEEP = Rq + \frac{V}{C}\ ,\ q = \frac{dV}{dt} \tag{5.2}$$

where *PEEP* is the positive end-expiratory pressure (assumed zero). To estimate *R* and *C*, a symmetric Weibel network [59] is chosen beyond each CT model outlet (see Fig. 1b), and resistance was calculated based on steady flow through the Weibel model. The total compliance value was taken from the literature. Because the Weibel model bifurcates into two symmetric branches, beyond generation G*j* of our CT model, the flow rate ($q_b(t)\big|_i$) at each subsequent generation *i* (=*j*+1) was evaluated as:

$$q_b(t)\big|_i = \frac{q(t)_{outk_j}}{2^{i-j}} \tag{5.3}$$

The total pressure loss from the outlet of the CT model to the alveoli due to resistance in all airway segments was then calculated as (see Fig. 5.1):

$$p(t)_{outk_j}\Big|_{\Delta p-resist} = q(t)_{outk} \sum_{i=j+1}^{23} \frac{R(t)_i}{2^{i-j}} \tag{5.4a}$$

Additionally, the pressure loss due to compliance was computed as

$$p(t)_{outk_j}\Big|_{\Delta p-comp} = \frac{\int_0^T q(t)_{outk_j}\, dt}{C_{outk_j}} \tag{5.4b}$$

where $\int_0^T q(t)_{outk_j}\,dt$ is the delivered volume V during a period from $t = 0$ to $t = T$. Using equation (5.2), the total pressure at the k^{th} CT-Model's outlet is calculated as a sum of the total pressure loss at each time step due to R&C in all airways segments:

$$p(t)_{outk_j} - PEEP = \left[q(t)_{outk_j} \sum_{i=j+1}^{23} \frac{R(t)_i}{2^{i-j}} + \frac{\int_0^T q(t)_{outk_j}\,dt}{C_{outk_j}} \right] \tag{5.4c}$$

A time-dependent resistance [$R(t)$] at each branch is computed using the formula introduced by Barbini *et al* [170]:

$$R(t)_i = R_{L,i}[1 + k_{bi}\,|q_{bi}|] \tag{5.5}$$

where $R_L = 128\mu L/\pi d^4$ is the Poiseuille (laminar) resistance, L and d are the length and diameter of each Weibel segment, μ is the fluid viscosity, q_{bi} is the volume flow rate at each branch of generation i, and, k_{bi} is a constant estimated based on the inlet flow rate. For the current study, the inlet flow rate ranged from 56.5 L/min to 141 L/min and a range of values of 6.4285 s/l to 0.047 s/l, representing G5 to G10, were chosen for k_{bi}. For generations G11- G23, the value was taken as zero [170]. The second term in eqn. (5.5) accounts for a high flow rate, where turbulence effects may be present [170]. However, this term was found to have no significant effect on the solutions under the present HFOV conditions as the low flow rate at the terminal units leads to a very small contribution from this term ($0.013 < Re < 1823$). Additionally, the compliance in eqn. (5.4c) dominated the pressure level at each outlet for the current HFOV and geometry

conditions. Our findings are consistent with High *et al* [171], who reported that lung-compliance dominates the pendelluft flow. The compliance for each generation is calculated by adopting the formula introduced by Barbini *et al* [170]:

$$C_{outk_j} = C_o / 2^j \tag{5.6}$$

where C_0 is the total compliance and *j* is generation number of outlet number k^{th}. Grimby *et al* [172] measured the total compliance for a group of patients suffering from COPD, bronchial asthma, and cysts; the compliance ranged from 0.15 to 0.55 *l/cm* H_2O. A value of 0.2 *l/cm* H_2O for C_0 was adopted in the present study.

Wall boundary condition: No-slip wall BCs were used [34] and the number of cycles required to reach statistical convergence was investigated. The solution statistically converged after two-three cycles for the range of frequency reported in this work. Four cycles were considered adequate, and the values reported are from the fourth cycle [166]. Table 5.1 presents all cases considered in the current study.

Table 5.1 HFOV and lung conditions used for the current study (V_T = 50 mL).

Case No.	Frequency (Hz)	Compliance ratio (*CR*)
1-3	10	1, 4, 10
4*	10	10 (local variation)
5-6	15	1, 10
7-8	6	1, 10

The compliance ratio ($CR = C_R / C_L$, where C_R and C_L is the compliance of the right and left lung respectively) was varied by keeping the compliance in each generation in the left lung fixed and the corresponding generation in the right lung is multiplied by a different

factor. For case 4 (see Table 5.1), the compliance ratio of the selected local lung adjacent units was varied by multiplying the compliance of outlets in one unit by 10, while the compliance at the outlets of the neighbor unit were kept fixed. For more illustration, Figure 5.2 shows an example of the local compliance ratio variation (CR_{Local}) between two units. The local *CR* variation is made, while the global *CR* in both the left and right lungs was kept 1. The selected adjacent units are (unit1 and unit2), (unit3 and unit4), (unit11 and unit 12), and (unit 25 and unit 26); see Fig. 5.1a.

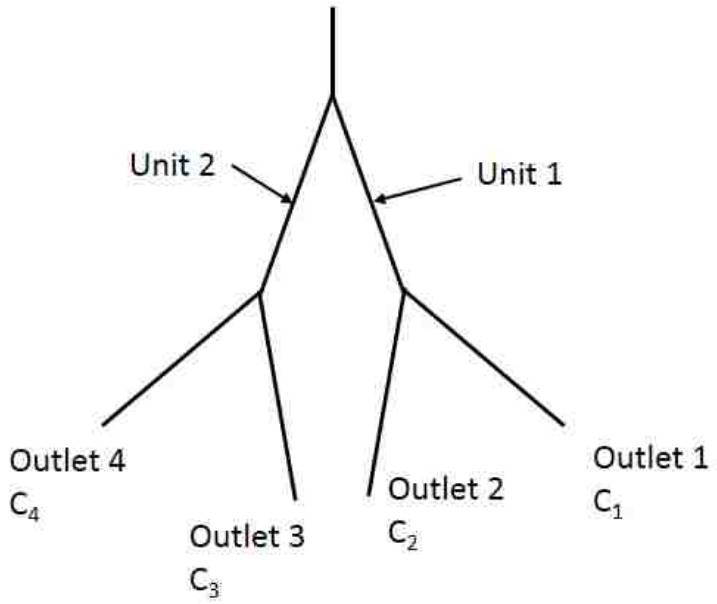

Figure 5.2 An example of local variation of the lung compliance ratio, CR_{Local}. Considering two adjacent units (1 and 2), the compliance ratio CR of unit 1 to unit 2 was set 10, [$CR_{Local}=C_{unit1}/C_{unit2}=10$], as follows: $CR_{Local}=C_{unit1}/C_{unit2}$, $CR_{Local}=10$, $C_{unit1}=10\times C_{unit2}$, ($C_1$ or C_2)$=10\times$ (C_3 or C_4)

5.3. Experimental Validation

The computational results with coupled resistance-compliance BCs were validated with the experimental data of Lee *et al* [173] who investigated the flow transport in a symmetric single Y-shaped bifurcation representing G18- G19 based on the Weibel description [59]. Two cases with highest and lowest air volume ratio (*VR*) were considered at HFOV frequency of 15 Hz, i.e., *VR* = 8 and 1. The air volume ratios is defined as the ratio of volume in left branch to volume in right branch *al* [173]; and it was calculated by integrating the flow rate over one ventilation cycle. The time-dependent pressure BCs were used at the outlets [eqn. (5.4)] and resistance was computed using eqn. (5.5). The compliance at outlets of G19 was computed using the technique described in the previous section and the *CR* was varied until reaching the volume ratio. A very small time step was used (i.e., $\Delta t=10^{-5}$ s) to properly resolve the pendelluft movements. The coupled R&C BCs successfully replicated the experimental data (*VR* 8:1 and 1:1), which demonstrated the maximum and minimum pendelluft flow in the experiment. The simulation results show the flow swings between the two branches at EnIn and EnEx phases (Fig. 5.3a), mimicking the experimental observations (Fig. 5.3b).

For further comparison between the experimental and computational results, the elapsed time during the pendelluft (T_P) was quantified and compared in Table 2 for both cases. T_P signifies the period from the beginning to the end of the pendelluft flow; and it was calculated as the total time-period between instances when the flow-rate curves for the mother and daughter branches crosses the zero flow phase. T_P was in close agreement with experimental measurements at the EnIn phase. A maximum difference of 10% in T_P was found at the EnEx phase in case of *VR*=8; and was attributed to approximations in

model geometry, especially at the transition region of the bifurcation. In general, modeling results were in good agreement with the experimental data, validating that R&C BCs are important to modeling lung ventilation and gas transport under HFOV conditions.

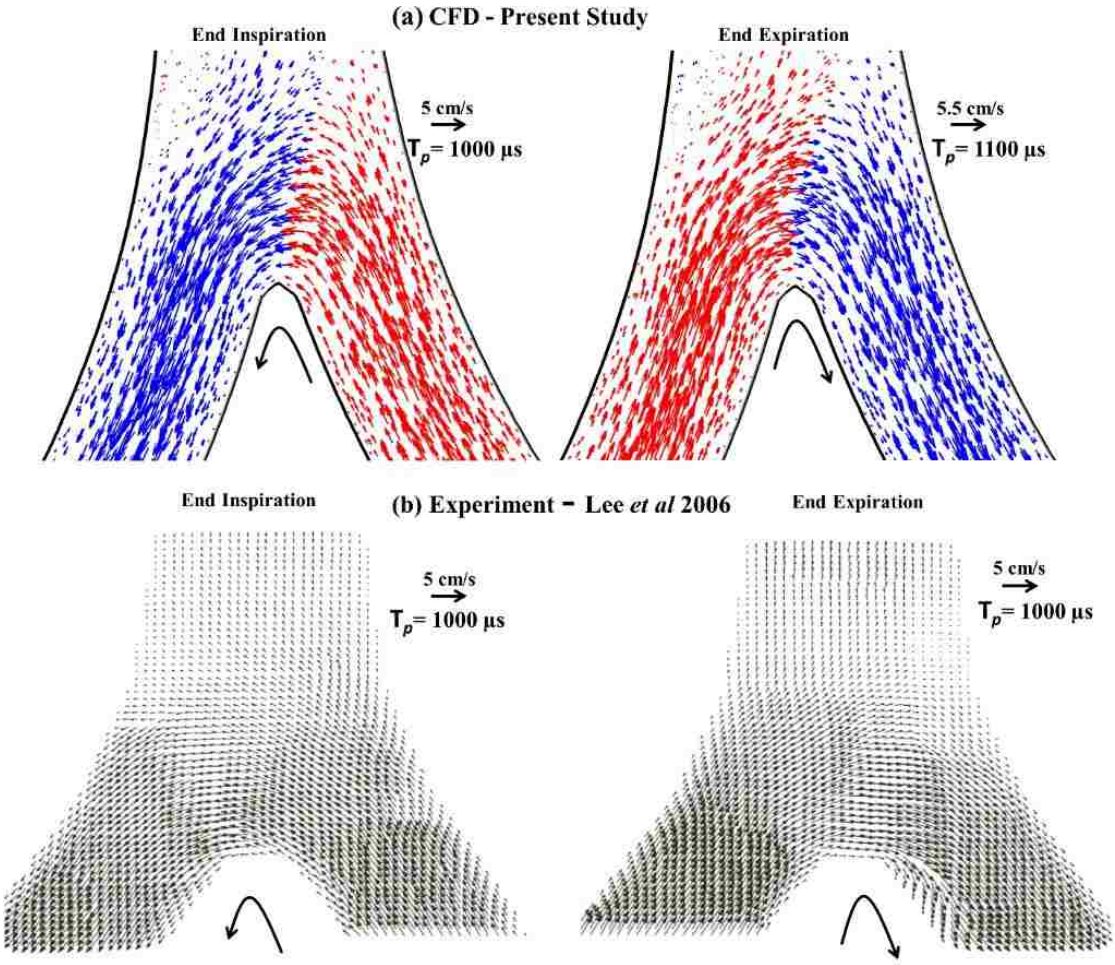

Figure 5.3 (a) Results from the validation study and comparison with (b) experimental data of Lee *et al*, 2006 [173]. Data were taken at time of t/T=0.5, where T=1/f is the total cycle time, f=15 Hz. In (a), the red vectors move upward, indicating the expiratory flow and blue vectors move downward, indicating inspiratory flow. Images in (b) were taken (with permission from Institute of Physics Publishing) from Lee *et al*, 2006 [173].

Table 5.2 Comparison of predicted and measured elapsed time during Pendelluft flow (T_P) for different cases.

Case No.	Volume ratio (*VR*)	Compliance ratio (C*R*)	Phase	T_P (μs)		Percent Difference
				Experimental measurement Lee *et al* [24]	Predicted values (Present study)	
1	8	9.35	EnIn	1000 μs	1000 μs	0%
			EnEx	1000 μs	1100 μs	10%
2	1	1.04	EnIn	100 μs	95.9 μs	4.1%
			EnEx	100 μs	101.92 μs	1.92%

5.4. Results and Discussion

5.4.1. Flow Distribution

The flow distribution throughout the major lung divisions (left and right lung) was computed as a fraction of the total inlet mass flow rate and compared with different computational and experimental (both *in vitro* and *in vivo*) studies. The flow distribution under coupled R&C BCs demonstrated a significant change in the cases when traditional BCs were employed. To illustrate the difference in the BCs, a flow distribution ratio (*FR*) was defined as the ratio of the flow rates between the left and right lungs. Table 3 presents the percentage of the total flow defined as the flow distribution in the left and right lung as a percentage of the total flow in the trachea and compares the *FR* values for various pulmonary CFD studies reported in the literature using different types of BCs. The values of *FR* based on utilizing coupled R&C in the present work ranged from 0.62 to 0.69 for a healthy lung (i.e., *CR*=1) and 0.45 to 0.49 for a diseased lung (i.e., *CR*>1).

For brevity, only four cases are presented in Table 3. De Backer *et al* [97] conducted *in vivo* flow measurements (for a COPD patient) using clinical scintigraphy imaging techniques and reported a *FR* value of 0.41. This value is in good agreement with our computational results utilizing coupled R&C BCs with diseased lung scenario (*CR*>1). However, previous CFD studies using traditional BCs predicted a value of *FR* that was twice as large. A value of 0.79 was reported by De Backer *et al* [97] with the type-II BCs. A value of 0.83 was obtained in our previous work [166] with Type III BCs based on MF values prescribed by Horsfield *et al* [51]. Moreover, *in vitro* experiments by Cohen *et al* [174] reported a *FR* of 0.67; this value is in agreement with the cases of the healthy scenario (*CR*=1). Therefore, it is clear that the lung *CR* plays an important role in flow distribution between the two lung lobes and physiological BCs based R&C must be used to capture relevant HFOV flow mechanism.

To investigate the effects of lung compliance on flow distribution, the *CR* was varied from 1 to 10. When the compliance is higher in one lung or unit, a higher volume is delivered due to the decrease in pressure in that region. To study the influence of the frequency on the flow ratio, simulations with three values of frequency (6, 10 and 15Hz) were run, while the *CR* was held constant. Additionally, a parametric study was also performed by varying the *CR* from 1 to 10 for each frequency.

Table 5.3 Comparison of the flow distribution between the left and right lungs with the available published data.

	Percent total flow (the flow distribution in the left and right lung as a percent of the total flow in the trachea)							
	10 Hz, CR=10	15 Hz, CR=10	6 Hz, CR=10	6 Hz, CR=1	Cohen[a]	De Backer[b]		Alzahrany[c]
BCs Type	R&C BCs				P=const.	*In vivo*	Type-II	Type-III
Left Lung	32.29	33.02	30.83	40.88	40	29	44	45.4
Right Lung	67.71	67.98	69.17	59.12	60	71	56	54.6
FR	0.48	0.49	0.45	0.69	0.67	0.41	0.79	0.83

[a]Experimental study on the human tracheobronchial cast under cyclic inspiratory (up to G10) with constant pressure at the outlets (P=const.). The values are reported for the mean of range of inlet flow rate conditions [174] and Q = 7.5 – 60 L/min.
[b]Clinical gamma scintigraphy measurements (Q = 23 L/min) (left column) and CFD with Type-II BCs (Right column) uniform pressure at all outlets. The geometry consists of ~ 6-7 generations [97].
[c]CFD study on the same considered geometry in the current study using pre-specified mass flow rate fraction at outlets based on the Horsfield **[51]** Model (Type-III BCs) [166].

The flow distributions demonstrated strong dependency on the HFOV frequency with a variation in lung *CR*. Upon changing *CR* from 1 to 10, the *FR* decreases by approximately 21%, 24%, and 35% for the HFOV frequencies of 6, 10, and 15 Hz, respectively. This is attributed to the higher pressure at the inlet associated with the increased operating frequency and to the change in the time constants of the system [78, 169].

5.4.2. Pendelluft Mechanism

To demonstrate the presence of pendelluft flow, vectors and streamlines at EnIn in a selected lung unit (# 26, see Fig. 5.1) are plotted in Fig. 5.4. The red vectors denote inspiratory flow and blue denotes expiratory flow. As observed in Fig. 5.4a, the flow in branch 45 began expiring and filled into branch 44, which was still inspiring (see delineated regions 1 and a close-up). However, simulations with Type-III BCs failed to predict pendelluft behavior (see delineated regions 2 and close-up view in Fig. 5.4b) as both branches respired in the same phase.

Table 4.4 briefly summarizes previous CFD studies with different outlet BCs for the occurrence of pendelluft flow. Choi *et al* [47] studied the airflow during HFOV in a large-scale realistic model (up to G7) using type-II BCs. A HFOV frequency of 6.28 Hz was used for which the authors report the absence of any pendelluft flow. Nagels and Cater [48] studied HFOV at 25 Hz frequency in an idealized double bifurcation model with type-II BCs employed at the outlets. Pendelluft flow was captured between the main bronchi. Similar observations have been reported by Alzahrany *et al* [166] where Type-III-based BCs were imposed. In both studies [48, 166], the existence of pendelluft flow was merely geometry (asymmetry) dependent and was only captured at the main bronchi. In contrast, in the present study, coupled R&C BCs successfully captured the pendelluft flow in different lung regions due to asymmetry in the R&C of the lung units.

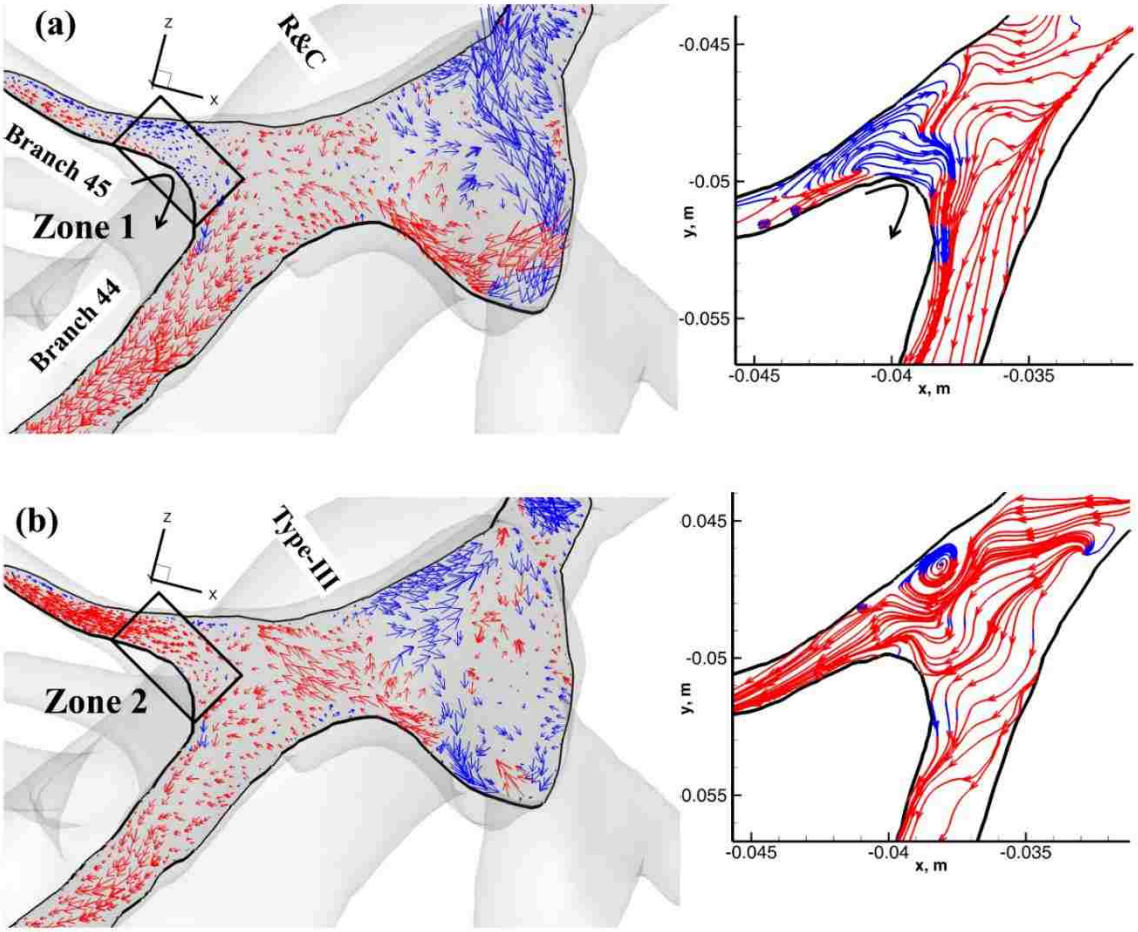

Figure 5.4 Comparison of the flow field vectors and stream-trace at the EnIn phase for frequency of 10 Hz at unit 26 using: (a) coupled R&C BCs; and (b) MF (Type-III) BCs. The red vectors denote the inspiratory flow and blue vectors denote the expiratory flow. The Pendelluft flow occurs in the case of using coupled R&C, while it is absent in case of using Type-III BCs. Data are shown for t/T=0.49 and *f*=10 Hz.

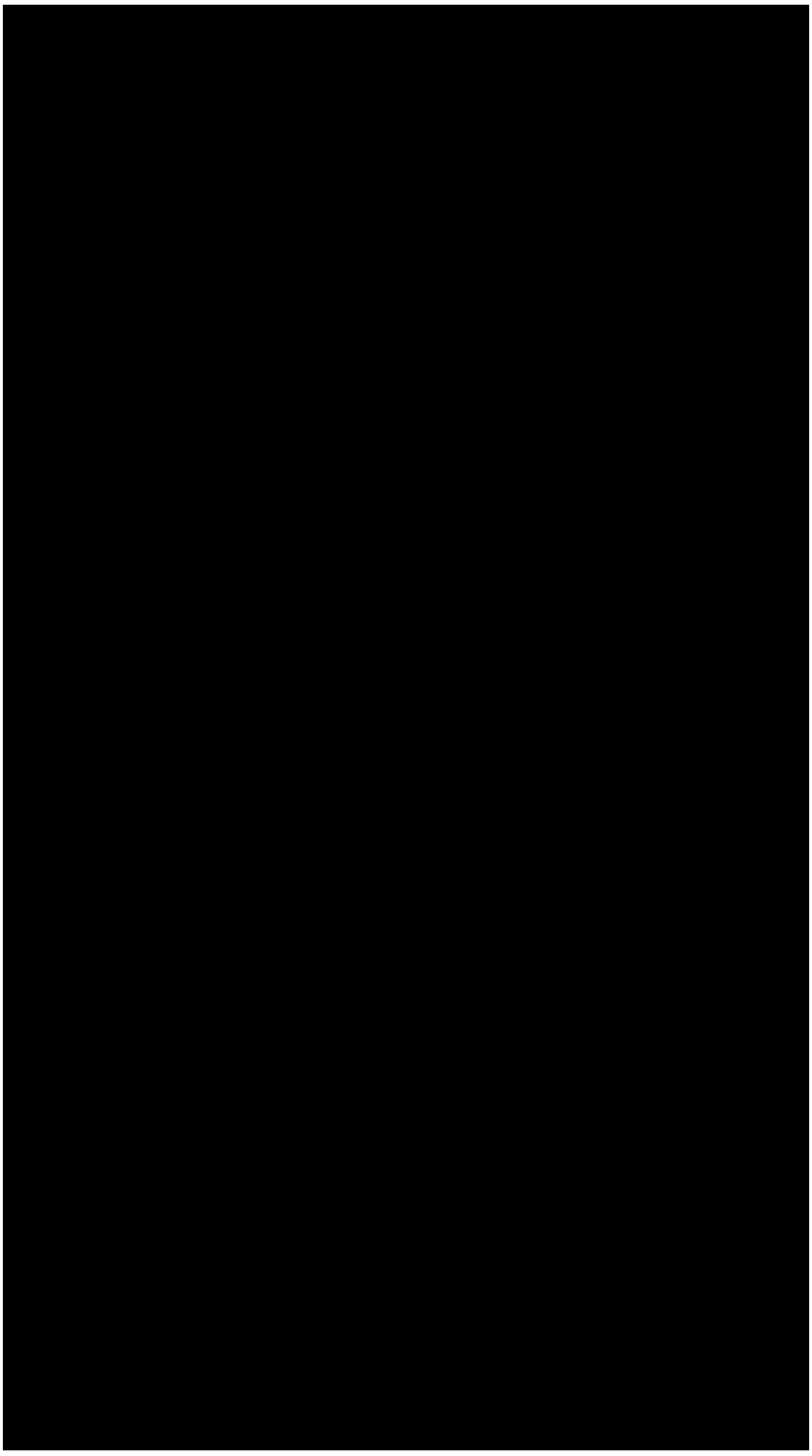

5.4.2.1. Pendelluft Time and Volume

The pendelluft intensity was characterized based on the pendelluft time percent (f_P) and Pendelluft volume percent (V_p). Figure 5.5 shows a representation of the pendelluft characteristics and the definitions of the relevant parameters. For any unit, Q_u, Q_1 and Q_2 are the flow rates in the mother and daughter tubes (branches 1 and 2). T_P is the Pendelluft time defined as the total time-period between instances when the flow-rate curves for the mother and daughter branches crosses the zero flow phase. The pendelluft time percent (f_P) is defined as the percent of the total cycle time that pendelluft occurs. The pendelluft volume percent (V_p) is defined as the ratio of the volume exchanged between the daughter branches [V_{T1} branch 1 at EnIn or V_{T2} branch 2 at EnEx] to the total volume delivered to the unit (V_u) and is calculated by integrating the flow rate over one cycle [175].

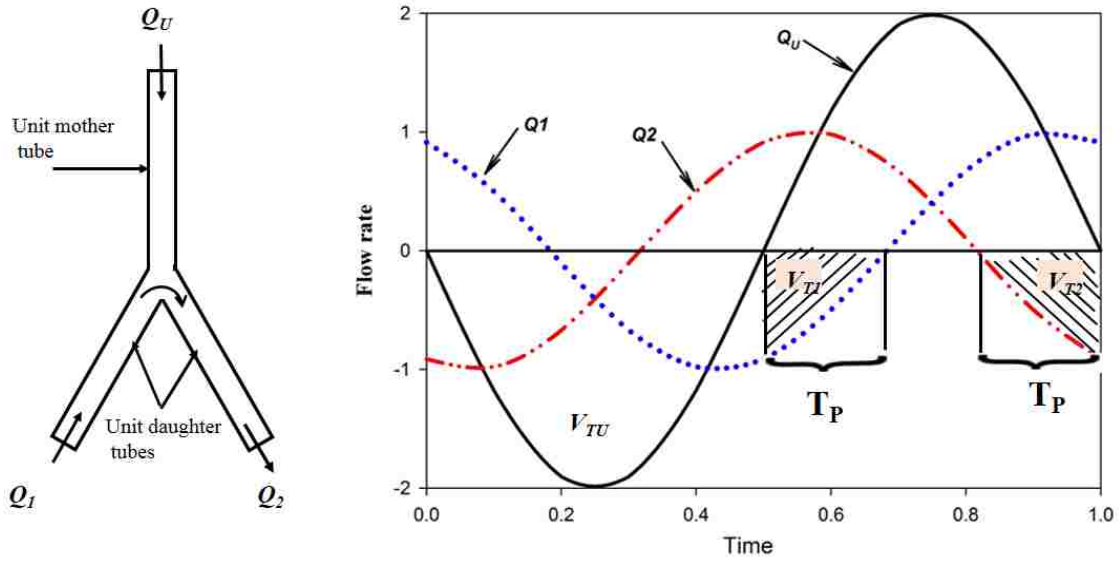

Figure 5.5 Representation of the pendelluft characteristics and relevant parameters. Q_u is the flow rate in the mother tube of the unit. Q_1 and Q_2 are the flow rates in the daughter tubes (branches 1 and 2), respectively. T_P is the Pendelluft time. V_u the total volume delivered to the unit. Shaded area, the gas volume exchanged between the daughter tubes (V_{T1} branch 1 and V_{T2} branch 2) during the pendelluft time [175].

5.4.2.2. Varying the Compliance Ratio

Figure 5.6 presents f_P and V_P for the case of f = 10 Hz and different CR (1, 4 and 10 between the right and left lung; CR_{local}= 10 between selected regional units). To facilitate a comparison between the different cases, a few specific examples are listed in Table 5.5. Pendelluft was observed at different lung units with varying intensity. For example, at the EnIn phase and CR=10 (see Fig. 5a), f_P (V_P) in unit 1 was approximately less than 0.3% (1.5%), but these values were five-fold higher in unit 26, which was located in the more compliant lung. Various scenarios were observed by varying the CR. In units that were located in the less compliant lung, only small changes occurred in (f_P and V_P) by changing CR, while a significant change occurred in the units located in the higher compliant lung (see Example 1, Table 5.5). However, this feature was location (geometry) dependent (see example 2); an increase in CR (from 4 to 10) resulted in a decrease in f_P (33.9%) and V_P (42.44%) in the LLL lobe (less compliant).

Both the parameters were also compared across different HFOV phases (EnIn and EnEx). It was observed that both f_P and V_P were higher at EnIn phase compared to EnEx when both lungs were equally compliant (Fig. 5.6b). However, upon increasing the CR, the scenario was reversed in some units, depending on the locations and CR value (see Example 3). The largest increase (> 500%) in both parameters was obtained for case 4 when CR was varied between selected local units while keeping the global CR at unity between right and left lungs (see example 4). This mimics a scenario in which a patient may have local blockage in the lungs due to presence of a tumor that would change CR locally in an otherwise healthy lung. Two conclusions can be made based on these observations. First, f_P and V_P were weakly dependent on global lung compliance in the

less compliant airways with only a slight increase or decrease (±5%) in both parameters. Second, both parameters were strongly dependent on local lung compliance, as both f_P and V_P were drastically changed in those units. Furthermore, these observations were independent of the phase of HFOV and were similar in both EnIn and EnEx phases. The dependency of the pendelluft intensity on the locations was observed by Andrey *et al* [176] in their *in vivo* study and was attributed to the differences in the distribution of the volume between lungs and major lobes and the effect of the regional features, such as diameter, length, asymmetry and sharp transitions in geometry.

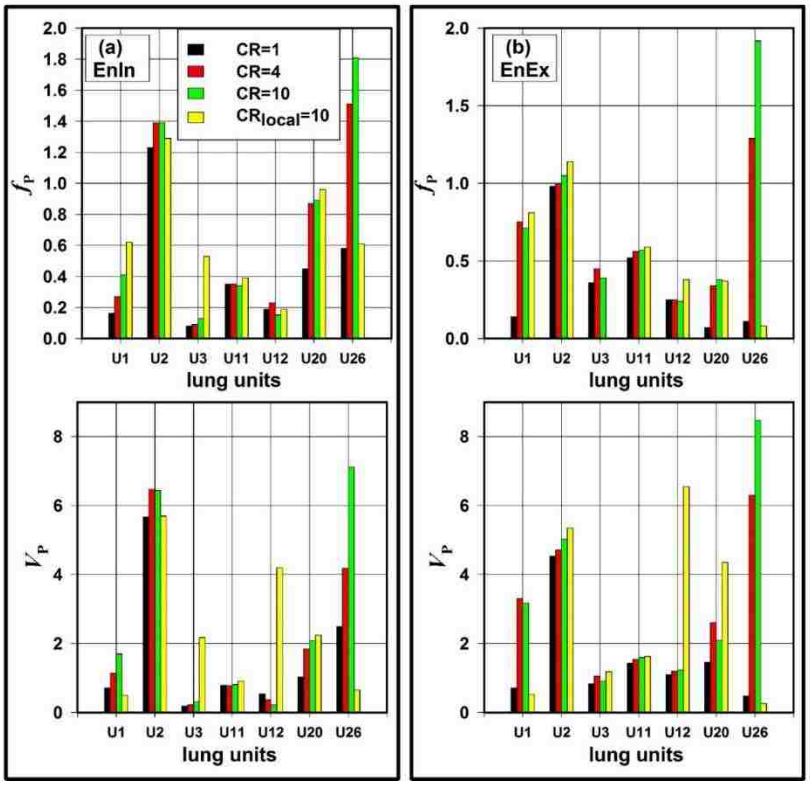

Figure 5.6 Pendelluft time percent (f_P) and Pendelluft volume percent (V_P**)** between the selected lung units for f=10 Hz. The data are for cases 1 to 4 (CR=1-10) at (a) at EnIn, and (b) EnEx.

Table 5.5 Illustration of the effects of a varying *CR* on the pendelluft intensity for *f*=10 Hz.

Example No.	*CR*	Lung Anatomy	Terminal Unit	Generation (lung unit)	f_P	V_P	Status
1	1,10	LUL: Anterior *Less compliant*	Unit2	G5 (L)	12%	13%	Increase as *CR* Increases
		RUL: Apical *Higher compliant*	Unit20	G5 (R)	95.56%	100.3%	
2	4,10	LLL: Anterior Basal	Unit12	G7 (L)	-33.9%	-42.44%	Decrease as *CR* Increases
3	1	RLL: Medial basal	Unit26	G6 (R)	81.3%	81%	Increase at EnIn
	10				6.19%	18.33%	Increase at EnEx
4	10 (local)	LUL: Posterior	Unit3	G6 (L)	533.6%	897%	Increase from *CR*=1

5.4.2.3. Effect of HFOV Frequency

To examine the effect of the frequency on the pendelluft flow, simulations were run at HFOV frequencies of 6, 10 and 15 Hz (*CR* =1). It was found that the oscillating frequency had a significant impact on the pendelluft intensity; the general trend that was observed was f_P and V_P tended to increase as the frequency increased. This is attributed to the elevation of the inlet pressure due to the frequency increase, which leads to a higher pressure gradient and changes the system's time constants, leading to more pronounced phase-shift that enhances the pendelluft flow [78, 169]. It was also dependent on the location. For example, in unit 2 (located in LUL), both values increased substantially (f_P by 199.78% and V_P by 190.3%) when changing the frequency from 6 to 15 Hz. However,

an increase of 43.8% in f_P and 37.6% in V_P was observed in unit 28 located in RLL lobe. This is most likely due to the proximity of unit 2 to the branch that feeds LUL lobe. Unit 2 receives 23.3% of the total volume that enters that lobe. On the other hand, unit 28 is located in the distal end of RLL lobe and it receives 12.9% of the total volume feeds that lobe. Similar observations of increasing pendelluft intensity with increasing frequency were also reported by Elad *et al* [169]. In their study, however, a lumped method was used to analyze flow in single bifurcation. At the EnEx phase, similar observations to those of the EnIn phase were found.

5.4.2.4. Pendelluft Intensity between the Lung's Major Lobes

The pendelluft intensity (f_P and V_P) was computed for all frequencies between major lobes for *CR*s of 1 and 10, respectively (see Figure 5.7). For the case of *CR = 1* at EnIn phase, (Fig. 5.7a), both the pendelluft parameters increased with an increase in HFOV frequency. The Pendelluft intensity was strongest at location B (i.e., between RUL and the branch leading to RML and RLL). During EnEx phase, a drastic decrease in f_P and V_P was observed compared to that at EnIn phase, particularly at locations B and C. In contrast to the inspiration phase, where the flow diverged at the bifurcation site, a strong merging of the flow occurred during the expiration phase, which caused a reduction in the pendelluft intensity. Simulations with *CR* of 10 (Fig. 5.7b) exhibited slightly different features of pendelluft flow. The pendelluft intensity increased at locations in the right lung (more compliant) and decreased at locations in the left lung when increasing the *CR* (see Fig. 5.7) and is attributed to the increase/decrease of the flow in the higher/lower compliant lung. At the EnIn phase, different behavior of the pendelluft at location C

(right lung) was observed when the *CR* increased to 10. A further increase in the frequency (to 15 Hz) decreased the intensity of pendelluft (Fig. 5.7b). This was most likely due to a combination of changes in the flow features when increasing the frequency and *CR* along with the effect of the irregular structures of this branch. The right lung (more compliant) received the majority of the flow. Additionally, this branch had irregular structures with sudden contractions, followed by an expansion at the junction that fed all successive branches. At the EnEx phase (Fig. 5.7b), similar trends were observed for a *CR* value of 10, as both f_P and V_P were consistently higher than the case of using *CR*=1.

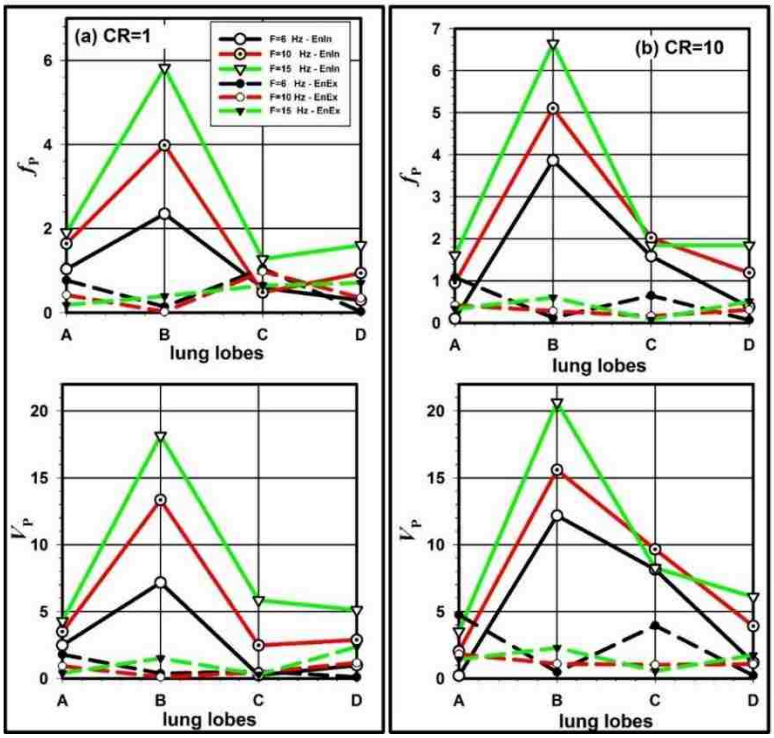

Figure 5.7 Pendelluft time percent (f_P) and Pendelluft volume percent (V_P) between the lung major divisions (lobes) at different HFOV frequencies (6, 10 and 15 Hz) for (a) CR = 1; and, (b) for CR = 10. The solid lines are at the EnIn phase, while the dashed lines are at the EnEx phase.

5.4.2.5. Physiological Relevance of Pendelluft Flow

Ultman *et al* [175] reported challenges in assessing the physiological relevance of Pendelluft flow in an idealized single bifurcation model mostly due to the lack of a direct measurement of the pendelluft in the lungs. A study by Andrey *et al* [176], using the method of sounds mapping to detect the lead and lag time of the pendelluft in the lung (at 14 sites), was therefore used as a guide to discuss the physiological relevance of our simulations. Andrey *et al* [176] reported mean and standard deviation (s.d.) values of the lead time (T_p at EnEx) and lag time (T_p at EnIn) for groups with subjects classified into a control group and those suffering from COPD. The measured values in all 14 sites were averaged, and then the mean and s.d. values of each group were reported as a percent of the lead and lag time to the inspiratory time, $f_{PI} = (T_p)/$ (inspiration time) $\times 100$. Values of f_{PI} were reported as 4%±5% (mean ± s.d.) for the control group, while a value of 14%±13% was reported for the COPD group. The values of reported lag time were 13%±12% and 28%±25% for the control and COPD groups, respectively. In the present CFD study, the values of f_{PI} varied based on the different factors (e.g., units and lobes' locations, *CR* and frequency). The mean values of f_{PI} for the selected 13 units (see Fig. 5.1) were 1.94% and 1.51%, for the case of f=15 Hz and *CR*=10, at EnIn (lag time) and EnEx (lead time), respectively. These values fit into reported ranges of the *in vivo* study [176].

5.4.3. Coaxial Counter Flow

The bidirectional flow that exists at the beginning/end of the inspiration and expiration phases was compared for different BCs. Figure 5.8 presents the counter flow at

the vertical slice (made by a plane that cuts through trachea and the main bronchi) at the EnIn phase for f = 10 Hz. The red vectors represent the inspiratory flow and blue vectors represent the expiratory flow. In addition to the existence of the pendelluft flow in the case of using coupled R&C BCs (Fig. 5.8a), the expiratory flow moved uniformly at the vicinity of the outer wall of the right bronchus and continued along the right side of the trachea. This is in agreement with observed coaxial counter flow in the experimental study of Heraty *et al*. [98], a feature that is not replicated with traditional MF BCs. In the case of MF BCs, the released flow from ETT (inspiratory flow) deviated toward the right bronchus instead of impinging on the carina ridge. Subsequently, the upcoming expiratory flow was forced to swirl inside this airway segment and is highlighted in close-up regions 1 and 2 in Figure 5.8.

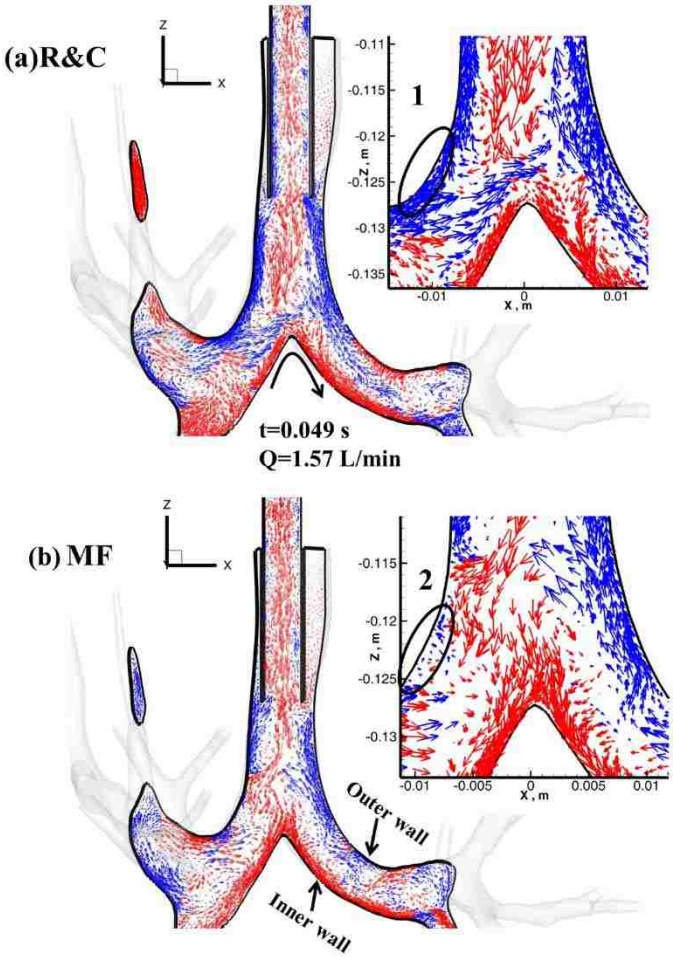

Figure 5.8 Comparison of the coaxial counter flow during the EnIn phase (t/T=0.49, *f*=10 Hz) at the vertical slice (made by a plane that cuts through the trachea and the main bronchi) using the following: (a) coupled R&C BCs and (b) Type-III BCs. Red vectors denote the inspiratory flow and blue vectors denote the expiratory flow.

5.4.4. Effect of Coupled R&C on the Flow Field

To examine the effect of using coupled R&C BCs on the flow field, the contour of the instantaneous velocity (Figs. 5.9a - b) and time-averaged velocity (Figs. 5.9c - d) for both coupled R&C and Type-III BCs were compared at a slice in unit 26. Contours were plotted at the peak expiration phase (t/T = 0.75). The differences in flow structure and velocity magnitude in Fig. 5.9 indicated transient features of the flow field [177].

Furthermore, comparing Figs. 5.9a and c (Type-III BCs) to Figs. 5.9b and d (coupled R&C BCs), a significant change in the flow structure and velocity magnitude (in both instantaneous and mean flow) was observed. This is due to the deviation in the pressure drop magnitudes throughout the domain between the two cases.

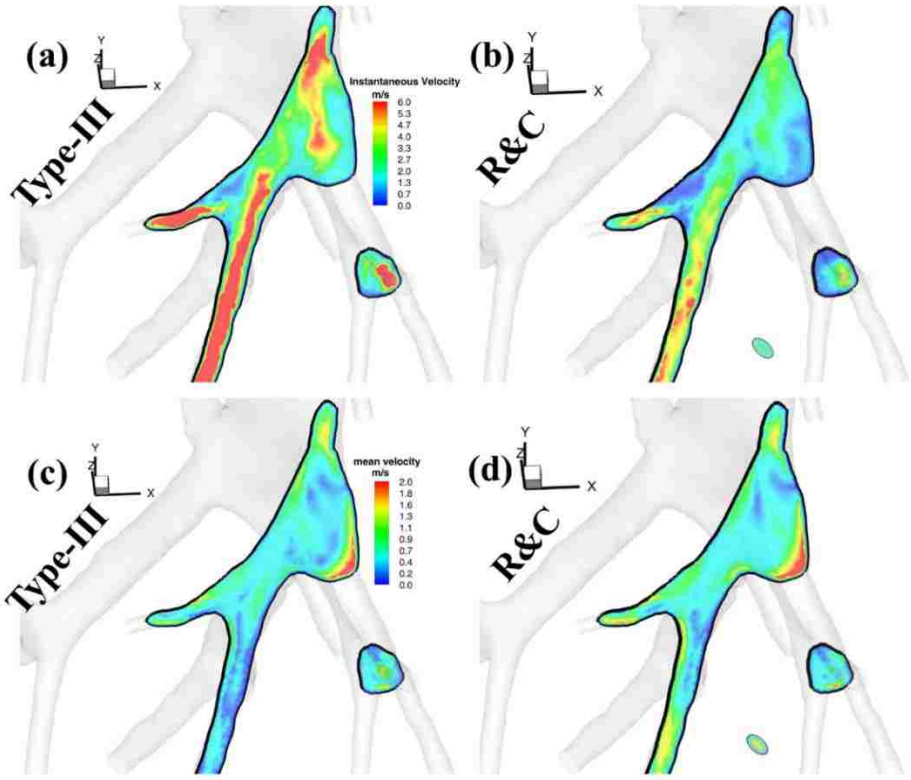

Figure 5.9 Comparison of the effect of BCs on the flow structures. (a) and (b) are the instantaneous velocity and (c) and (d) are time-averaged velocity. The velocity contour is for unit 26 during peak expiration (t/T=0.75, *f*=10 Hz).

Figure 5.10 shows the pressure gradient distribution at the line extending from G2 to the lower regions of both left and right lungs at peak inspiration for the cases of using R&C and MF BCs. Relatively, similar trend of distribution in both cases was observed. The differences in the pressure gradient magnitudes, however, were very significant

throughout the domain. This is because when forcing mass fraction at the outlets, the pressure inside the domain adjusts accordingly to achieve that specified fraction and will not account for the geometry morphology [97] as the present time-dependent pressure boundary conditions. This indicates that using traditional boundary conditions could lead to unrealistic prediction of the flow distribution.

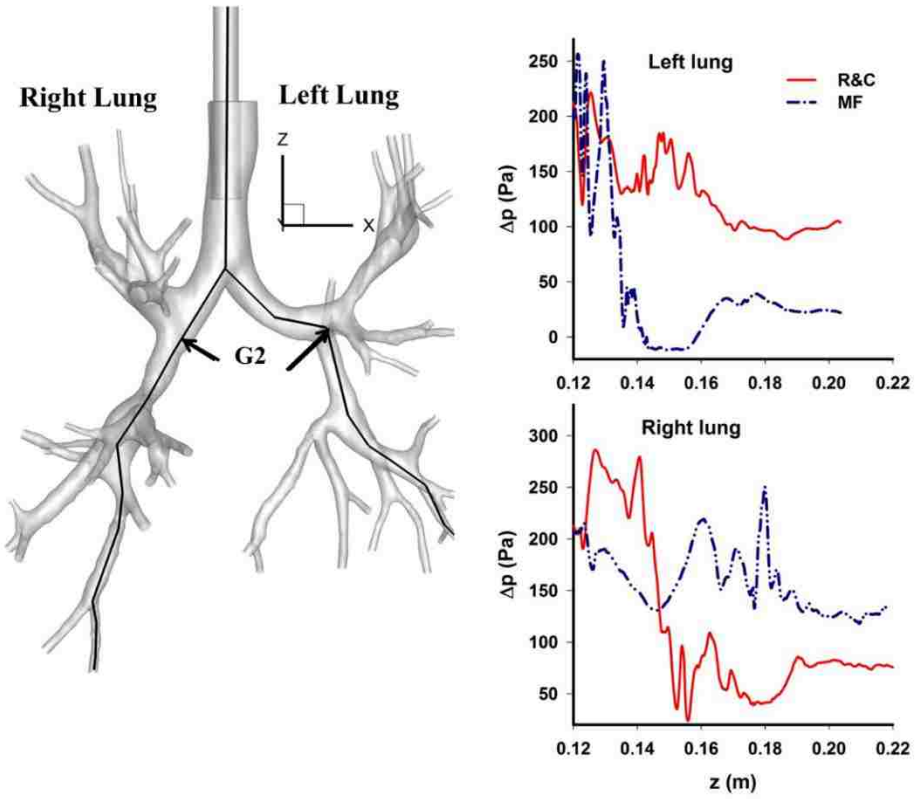

Figure 5.10 Comparison of the pressure gradient distributions throughout the lungs between cases of using coupled resistance-compliance R&C (*CR*=1) and using mass fraction MR boundary conditions. The pressure gradient was computed along line extends from G2 to G7 at peak inspiration in both Left and Right lungs.

The difference and fluctuation in the pressure gradient between the right and left lung were due to the highly asymmetric lung geometry and the variation of the airways

dimensions. This was also observed and reported by Comerford *et al* [178] in their study of structured tree outflow boundary conditions for modeling the airflow in patient specific human lungs. These observations are different from that inside classical simplified models where the pressure uniformly drops throughout the domain as results of the symmetric and uniform geometries [178]. Figure 5.11 shows the wall shear stress (WSS) distribution along unit 26 for the cases of using MF and R&C BCs. The data presented correspond to the EnIn phase. Regions of high WSS occurred around the daughter tubes while using MF BCs (see Fig. 5.11a).

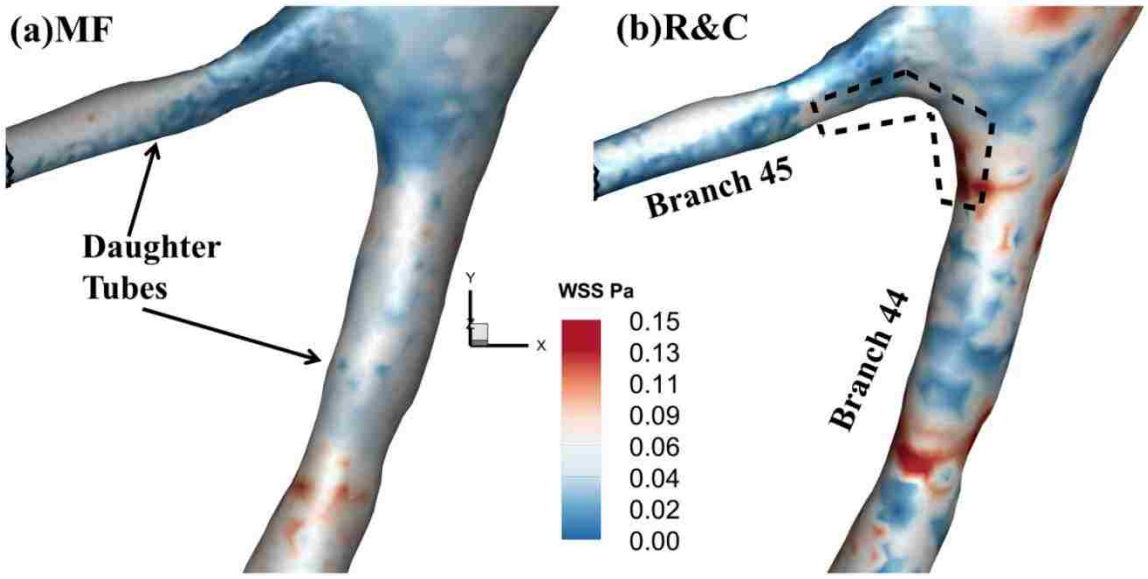

Figure 5.11 Comparison of the wall shear stress (WSS) distributions at unit 26 between the cases of using coupled R&C (*f*=10 Hz, CR=1) and using MF BCs. The WSS was computed at EnIn (t/T=0.49, *f*=10 Hz). (a) The mass flow rate fraction BCs (MF) and (b) coupled R&C BCs.

While using R&C BCs, a drastic change in the WSS distribution was observed. A high WSS was noticed in the region surrounding the flow divider (carina ridge, see

demarcated region in Fig. 5.11b) as opposed to the case of MF BCs, where a minimal WSS occurred at the same site (Fig. 5.11a). This is a consequence of the pendelluft flow, which occurred during this period (i.e., EnIn) while using R&C BCs. The gas flows from branch 45 to branch 44, moving over the carina ridge; consequently, a high velocity gradient is created near the wall, which causes the higher WSS.

5.5. Conclusions

A LES model was used to study the flow transport under HFOV conditions with physiologically relevant outlet BCs. A time-dependent pressure was employed as a function of the instantaneous flow rate and coupled airways resistance-compliance. A significant change in the regional flow distribution was observed when using coupled R&C BCs for healthy and diseased lungs. In addition, the pressure drop throughout the lung domain demonstrated a significant deviation from the case of MF BCs due to the ability of the applied physiological resistance-compliance BCs to account for the geometry morphology. Unlike traditional BCs, the coupled R&C BCs successfully captured pendelluft flow in all of the lungs' major lobes and terminal units, which enables accurate HFOV modeling. Varying compliance between the right and left lungs demonstrated a significant effect on the flow distribution, and it was more pronounced for the highest HFOV frequency. Increasing the *CR* locally between lung units induced maximum pendelluft flow with a five-fold increase in some units. The coaxial counter flow and flow structures were significantly influenced by the modified BCs. The pendelluft flow significantly induced a WSS surrounding carina due to gas exchange between the units' branches. The pendelluft intensity in different regions may be used as

an important indication of the respiratory diseases and the severity of lung pathway diseases. The intensity of the pendelluft flow associated with the ventilator setting (e.g., frequency, tidal volume, and waveform shape) could help in improving treatment protocols for patients undergoing HFOV treatment.

CHAPTER 6[3]

AEROSOLIZED DRUG DELIVERY IN SPECIFIC-PATIENT LUNG MODEL DURING INVASIVE HIGH FREQUENCY OSCILLATORY VENTILATION

[3] *This chapter was based on:*

Alzahrany M. and Banerjee A. Aerosolized Drug Delivery in Specific-Patient Lung Model during Invasive High Frequency Oscillatory Ventilation. *Journal* of *Aerosol Science. Under review September 2014.*

6.1. Introduction

Invasive mechanical ventilation is typically used to substitute spontaneous breathing of patients admitted to the intensive care unit [1]. In many situations, aerosol drug therapy using bronchodilators, antibiotics, and surfactants becomes inevitable during the ventilation process to stabilize the patient [36, 37]. Aerosolized drug delivery to a mechanically ventilated patient is complex and very low amount of aerosols successfully reach the lower lung leading to complications during ventilation therapy [37, 41, 179]. This complexity increases significantly during invasive HFOV because of high frequency and low tidal volumes [42]. Efficacy of aerosol deposition relies on various parameters that are: (1) ventilator related, e.g. ventilation mode or tidal volume inspiration waveform; (2) circuit related, e.g. endotracheal tube size or density of inhaled gas; and, (3) device related, e.g. type of device and its positions [37, 41]. Due to the absence of the knowledge of the role of the these factors on drug aerosol delivery, the current practice is to remove the patient from HFOV and perform manual ventilation during inhaled drug administration [42]. The advantages of HFOV therapy is a current topic of discussion in the medical community [180, 181]. However, there are only limited *in vivo* and *in vitro* studies investigating drug delivery under HFOV.

Computational fluid dynamics (CFD) studies have been carried out to understand and optimize flow and drug delivery to human lungs under normal breathing conditions, a comprehensive review can be found elsewhere [34, 53, 182]. However, particle transport and deposition during HFOV has been overlooked and thus not sufficiently understood. Amongst a few reported in the literature include an *in vitro* study by Garner *et al* [42] to investigate drug (albuterol) delivery by a metered-dose inhaler in a pediatric lung model

under HFOV. A lung simulator with 4.5-mm endotracheal tube was used and operating frequencies of 5 and 15 Hz were used to administrate albuterol repeatedly. It was found that only <1% of the administered dose was delivered to the lung simulator regardless of the HFOV operating conditions (i.e., frequency and inspiratory time). In contrast, a more recent study by Sood *et al* [50] found that pulmonary aerosol delivery during HFOV was effective and was at least as efficient as conventional mechanical ventilation (CMV). Aerosolized drug were administered to piglets using the HFOV circuit and MRI was used to visualize contrast before and after delivery; the effectiveness of the drug delivery was assessed by signal intensity (SI) changes. None of the reported studies perform exhaustive parametric analysis to quantify the actual percent of aerosol delivered to the lungs and characterize the local deposition properties.

The main objective of this study is to investigate the aerosol-drug transport in a patient subjected to HFOV management. CFD based methods is used to estimate global and local deposition characteristics of various aerosol particles in a realistic large-scale lung model. Primary flow mechanisms that govern gas transport and mixing during HFOV can be classified as : (a) bulk convection; (b) gas exchange between respiratory units or pendelluft, where the gas exchange between adjacent units at the end/beginning of the respiratory phases due to the regional asymmetric resistance and compliance; (c) coaxial counter flow; (d) longitudinal mixing; and (e) gas exchange by molecular diffusion [32, 166]. Physiologically relevant boundary conditions that are capable of capturing those crucial flow mechanisms are required for accurate computational modeling of HFOV. Traditionally, flow rate, or velocity at each outlet is specified (Type-I boundary condition). Alternately, several studies use uniform pressure (Type-II

boundary condition), while others use the mass fraction (MF) at each outlet of the statistical lung models (Type-III boundary condition). These boundary conditions entail several limitations; for example, utilizing them forces the solver to adjust the pressure inside the domain to attain the specified velocity, pressure or flow, which ignores the non-uniformities in lung ventilation [46]. It is also deemed essential to model pendelluft between adjacent units during HFOV and traditional boundary conditions discussed above cannot capture this mechanism due to inability of modeling the asymmetry in airways resistance and compliance between adjacent units. A recent study by Makris *et al* [183] that investigated particle transport and deposition under HFOV and normal breathing conditions at 16 Hz and 0.25 Hz frequencies concluded that HFOV resulted in higher particle deposition than normal breathing due to stronger secondary and counter flows. However, the deposition was only characterized inside a single bifurcation representing generations G3 to G4 using one of the aforementioned traditional boundary conditions that are unable to recreate the pendelluft mechanism. In chapter 5, it has been demonstrated that the use of a coupled airways resistance-compliance (R&C) boundary condition that successfully captured important gas mechanisms in HFOV, especially pendelluft flow [184]. These physiologically relevant time-dependent pressure boundary conditions based on a coupled resistance-compliance of the airways were used along with a large eddy simulation (LES) coupled to a Lagrangian particle transport model to investigate a gas-solid two-phase flow under HFOV

6.2. Method

6.2.1. Continuous Phase Model

Figure 6.1 displays the model, which was identified by the major lung lobes as: main bronchi left upper lobe left lower lobe, right upper lobe, and right middle and lower lobes. The continuous phase (airflow) was modeled using LES with the numerical techniques described in the previous chapters.

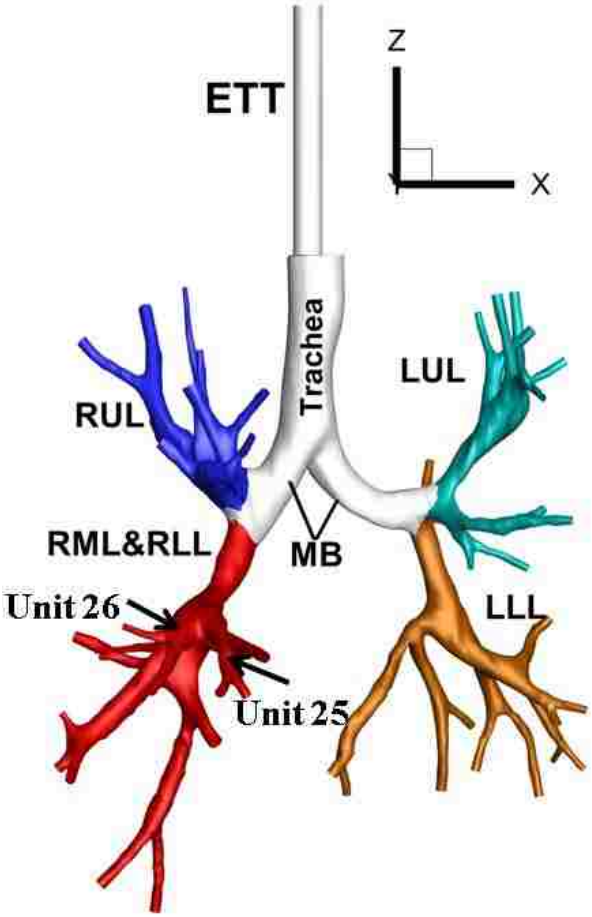

Figure 6.1 tracheobronchial tree model with an endotracheal tube (ETT) inserted into the trachea. MB: main bronchi, LUL: left upper lobe, LLL: left lower lobe, RUL: right upper lobe and RML&RLL: right middle and right lower lobes.

6.2.2. Particle Transport Modeling

The Lagrangian tracking approach was implemented to model the particle transport during HFOV simulation. The Newton's second law of motion is used in Lagrangian method to track each individual particle. The force balance leads to the first order differential equation for the particle momentum as follows [185]:

$$m_p \frac{du_p}{dt} = \sum F_P \tag{6.1}$$

where m_p is the mass of the particle, which is calculated as the particle density (ρ_p) times the particle volume density (V_p), u_p is the particle velocity, and $\sum F_P$ is the summation of the forces acting on the particle. There are many forces affect that particle motion and trajectory in a fluid, such as drag, gravitational, lift, diffusion, virtual mass, pressure gradient, and basset force. However, the inclusion of any force depends on the flow conditions, computational model features, and particle properties. Monodispersed spherical solid particles with diameters (d_p) ranging from 0.5 to 5 μm and density (ρ_p) of 1000 kg/m^3 were considered [186], which led to very high particle to fluid density ratio $\rho_p / \rho >> 1$. Therefore, all the forces that depend on the ρ_p / ρ, such as virtual mass, pressure, and basset forces, were neglected. Furthermore, the effect of gravity were not considered. Since the study was conducted for a patient under invasive mechanical ventilation, the orientation of the patient was assumed in lying position (horizontal position) during drug delivery. Mark Brouns [187] studied the particle deposition in an extrathoracic model including trachea with different orientation positions. He concluded that due to dominant drag force, the gravity force has no effect in case of the horizontal

position of the model. Furthermore, in current study, the particles transport under very rapid ventilation, which does not allow enough time for the particle to settle down [188]. The ignorance of the gravity force has also been assumed in many past studies [189-194]. The important forces that considered in present study include the drag force, the Saffman lift force, and the Brownian motion force [125]. User-defined FORTRAN was used to implement these forces in ANSYS® CFX®. The final particle momentum equation was considered as follows [125]:

$$m_p \frac{du_p}{dt} = \rho \pi C_D d_p^2 \left| u - u_p \right| (u_i - u_{p_i}) / 8 C_c + f_{lift} + f_{Brownian} \tag{6.2}$$

u is the fluid velocity. The first term on the right side of the equation represents the drag force. C_D is the drag coefficient and is defined based on the expression of Morsi and Alexander [195]:

$$\begin{array}{ll}
CD = 24/\mathrm{Re} & \mathrm{Re} < 0.1 \\
CD = 22.73/\mathrm{Re} + 0.0903/\mathrm{Re}^2 + 3.69 & 0.1 < \mathrm{Re} < 1 \\
CD = 29.1662/\mathrm{Re} - 3.8889/\mathrm{Re}^2 + 1.222 & 1 < \mathrm{Re} < 10 \\
CD = 46.5/\mathrm{Re} - 116.67/\mathrm{Re}^2 + 0.6267 & 10 < \mathrm{Re} < 100 \\
CD = 98.33/\mathrm{Re} - 2778/\mathrm{Re}^2 + 0.3644 & 100 < \mathrm{Re} < 1000 \\
CD = 148.62/\mathrm{Re} - 4.57 \times 10^4/\mathrm{Re}^2 + 0.357 & 1000 < \mathrm{Re} < 5000 \\
CD = -490.546/\mathrm{Re} + 57.87 \times 10^4/\mathrm{Re}^2 + 0.46 & 5000 < \mathrm{Re} < 10000 \\
CD = -1662.5/\mathrm{Re} + 5.4167 \times 10^6/\mathrm{Re}^2 + 0.5191 & 10000 < \mathrm{Re}
\end{array} \tag{6.3}$$

Cunningham correction factor C_c is used based on Crowe [196] to account for Non-continuum slip effects on the drag of nanoparticles. It is defined as:

$$C_c = 1 + \frac{\lambda}{d_p}\left(2.34 + 1.05e^{-0.39\frac{d_p}{\lambda}}\right) \tag{6.4}$$

where λ is the mean free path and was taken to be 65 nm. The Cunningham correction factor increases as the particle diameter decreases. The C_c behavior for the considered particle size range in the current study can be seen in Figure 6.2.

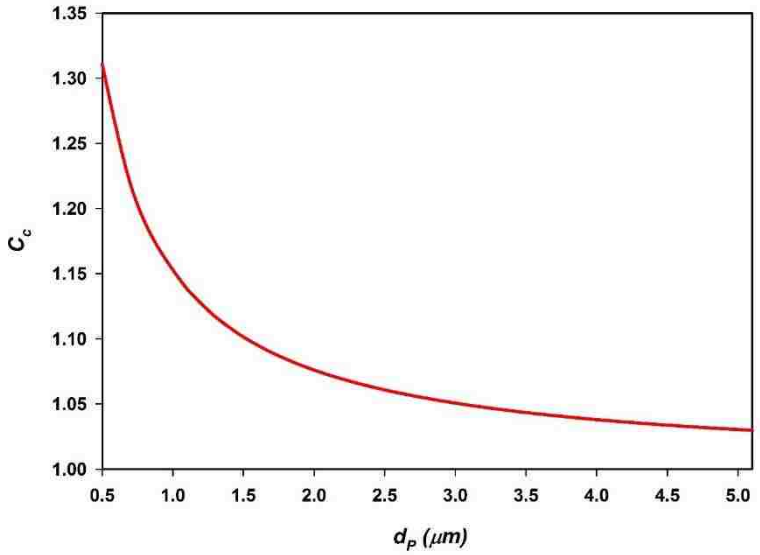

Figure 6.2 Cunningham correction factor for the particle size ranging from 0.5 to 5 μm.

The shear-induced Saffman lift force f_{lift} is expected to play a large role in the micrometer particles with significant inertia in areas with rapidly changing geometry or significant turbulence [39]. It is perpendicular to the direction of the flow due to velocity shear. It is defined as [197]:

$$f_{lift_i} = \frac{-\rho d_p^2 \hat{n}_i}{4m_p}\left[u_s^2 . g(\kappa, \Lambda)\right] \tag{6.5}$$

where $\hat{n}$ is the unit wall normal vector pointing out of the domain. u_s is the wall-tangent slip velocity is defined by [197]:

$$u_s = v \cdot \hat{t} - u \cdot \hat{n} \tag{6.6}$$

where $\hat{t}$ is the unit wall-tangent vector in the direction of the particle velocity described as:

$$\hat{t} = \frac{(\hat{n} \times v) \times \hat{n}}{|(\hat{n} \times v) \times \hat{n}|} \tag{6.7}$$

The function g is used from Cherukat and McLaughlin as [198]:

$$\begin{aligned} g(\kappa, \Lambda) = & \left[1.7631 + 0.3561\kappa - 1.1837\kappa^2 + 0.845163\kappa^3\right] \\ & - \left[\frac{3.24139}{\kappa} + 2.6760 - 0.8248\kappa - 0.4616\kappa^2\right]\Lambda \\ & + \left[1.8081 + 0.8796\kappa - 1.9009\kappa^2 + 0.98149\kappa^3\right]\Lambda^2 \end{aligned} \tag{6.8}$$

The parameters κ and Λ are defined as [198]:

$$\kappa = \frac{2h_p}{d_p} \tag{6.9}$$

where h_p is the distance from the wall to the particle, and

$$\Lambda = \frac{\dot{\gamma} d_p}{2u_s} \tag{6.10}$$

where $\dot{\gamma}$ is the shear rate and is approximated for particles near the wall by [198]:

$$\dot{\gamma} \approx \frac{u \cdot \hat{t}}{h_p} \tag{6.11}$$

$f_{Brownian}$ is the Brownian force [39]. The effects of this force are most noticeable on particles that have very low inertia, i.e. particles with a diameter less than 1μm. The submicron particle is subjected to the collision of the gas molecules, particularly in very small airways [39]. It is modeled using the approach by Li and Ahmadi [199]:

$$f_{i\,Brownian} = \frac{\zeta_i}{m_p}\sqrt{\frac{1}{\tilde{D}}\frac{2k_B T_f^2}{\Delta t}} \tag{6.12}$$

where k_B is the Boltzman constant, T_f is the absolute temperature of the fluid, Δt is the particle integration time step, and ζ is a vector of 3 randomly generated numbers each taken from a Gaussian distribution with zero mean and unit variance. The Brownian diffusivity $\tilde{D}$ is defined as [199]:

$$\tilde{D} = \frac{k_B T_f C_c}{3\pi\mu d_p} \tag{6.13}$$

The obtained particle velocity (u_p) from Equation (6.2) is used to calculate the particle displacement as follows:

$$\frac{dx_p}{dt} = u_p\,, \tag{6.14}$$

where, x_p is the particle position. Forward Euler was used to solve Equation (6.14) as follows:

$$x_p^{n+1} = x_p^n + u_p^n \Delta t \tag{6.15}$$

Δt is the particle tracking time step size. The subscript n in Equation (6.15) indicates the particle tracking step number.

The one-way coupling of particle-fluid interaction was employed [39]. In this approach, the continuous phase (flow field) affects the dispersed phase (particles trajectories) but the particles do not influence the fluid. Furthermore, the particle –particle interaction was not considered. A user-defined FORTRAN subroutine was compiled with a CFX solver to track each individual particle at each time step. The particle was allowed

to deposit at the wall (when the distance between the wall and particle center was less than the particle radius [39]), exit the domain, or stay active inside the model. Another FORTRAN subroutine was also used so that the rate of particles injected scaled with the inlet mass flow rate such that gives the desired number of injected particles. The particles were injected uniformly over the ETT inlet cross-section area over the inspiration phase of the fourth HFOV cycle to avoid start-up effect [94, 200]. At the site of injection, the velocity of the particles was set to match the velocity of the fluid.

6.2.3. Breathing and Boundary Conditions

Inlet condition: A blunt velocity profile was imposed at the inlet of the ETT as [90, 95]:

$$u(r,t) = 1.224\, U(t)\left(1 - \frac{r}{R_{ETT}}\right)^{1/7} \tag{6.16}$$

$U(t) = u_{amp}\sin(2\pi ft)$ is the obtained velocity from the sinusoidal HFOV waveform;

$u_{amp} = fV_t / R_{ETT}^2$ is the amplitude velocity.

Outlet condition**:** The developed time-dependent pressure outlet boundary conditions in chapter 5 have proven effective way to capture the crucial gas transport by high frequency oscillatory ventilation allowing accurate modeling. It was therefore utilized to investigate the particle transport and deposition during HFOV.

Walls**:** No-slip wall BCs were used [34]. Table 6.1 presents HFOV conditions, flow and particle parameters under consideration.

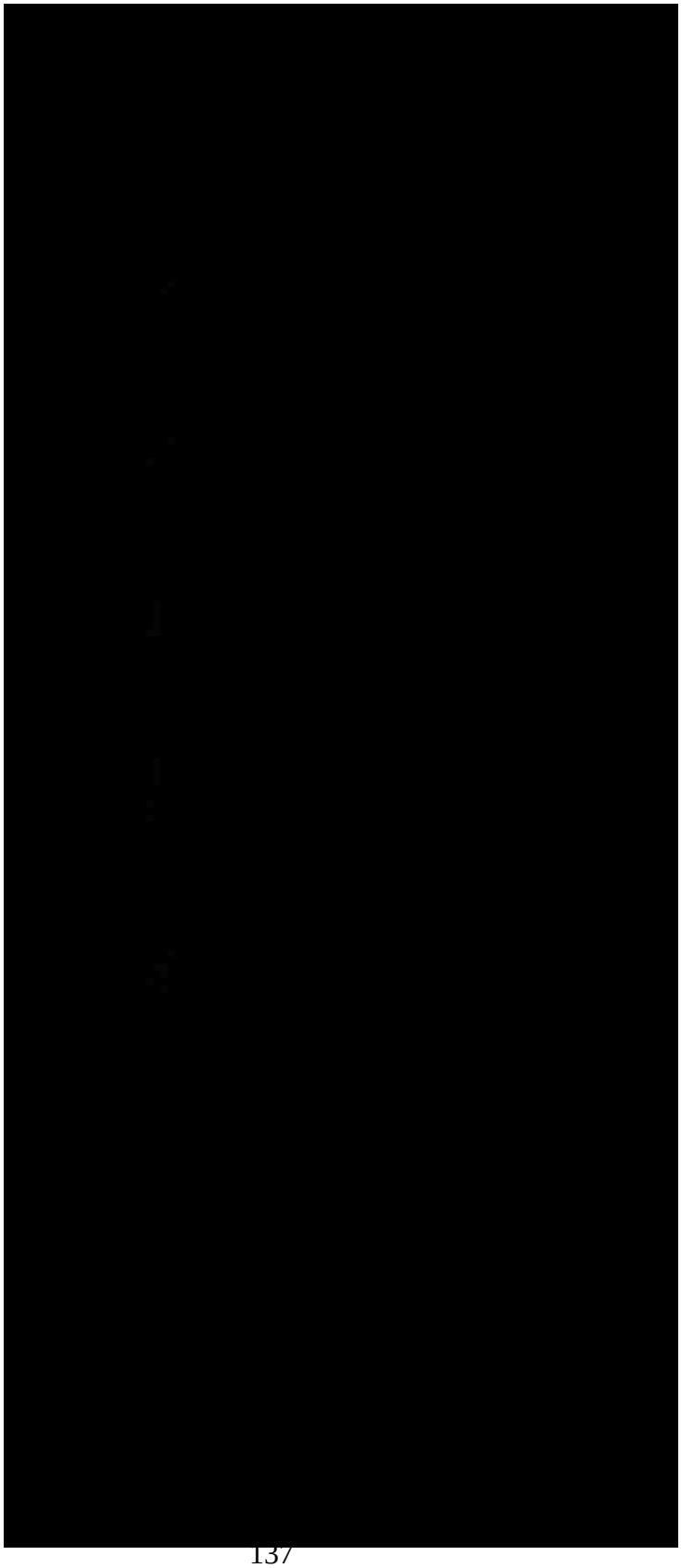

6.2.4. Validation

To examine the particle modeling technique, the present numerical code was validated against available experimental data of Kim and Garcia [201] and Kim and Iglesias [202]. These experiments are considered appropriate for the purpose of particle modeling validations [34] and have widely been used in the past studies [151, 194, 200]. A single bifurcation geometry was reconstructed to match the experimental model. Cyclic inlet flow with *Re*= 1500 and 4000 and particles with St_k number ranging from 0.01 to .25 were simulated and compared to experimental data from Kim and Garcia [201] for frequencies of 16 to 50 cycles/min, and the *in vitro* study of Kim and Iglesias [202] for constant flow. Figure 2a shows that the predicted deposition efficiency fits well with experimental data, which validates the present numerical code. To determine the global and local deposition fraction independence of the total number of injected particles, different groups of particles were examined. Group 1 that consist of a total of 4000 particles was first studied, the number of particles was then increased by a factor of two to 8000 and 16000 particles (groups 2 and 3 respectively). The global and local deposition fractions are defined as [203, 204]:

$$DF_G = \frac{Total\ particles\ deposited\ in\ whole\ domain}{Total\ particles\ at\ ETT\ inlet}$$
$$DF_L = \frac{Total\ particles\ deposited\ in\ region\ of\ interest}{Total\ particles\ at\ ETT\ inlet} \quad (13)$$

The difference in DF_G was found to be <1% between the three groups. Furthermore, the DF_L in the five major lung subdivisions was depicted in Fig. 2b during both inspiration

and expiration phases. It was found that the local deposition factor was converged for all groups of particles. Due to the low tidal volume, a total of 8000 particles was selected for the all simulations in this study to keep the volume fraction very low (i.e. dilute flow) such that a one-way coupling approach is valid [39]. The current validation is restricted to low *Re* <4000 due to unavailability of experimental data at large values of *Re* used in the work. We believe that the high values of *Re* (due to high HFOV frequency) will increase the impaction role, which is represented by the drag terms in eq. 6; the other terms are not sensitive to change in *Re*.

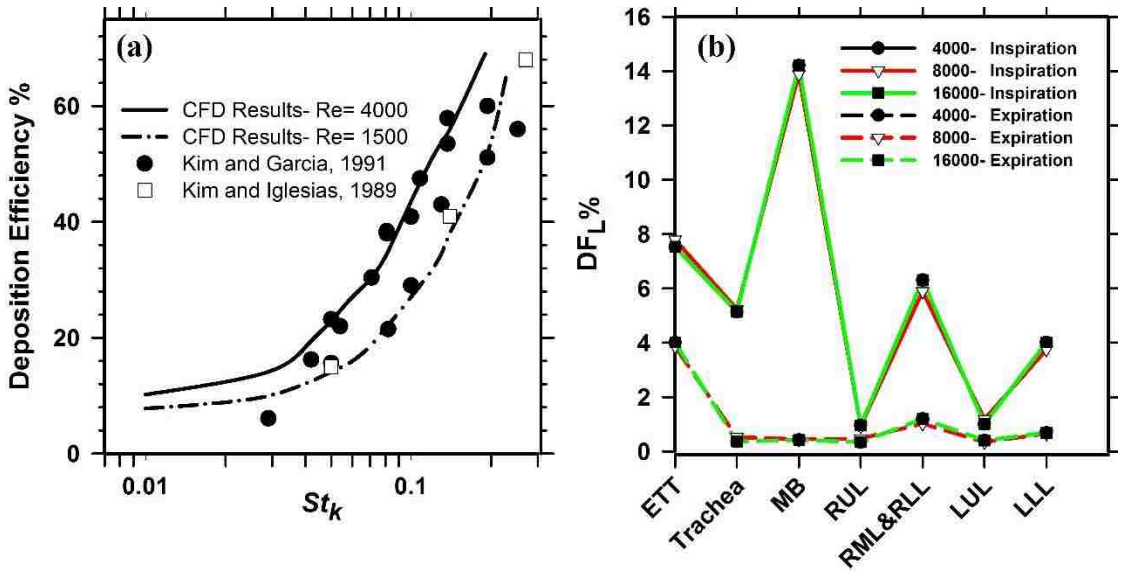

Figure 6.3 (a) comparison of the particle deposition efficiency between numerical results and different experimental data of Kim and Garcia [201] and Kim and Iglesias [202]. (b) Local deposition fraction for different particles count.

6.3. Results and Discussion

The airflow characteristics based on the non-dimensional numbers, Reynolds number and Womersley number are presented in Table 1. Reynolds number based on the ETT diameter ranged from 9458 to 23644. Reynolds number ranged from 26914 to 64791 based on the trachea diameter. The higher values of *Re* in the trachea was due to the high-speed ETT-jet that was released in the trachea environment. Likewise, Womersley number ranged from 6.17 to 9.75 and 11.5 to 18.18 based on the ETT diameter and the trachea average diameter, respectively. The spatial and temporal particle deposition inside the 7-generations tracheobronchial tree model was quantitatively and qualitatively analyzed in terms of global deposition DF_G, local deposition, DF_L and deposition patterns under various HFOV parameters and lung conditions.

6.3.1. Global Deposition

Detailed quantifications of the particle deposition, i.e. global deposition during inspiration phase, expiration phase, total deposition during the whole cycle period, and global deposition in the left lung and right lung for the cases of *CR*=1 and 10 at HFOV operating frequency of 10 Hz are presented in Table 6.2. The deposition of the transported particles throughout the domain occurs during the inspiration phase as well as the expiration phase. However, the global deposition fraction during inspiration phase was 5 times greater than during the expiration phase when *CR*=1. Similar observation was reported by Zhang *et al* [200] for the particle deposition in a triple bifurcation model. This is due to domination of the inertial impaction mechanism, which is also strongly enhanced by the presence and impingement of the high speed ETT-jet during the inspiration phase. A ten-fold increase of *CR* enhanced and doubled the deposition during

expiration phase due to the enhancement of the pendelluft [184], which enhanced gas mixing and particle dispersion. Consequently, the global deposition during the whole cycle increased from 45.94% when *CR*=1 to 54.2% when *CR*=10. The right lung was found to have relatively more deposited particles compared to the left lung, which was due to asymmetric airflow distribution. The majority of the airflow is always directed to the right lung due to the orientation of the right bronchus and its large diameter. Furthermore, increasing *CR* to 10 decreased the left lung compliance, which allowed the more compliant lung (i.e. right) to receive additional airflow [184] that resulted in right to left lung deposition ratios of 1.29 and 1.34 for cases of *CR*=1 and 10, respectively.

Table 6.2 Details of global particle deposition during different HFOV and lung conditions.

Case	DF_G%				
	In	Ex	Left Lung	Right Lung	Total[a]
10 Hz - CR=1	38.65	7.30	12.18	15.71	45.94
10 Hz - CR=10	38.94	15.26	15.03	20.13	54.20
MF	36.38	10.85	16.39	14.90	47.23

In: inspiration phase.
Ex: expiration phase.
[a]The total deposition = deposition during In + deposition during Ex.

Fig. 6.4 plots the particle deposition as a function of Stokes number during inspiratory and expiratory phase. The Stokes number is defined as $St = \rho_p d_p^2 u / 18\mu L$, where u is the velocity and L is a characteristic length, which is assumed to be the diameter of the ETT diameter. In the present study, *St* number ranged from 0.002 to 0.51 for all cases, see Table 6.1. During inspiration phase (Fig. 6.4a), the deposition increases

with an increase in the Stokes number up to a value of 0.1. For Stokes number values greater than 0.1, the deposition fraction undergoes a steep rise upon increase in the particle diameter due to the strong effect of the impaction mechanism and ETT-jet on the particles. The deposition fraction for the case of *CR*=1 was relatively higher than the case of asymmetric lung compliance (*CR*=10). This behavior reversed itself during expiration phase (Fig.6.4b). Additionally, the deposition rate decreased for the particles with $St > 0.1$ in the case of *CR*=1 during expiration phase and could be attributed to two factors; Firstly, the majority of the particles with a higher Stokes number were filtered during inspiration phase for the case of *CR*=1, noticeably for the $St > 0.1$(see Fig. 6.4a). Secondly, asymmetric lung compliance increases pendelluft flow intensity, which could enhance diffusion process of the particles. Consequently, more particles have the potential to deposit during the expiration phase for the case of *CR*=10.

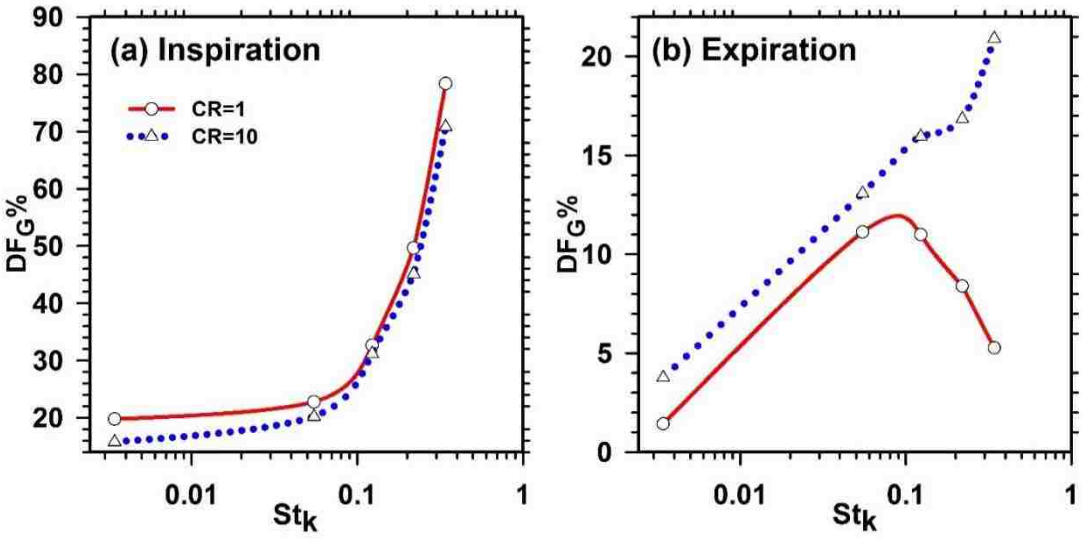

Figure 6.4 the particle deposition as a function of Stokes number St_k for HFOV operating frequency of 10 Hz and CR=1 and 10. (a) Deposition during the inspiration phase and (b) deposition during the expiration phase.

6.3.2. Temporal Deposition

The particle deposition factor DF_t was plotted as a function of the cycle time (t/T) (see Figure 6.5) for a HFOV frequency of 10 Hz with CR=1. Various particle size ranges were investigated. DF_t is defined as the total amount of particles deposited at time t relative to the total particles injected during the cycle. The particle deposition rate demonstrated strong dependency on the cycle time, and is considered to be of vital importance for the particle release strategy over the ventilation cycle. In general, DF_t demonstrated a similar pattern to the airflow, and the highest deposition occurred during peak inspiration. Li *et al* [192] observed similar particle deposition characteristics in an idealized lung model during cyclic inspiratory flow. In the present case, a predominant impaction mechanism coupled with the ETT-jet impingent resulted in higher the deposition rate for the larger particles. However, when the ventilation phase turned to expiration, different events were observed. Although the deposition shared similar patterns between the two phases, the deposition rate increased inversely with the diameter size during expiration. This is because high population of smaller particles stayed active until the cycle changed to expiration phase while majority of the larger diameter particles were filtered during inspiration phase. In addition, the effect of impaction that mostly influences the large particles was mitigated due to absence of the ETT-jet during expiration phase. This occurred while the small particles were still heavily influenced by the turbulence dispersion, secondary motion, and pendelluft flow, all of which enhanced the particle dispersion.

Particles with d_p < 1 μm had remarkably different deposition pattern (see Fig. 6.5a), the deposition rate increased at the end of the inspiration phase which may be

attributed to the presence of the pendelluft and coaxial counter flow in addition to strong secondary flow during this period. These flow features in turn enhances mixing and diffusion of the submicron particles. For further illustration, the Pathlines travelled by randomly selected particles with different diameters throughout the lung as a function of total time (i.e. the time it takes the particle to move from the released point to the current location) is shown in figure 6.5b. The data reported is based on the trachea, main bronchi, and the right lower lobe (see inset in Fig. 6.5b). For visualization purposes, the particle size was magnified 500 times. The larger particles do not follow the flow streamlines due to inertia and tends to stay in a straight path; taking a very short time to reach the main bronchi. Consequently, these large particles had a higher probability to deposit in the upper generations resulting in a high deposition rate during the inspiration phase. In contrast, the smaller particles tends to follow the flow streamlines and are influenced by the secondary motion and turbulent eddies. As a result, the trapped particles in a complex flow structure stayed active for longer time, causing part of the particles to deposit at the airways walls due to enhancement of the diffusion and random motion (marked regions 1 and 2 in Fig. 6.5b). Meanwhile, the remaining particles remain active and continues to the next phase. Region 3 shows an interesting behavior of the complex particle motion, the particle at the end of the inspiration

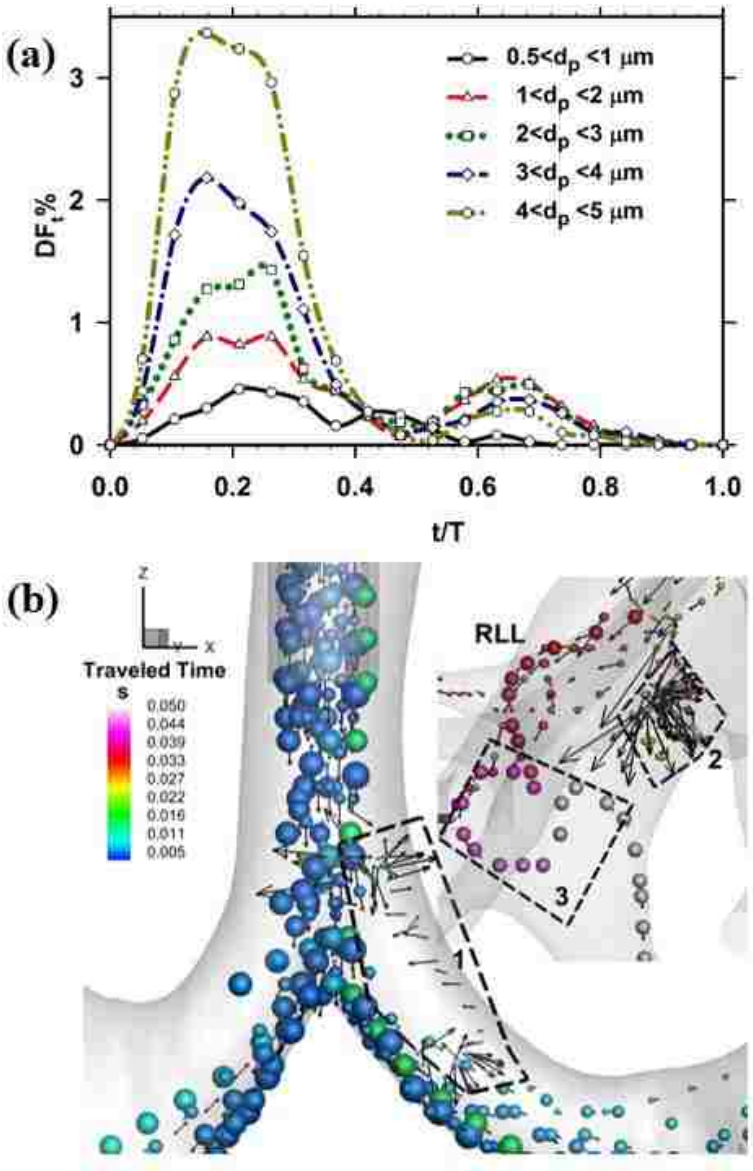

Figure 6.5 (a) particle deposition as a function of the cycle time for HFOV operating frequency of 10 Hz and CR= 10; the time was normalized by the total cycle time T=1/*f*. (b) The travel of selected particles throughout the domain during the inspiration phase, colored by the traveled time.

phase, instead of moving through right branch of RLL lobe, changes its path and penetrates the left branch. This is most likely due to the pendelluft flow between the right

branch and the left branch. The pendelluft intensity is strong enough to force upstream particles to change their paths.

Figure 6.6 presents snapshots of three-dimensional particle dynamic at different times from the beginning of the inspiratory flow of the fourth cycle. The labeled distance in Fig. 6.6 is the vertical distance (Z) from the ETT outlet to the location indicated by an arrow. The ETT tube releases the particles in the trachea, which rapidly impacts the first carina ridge due to the proximity of the ETT to this bifurcation site. At t/T=0.15 (where T=1/f is the total cycle time), the cloud of the particles bifurcated and penetrated into the main bronchi, with particles of higher momentum penetrating deeper into the right bronchus to the beginning of G2, where Z=4.7 cm. Upon completion of 25% of the cycle, the ETT-jet was developed and more particles were injected, resulting in deeper penetration inside all of the five major lobes (Z=12.2 cm). The dispersion of smaller particles was evident, due to their response to developments of the flow structures and reverse flow along the ETT-jet. At t/T=0.35, the particles reached and left throughout the majority of the domain outlets from all lung major lobes (see Fig. 6.6).

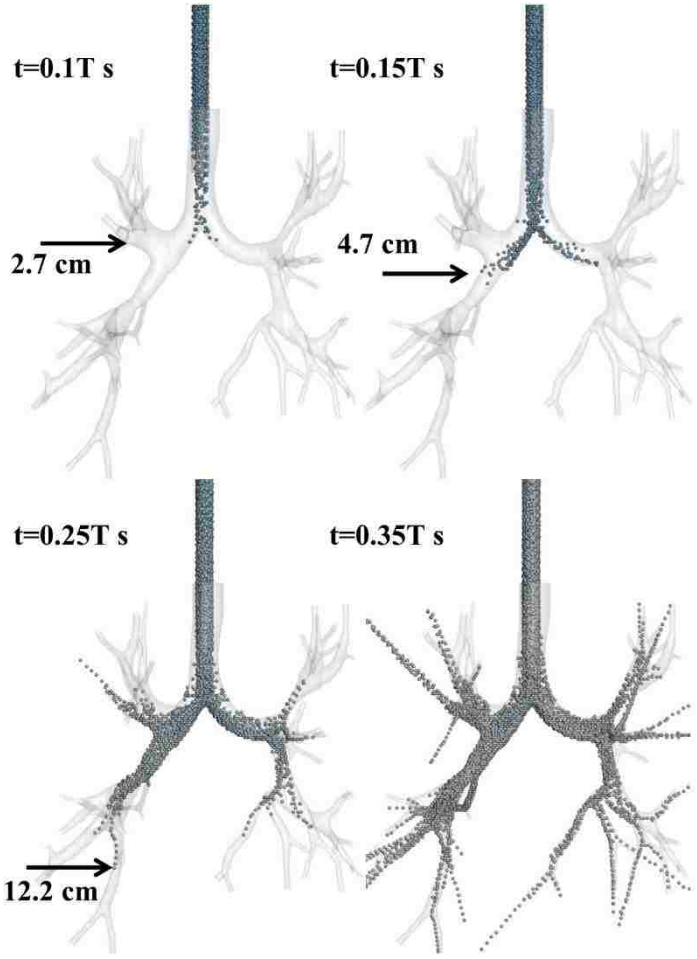

Figure 6.6 a snapshot of the particle dynamic at different times of the inspiration phase. The labeled distance is the vertical distance (Z) from the ETT outlet to the site indicated by the arrow.

6.3.3. Local Deposition

The local particle deposition assessment is a crucial measure of aerosolized drugs for therapeutic purposes. It could be of great importance for targeted delivery as well as an indication of localized deposition concentrations, which is deemed vital for assessment of administering a bolus dosage of the drug aerosols. The local deposition fraction in ETT, trachea, main bronchi, and in the five major lung lobes (i.e. LUL, LLL, RUL, and RML and RLL) is presented in Figure 7.7. For deeper insight, local deposition was

quantified and plotted for both inspiratory/expiratory flow and total deposition during the whole cycle for different ranges of particle sizes. The results are presented for the operating 10 Hz HFOV frequency for cases of both symmetric and asymmetric lung compliance (*CR*=1 and *CR*=10). During inspiration phase, the particles with $d_p < 3\ \mu m$ demonstrated largest local deposition DF_L in the ETT. In addition, more particles penetrated deeper in the lower lobes of the lung, which led to a high-localized deposition in the RML, RLL and LLL lobes while the upper lobes (i.e., RUL and LLL) received the lowest amount of the aerosol-drug, see Fig 7.7a. During expiration phase, the magnitude of the DF_L significantly decreased compared to the deposition rate during inspiration phase. Additionally, in different regions, i.e. MB, LUL and LLL (in the case of asymmetric lung compliance), DF_L was 8 times greater than symmetric lung compliance. This was due to the change in airflow distribution and increasing pendelluft intensity for the larger compliance ratio. For particles with $d_p > 3$ μm (Fig. 7.7b), the effects of the impaction and ETT-jet impingement were more pronounced and the peak localized deposition was shifted to the main bronchi. The deposition at the main bronchi was drastically amplified for asymmetric lung compliance (*CR*=10) during the expiration phase as result of the variations in the flow distribution and strong flow structure events at the main bronchi. The total local deposition trends (for each individual particle diameter range) followed the pattern of deposition rate during inspiration phase. This was because the deposition during the inspiration phase was much greater than during the expiration phase. For the range of particle size investigated in this work, the main bronchi received the greatest amount of the aerosol-drug compared to other sites. As an example, the local deposition fraction in the main bronchi was 3-fold and 16-fold greater than

deposition in the LLL and RUL lobes, respectively. This arose from the impingement of the high speed of the ETT-jet at main bronchi during the inspiration phase. The observation of the lowest deposition in the RUL and LUL lobes has been previously reported in different studies [39, 119].

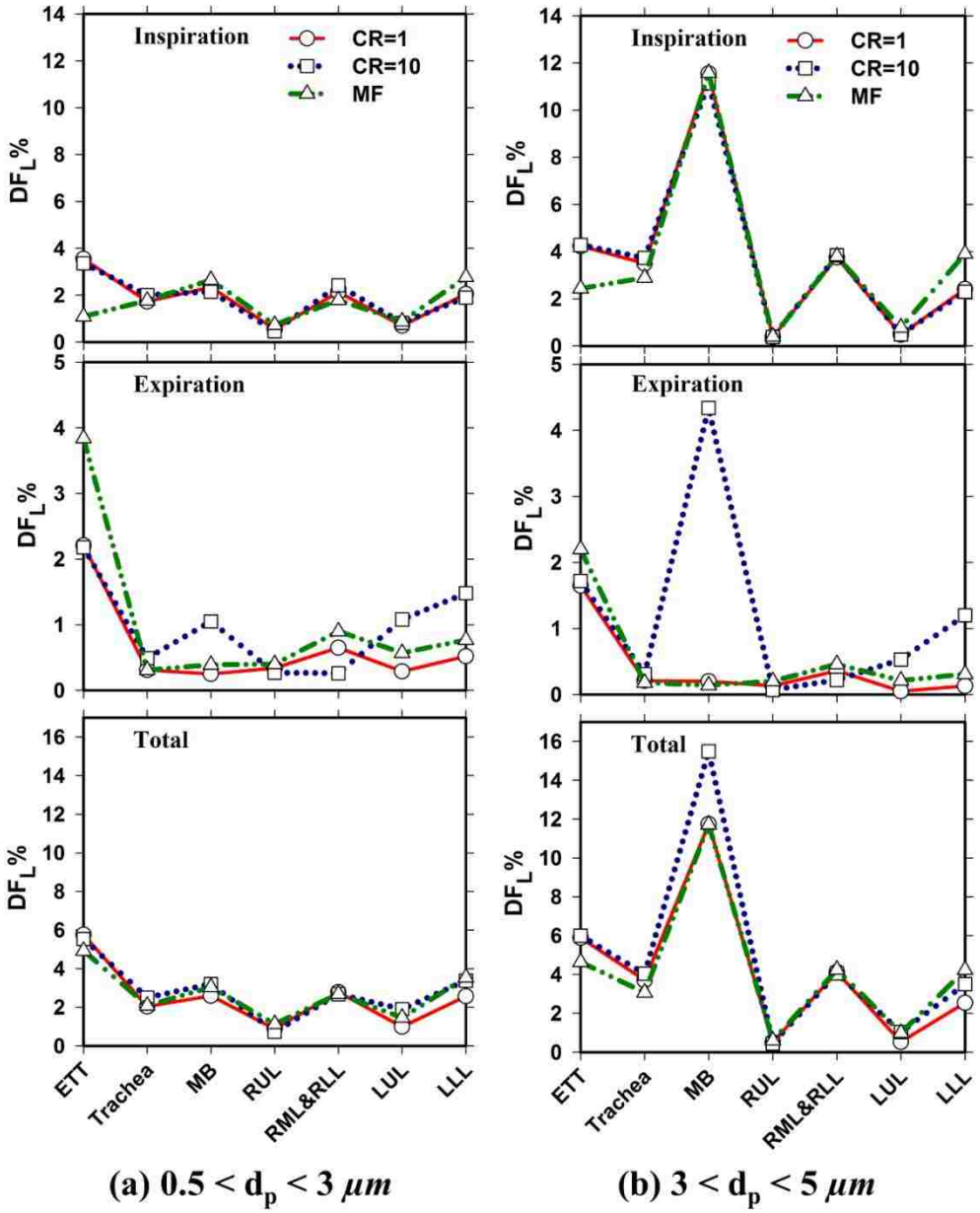

Figure 6.7 The local particle deposition of various particle size ranges in different lung lobes for HFOV frequency of 10 Hz and cases of CR=1 and 10.

Figure 7.8 shows the regional deposition pattern when the local compliance ratio between adjacent units was changed. The local compliance ratio CR_{Local} of selected units (i.e. unit25 and unit26, see Fig. 7.1 for the location of the selected units) was varied by multiplying the compliance of outlets in unit 25 by 10 while the compliance at the outlets of the neighbor unit 26 were kept fixed. This variation was made while the global *CR* in both left and right lungs was unchanged (*CR*=1). Changing the compliance ratio locally allows the more compliant unit (i.e. unit 25) to receive more airflow and increases the pendelluft intensity. Consequently, more particles were convected through unit 25 (the more compliant unit) and the dispersion, as well as secondary motion, were enhanced, which resulted in more particles being deposited in this region. Furthermore, the enactment of the deposition was observed in the less compliant unit (unit 26) as well, though to a lesser degree than unit 25. This can be seen by comparing the right branch of unit 26 in the case of *CR*=1 and CR_{Local}=10 in Fig. 7.8. While there were no particles observed at that branch when *CR*=1, a few particles were observed to penetrate and deposit in the right branch of unit 26, see Fig.7.8. This is attributed to the pendelluft effect. The pendelluft flow exchange between adjacent units was found to increase as the asymmetric compliance increased and as a result, the regional particle depositions were enhanced.

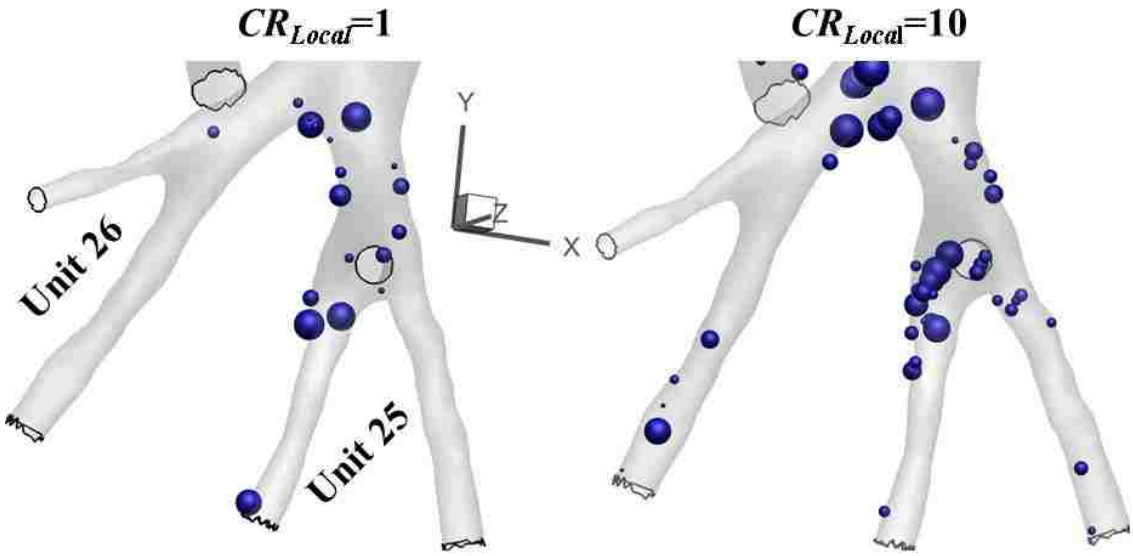

Figure 6.8 the regional deposition pattern under an asymmetric local compliance ratio between unit 25 and unit 26. For clarity, the particle sizes were magnified.

6.3.4. Effect of Boundary Conditions on the Particle Deposition

The specification of the outlet boundary condition at the truncated levels of the tracheobronchial tree is of paramount importance for accurate gas and particle transport modeling [205]. The global deposition factor was estimated based on MF (Type II) boundary conditions and compared to the simulation run using R&C boundary conditions. Results are listed in Table 6.2. Data are shown for HFOV frequency of 10 Hz, *CR*=1 &10 for R&C boundary conditions and compared to the case of MF. Minimal differences were observed in the global deposition as both cases share the same flow rate, Reynolds number and Womersley number, spanning the same range of *St* number. As a result, the effects of the ETT-jet and impaction mechanism are similar and predominant, regardless of the boundary condition type. The local deposition, however, was drastically changed between the two cases. The trends and quantities of the local deposition fraction significantly changed in different lung regions based on the sensitivity of the boundary

condition to the local compliance (see Fig 6.7a-e). For example, Type II boundary conditions resulted in the local deposition fraction being 35-fold greater than the case of *CR*=10 at RML and RLL lobes during the expiration phase for d_p<3 μm. Similarly, during expiratory flow, the local deposition fraction at the main bronchi was 40-fold greater when using R&C boundary condition for d_p>3 μm, see Figs. 6.7c-e. This is attributed to the variation in the airflow distributions between lung lobes and the presence of pendelluft flow when considering airways resistance and compliance, which could significantly change the particle activity and dynamics. For further illustration, the variation in the deposition pattern in different lung regions between the cases of using different boundary conditions is presented in Figure 6.9. The influences of the airflow redistribution and pendelluft gas exchange on the deposition patterns are evident. When using MF based boundary conditions, the particles deposition were more localized at the carina ridge and branches. However when using the R&C boundary conditions, besides the dense deposition surrounding the carina ridge, a greater particle deposition was observed in the regions surrounding the airways segment walls (compare Fig. 6.9a and b).

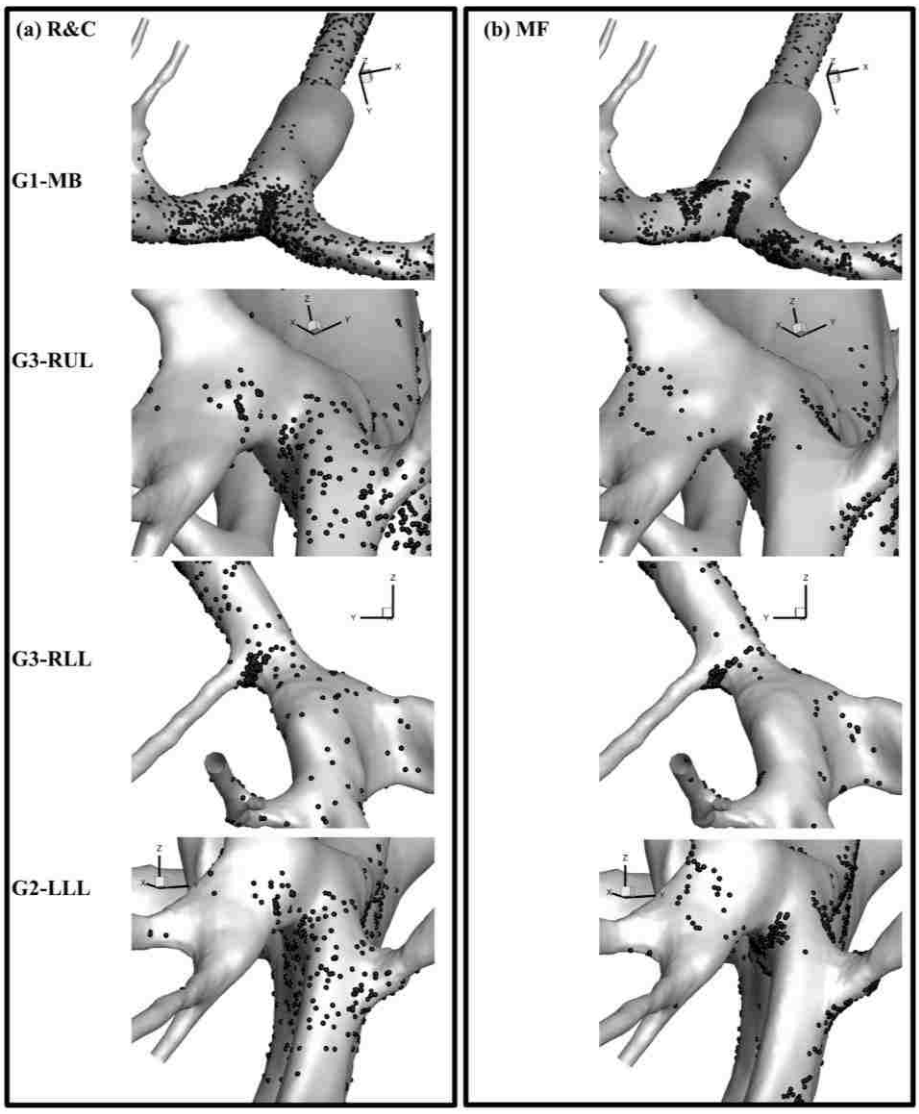

Figure 6.9 the deposition pattern in different lung regions. (a) When using R&C boundary conditions and (b) when using MF boundary condition.

6.3.5. Drug Delivery under Various HFOV Operating Frequency

To examine the influence of different HFOV settings on the particle deposition, the particle transport under various HFOV frequencies was modeled. The results were analyzed and quantified in terms of global deposition, local deposition in the different major lung lobes, and deposition pattern.

6.3.5.1. Global Deposition

Figure 6.10 compares the global deposition fraction for HFOV frequency of 6, 10 and 15 Hz, for cases of symmetric (*CR*=1) and asymmetric (*CR*=10) lung compliance. It was found that the particle deposition increased almost linearly as the operating frequency increased. Changing the frequency from 6 Hz to 10 Hz resulted in 57% increase in the global deposition fraction (relative difference). Further increase of the frequency to 15 Hz enhanced the deposition fraction by 109%. Three mechanisms are seen to strongly affect the deposition process as the frequency increased. First, the flow rate increases as the frequency increases, which enhances the role of impaction, turbulence dispersion, and secondary motion [34, 206]. Secondly, the pendelluft flow intensity is found to increase significantly with the HFOV frequency [169, 184] which results in enhancement of the diffusion process and the random motion of the particle in the flow which in turn enhances the particle deposition. Thirdly, the boundary layer thickness (δ) in an oscillatory flow is inversely proportional to the dimensionless Womersley number, i.e. $\delta = L/\alpha$, where L is a characteristic length [207]. Thus, elevating oscillating frequency reduces the boundary layer thickness, which enhances the convective diffusion and allows more particles to pass through toward the airways wall. The deposition rate trend in the case of *CR*=1 and 10 showed similar behaviors as the frequency changed; however, the deposition fraction was consistently higher when *CR*=10.

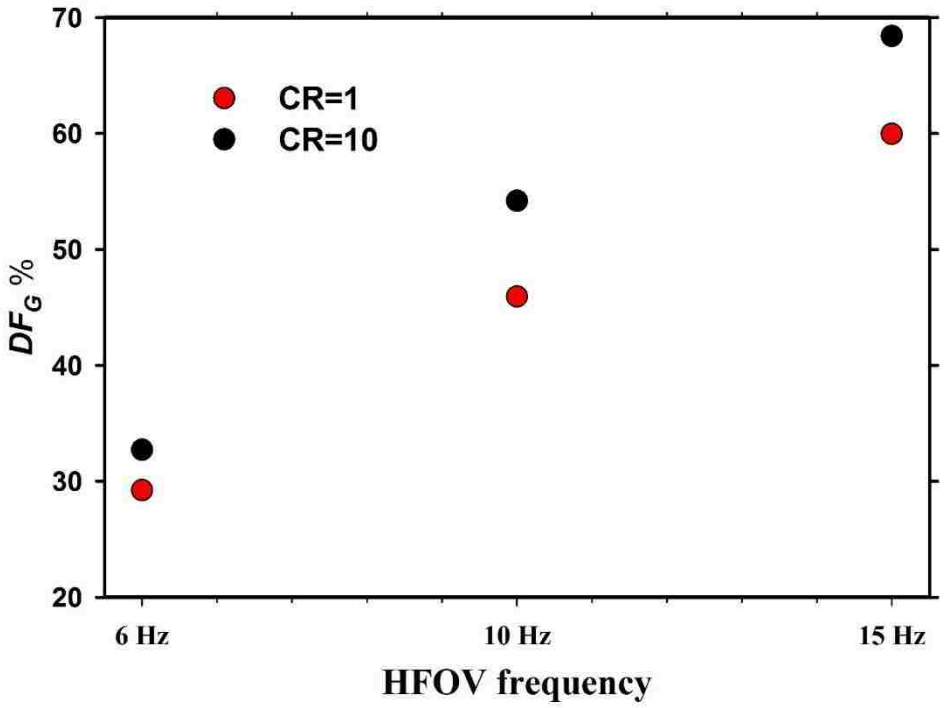

Figure 6.10 global deposition during different HFOV operating frequencies and CR=10.

6.3.5.2. Local Deposition

The local deposition fraction in different lung lobes was also quantified during inspiratory/expiratory flow for three different HFOV frequencies of 6, 10 and 15 Hz. The results are plotted in Fig. 6.11 for asymmetric compliance ratio (*CR*=10). During the inspiration phase, the local deposition rate trend was similar for all frequencies. The magnitude of DF_L, however, was significantly different depending on the lobe location. For example, at the main bronchi, the location that showed the greatest deposition, DF_L was 3.88-fold greater for a flow with frequency of 15 Hz as compared to the case of 6 Hz. However at lower generation, the effect of frequency variation was diminished, e.g. at RUL lobe, the deposition was lowest with no difference between all frequencies. During

the expiration phase, the deposition at all locations for the three frequencies was significantly lower than the inspiration phase. Furthermore, the frequency of 6 Hz had a consistently lower deposition rate compared to other cases, indicating more particles delivered to the deeper regions of the pulmonary tract. Interesting behaviors were observed during expiratory flow when using 10 and 15 Hz frequency. The local deposition rate peaked most significantly at RML and RLL and was 14-fold higher when using a HFOV frequency of

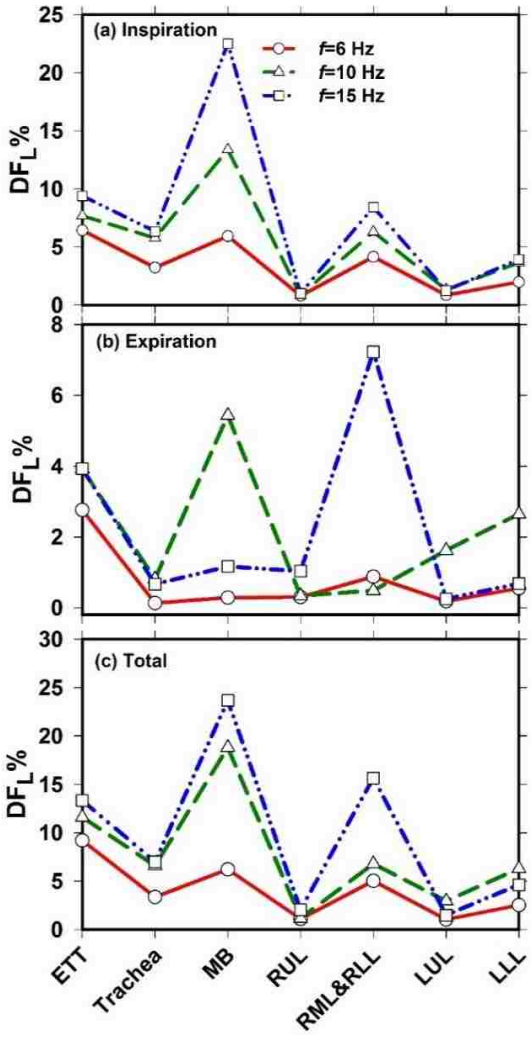

Figure 6.11 a comparison of the local deposition fraction for various HFOV operating frequencies.

15 Hz. The local deposition at the main bronchi was 5-fold higher when reducing the frequency from 15 Hz to 10 Hz. This is probably due to the airflow redistribution and flow feature changes as consequences of the frequency and *CR* changes, along with the effect caused by the irregular structures of the branch that feeds the RML and RLL regions Although these observation during the expiration phase contributed a nontrivial amount to the total local deposition, the total deposition behavior always followed the deposition rate during the inspiration phase, see Fig. 6.11.

6.3.5.3. Deposition Pattern

The visualization of the deposition pattern provides a profound insight into the role of the geometry and flow features on the particle deposition hot-spots. Figure 6.12 presents and compares the deposition pattern in the tracheobronchial tree for different HFOV frequencies. We illustrate the anterior lung side for clarity. Similar to the observation under normal breathing in many past studies [95, 96, 119, 191, 194], the enhancement of the particle deposition at the carinas was evident throughout the domain as a consequence of the flow diverging at the bifurcation sites, leaving particles to impact at the flow divider (carina). In addition, notable enhancement of the deposition occurred at the sites of sharp transition. A unique deposition characteristic was identified under invasive HFOV. Besides the normal hot-spots that have been previously identified, high particle deposition concentrated along the inner and side walls of the main bronchi tubular segments due to the effects associated with the presence of the ETT-jet. The ETT releases a high-speed jet at the lower region of the trachea that impinges at the first carina and creates a large recirculation zone extending from the outer walls of the main bronchi

to the jet sides. These flow structures reduce the area available for the flow to pass through, and, as a result, higher velocities are created at the inner walls of the bronchi [166]. Thus, the role of the inertial impaction is greatly enhanced at these locations resulting in a highly localized and concentrated deposition inside the main bronchi segments. The ETT jet effects resembled the effects of the laryngeal jet reported by [95] undertaken to quantify particle deposition inside the tracheobronchial tree. The influence of the ETT-jet on the deposition concentration at the main bronchi was more significant and maybe attributed to the strength

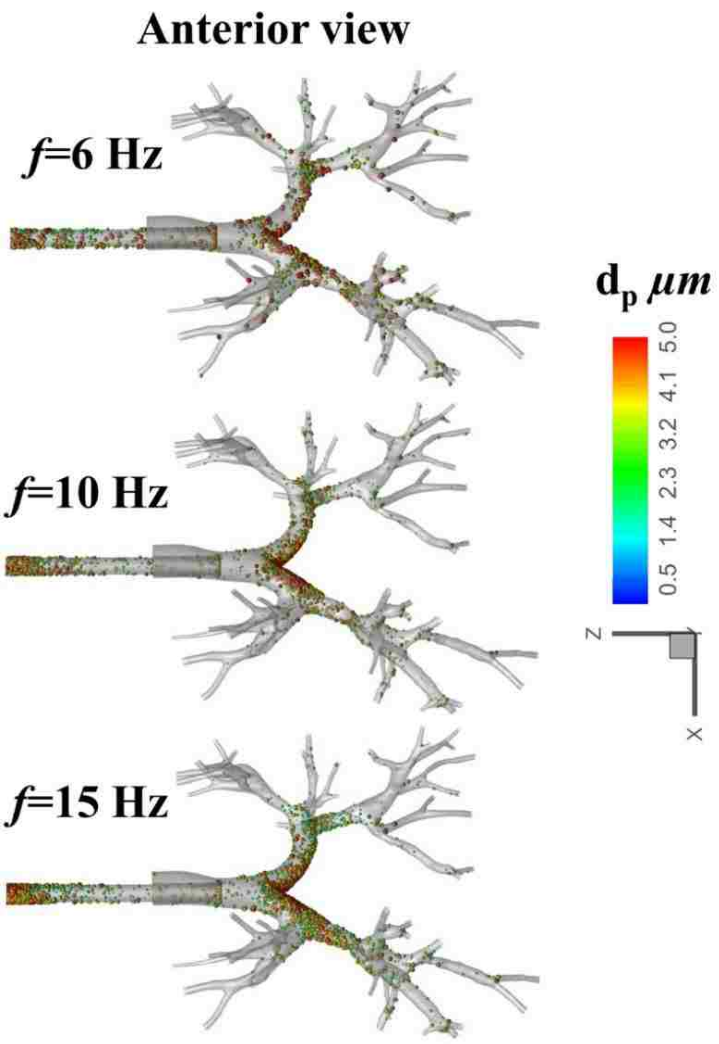

Figure 6.12 the pattern of aerosol-drug deposition under different HFOV conditions.

and proximity of the ETT-jet at the first bifurcation site. It is evident that the localized deposition concentration increased as the HFOV frequency increased due to the effect of the flow rate. Furthermore, the particles with larger diameter tended to deposit at the carinas, sharp transition locations and inner walls of the main bronchi, due to predominant impaction and jet impingement. The smaller particles had a tendency to deposit at the sidewalls, such as at the trachea, as a consequence of the turbulent

dispersion, secondary flow, and pendelluft mechanism. For further illustration, the deposition patterns of small particles, mainly $d_p < 1\mu$m and larger particle $d_p > 4\ \mu$m, are depicted in Figure 6.13. Clearly, the particles with $d_p > 4\ \mu$m concentrated at the carinas and the inner walls of the main bronchi due to the high inertial impaction effect, which was strongly enhanced by ETT-jet. The small particles $d_p < 1\mu$m, however, more uniformly deposited throughout the domain. This was because the smaller particle was principally influenced by the turbulence dispersion and secondary flow as it complied to the flow streamline. As a result, the diffusion of the particles was enhanced resulting in the deposition at the airway walls throughout the domain.

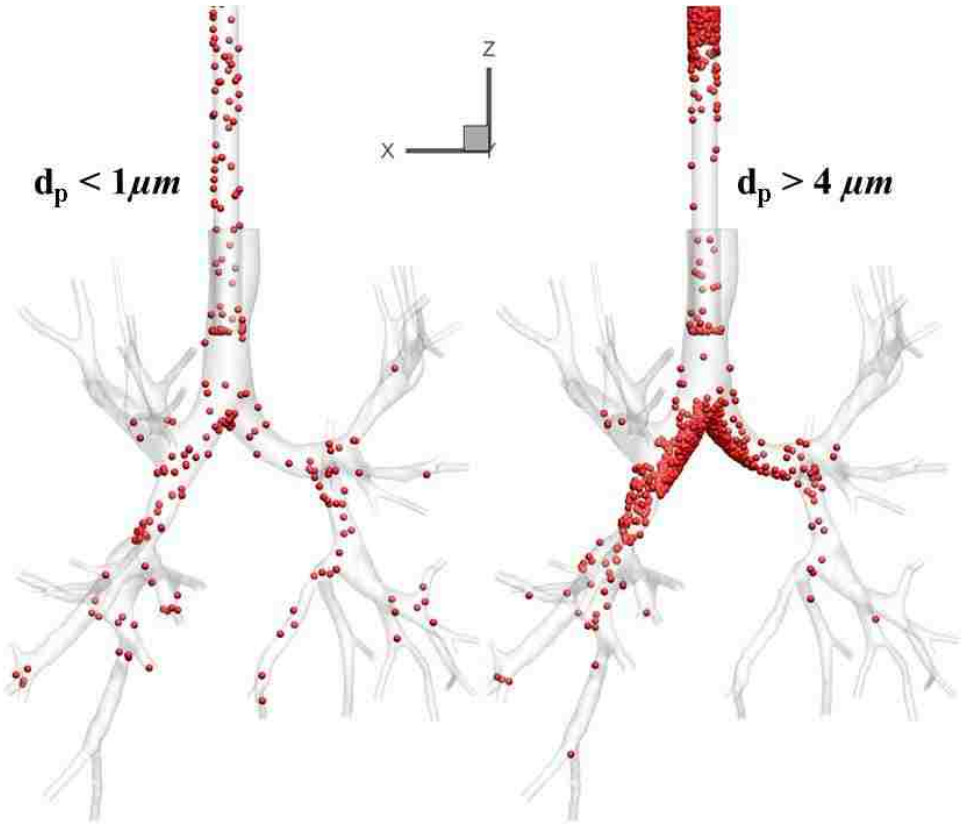

Figure 6.13 the deposition pattern of particles with a d_p < 1μm and > 4 μm.

6.3.6. Potential of Drug Delivery to a Patient under HFOV Management

The feasibility of drug delivery during HFOV has long been debated due to the numerous challenges that arise due to the high frequency associated with this mode [42, 208]. Fink *et al* [208] studied drug delivery to the lung using different aerosol nebulizers that were compatible with HFOV, including a novel nebulizer (Aeroneb Pro) and jet nebulizers [MistyNeb (Allegiance) and Vix One (Westmed)]. They concluded that the drug delivery during HFOV management is possible and the Aeroneb Pro delivered 2.9 times greater Albuterol to the end of ETT than the other two devices. Recently, Longest *et al* [209] demonstrated a 50% improvement in drug dosage delivery through the mechanical ventilator circuits by redesigning the circuit components using a streamlining approach. Our simulations suggest that the global aerosol-drug delivery (relative to the total particles injected at the ETT entrance) under HFOV parameters was equivalent to cases of normal breathing and CMV. Upon comparing the current particle deposition fractions to values reported in the literature for different flow rates and particle sizes (d_p =1 and 5 μm) using CFD [210] and experiments [211], the deposition fraction values under HFOV were found to be comparable to the particle deposition during normal breathing for the same range of flow rates, see Table 4 and Fig. 6.14. However, the reported value of the deposition in realistic 6-generation model by Inthavong *et al* [94] for the case of (Q=66 L/min) was relatively lower than the present prediction for the similar case (Q=54 L/min), see Table 4. This is because, unlike the geometry in Jin *et al* [210] and Zhang and Finlay [211] , the model in Inthavong *et a*l [94] lacks the effects of the extrathoracic geometry (mouth to larynx). This emphasizes the importance of the effect of the geometry features on the aerosol transport throughout the human lung. The

total particle deposition during HFOV, for different frequencies, ranged from 29% to 69%, which could be equivalent to the CMV. This is consistent with the *in vitro* findings [212] which compared the albuterol delivery under HFOV and CMV and concluded that albuterol deposition during HFOV was two-fold higher than CMV. These findings are supported by the other *in vivo* studies [50] of pulmonary aerosol delivery during HFOV in piglets. They concluded that the aerosol-drug delivery was effective and was at least as efficient as conventional mechanical ventilation.

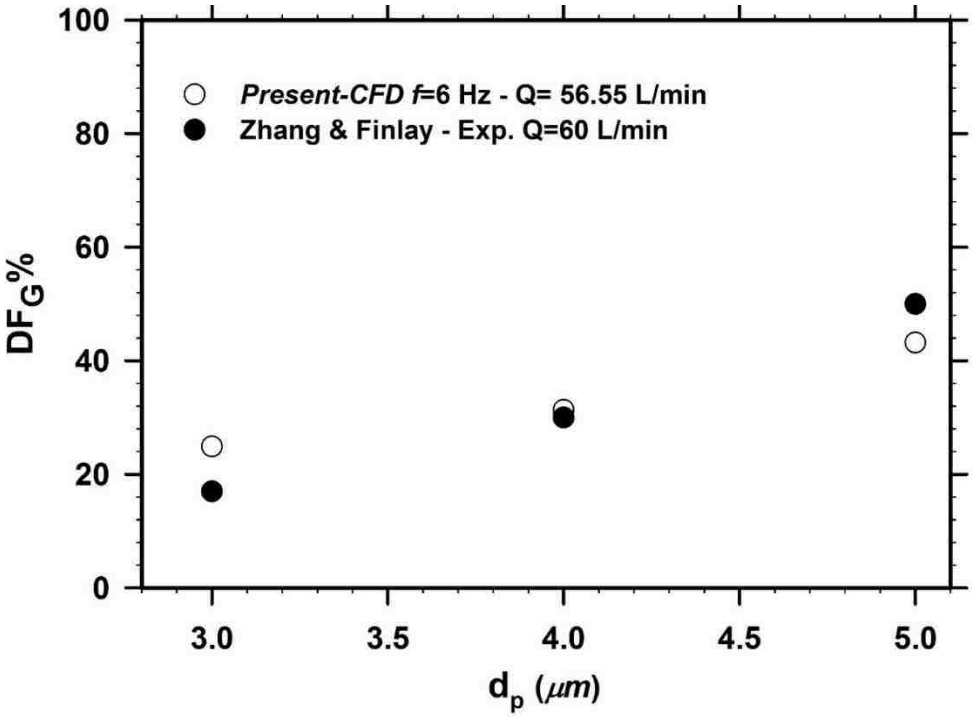

Figure 6.14 a comparison of the particle deposition fraction of the present study of HFOV with the experimental measurements for normal breathing by Zhang and Finlay [211] for a particle diameter range of 3 to 5 μm in a model extends from mouth to G3.

The local deposition under HFOV, however, were significantly different form the normal breathing. High deposition concentrations at the main bronchi and the subsequent generations (lobar-to-segmental bifurcations) resulted from the great inertial impaction and ETT-jet impingement. This observation along with strong deposition dependency on the operating frequency could be beneficial for the aerosol-drug drug delivery under HFOV management. The lobar and segmental airways are highly susceptible to lung cancer [95, 213]; a patient suffering from lung cancer could receive HFOV support and possibly benefit from the peak localized aerosol-drug deposition at the upper airways generations. In addition, the upper generations, including large airways (G0 to G5), are most vulnerable to many diseases e.g. asthma and chronic inflammation [214]. Medicines administered, such as bronchodilators and anti-inflammatory agents to treat such disease, would then require upper tracheobronchial targeting [95, 214], which could be achieved under HFOV management due to the high deposition concentration at those locations. More importantly, the dependency of the localized deposition on the ventilator frequency could be used to effectively control the regional deposition. For example, using a lower HFOV frequency (6 Hz) was found to reduce the local deposition of the aerosol at the main bronchi while the deposition in the lower lobes was comparable for all frequencies and high chance to deliver more particles to deeper region of the lung. Thus, when considering the risk of side effects at the sites of highly concentrated deposition, reducing the ventilator frequency could prevent drug overdose side effects while bringing a considerable portion to the lower lobes.

Table 6.3 Comparison of the present prediction of total particle deposition under HFOV conditions to the existing results in the literature for normal breathing.

Study	Geometry	d_p (μm)	Flow rate (L/min)	Total deposition%
Jin *et al* [210] CFD	Mouth – G3 idealized	1	60	10.4
		5		45
		1	90	17.6
		5		71
Zhang and Finlay [211] Experiment	Mouth – G3 idealized	5	90	71
Inthavong *et al* [94] CFD	Trachea –G6 realistic	5	66	30.1
Present CFD	ETT- G7 realistic	1	56.55	14.74
		5		42.78
		1	94.25	23.32
		5		90.96
		1	141.37	36.67
		5		97.20

6.4. Conclusion

The aerosol-drug delivery under high frequency oscillatory ventilation was carried out under various ventilator settings and lung conditions. Large eddy simulation was performed to model the continuous phase and the Lagrangian tracking method was implemented to model the dispersed phase. User-enhanced FORTRAN subroutines were compiled with the solver to implement the Lagrangian model. A physiological time-dependent pressure boundary condition was employed as a function of the coupled airways resistance-compliance and compared to the traditional boundary condition. The main observations can be summarized as the follows:

- The particle deposition during the inspiration phase was five-fold greater than expiration phase, and the asymmetric lung compliance was found to significantly affect the deposition, especially during expiration phase. Furthermore, the deposition fraction was strongly influenced by the release time of the particles' injection.
- The existence of the pendelluft flow and airflow redistribution due to resistance-compliance BCs application demonstrated a significant influence on the local deposition magnitude and pattern compared to the traditional mass fraction BCs.
- The ETT-jet was observed to have a major impact in enhancing the inertial impaction, resulting in highly localized deposition at the main bronchi and the few subsequent generations. The lower lung lobes significantly received more aerosol-drug compared to the upper lobes, which was consistent with existing results in the literature for normal breathing.
- The asymmetric compliance ratio between adjacent regional units was found to enhance the regional deposition as a consequence of the flow redistribution and effect of the pendelluft flow.
- A 2.5-fold increase of the operating frequency resulted in a 2.1-fold increase in the global deposition fraction in the upper tracheobronchial tree. Meanwhile, a 2.5-fold reduction in the frequency resulted in 3.88-fold reduction of the local deposition at the main bronchi allowing more particles to penetrate deeply in the lung and reduce the drug side effect risk associated with sites of high deposition concentrations. This indicates that the operating frequency has strongly influence the global and local particle deposition fractions and the deposition magnitude

could be controlled by changing the frequency, which could be beneficial for targeted drug delivery.

- Considering the particle deposition relative to the injected particle at the ETT inlet, aerosol drug delivery during HFOV could be equivalent to and as efficient as normal breathing and conventional mechanical ventilation, despite rapid ventilation cycles.

CHAPTER 7
EFFECT OF CARRIER GASES ON TRANSPORT AND AEROSOL DRUG DELIVERY BY INVASIVE HIGH FREQUENCY OSCILLATORY VENTILATION

7.1. Introduction

Various inert gases and gas mixtures can be used during the mechanical ventilation process to enhance gas exchange and mixing during mechanical ventilation management [27, 215]. Carrier gas properties like density and viscosity plays an important role and can be tuned to enhance aerosol deposition for patients under therapy management [216]. Changing carrier gas density will alter the fluid dynamics in the airways; the resistance of the airways will vary depending on the gas properties. In addition, the flow regimes (i.e., laminar, transitional, turbulence) will also be altered with a variation in properties. Using a carrier gas with lower density and higher kinematic viscosity (e.g., Heliox, which is a mixture of helium and oxygen) reduces the flow inertia and also increases the viscous force [217]. As a result, the Reynolds number (*ratio of inertial force to viscous force*) could be drastically reduced. This reduction is a mechanism that effectively diminishes or suppresses the turbulence and is dependent on the *Re* number. Particle transport throughout the pulmonary domain is directly influenced by various flow transport mechanisms [34]; the trajectory of the particles is therefore strongly affected by utilizing different gas mixtures, which in turn alters the deposition rate and sites.

Heliox has long been used for inhalation therapy [215] as the density of the gas mixture can be altered depending on the helium concentration. This feature is exploited to facilitate gas transport and to maximize aerosol-drug delivery in a diseased lung. Thus, density change could be used to offset increased flow resistance due to narrowing of the airways. The therapeutic outcomes are, however, still a subject of much debate in clinical practice. A comprehensive review of the outcomes of using different gas mixtures under

different ventilation modes and strategies can be found in [215, 218, 219]. Aerosol transport under different carrier gases has attracted the attention of many researchers [27, 120, 177, 220, 221] in their attempts to understand and optimize the inhalation therapy process. Sandeau *et al* [220] conducted a CFD study of aerosol transport with an extrathoracic (ET) model using Heliox as a carrier gas. A reduction of the respiratory effort and particle deposition in the ET model was observed indicating a positive outcome of the Heliox inhalation therapy. Similar conclusion was drawn by I. Katz *et al* [122] in their recent study of the regional particle deposition in the human lung model utilizing a helium-oxygen gas mixture. *In vitro* study of albuterol delivery using Heliox and air was carried out by Ari *et al* [221] through a pediatric high-flow nasal cannula. They concluded that using a lower density gas (Heliox) at a high flow rate (6 L/min) increased the delivered aerosol by >2-fold; however, the benefits of Heliox diminishes with decreasing inspiratory flow rate (3 L/min).

High frequency oscillatory ventilation has become a commonly used ventilation method in the intensive care unit. The gas transport mechanisms is more complicated than during CMV as a tidal volume less than the dead space volume is delivered at high operating frequencies. Thus additional mechanisms that include coaxial counter flow, pendelluft flow, Taylor-dispersion, and molecular diffusion [32, 166] become relevant for HFOV in addition to bulk convection which is present for both cases. Understanding the gas transport and mixing during this mode of ventilation is therefore essential for optimize ventilation management. A recent study by the authors derived and used physiological time-dependent pressure outlet boundary conditions based on coupled airways resistance-compliance at the truncated level of the tracheobronchial tree has

successfully captured the important gas transport mechanisms under HFOV parameters [184]. In particular, the pendelluft flow mechanism was captured in different lung regions, and the pendelluft intensity was successfully quantified. The robustness of the developed resistance-compliance boundary condition led to more accurate modeling of the particle transport under the HFOV management mode [222]. It was found that the particle deposition, relative to the injected particles at the endotracheal tube inlet, under the HFOV conditions, could be as efficient as normal breathing and conventional mechanical ventilations, despite the very rapid ventilation cycle. Furthermore, the deposition rate was highly frequency dependent. The usage of a Heliox gas mixture is seen to enhance the gas exchange during HFOV, and it is postulated that the enhancement occurs via different flow transport mechanisms, particularly pendelluft flow [223, 224]. It is, however, not fully understood how gas mixtures affect transport mechanisms and how the particles respond to changes of constituent gas properties during HFOV [223].

In the current study, various carrier gases and gas mixtures that include He, He-O_2 (Heliox), Xe-O_2 and SF_6-O_2 were utilized as the working fluid under HFOV; the main objective was to investigate the influence of the carrier gas on the flow transport and particle deposition, which may allow for optimum drug delivery and ventilation strategy. The study was conducted using a high-order turbulent model LES along with user-defined subroutines to implement a Lagrangian particle tracking model. To account for the complex airways morphology, the realistic tracheobronchial model was reconstructed using computed tomography scans. An 8 mm interior diameter ETT was inserted into the

trachea to account for the invasive device and a portion of the ventilator circuit. A comprehensive list of parameters is provided in Table 7.1.

7.2. Method

The gas and particle modeling methods, boundary conditions and validations have been discussed in previous chapters. Figure 7.1 presents the model, the lung divisions and considered units for the analysis.

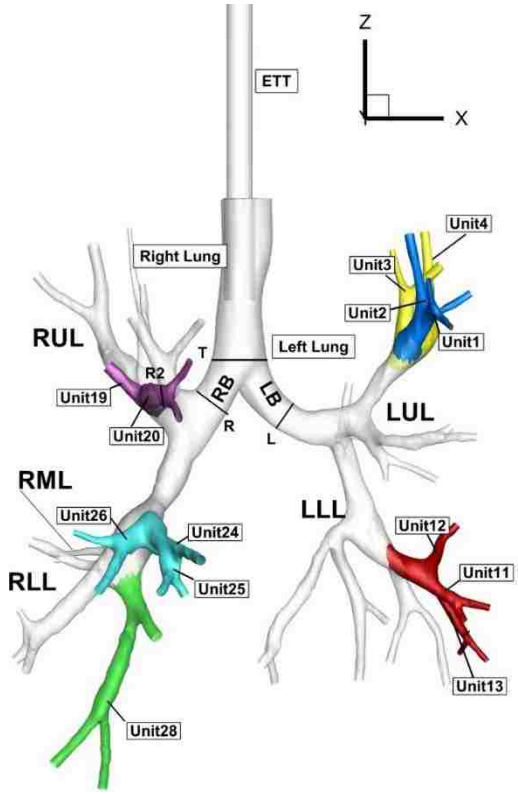

Figure 7.1 Tracheobronchial tree model with an endotracheal tube (ETT) inserted into the trachea. RB: right main bronchus, LB: left main bronchus, LUL: left upper lobe, LLL: left lower lobe, RUL: right upper lobe, and RML&RLL: right middle and right lower lobes.

Table 7.1 presents the carrier gases under consideration, the HFOV conditions, and the flow and particle parameters. The compliance ratio was kept at 1. To investigate the role of the carrier gas density, four different gas mixtures were considered. The density of the heavier gas (sulfur hexafluoride-oxygen, SF_6-O_2) was 29-fold higher than the lighter gas (He); the He was considered to investigate the lower end of the gas density. Reynolds number ($\mathrm{Re}_\tau = D_{ave}U_{mean}/\nu$) based on the mean velocity (U_{mean}) and trachea-averaged diameter ranged from 1305 to 27100 for the lowest gas density (He) and highest gas density (SF_6-O_2), respectively. Likewise, the Womersley number ranged from 5.43 to 25.28 based on the trachea average diameter, as seen in Table 7.1.

Table 7.1 Properties of the considered carrier gases and flow parameters; HFOV *f*= 10 Hz.

Gas mixture	ρ_G (kg/m^3)	ν_G (m^2/s)	Reynolds number $\mathrm{Re}_{trachea}$	Womersley number $\alpha_{trachea}$
He	0.166	11.9×10^{-5}	1305	5.43
He-O_2[a]	0.4	4.95×10^{-5}	3039	8.35
air	1.185	1.511×10^{-5}	5843	14.83
Xe-O_2[b]	2.597	0.81×10^{-5}	18280	20.64
SF_6-O_2[c]	4.8	0.54×10^{-5}	27100	25.28

Gas composition: [a]80%He-20%O_2, [b]40%Xe-60%O_2 [177], [c]71% SF_6-21%O_2 [27]

7.3. Results and Discussion

The results of the gas transport and particle deposition in the ETT and tracheobronchial tree under different carrier gases were obtained in terms of flow regimes, turbulence, pendelluft intensity ratio, and global and local deposition. The findings are reported and discussed next.

7.3.1. Flow Regimes Characteristics

The typical flow regimes under HFOV parameters are characterized into three regimes [225]. Regime I consists of unsteady flow where a well-known Womersley linear solution can be approximated. Regime II covers viscous flow where the convective inertia and secondary flow effects are negligible (Poiseuille solution). Finally, regime III encompasses convective flow, which is distinguished by complex flow structures and can be further sub-divided into two zones, IIIa-convective and IIIb-convective depending on its location from the unsteady and viscous regimes. This characterization based on Jan *et al* [225] depend on two non-dimensional parameters; the Womersley number, and stroke length (L/a) where L is the stroke volume per average area of the cross-section airway segment, V_T/A, and V_T is the local tidal volume of the airway segment. These defined flow regimes were used in many past studies [47, 154, 226, 227] as a guidance to anticipate the flow key features in different regions of the conducting airways model. Figure 7.2 shows the delineations of these three regimes and the flow characteristics through our lung geometry for different carrier gases that were considered in the present study. The boundary lines between different regimes are according to the constant Reynolds number values at 30 and 1500. The flow regime in the trachea was presented for all five-carrier gases. The characteristics of the flow regimes in selected airways segments from trachea to G7 are presented for He and SF_6-0_2 mixture, which have the lowest and highest gas density, respectively. The results were compared to simulation with air as the carrier gas. The flow at the trachea (for all combinations tested) was located in the turbulent regime signifying very complex flow [225]. Since all cases had similar values of the dimensionless local tidal volume (L/a), the distance from the

Re=1500 line was governed by α^2. This is due to the dependency of the Womersley number on the gas kinematic viscosity. Consequently, as the gas density (kinematic viscosity) increased (decreased), the flow was located far away from the *Re*=1500 line (convective regime), see Fig. 7.2. The range of the dimensionless parameters for the three carrier gases compared in Fig. 7.2 are presented in Table 7.2. For SF_6-O_2, all airways segments were characterized by turbulent flow regimes and was located far away from the convective regime. When using air, the curve evidently shifted to the left; however the turbulent regime was predominant in all airways segments. Thus, the combination of higher density and lower kinematic viscosity of carrier gases when used in the presence of an ETT caused turbulent flow to exist at location that were deeper into the tracheobronchial tree. However, when using air, the peripheral segments (e.g., G7) were located near the convective regime indicating less turbulence. The lowest density gas (i.e., helium) noticeably mitigated the flow complexity. The curve was shifted towards the convective regime as some airway segments collapsed into this regime indicating diminished turbulence.

Based on these observations, the linear solutions of Womersley or Poiseuille cannot be approximated in any airways segments for HFOV. It was therefore evident that the flow complexity existed for all cases and increased as the gas density increased. However, according to the curves behavior in Fig. 7.2, using a carrier gas with lower density could significantly enhance gas transport and aerosol-drug delivery during HFOV management.

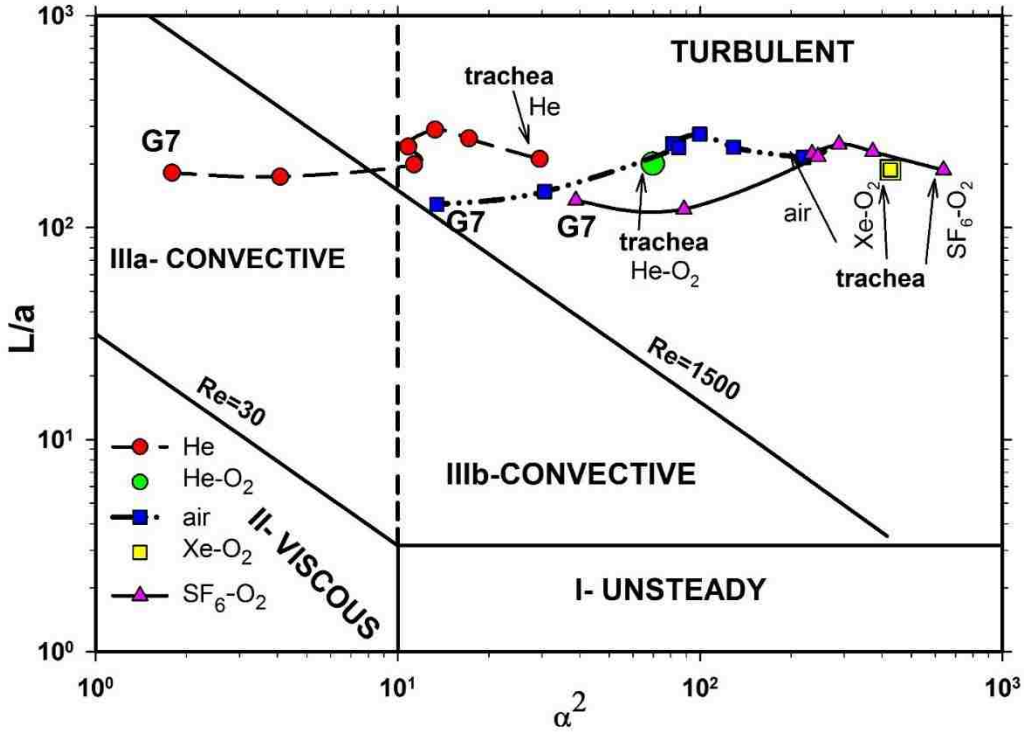

Figure 7.2 Flow regime characterization under different carrier gases at an operating frequency of 10 Hz and tidal volume of 50 ml, based on Jan *et al [225]*.

Table 7.2 The range of squared Womersley number and stroke length for different carrier gases.

Carrier gas	α^2		*L/a*	
	G7	Trachea	G7	Trachea
He	1.79	29.48	173.62	289.07
air	13.44	219.92	128.59	275.68
SF_6-O_2	38.84	639.08	122.03	247.19

7.3.2. Flow Structures

The use of various carrier gases revealed significant differences on the flow structures, respiratory mechanics and gas transport features during HFOV.

7.3.2.1. Spatial and Temporal Evolution of ETT-jet

The presence of intubation (i.e., ETT) caused a strong jet (henceforth referred to as the ETT jet) that was released in the trachea region and impacted at the first carina ridge. The spatial and temporal evolution and the stability of the jet could be influenced by the carrier gas properties, which subsequently affect the inhalation therapy outcomes. Fig. 7.3 compares the flow structure and ETT-jet evolution in the case of using He and compared the results with simulations that used air. The snapshots of the velocity contours were taken at different times corresponding to 4%, 6%, 9% and 25% (peak inspiration) of the cycle time. To illustrate the spatial differences of the jet development, the vertical distance (Z) of the developed jet from the ETT exit at each time was labeled in Fig. 7.3 in terms of ETT diameter. The ETT jet was observed to develop rapidly in the case of using He gas, which has a density 7.3-fold lower than air. At the beginning of the cycle, the jet had similar features in both cases. As the cycle advanced (t/T =0.06), the lighter He jet traveled a longer distance ($2.13D_{ETT}$ compared to $1.5D_{ETT}$ of the air jet, see Fig. 7.3) than the heavier air jet. At t/T =0.09, the air jet approached the tracheal crania ridge (no impingement yet) while the He jet had already impinged on the flow divider, bifurcated and penetrated into the main bronchi (see demarcated areas 1 and 2 in Fig. 7.3a and b). As the inspiratory flow reached the peak acceleration phase, the jet in both cases was fully developed, and deeper penetration occurred for the He jet. The rapid development of the He jet indicates that for a given driving pressure, using a low-density gas mixture such as Heliox could deliver more tidal volume, which may enhance gas exchange. The turbulence inside the ETT, the core region of the ETT jet and the jet

surrounding area was evident, particularly in the case of using air. It was initiated as the jet developed and was more pronounced at peak inspiratory flow. This was due to the difference in constituent properties, which resulted in a Reynolds number that was 4.5-fold higher in the case of using air. The turbulence when using air could have a strong effect on the particle transport, which will be discussed later. The observation of the higher jet velocity with lower turbulence when using He gas is consistent with the reported observation by Sandeau *et al* [220] in their study of flow in a extrathoracic model under Heliox and air for normal breathing conditions.

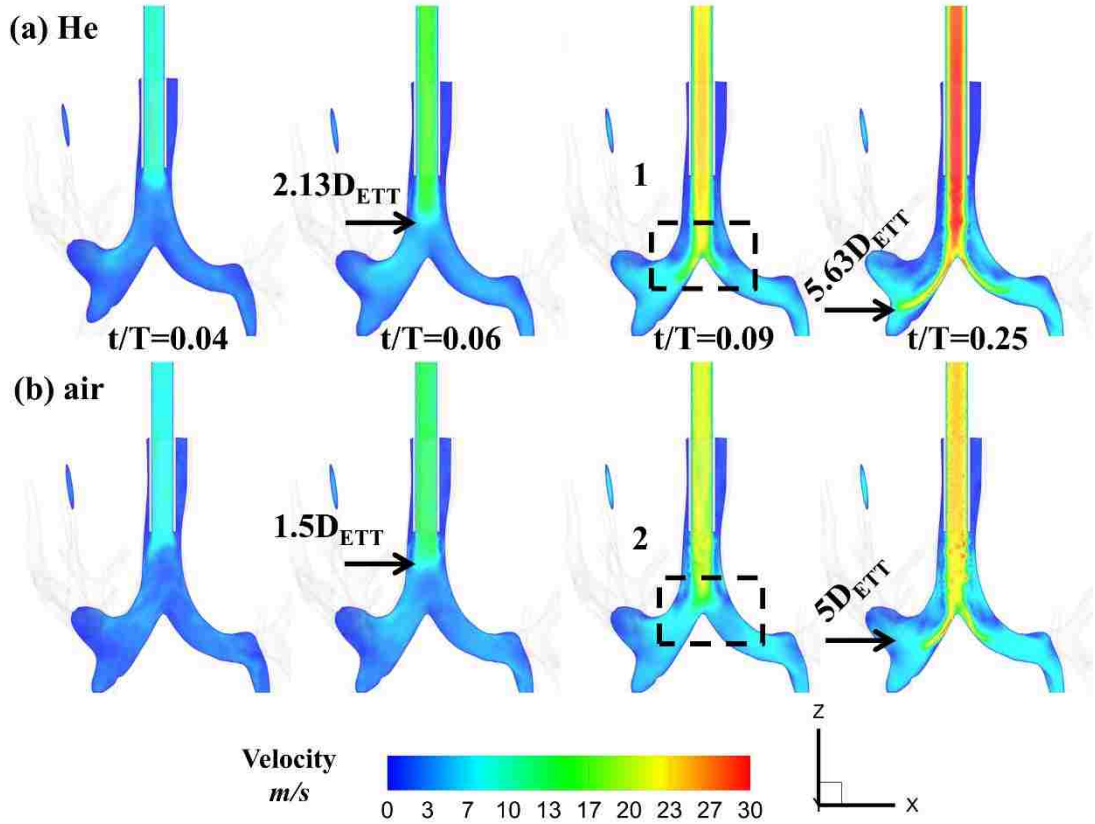

Figure 7.3 Velocity contour and ETT-jet evolution at different inspiratory flow cycles, (a) He and (b) air. The labeled distance is a measure of the vertical distance from the ETT exit to the location where the arrows point out.

7.3.2.2. Turbulence and Airways Resistance under Different Gases

To investigate the influence of gas density on the turbulence inside the domain, turbulence kinetic energy was plotted in Fig. 7.4 as a function of inspiration time. The data is shown for the lowest and highest carrier gases and compared to air. The TKE was computed and averaged at a vertical plane that cuts throughout the ETT, trachea and main bronchia. In all cases, TKE increased as the flow accelerated; due to higher disturbance during the deceleration phase, a further increase in the TKE was also observed [135, 166]. The TKE in the case of the highest density mixture (SF_6-O_2) was ~1.55-fold and ~1.9-fold higher than air and the lowest gas density (He), respectively. This corresponded to an increase of the mean Reynolds number by a factor of 4.64 and 20.77 respectively in the case of SF_6-O_2 mixture when compared to air and He respectively. The occurrence of the turbulence in the trachea and the main bronchi, even with low-density gas like He, was due to three significant factors. Firstly, the presence of the ETT released a strong jet in the trachea region, which created a flow reversal along the jet sides. The interaction between the jet and flow reversal formed a free shear layer, which initiated the turbulence in this region [95]. Secondly, the transition to turbulence is determined by the Stokes layer Reynolds number (Re_δ) that is defined as $\mathrm{Re}_\delta = U\delta/\upsilon$, where $\delta = \sqrt{\upsilon/\pi f}$ is the Stokes layer thickness [135]. Eckmann and Grotberg [136] found that the transition to turbulence occurs when $500 < \mathrm{Re}_\delta < 856$ for oscillatory flow in a straight pipe. Furthermore, Winter *et al* [135] determined the critical Reynolds number to be between 400 and 575 for a purely oscillatory flow in a circular tube. The Stokes-layer Re based on the present HFOV flow conditions for (He) was higher than the critical value (i.e.,

$\mathrm{Re}_\delta \sim 810, 589$ and 501 in the trachea, right and left bronchus, respectively), indicating turbulence at the trachea and main bronchi. This was confirmed by the flow regimes characteristic based on Jan *et al* [225], as discussed previously in section 7.3.2. Thirdly, the ETT and complexity in geometry due to curvatures, asymmetry, successive branching angle, and nonuniform cross-sections contribute additional disturbances to the flow. Consequently, the critical values of Re_δ, where the transition to turbulence is initiated, become lower in bifurcated tubes [135]. Nerem *et al* [228] reported critical Re_δ value of 150 for a blood flow in the aorta of dogs.

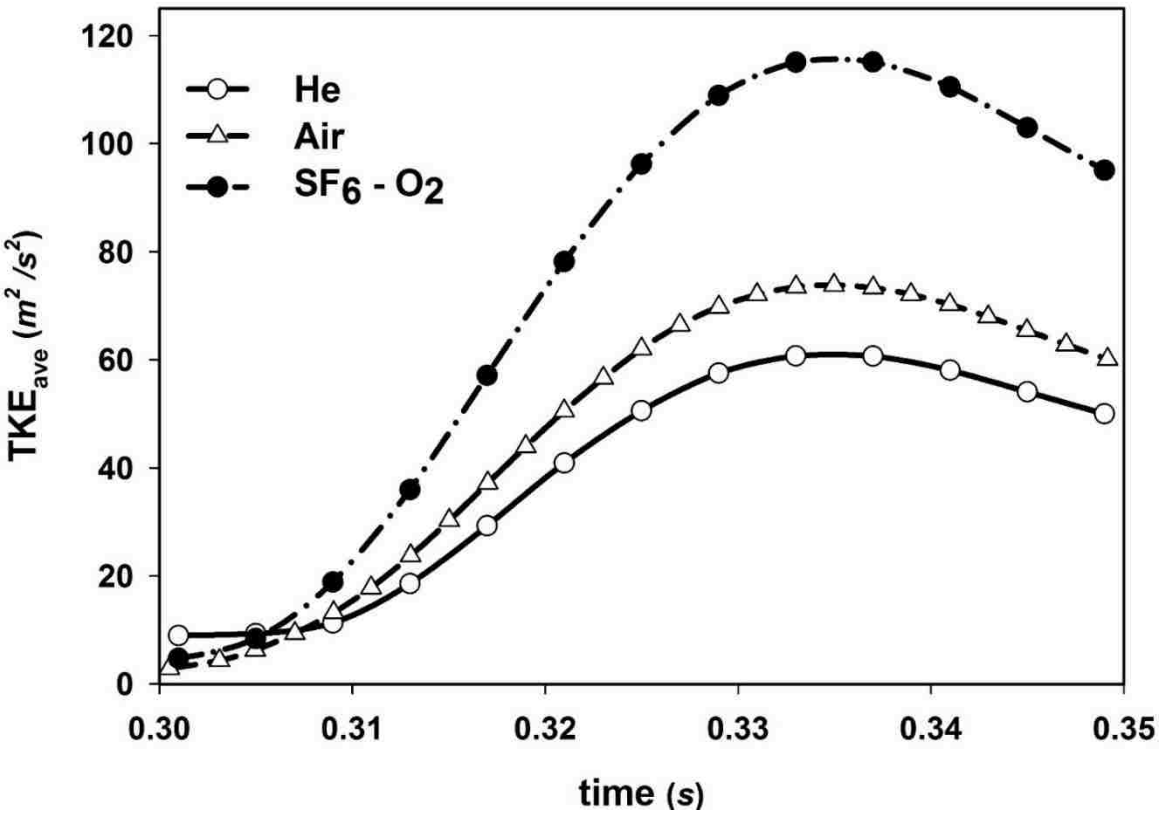

Figure 7.4 Temporal variation of the turbulence kinetic energy for different carrier gases during the inspiration phase.

To examine the effect of the carrier gas on the respiratory mechanics, the global tracheobronchial resistance (R_{TB}) was computed for each case following Miyawaki *et al* [177]:

$$R_{TB} = \frac{\Delta P_{TB}}{Q_{in}} = \frac{p_{in} - \sum_{k=1}^{N,out} p_{out,k} / N_{out}}{Q_{in}} \tag{7.1}$$

where p_{in} and Q_{in} are the pressure and the inlet flow rate at the ETT entrance, respectively. $p_{out,k}$ is the pressure at the k^{th} outlet, and N_{out} is the total number of the outlets. R_{TB} is plotted in Fig. 7.5 and was normalized by the highest computed value, i.e., R_{TB} (SF_6-O_2) = 2.454 *cm of* H_2O*/l/s.* The value of R_{TB} increased as the Re increased (i.e., density increases) which was strongly correlated with the associated turbulence with each carrier gas. It was observed that the R_{TB} in the case of SF_6-O_2 is ~5.10-fold and ~1.74-flod higher than He and air due to higher Re number. Furthermore, an 18% decrease in the TKE when using He rather than air led to a ~65% decrease in the R_{TB}. This could play a major role in gas and particle transport, which may reduce the respiratory effort and increase aerosol-drug delivery. The values of R_{TB} and its observed linear behavior with Re number agreed with earlier reported trends by Miyawaki *et al.* [177] for the same range of *Re* numbers. In their study of flow in a realistic model extending from the mouthpiece to G7, R_{TB} was 0.421 and 0.732 *cm of* H_2O*/l/s* corresponding to *Re* numbers of 1300 and 2800, respectively. For a similar *Re* range of 1305 (for He) and 3039 (for He-O_2 mixture), R_{TB} was estimated as 0.4811 and 0.8989 *cm of* H_2O*/l/s*, respectively. The difference was due to the variations in the models configurations and complexity.

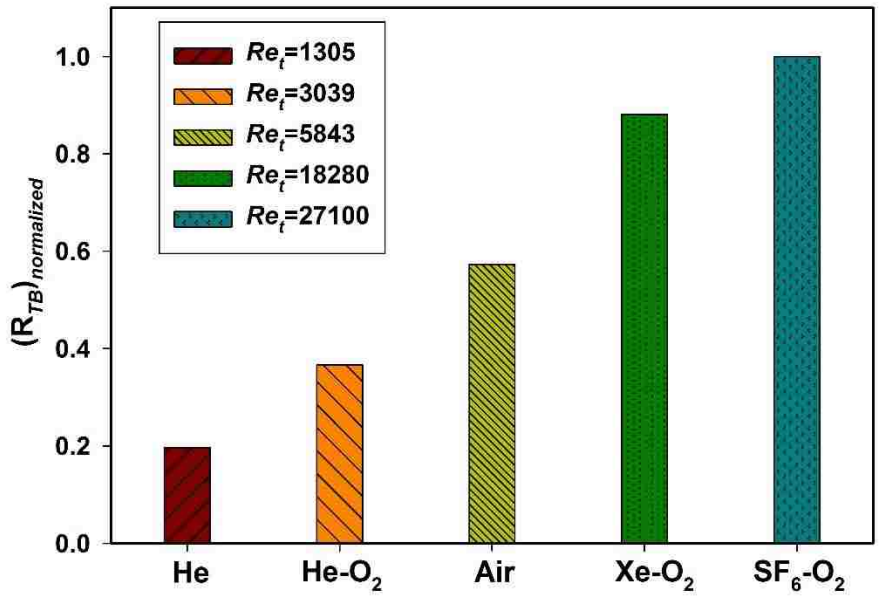

Figure 7.5 The predicted airways global resistance under different carrier gases. R_{TB} was normalized by the highest computed value, i.e., R_{TB} (SF_6-O_2) = 2.454 $cmH_2O/l/s$.

7.3.2.3. Secondary Flow

Temporal variation of the secondary flow strength for the cases of He, air and SF_6-O_2 are presented in Fig. 7.6. SFS is defined as the ratio of the radial component of velocity (*Vr*) to the axial velocity component at a given location [161, 166]. SFS was characterized as strong when the ratio was greater than 0.6, moderate when $0.3 \leq SFS \leq 0.6$, and weak when $SFS < 0.3$ [166]. SFS was averaged at two different cross-sectional planes, *T* at the trachea and *L* at left bronchus (see Fig. 7.1 for locations). At location T in the trachea, a moderate secondary flow $SFS < 0.6$ existed for all cases; however, strong enhancement in secondary motion was observed at the beginning and end of the inspiration and expiration phases (i.e. $SFS > 0.6$). Comparing secondary flow at the flow reversal, the SFS was ~30% higher for the cases of air and SF_6-O_2 than He. As expected,

the secondary flow was strong (SFS > 0.6) at location L in the left bronchus due to the effect of the curvature. The enhancement of secondary flow at flow reversal was evident as well, and its strength was comparable in all cases. This observation indicated that geometry features dominate the secondary flow motion more than the properties of the gas. As a result, the contribution of secondary motion to the gas dispersion and mixing could have the same significance in all carrier gases, except at the flow reversal where a decrease in SFS values was observed for He-gas.

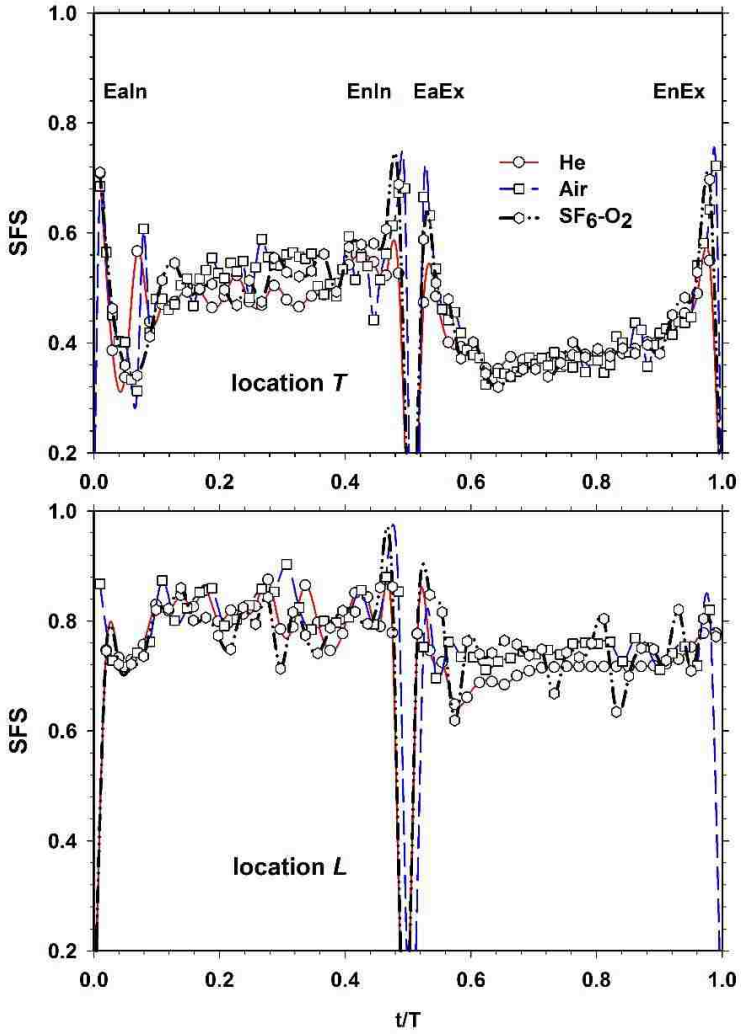

Figure 7.6 Temporal variation of the secondary flow strength (SFS) for different carrier gases at different locations.

7.3.3. Pendelluft Mechanism

The regional gas exchange between adjacent branches or units is referred to as a pendelluft flow. The heterogeneity of the time constant ($\tau = CR$) causes the flow to alternate between the units at the end of inspiration/expiration phases [168, 184]. In chapter 5, using coupled resistance-compliance boundary conditions [184], the pendelluft flow in different lung regions was captured and characterized in terms of pendelluft intensity as a pendelluft volume percent. For any unit consisting of a mother tube that bifurcated into two branches (daughter tubes), V_P is defined as the ratio of the volume exchanged between daughter branches during pendelluft time-period to the total volume delivered to the unit in one cycle [184]. The results of the pendelluft flow for different carrier gases in the present study were obtained and compared in terms of the pendelluft volume ratio (V_{ratio}) in Fig. 7.7. The pendelluft volume ratio is defined as $V_{ratio} = V_{P\,gas1} / V_{P\,gas2}$, where the $V_{P\,gas1}$ and $V_{P\,gas2}$ are the pendelluft volume percent of the first selected carrier gas to the pendelluft volume percent of the second selected carrier gas. In Fig. 7.7, Gas 1 was selected to be He (lowest density) and compared to Gas 2 (air and SF_6-O_2 mixture). It was found that, in general, the carrier gas with a lower density increased the pendelluft flow, signifying enhancement of the gas exchange. This is attributed to the lower gas density and higher kinematic viscosity [223, 224], which increases the gas velocity and modifies the system time constants [229, 230]. The magnitude of the increasing pendelluft intensity, however, strongly depends on the unit location. For example, in unit 4, V_P when using He was ~1.55-fold higher than air while in unit 26 it was ~15-fold higher. This is attributable to the flow conditions and the

regional geometry features, such as branching angle, diameter, unit orientation, and structure abnormity, which could play a major role in the pendelluft intensity [184]. Comparing the V_{ratio} of He to denser gas mixtures than air (i.e., SF_6-O_2), the ratio further increased, depending on the location, which emphasizes the impact of the gas density on the gas exchange (see Fig. 7.7).

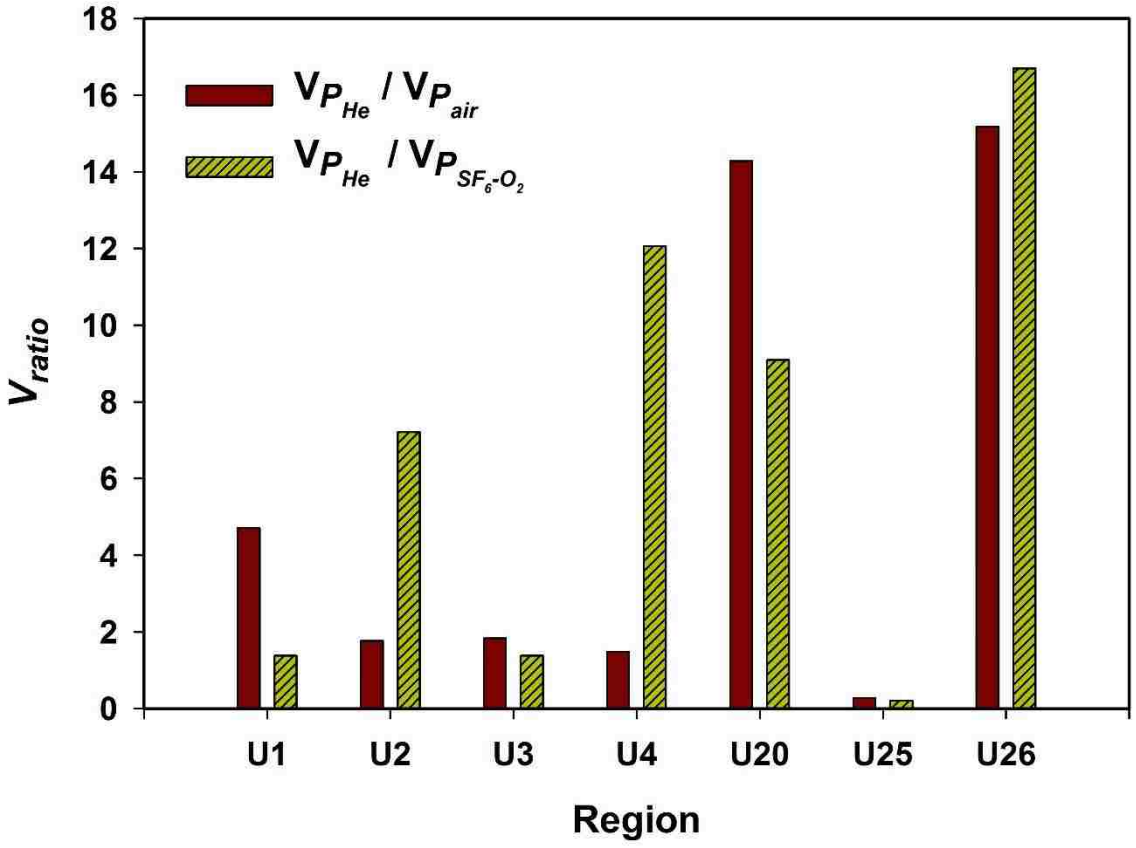

Figure 7.7 The pendelluft volume ratio (V_{ratio}) for He to air and He to SF_6-O_2. The ratio is defined as $V_{ratio} = V_{P\,gas1} / V_{P\,gas2}$. $V_{P\,gas1}$ and $V_{P\,gas2}$ are the pendelluft volume percent of gas 1(He) and gas 2 (air and SF_6-O_2).

7.3.4. Particle Deposition

The role of carrier gas properties in particle transport and deposition at the ETT and tracheobronchial tree during HFOV were explored and presented in terms of global and local deposition fractions.

7.3.4.1. Global Deposition

The global deposition fraction was defined as the total particles deposited in the whole domain to the total particles entering the ETT [222]. The global deposition characteristics under different carrier gases were presented in Table 7.3. The deposition associated with inspiratory flow was always higher than with the expiration phase as found in chapter 6. However, the ratio of the deposition during inspiration phase (In) to expiration (Ex) phase (In/Ex ratio) significantly increased as the carrier gas density increased, ranging from 2.51 to 6.77 for the lowest to highest gas density (see Table 7.3). A decreasing gas density minimizes the particle relaxation time, as well as the turbulence and flow resistance, which effectively reduces the impaction role and particle dispersion [120]. Consequently, the particle deposition during the inspiration phase increases (decreases) for higher (lower) carrier gas density. This resulted in the wide range of In/Ex ratios, which significantly affected the total global deposition throughout the whole domain. For example, He and Heliox reduced the deposition on the upper tracheobronchial tree by ~32% and ~25.36% (relative difference) compared to air. This suggests that using Heliox with high concentrations of Helium could deliver more particles into deeper regions of the pulmonary tract. The total deposition for the highest density carrier gases (i.e., Xe-O_2 and SF_6-O_2) was significantly enhanced and was

identical for both gases. It was ~70% higher than the lowest density gas (see Table 7.3). The identical deposition indicates that by increasing density beyond that of Xe-O_2, the deposition rate becomes independent of the density under HFOV conditions. The deposition in the right lung is consistently higher than the left lung with insignificant differences between considered carrier gases.

Table 7.3 Details of global particle deposition under different carrier gases.

Carrier Gas	DF_G%				
	In	Ex	In/Ex ratio[a]	R/ L ratio[b]	Total
He	22.35	8.91	2.51	1.31	31.26
He-O_2	26.46	7.83	3.38	1.36	34.29
air	38.65	7.30	5.30	1.29	45.94
Xe-O_2	45.33	8.30	5.46	1.18	53.63
SF_6-O_2	46.49	6.87	6.77	1.23	53.36

[a]In/Ex ratio is the ratio of the total deposition during inspiratory flow to the total deposition during expiratory flow.
[b]R/ L ratio is the ratio of total deposition in the right lung to the total deposition in the left lung.

For further insight on the role of the carrier gas on the deposition, the global deposition for various particle size ranges under He-gas (lowest density) is compared to air in Table 4. Katz *et al* [120] derived a formula for the relaxation time ratio (R_τ) of the particles in the case of Heliox to air (applicable to any carrier gas), and it is defined as the following:

$$R_\tau = C(d)_{gas}\mu_{air} / C(d)_{air}\mu_{gas}$$

where $C(d)$ is a factor that accounts for non-continuum slip effects of the interaction between particles and the gas. $C(d)$ is a function of the Knudsen number, $Kn = 2\lambda / d_p$,

where λ is the gas mean free path. Based on the observation of Katz *et al* [120], the deposition is enhanced for the particles with $R_\tau > 1$ and vice versa. For the Heliox mixture, $R_\tau < 1$ was found for the particle diameter greater than 0.4 μm. For the range of the particle size (5> d_p > 0.5 μm) used in the present study, the deposition under air was ≥ 40% higher than He (see Table 4). This is due lower relaxation time ratio ($R_\tau < 1$) as indicated by the theoretical formula of Katz *et al* [120] when using Heliox in addition to the reduction in turbulence and flow resistance.

Table 7.4 Comparison of the total global deposition for a wide range of the particles' diameters in the case of He and air carrier gases.

d_p range (μm)	DF_G		Relative difference% $= \frac{DF_{He} - DF_{air}}{DF_{He}} \times 100$
	He	air	
0.5< d_p<1	1.26	2.12	68.25
1< d_p<2	4.56	6.78	48.68
2< d_p<3	5.99	8.73	45.74
3< d_p<4	7.17	11.60	61.79
4< d_p<5	12.50	17.44	39.52

7.3.4.2. Local Deposition under Different Carrier Gases

The local deposition in the major lobes of the lung was quantified during inspiratory, expiratory, and whole cycle flow and presented in Fig. 7.8. The local deposition fraction is defined as the total particles deposited in a selected region to the total particles entering the ETT [222]. The local deposition behavior had similar trends regardless of the carrier gas type. During the inspiration phase, the main bronchi received the majority of the particle deposition, due to enhancement of the impaction role and ETT-jet impingement [222], followed by the lower lobes; however, the deposition in any

lobe was consistently lower as the gas density decreased. Consequently, in the case of using a carrier gas with low density such as Heliox ($He-O_2$), the aerosol-drug could penetrate deeper into the lung and have a better chance to deposit in the lower region of the pulmonary tract. During expiratory flow, the local deposition was almost the same in all lung lobes without any significant differences between all carrier gases. The deposition in the ETT was highest during the expiration phase. This is because a high population of the particles stayed active and were convected with the flow that experienced sudden contraction, which may have enhanced impaction and particle dispersion in this region. The total local deposition trend

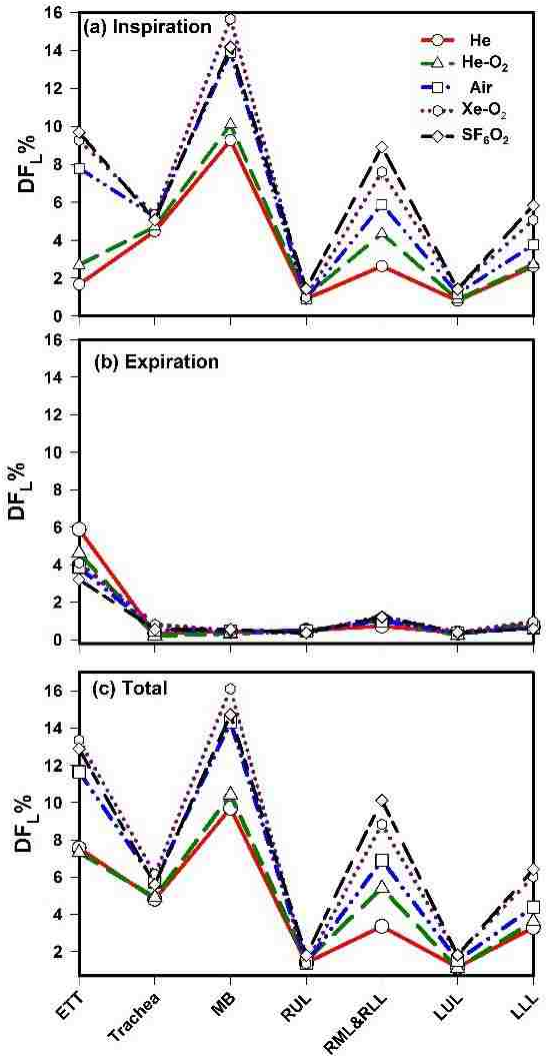

Figure 7.8 Particle local deposition for different carrier gases: (a) during the inspiration phase, (b) during the expiration phase, and (c) the total deposition during the whole cycle.

followed the trend during inspiratory flow due to high deposition that occurred during this phase [222]. However, the differences in the deposition fraction magnitude in each lobe diminished as the carrier gas density increased, and the differences became insignificant for gases with densities higher than the density of air. The ventilatory circuit is a key factor for reducing the aerosol-drug, and allows only a small portion of the drug

to reach the lung [41]. It is therefore essential to reduce the deposition in the circuit to maximize the drug delivery to the lung.

For deeper insight on the role of the carrier gas on the aerosol particles deposited in the ventilator circuit, the local particle deposition and pattern of the deposition on the ETT are presented in Fig. 7.9. Employing carrier gases with low gas density was observed to drastically change the deposition rate in the circuit (see Fig. 7.9). The deposition was highly concentrated around the ETT in the case of high gas density (i.e., air and SF_6-O_2).

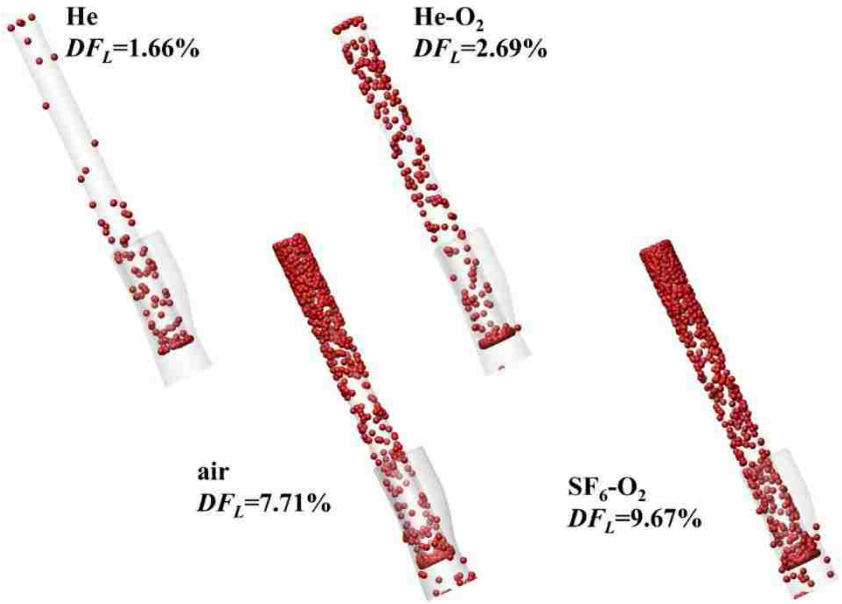

Figure 7.9 Comparison of the deposition pattern at the endotracheal tube wall for different carrier gases.

The local deposition factor DF_L in the ETT was drastically reduced by ~79% and ~83% in the case of using He-gas compared to air and SF_6-O_2, respectively. Likewise, DF_L was reduced by ~65% and ~72% when using Heliox rather than air and SF_6-O_2, respectively.

Table 7.5 compares the decreased deposition fraction in the ventilator circuit between the current study and existing experimental studies when using Heliox instead of air. A mean reduction of 38% of the deposition at the ETT was observed by Katz *et al* [120] in their clinical measurement of using Heliox as a carrier gas. Similarly, Goode *et al* [231] achieved 50% reduction of the lost particles in the ventilator circuit. The difference between the current predictions (65%) to their measurement arises from a couple of factors. First, the reported local deposition in the present CFD study was only for a part of ETT. Second, their studies were conducted under conventional mechanical ventilation, i.e., lower flow rate and longer respiratory cycle time.

Table 7.5 Comparison between current prediction and experimental studies of the decreased deposition fraction in the ventilator circuit due to the use of Heliox as a carrier gas

Study	Approach	Flow rate (L/min)	Ventilation mode	Decreased DF*
Katz *et al* [120]	*In vivo*	18	CMV	38%[+]
Goode *et al* [231]	*In vitro*	40	CMV	50%
Present study	CFD	94	HFOV	65%

[+]It is a mean value for different cases.

[*]Decreased DF is calculated as $\frac{DF_{air} - DF_{Heliox}}{DF_{air}} \times 100$

7.3.4.3. Deposition Pattern

The pattern of the deposition, which illustrates the most localized and concentrated deposition sites, is displayed in Fig. 7.10 for the cases of He, He-O_2, air, and SF_6-O_2. The reduction of the localized deposition when using a low-density carrier gas was evident. The relaxation time of the particles, the turbulence intensity, and the airways resistance decreased as the density decreased, which reduced the role of the deposition mechanisms, i.e., impactions and particle diffusion. Consequently, more particles escaped the domain and had a greater chance to deposit in the lower region of the lung. This can be seen by comparing the pattern of the deposition in the case of low-density gas (He and Heliox) to high-density gas (air and SF_6-O_2) in Fig. 7.10. The particles were more concentrated at the main bronchi covering the inner walls in all cases, however, as the gas density increases, the concentration increases. When using He or Heliox, mostly large particles deposited in the tracheobronchial domain; in contrast, the dense gases led to a deposition of a wide range of particle sizes. In general, the deposition on the usual sites was reduced by utilizing a carrier gas with low density. This can be observed by comparing the deposition in the encircled region of the domain (1-4) in Fig. 7.10 in all cases. Furthermore, the deposition on the sharp transition region (constrictions) are compared in the enlarged plot (see insets in Fig. 7.10).

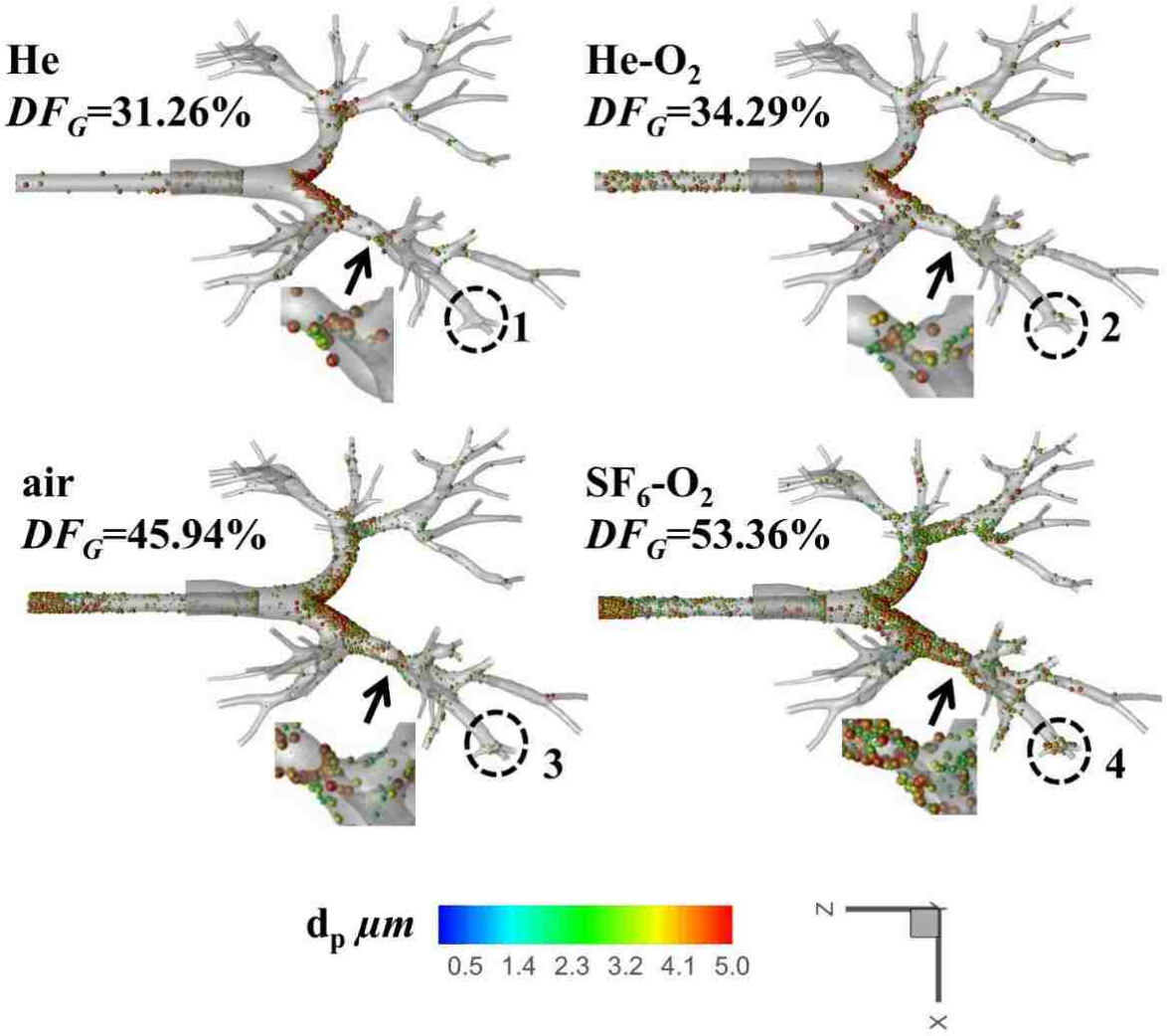

Figure 7.10 Deposition pattern at the tracheobronchial tree as a function of the particle diameter for different carrier gases.

Clearly, lower localized deposition occurred when using He and He-O_2 compared to air and SF_6-O_2, where highly concentrated deposition was observed. This affirms the importance of the role of the carrier gas on aerosol-drug delivery and the requirement for lower density gas to deliver more drug to deeper regions of the lung under rapid ventilation cycles.

7.3.5. Enhancement of HFOV Therapy

The carrier gas properties were found to have significant impact on the gas transport and drug delivery under HFOV conditions. Several past studies recognized an enhancement of drug delivery using a helium-oxygen mixture, yet the majority of these studies have been conducted under normal breathing conditions in an extrathoracic model [220, 232]. In our previous study of drug delivery under HFOV parameters, it was found that the strong dependency of the global and regional deposition rate on the operating frequency could be used for targeted drug delivery [222]. For further insight on the role of coupled ventilator frequency and carrier gas on particle deposition, a simulation of HFOV frequency of 6 Hz was carried out using helium gas. The deposition was found to be significantly affected with reductions of ~35% and ~ 56% observed in the global deposition in the tracheobronchial tree for the cases of He and air when compared to the case of 10 Hz frequency. This implies that more particles penetrated deeper into the pulmonary tract and increased the chance of higher deposition in the lower generations. Consequently, systemic drug delivery could be enhanced under coupled low-density gas and low operating frequency. Furthermore, during the inspiration phase the local deposition on the considered portion of the ETT was drastically reduced by decreasing ventilator frequency to 6 Hz. A ~13-fold reduction of the deposition in ETT occurred indicating that higher amounts of the aerosol-drug could pass the ventilator circuit and be delivered to the lung. This is because decreasing frequency reduces the flow rate, which, along with low density, tend to stabilize the flow field. As reported in section 3.3.2, a reduction of 18% in the TKE effectively decreased the airways' resistance, which reduced the deposition in the ETT and upper

tracheobronchial tree. The effectiveness of reducing the TKE on decreasing particle deposition on the extrathoracic region has been observed by Ari *et al* [221] even with very low difference in TKE between cases of using Heliox and air (i.e., 5%). The improvement of the gas exchange under HFOV management employing low-density gas was observed by different studies in animal models [223, 224]. However, the effect of utilizing different carrier gases on the flow mechanisms cannot be quantified during *in vivo* studies. In contrast, the current CFD study successfully quantified the effect of carrier gas on the pendelluft flow in different lung regions. Great enhancement of the pendelluft flow occurred by reducing (increasing) carrier gas density (kinematic viscosity) and indicated improvement of the regional ventilation and gas mixing during HFOV. The reduction of the airways' resistance by employing low-density carrier gas not only improves drug delivery, it is most likely to reduce the risk of hyperinflation of the lung [229].

7.4. Conclusion

The effects of carrier gas properties on HFOV therapy outcomes were studied. A large eddy simulation model was used to simulate the continuous phase while user-defined Fortran subroutines were used to implement a Lagrangian approach model for the dispersed phase. A physiological pressure boundary was employed using resistance and compliance of the airways. Gases with a wide range of densities and kinematic viscosities were used and compared to the use of air. The main conclusions can be summarized as the follows:

1. The carrier gas density was found to play a major role on the flow structures under HFOV conditions. A reduction (increase) of 7-fold in the gas density (kinematic viscosity) reduced the turbulence kinetic energy by 18%, which significantly decreased the tracheobronchial tree resistance by 65%. The significant reduction of the airways resistance could effectively reduce the risk of lung hyperinflation.
2. The pendelluft flow was significantly enhanced by reducing the carrier gas density. An increase of 15-fold of the pendelluft flow in some lung regions was observed, indicating improvement of the gas exchange under HFOV when employing low-density gas.
3. Use of low-density helium, which has the lowest gas density, significantly reduced deposition in the "hot-spots" and constriction sites in the upper tracheobronchial, and resulted in a ~32% reduction of the global deposition factor, indicating that the more Helium concentration in the Heliox, the greater benefit of the gas mixture.
4. Heliox can be effectively used to enhance lung periphery aerosol-drug delivery under HFOV therapy, whereas carrier gases with higher density can be used to enhance lobar- to-segmental airways treatment.
5. Significant reduction of aerosol-drug deposited in the ETT was achieved by using a low-density carrier gas; this implies that Heliox could improve drug delivery to the lung during HFOV.
6. Coupling low-frequency ventilation with a Heliox carrier gas resulted in further decreasing the deposition throughout the ETT and upper

tracheobronchial tree, and indicated further enhancement of lung periphery delivery.

CHAPTER 8

CONCLUSIONS AND FUTURE WORKS

8.1. CONCLUSIONS

The gas transport and drug delivery by high frequency oscillatory ventilation were computationally investigated and validated against available measurements in the literature. The lung model was reconstructed from CT- scans data set for a mechanically ventilated patient. Large eddy simulation along with WALE subgrid scale model were implemented to model the airflow inside the lung model. Lagrangian approach was used to model the solid particle transport. The main results can be summarized as follows:

(i) Flow Transport and Gas Mixing during Invasive High Frequency Oscillatory Ventilation

Gas transport and mixing in HFOV for three different waveform shapes and frequencies. The primary focus was to understand how different flow mechanisms were altered as a result of changes to waveform and frequencies. It is concluded from the study that:

1- The coaxial counter flow existed near flow reversal for all three waveforms with different features. The non-sinusoidal waveforms exhibited a uniform coaxial counter flow compared to the sinusoidal case at End-Inspiration/Early Expiration phase.

2- Pendelluft flow was present for the sinusoidal waveform at all frequencies but occurred only at early inspiration for the square waveform at highest frequency, whereas this was absent in the case of using exponential waveform.

3- A square waveform shape resulted in higher secondary flow strength (SFS>0.6) and higher turbulence intensity, which could lead to more efficient mixing.

4- A reduction of ~87% in the wall shear stress occurred during inspiration phase when the intubation was absent. The turbulence kinetic energy in the case of using ETT was found to be 20 times greater than when the ETT was absent.

5- The square waveform resulted in the least wall shear stress on the lung epithelium layer and may be used in patients without the risk of barotrauma to both airways and the alveoli.

(ii) The Role of Coupled Resistance-Compliance in Upper Tracheobronchial Airways under High Frequency Oscillatory Ventilation

The gas transport under HFOV conditions with physiologically relevant outlet BCs was studied. A time-dependent pressure was employed as a function of the instantaneous flow rate and coupled airways resistance-compliance. A significant change in the regional flow distribution was observed when using coupled R&C BCs for healthy and diseased lungs. In addition, the pressure drop throughout the lung domain demonstrated a significant deviation from the case of MF BCs due to the ability of the applied physiological resistance-compliance BCs to account for the geometry features of the model. Unlike traditional BCs, the coupled R&C BCs successfully captured pendelluft flow in all of the lungs' major lobes and terminal units, which enables accurate HFOV modeling. Varying compliance between the right and left lungs demonstrated a significant effect on the flow distribution, and it was more pronounced for the highest HFOV frequency. Increasing the *CR* locally between lung units induced maximum pendelluft flow with a five-fold increase in some units. The coaxial counter flow and flow structures were significantly influenced by the modified BCs. The pendelluft flow

significantly induced a WSS surrounding carina due to gas exchange between the units' branches. The pendelluft intensity in different regions may be used as an important indication of the respiratory diseases and the severity of lung pathway diseases. The intensity of the pendelluft flow associated with the ventilator setting (e.g., frequency, tidal volume, and waveform shape) could help in improving treatment protocols for patients undergoing HFOV treatment.

(iii) Aerosolized Drug Delivery in Specific-Patient Lung Model during Invasive High Frequency Oscillatory Ventilation

The aerosol-drug delivery under high frequency oscillatory ventilation was carried out under various ventilator settings and lung conditions. The Lagrangian tracking method was implemented to model the dispersed phase. User-enhanced FORTRAN subroutines were compiled with the solver to implement the Lagrangian model. A physiological time-dependent pressure boundary condition was employed as a function of the coupled airways resistance-compliance and compared to the traditional boundary condition. The main observations can be summarized as the follows:

- The particle deposition during the inspiration phase was five-fold greater than expiration phase, and the asymmetric lung compliance was found to significantly affect the deposition, especially during expiration phase. Furthermore, the deposition fraction was strongly influenced by the release time of the particles' injection.
- The existence of the pendelluft flow and airflow redistribution due to resistance-compliance BCs application demonstrated a significant influence on the local deposition magnitude and pattern compared to the traditional mass fraction BCs.

- The ETT-jet was observed to have a major impact in enhancing the inertial impaction, resulting in highly localized deposition at the main bronchi and the few subsequent generations. The lower lung lobes significantly received more aerosol-drug compared to the upper lobes, which was consistent with existing results in the literature for normal breathing.
- The asymmetric compliance ratio between adjacent regional units was found to enhance the regional deposition as a consequence of the flow redistribution and effect of the pendelluft flow.
- A 2.5-fold increase of the operating frequency resulted in a 2.1-fold increase in the global deposition fraction in the upper tracheobronchial tree. Meanwhile, a 2.5-fold reduction in the frequency resulted in 3.88-fold reduction of the local deposition at the main bronchi allowing more particles to penetrate deeply in the lung and reduce the drug side effect risk associated with sites of high deposition concentrations. This indicates that the operating frequency has strongly influence the global and local particle deposition fractions and the deposition magnitude could be controlled by changing the frequency, which could be beneficial for targeted drug delivery.
- Considering the particle deposition relative to the injected particle at the ETT inlet, aerosol drug delivery during HFOV could be equivalent to and as efficient as normal breathing and conventional mechanical ventilation, despite rapid ventilation cycles.

(iv) Effect of Carrier Gases on Transport And Aerosol Drug Delivery By Invasive High Frequency Oscillatory Ventilation

The effects of carrier gas properties on HFOV therapy outcomes were studied. A large eddy simulation model was used to simulate the continuous phase while user-defined Fortran subroutines were used to implement a Lagrangian approach model for the dispersed phase. A physiological pressure boundary was employed using resistance and compliance of the airways. Gases with a wide range of densities and kinematic viscosities were used and compared to the use of air. The main conclusions can be summarized as the follows:

1. The carrier gas density was found to play a major role on the flow structures under HFOV conditions. A reduction (increase) of 7-fold in the gas density (kinematic viscosity) reduced the turbulence kinetic energy by 18%, which significantly decreased the tracheobronchial tree resistance by 65%. The significant reduction of the airways resistance could effectively reduce the risk of lung hyperinflation.
2. The pendelluft flow was significantly enhanced by reducing the carrier gas density. An increase of 15-fold of the pendelluft flow in some lung regions was observed, indicating improvement of the gas exchange under HFOV when employing low-density gas.
3. Use of low-density helium, which has the lowest gas density, significantly reduced deposition in the "hot-spots" and constriction sites in the upper tracheobronchial, and resulted in a ~32% reduction of the global deposition

factor, indicating that the more Helium concentration in the Heliox, the greater benefit of the gas mixture.

4. Heliox can be effectively used to enhance lung periphery aerosol-drug delivery under HFOV therapy, whereas carrier gases with higher density can be used to enhance lobar- to-segmental airways treatment.
5. Significant reduction of aerosol-drug deposited in the ETT was achieved by using a low-density carrier gas; this implies that Heliox could improve drug delivery to the lung during HFOV.
6. Coupling low-frequency ventilation with a Heliox carrier gas resulted in further decreasing the deposition throughout the ETT and upper tracheobronchial tree, and indicated further enhancement of lung periphery delivery.

8.2. FUTURE WORKS

Several related topics are suggested for the future work:

1. The lung airways (up to 15 generations) are lined with thin liquid layers consisting of a Newtonian fluid layer attached to the airways wall (watery serous layer) and a non- Newtonian fluid layer (MUCUS) between the serous layer and the gas [70]. The mucus layer drastically increases due to the exacerbation of the mucus secretion in diseased lung and could lead to airflow obstructions [233]. It is considered as a Bingham fluid [234]. Strong interaction between the mucus layer and the gas transport during the breathing cycle is expected. A wavy motion exists at interface between the high viscous layer and the gas flow [235]. It is then expected to have a crucial role on the gas transport and the drug delivery [236]. Therefore, modeling mucus layer with different thickness could reveal important results that help in advancing our understanding of HFOV therapy.
2. The use of coupled resistance-compliance BCs has successfully captured the pendelluft flow between the lung units. The pendelluft characteristics in terms of pendelluft time and volume percent demonstrated strong dependences on the geometry features. Moreover, R&C BCs properly predicted the flow ratio between lung major lobes. These two results can be used to develop an appropriate diagnostic tool for lung pathway diseases in two steps. First, conduct *in vivo* study for sample group of patients with different diseases, using gamma scintigraphy imaging technique before and after recovering, where the flow ratio can be obtained. Second, obtain CT- scan sets and reconstruct lung models for the

same patients; and then preform a systemic study to characterize the pendelluft intensity in all obtained models.

3. The use of mechanical ventilation is often associated with humidifier [236]. Thus, the particles are affected by the gas and lung status (e.g. temperatures & humidity). The temperature and concentration differences between the gas and the particles cause a heat and mass transfer [236, 237]. It is then essential to model particle transport with evaporation/condensation process, which affects the particle size.
4. Most of the aerosolized drug is lost in the ventilator circuit components (e.g. spacer chamber, the ventilator circuit and the endotracheal tube [37, 41]) and only a small fraction of the drug successfully reaches the lung. Longest *et al* [209, 238] have observed the ventilator components of conventional mechanical ventilator. They redesigned T-connectors, Y-connector and ETT. Furthermore, they studied the components of both invasive and non-invasive ventilator. Significant enhancement of the drug delivery was achieved through the modified circuits. Similar approach could be used to minimize the lost particles in the ventilator circuit of the HFOV ventilator machine. In addition, the aerosol nebulizer devices should also be tested for efficient drug delivery.
5. The invasive ventilation entails many complications due to the intubation, which could lead to serious injury or damage of the patient lung. Segmentation of the extrathoracic passages could be used to investigate gas and particle transport under non-invasive HFOV with different nasal, oral and facial devices. The

results will be compared to the invasive ventilation, which could result in a better ventilation strategy.

6. The airways are compliant structures. Considering fluid-structure interactions could reveal important effects in the lung ventilation and the particle trajectory. Starting with simple bifurcation and then increasing the geometry complexity may result in more accurate modeling.
7. Experimental work: Develop a 3D realistic multi-generation lung model including the larynx, and fabricate a physical model with a material that satisfies the experimental and optical conditions. Design experiment components to allow for advanced diagnostics and to allow investigation of a wide range of lung ventilation strategies (i.e. normal breathing, conventional mechanical ventilation (CMV), and high frequency ventilation (HFOV)). The physical model can be made with separate regions and connected with appropriate methods such that it allows for local particle deposition measurements. Furthermore, to include the effect of resistance and compliance, rubber tubes with different lengths and material properties can be connected to the model outlets.

REFERENCES

1. MacIntyre NR, Branson RD, "Mechanical ventilation". 2009, St. Louis, Missouri: Elsevier.
2. Pierce LN, "Management of the mechanicalally ventlated patient". 2nd ed. 2007: Elsevier.
3. Jacob A-M, Gaver DP. Atelectrauma disrupts pulmonary epithelial barrier integrity and alters the distribution of tight junction proteins zo-1 and claudin 4. Journal of Applied Physiology 2012; 113:1377-1387.
4. Ranieri V, Suter PM, Tortorella C, et al. Effect of mechanical ventilation on inflammatory mediators in patients with acute respiratory distress syndrome: A randomized controlled trial. JAMA 1999; 282:54-61.
5. Rubenfeld GD, Caldwell E, Peabody E, Weaver J, Martin DP, Neff M, et al. Incidence and outcomes of acute lung injury. New England Journal of Medicine 2005; 353:1685-1693.
6. Network TARDS. Ventilation with lower tidal volumes as compared with traditional tidal volumes for acute lung injury and the acute respiratory distress syndrome. New England Journal of Medicine 2000; 342:1301-1308.
7. *Breathing process* Available from: http://www.e-breathing.com/respiration/.
8. Papadakos P, Lachmann B, "Mechanical ventilation: Clinical applications and pathophysiology". Vol. 23. 2007: Elsevier Health Sciences. 665.
9. Krishnan JA, Brower RG. High-frequency ventilation for acute lung injury and ards. Chest 2000; 118:795-807.
10. Haitsma JJ, Uhlig S, Goggel R, Verbrugge SJ, Lachmann U, Lachmann B. Ventilator-induced lung injury leads to loss of alveolar and systemic compartmentalization of tumor necrosis factor-alpha. Intensive care medicine 2000; 26:1515-22.
11. Slutsky AS. Lung injury caused by mechanical ventilation. Chest 1999; 116:9S-15S.
12. Muller WJ, Gerjarusek S, Scherer PW. Studies of wall shear and mass transfer in a large scale model of neonatal high-frequency jet ventilation. Annals of Biomedical Engineering 1990; 18:69-88.
13. Evans DJ, Green AS, Thomas NK. Wall shear stress distributions in a model of normal and constricted small airways. Proceedings of the Institution of Mechanical Engineers, Part H: Journal of Engineering in Medicine 2014; 228:362-370.
14. Bilek AM, Dee KC, Gaver DP. Mechanisms of surface-tension-induced epithelial cell damage in a model of pulmonary airway reopening. Journal of Applied Physiology 2003; 94:770-783.
15. Viana MEG, Sargentelli GA, Arruda ALM, Wiryawan B, Rotta AT. O impacto de estratégias de ventilação mecânica que minimizam o atelectrauma em um modelo experimental de lesão pulmonar aguda. Jornal de Pediatria 2004; 80:189-196.
16. Dos Santos CC, Slutsky AS. Invited review: Mechanisms of ventilator-induced lung injury: A perspective. Journal of Applied Physiology 2000; 89:1645-1655.

17. Mireles-Cabodevila E, Diaz-Guzman E, Heresi GA, Chatburn RL. Alternative modes of mechanical ventilation: A review for the hospitalist. Cleveland Clinic Journal of Medicine 2009; 76:417-430.
18. DiRocco J, Carney D, Nieman G. "The mechanism of ventilator-induced lung injury: Role of dynamic alveolar mechanics. in Yearbook of intensive care and emergency medicine 2005", J.-L. Vincent, Editor. 2005, Springer New York. p. 80-92.
19. Schiller HJ, McCann UGI, Carney DE, Gatto LA, Steinberg JM, Nieman GF. Altered alveolar mechanics in the acutely injured lung. Critical Care Medicine 2001; 29:1049-1055.
20. Nucci G, Suki B, Lutchen K. Modeling airflow-related shear stress during heterogeneous constriction and mechanical ventilation. Journal of Applied Physiology 2003; 95:348-356.
21. Pillow JJ. High-frequency oscillatory ventilation: Mechanisms of gas exchange and lung mechanics. Critical Care Medicine 2005; 33:S135-S141
22. Green AS. Modelling of peak-flow wall shear stress in major airways of the lung. Journal of Biomechanics 2004; 37:661-667.
23. Mach WJ, Thimmesch AR, Pierce JT, Pierce JD. Consequences of hyperoxia and the toxicity of oxygen in the lung. Nursing Research and Practice 2011; 2011.
24. Brewis RAL. Oxygen toxicity during artificial ventilation. Thorax 1969; 24:656-666.
25. Chang WC, "Clinical application of mechanical ventilation ". 3rd ed. 2006: Thomson.
26. Krishnan JA, Brower RG. High-frequency ventilation for acute lung injury and ards*. CHEST Journal 2000; 118:795-807.
27. Jaeger MJ. High-frequency ventilation in dogs with three gases of different densities. Journal of Applied Physiology 1991; 70:2188-2192.
28. Chang HK. Mechanisms of gas transport during ventilation by high-frequency oscillation. Journal of applied physiology: respiratory, environmental and exercise physiology 1984; 56:553-63.
29. Pillow J. High-frequency oscillatory ventilation: Mechanisms of gas exchange and lung mechanics. Critical Care Medicine 2005; 33:S135-S141.
30. Hamel D, I. C. High - frequency oscillatory ventilation - a clinical approach. . Southern African Journal of Critical Car 2005; 21.
31. Fujioka H, Oka K, Tanishita K. Oscillatory flow and gas transport through a symmetrical bifurcation. Journal of biomechanical engineering 2001; 123:145-153.
32. Chang HK. Mechanisms of gas transport during ventilation by high-frequency oscillation. Journal of Applied Physiology 1984; 56:553-563.
33. *Mechanisms of gas exchange during hfov*. available from http://www.nursingconsult.com/nursing/books/978-0-7216-0397-1/full-image?eid=4-u1.0-B978-0-7216-0397-1..50019-4..gr1&isbn=978-0-7216-0397-1.
34. Kleinstreuer C, Zhang Z. Airflow and particle transport in the human respiratory system. Annual Review of Fluid Mechanics 2010; 42:301-334.

35. Gibson B. Long-term ventilation for patients with duchenne muscular dystrophy: Physicians' beliefs and practices. Chest 2001; 119:940-946.
36. Dhand R, Tobin MJ. Inhaled bronchodilator therapy in mechanically ventilated patients. American Journal of Respiratory and Critical Care Medicine 1997; 156:3-10.
37. Ari A, Fink JB. Factors affecting bronchodilator delivery in mechanically ventilated adults. Nursing in Critical Care 2010; 15:192-203.
38. JS Patil, S Sarasija. Pulmonary drug delivery strategies: A concise, systematic review. Lung India 2012; 29:44-49.
39. Jiyuan T, Inthavong K, Ahmadi G, "Computational fluid and particle dynamics in the human respiratory system". 2013, New Yourk: Springer.
40. C. Guerin, Fassier T, Bayle F, Lemasson S, Richard J. Inhaled bronchodilator administration during mechanical ventilation: How to optimize it, and for which clinical benefit? Aerosol Medicine and Pulmonary Drug Delivery 2008; 21 85-96.
41. Dhand R. Aerosol delivery during mechanical ventilation: From basic techniques to new devices. Journal of Aerosol Medicine and Pulmonary Drug Delivery 2008; 21:45-60.
42. Garner SS, Wiest DB, Bradley JW. Albuterol delivery by metered-dose inhaler in a pediatric high-frequency oscillatory ventilation model. Critical Care Medicine 2000; 28:2086-2089.
43. Singh J, Mehta S, Kacmarek R. Pro/con clinical debate: Is high-frequency oscillatory ventilation useful in the management of adult patients with respiratory failure? Critical Care 2002; 6:183 - 185.
44. Fessler HE, Hess DR. Does high-frequency ventilation offer benefits over conventional ventilation in adult patients with acute respiratory distress syndrome? Respiratory Care 2007; 52:595-608.
45. Hatcher D, Watanabe H, Ashbury T, Vincent S, Fisher J, Froese A. Mechanical performance of clinically available, neonatal, high-frequency, oscillatory-type ventilators. Critical Care Medicine 1998; 26:1081-1088.
46. Yin Y, Choi J, Hoffman EA, Tawhai MH, Lin C-L. Simulation of pulmonary air flow with a subject-specific boundary condition. Journal of Biomechanics 2010; 43:2159-2163.
47. Choi J, Xia G, Tawhai M, Hoffman E, Lin C-L. Numerical study of high-frequency oscillatory air flow and convective mixing in a ct-based human airway model. Annals of Biomedical Engineering 2010; 38:3550-3571.
48. Nagels MA, Carter JE. Large eddy simulation of high frequency oscillating flow in an asymmetric branching airway model. Medical Engineering and Physics 2009; 31:1148-1153.
49. James B. Fink, Paul Barraza, JamesBisgaard, Aerosol delivery during mechanical ventilation with high frequency oscillation: An in vitro evaluation, in American College of Chest Physicians Annual Meeting (ACCP) 2001.
50. Sood BG, Shen Y, Latif Z, Galli B, Dawe EJ, Haacke EM. Effective aerosol delivery during high-frequency ventilation in neonatal pigs. Respirology 2010; 15:551-555.

51. Horsfield K. Models of the human bronchial tree. Journal of Applied Physilology 1971; 31:207-217.
52. Dreyfuss D, Saumon G. From ventilator-induced lung injury to multiple organ dysfunction? Intensive Care Medicine 1998; 24:102-104.
53. Kleinstreuer C, Zhang Z, Donohue JF. Targeted drug-aerosol delivery in the human respiratory system. Annual Review of Biomedical Engineering 2008; 10:195-220.
54. *Respiratory tract* available from http://www.medical-exam-essentials.com/respiratory-system-diagram.html.
55. Browner B, Pollak A, Gupton C, "Emergency care and transportation of the sick and injured". 8 ed. 2002: Jones and Bartlett Publishers.
56. Divatia J, Bhowmick K, "Complications of endotracheal intubation and other airway management procedures". Vol. 49. 2005. 308-308.
57. Divatia J, Khan P, Myatra S, "Tracheal intubation in the icu: Life saving or life threatening?". Vol. 55. 2011. 470-475.
58. Mirkovic I, Matic I, Sakic-Zdravcevic K, Jurjevic M, Majeric-Kogler V, Hrgovic Z, "Comparison of invasive and noninvasive mechanical ventilation for patients with copd:Randomised prospective study". Vol. 52. 2008. 419-419.
59. Weibel ER, "Morphometry of the human lung". 1963, New York, NY: Academic.
60. *Tracheobronchial tree and its division*. available from http://www.nursingconsult.com/nursing/books/978-0-7216-0397-1/full-image?eid=4-u1.0-B978-0-7216-0397-1..50008-X..gr6&isbn=978-0-7216-0397-1.
61. Kleinstreuer C, Zhang Z, Li Z, Roberts WL, Rojas C. A new methodology for targeting drug-aerosols in the human respiratory system. International Journal of Heat and Mass Transfer 2008; 51:5578-5589.
62. Levitzky MG, "Pulmonary physiology". 2003: McGraw-Hill Proefessional. 278.
63. Knight DA, Holgate ST. The airway epithelium: Structural and functional properties in health and disease. Respirology 2003; 8:432-446.
64. Crystal RG, Randell SH, Engelhardt JF, Voynow J, Sunday ME. Airway epithelial cells. Proceedings of the American Thoracic Society 2008; 5:772-777.
65. Kim KC, Nassiri J, Brody JS. Mechanisms of airway goblet cell mucin release: Studies with cultured tracheal surface epithelial cells. American Journal of Respiratory Cell and Molecular Biology 1989; 1:137-143.
66. Vareille M, Kieninger E, Edwards MR, Regamey N. The airway epithelium: Soldier in the fight against respiratory viruses. Clinical Microbiology Reviews 2011; 24:210-229.
67. Soleas JP, Paz A, Marcus P, McGuigan A, Waddell TK. Engineering airway epithelium. Journal of Biomedicine and Biotechnology 2012; 2012:10.
68. Tam A, Wadsworth S, Dorscheid D, Man SF, DD S. The airway epithelium: More than just a structural barrier. Therapeutic Advances in Respiratory Disease 2011; 5: 255–273
69. Grotberg JB. Respiratory fluid mechanics and transport processes. Annual Review of Biomedical Engineering 2001; 3:421-457.

70. Grotberg JB. Pulmonary flow and transport phenomena. Annual Review of Fluid Mechanics 1994; 26:529-571.
71. Otis DR, Johnson M, Pedley TJ, Kamm RD. Role of pulmonary surfactant in airway closure: A computational study. Journal of Applied PhysiologyPublished 1993; 75:1323-1333.
72. Christopher M. Evans, Kyubo Kim, Michael J. Tuvim, Dickey BF. Mucus hypersecretion in asthma: Causes and effects. Curr Opin Pulm Med 2009; 15:4-11.
73. Hickey AJ, "Inhalation aerosols: Physical and biological basis for therapy". Vol. 94. 1996, New York, NY: Marcel Dekker.
74. Esteban A, Anzueto A, AlÍA I, Gordo F, ApeztéguÍA C, PÁLizas F, et al. How is mechanical ventilation employed in the intensive care unit? American Journal of Respiratory and Critical Care Medicine 2000; 161:1450-1458.
75. Cherng C-H, Wong C-S, Hsu C-H, Ho S-T. Airway length in adults: Estimation of the optimal endotracheal tube length for orotracheal intubation. Journal of Clinical Anesthesia 2002; 14:271-274.
76. Honeybourne D, Costello JC, Barham C. Tracheal damage after endotracheal intubation: Comparison of two types of endotracheal tubes. Thorax 1982; 37:500-502.
77. Varshney M, Sharma K, Kumar R, PG. V. Appropriate depth of placement of oral endotracheal tube and its possible determinants in indian adult patients. Indian J Anaesth. 2011; 55:488-493.
78. Bauer K, Brucker C. The role of ventilation frequency in airway reopening. Journal of Biomechanics 2009; 42:1108-1113.
79. Daniel F, W. Claus. Numerical simulation of the high–frequency oscillatory ventilation in generic models of the human airways. in 7th International Symposium on Turbulence and Shear Flwo Phenomena (TSFP-7). 2011. Ottawa, Canada
80. Straus C, Louis B, Isabey D, Lemaire F, Harf A, Brochard L. Contribution of the endotracheal tube and the upper airway to breathing workload. American Journal of Respiratory and Critical Care Medicine 1998; 157:23-30.
81. Wilson AJ, Murphy CM, Brook BS, Breen D, Miles AW, Tilley DG. A computer model of the artificially ventilated human respiratory system in adult intensive care. Medical Engineering and Physics 2009; 31:1118-1133.
82. Al-Majed SI, Thompson JE, Watson KF, Randolph AG. Effect of lung compliance and endotracheal tube leakage on measurement of tidal volume. Critical Care Medicine 2009; 8:398-402.
83. Fontan JJP, Heldt GP, Gregory GA. Resistance and inertia of endotracheal tubes used in infants durring periodic flow. Critical Care Medicine 1985; 13:1052-1055.
84. Comer JK, Kleinstreuer C, Kim CS. Flow structures and particle deposition patterns in double-bifurcation airway models. Part 2. Aerosol transport and deposition. Journal of Fluid Mechanics 2001; 435:55-80.
85. Comer JK, Kleinstreuer C, Zhang Z. Flow structures and particle deposition patterns in double-bifurcation airway models. Part 1. Air flow fields. Journal of Fluid Mechanics 2001; 435:25-54.

86. Zhang H, Papadakis G. Computational analysis of flow structure and particle deposition in a single asthmatic human airway bifurcation. Journal of Biomechanics 2010; 43:2453-2459.
87. Lieber B, Zhao Y. Oscillatory flow in a symmetric bifurcation airway model. Annals of Biomedical Engineering 1998; 26:821-830.
88. Zhao Y, Lieber B. Steady inspiratory flow in a model symmetric bifurcation. J Biomech Eng. 1994; 116:488-496.
89. Luo XY, Hinton JS, Liew TT, Tan KK. Les modelling of flow in a simple airway model. Medical Engineering & Physics 2004; 26:403-413.
90. Martonen T, Guan X, Schreck R. Fluid dynamics in airway bifurcations: I. Primary flows. Inhalation Toxicology 2001; 13:261-279.
91. Martonen TB. Effects of tumors on inhaled pharmacologic drugs. Ii. Particle motion. Cell Biochemistry and Biophysics 2001; 35:245-253.
92. Gefen Amit, "Patient-specific modeling in tomorrow's medicine ". Studies in mechanobiology, tissue engineering and biomaterial. Vol. 9. 2012: Springer. 529.
93. Choi J, Tawhai MH, Hoffman EA, Lin C-L. On intra- and intersubject variabilities of airflow in human lungs. Physics of Fluids 2009; 21:101901: 1-17.
94. Inthavong K, Choi LT, Tu J, Ding S, Thien F. Micron particle deposition in a tracheobronchial airway model under different breathing conditions. Medical Engineering and Physics 2010; 32:1198-1212.
95. Xi J, Longest PW, Martonen TB. Effects of the laryngeal jet on nano- and microparticle transport and deposition in an approximate model of the upper tracheobronchial airways. Journal of Applied Physiology 2008; 104:1761-1777.
96. Luo HY, Liu Y. Particle deposition in a ct-scanned human lung airway. Journal of Biomechanics 2009; 42:1869-1876.
97. De Backer JW, Vos WG, Gorle CD, Germonpre P, Partoens B, Wuyts FL, et al. Flow analyses in the lower airways: Patient-specific model and boundary conditions. Medical Engineering and Physics 2008; 30:872-879.
98. Heraty K, Laffey J, Quinlan N. Fluid dynamics of gas exchange in high-frequency oscillatory ventilation: In vitro investigations in idealized and anatomically realistic airway bifurcation models. Annals of Biomedical Engineering 2008; 36:1856-1869.
99. Collins TP, Tabor GR, Young PG. A computational fluid dynamics study of inspiratory flow in orotracheal geometries. Medical & Biological Engineering & Computing 2007; 45:829-836.
100. Inagaki G, Tanaka G, Hishida M, Haneishi H, Hu X. Numerical simulation of oscillatory flow in realistic model human airways. Journal of Fluid Science and Technology 2009; 4:602-613.
101. Ulzheimer S, Flohr T. "Multislice ct: Current technology and future developments. in Multislice ct", M.F. Reiser, et al., Editors. 2009, Springer Berlin Heidelberg. p. 3-23.
102. Mešanović N, Grgić M, Huseinagić H, Maleš M, Skejić E, Smajlović M. Automatic ct image segmentation of the lungs with region growing algorithm. in 18th International Conference on Systems, Signals and Image Processing, IWSSIP 2011. 2011. Sarajevo, Bosna i Hercegovina.

103. Drummond GB. Computed tomography and pulmonary measurements British Journal of Anaesthesia 1998; 80 665-671.
104. Paolo P, Marcelo GdA. Lung ct scan. The Open Nuclear Medicine Journal 2010; 2:86-98.
105. Brown S, Bailey D, Baldock C. Relationship between ct hounsfield units and linear attenuation coefficients for a number of single photon-emitting radionuclides. J NUCL MED MEETING ABSTRACTS 2006; 47:381P-b-.
106. Hu S, Hoffman EA, Reinhardt JM. Automatic lung segmentation for accurate quantitation of volumetric x-ray ct images. Medical Imaging, IEEE Transactions on 2001; 20:490-498.
107. De Backer JW, Vos WG, Vinchurkar SC, Claes R, Drollmann A, Wulfrank D, et al. Validation of computational fluid dynamics in ct-based airway models with spect/ct. Radiology 2010; 257:854-862.
108. Yim Y, Hong H. "Smoothing segmented lung boundary in chest ct images using scan line search progress in pattern recognition, image analysis and applications. J. Martínez-Trinidad, J. Carrasco Ochoa, and J. Kittler, Editors. 2006, Springer Berlin / Heidelberg. p. 147-156.
109. Hirahara H, Iwazaki K, Ahmmed MU, Nakamura M. Numerical analysis of air flow in dichotomous respiratory channel with asymmetric compliance under hfov condition. Journal of Fluid Science and Technology 2011; 6:932-948.
110. Inthavong K, Tu J, Young Y, Ding S, Subic A, Thien F. Effects of airway obstruction induced by asthma attack on particle deposition. Journal of Aerosol Science 2010; 41:587-601.
111. Adler K, Brucker C. Dynamic flow in a realistic model of the upper human lung airways. Experiments in Fluids 2007; 43:411-423.
112. de Jong PA, Long FR, Wong JC, Merkus PJ, Tiddens HA, Hogg JC, et al. Computed tomographic estimation of lung dimensions throughout the growth period. European Respiratory Journal 2006; 27:261-267.
113. Longest PW, Vinchurkar SC. Effects of mesh style and grid convergence on particle deposition in bifurcating airway models with comparisons to experimental data. Medical Engineering and Physics 2007; 29:350-366.
114. Vinchurkar SC, Longest PW. Evaluation of hexahedral, prismatic and hybrid mesh styles for simulating respiratory aerosol dynamics. Computers and Fluids 2008; 37:317-331.
115. Lin C-L, Tawhai MH, McLennan G, Hoffman EA. Characteristics of the turbulent laryngeal jet and its effect on airflow in the human intra-thoracic airways. Respiratory Physiology & Neurobiology 2007; 157:295-309.
116. Farkas A, Balashazy I. Simulation of the effect of local obstructions and blockage on airflow and aerosol deposition in central human airways. Journal of Aerosol Science 2007; 38:865-884.
117. Gemci T, Ponyavin V, Chen Y, Chen H, Collins R. Computational model of airflow in upper 17 generations of human respiratory tract. Journal of Biomechanics 2008; 41:2047-2054.

118. Xia G, Tawhai MH, Hoffman EA, Lin C-L. Airway wall stiffening increases peak wall shear stress: A fluid–structure interaction study in rigid and compliant airways. Annals of Biomedical Engineering 2010; 38:1836-1853.
119. Lambert AR, O'Shaughnessy P, Tawhai MH, Hoffman EA, Lin C-L. Regional deposition of particles in an image-based airway model: Large-eddy simulation and left-right lung ventilation asymmetry. Aerosol Science & Technology 2011; 45:11-25.
120. Katz I, Pichelin M, Montesantos S, Majoral C, Martin A, Conway J, et al. Using helium-oxygen to improve regional deposition of inhaled particles: Mechanical principles. Journal of Aerosol Medicine and Pulmonary Drug Delivery 2014; 27:71-80.
121. Xi J, Longest PW. Effects of oral airway geometry characteristics on the diffusional deposition of inhaled nanoparticles. Journal of Biomechanical Engineering 2008; 130:011008-1-011008-16.
122. Dehbi A. Prediction of extrathoracic aerosol deposition using rans-random walk and les approaches. Aerosol Science and Technology 2011; 45:555-569.
123. Isaacs KK, Schlesinger RB, Martonen TB. Three-dimensional computational fluid dynamics simulations of particle deposition in the tracheobronchial tree. Journal of Aerosol Medicine 2006; 19:344-352.
124. Lin C-L, Tawhai MH, McLennan G, Hoffman EA. Characteristics of the turbulent laryngeal jet and its effect on airflow in the human intra-thoracic airways. Respiratory Physiology and Neurobiology 2007; 57:295-309.
125. Xi J, Longest PW, Martonen TB. Effects of the laryngeal jet on nano- and microparticle transport and deposition in an approximate model of the upper tracheobronchial airways. Journal of Applied Physiology 2008; 104:1761-1777.
126. Zhang Z, Kleinstreuer C, Kim CS. Airflow and nanoparticle deposition in a 16-generation tracheobronchial airway model. Annals of Biomedical Engineering 2008; 36:2095-2110.
127. Choi J, Xia G, Tawhai MH, Hoffman EA, Lin C-L. Numerical study of high-frequency oscillatory air flow and convective mixing in a ct-based human airway model. Annals of Biomedical Engineering 2010; 38:3550-3571.
128. "Ansys icem 13.0 documentation". 2010: SAS IP, Inc.
129. Garimella RV, Shephard MS. Boundary layer mesh generation for viscous flow simulations. International Journal for Numerical Methods in Engineering 2000; 49:193-218.
130. Si H. Adaptive tetrahedral mesh generation by constrained delaunay refinement. International Journal for Numerical Methods in Engineering 2008; 75:856-880.
131. Anderson JD, "Computational fluid dynamics: The basics with applications". 1995: McGraw-Hill.
132. Versteeg HK, Malalasekera W, "An introduction to computational fluid dynamics the finite volume method". second edition ed. 2007: Pearson.
133. Fletcher CAJ, " Computational techniques for fluid dynamics". second edition ed. Vol. 1. 1991: Springer.
134. Frank MW, "Fluid mechanichs". 2003: Mc-Graw Hill.

135. Winter DC, Nerem RM. Turbulence in pulsatile flows. Annals of Biomedical Engineering 1984; 12:357-369.
136. Eckmann DM, Grotberg JB. Experiments on transition to turbulence in oscillatory pipe flow. Journal of Fluid Mechanics 1991; 222:329-350.
137. Wilcox D, "Turbulence modeling for cfd". 2008, La Canada, CA: DCW Industries.
138. Piomelli U. Large-eddy simulation: Achievements and challenges. Progress in Aerospace Sciences 1999; 35:335-362.
139. Pope S. B., "Turbulent flows". 2001: Cambridge University Press.
140. Sagaut P, "Large eddy simulation for incompressible flows". 2005, Heidelberg, Germany: Springer.
141. Wang Q, Squires KD. Large eddy simulation of particle deposition in a vertical turbulent channel flow. International Journal of Multiphase Flow 1996; 22:667-683.
142. Armenio V, Piomelli U, Fiorotto V. Effect of the subgrid scales on particle motion. Physics of Fluids 1999; 11:3030-3042.
143. Smagorinsky J. General circulation experiments with the primitive equations. Monthly Weather Review 1963; 91:99-164.
144. Ma J, Wang F, Tang X. "Comparison of several subgrid-scale models for large-eddy simulation of turbulent flows in water turbine. in Fluid machinery and fluid mechanics", J. Xu, et al., Editors. 2009, Springer Berlin Heidelberg. p. 328-334.
145. Baya Toda H, Cabrit O, Balarac G, Bose S, Lee J, Choi H, et al., A subgrid-scale model based on singular values for les in complex geometries, in Center for Turbulence Research Proceedings of the 2010 Summer 2010: Stanford, CA
146. Germano M, Piomelli U, Moin P, Cabot WH. A dynamic subgrid-scale eddy viscosity model. Physics of Fluids A: Fluid Dynamics (1989-1993) 1991; 3:1760-1765.
147. Nicoud F, Ducros F. Subgrid-scale stress modelling based on the square of the velocity gradient tensor. Flow, Turbulence and Combustion 1999; 62:183-200.
148. Vreman AW. An eddy-viscosity subgrid-scale model for turbulent shear flow: Algebraic theory and applications. Physics of Fluids (1994-present) 2004; 16:3670-3681.
149. Li Z, Kleinstreuer C, Zhang Z. Simulation of airflow fields and microparticle deposition in realistic human lung airway models. Part i: Airflow patterns. European Journal of Mechanics - B/Fluids 2007; 26:632-649.
150. Zhang Z, Kleinstreuer C. Transient airflow structures and particle transport in a sequentially branching lung airway model. Physics of Fluids (1994-present) 2002; 14:862-880.
151. Zhang H, Papadakis G. Computational analysis of flow structure and particle deposition in a single asthmatic human airway bifurcation. Journal of Biomechanics 2010; 43:2453-2459.
152. Lieber BB, Zhao Y. Oscillatory flow in a symmetric bifurcation airway model. Annals of Biomedical Engineering 1998; 26:821-830.

153. Mireles-Cabodevila E, Diaz-Guzman E, Heresi GA, Chatburn RL. Alternative modes of mechanical ventilation: A review for the hospitalist. Cleveland Clinic journal of medicine 2009; 76:417-30.
154. Tanaka G, Ogata T, Oka K, Tanishita K. Spatial and temporal variation of secondary flow during oscillatory flow in model human central airways. Journal of biomechanical engineering 1999; 121:565-573.
155. van Ertbruggen C, Hirsch C, Paiva M. Anatomically based three-dimensional model of airways to simulate flow and particle transport using computational fluid dynamics. Journal of Applied Physilology 2005; 98:970-980.
156. Tanaka G, Hatori A, Takano R. Spatial and temporal variation of turbulence during oscillatory flow in realistic model human airways. Journal of Fluid Science and Technology 2012; 7:53-63.
157. Lucangelo U, Bernabè F, Blanch L. Lung mechanics at the bedside: Make it simple. Current Opinion in Critical Care 2007; 13:64-72 10.1097/MCC.0b013e32801162df.
158. Le Rolle V, Samson N, Praud J-P, Hernández A. Mathematical modeling of respiratory system mechanics in the newborn lamb. Acta Biotheoretica 2013; 61:91-107.
159. Grimby G, Takishima T, Graham W, Macklem P, Mead J. Frequency dependence of flow resistance in patients with obstructive lung disease. The Journal of clinical investigation 1968; 47:1455-65.
160. Nikischin W, Gerhardt T, Everett R, Bancalari E. A new method to analyze lung compliance when pressure–volume relationship is nonlinear. American Journal of Respiratory and Critical Care Medicine 1998; 158:1052-1060.
161. Jiang J, Zhao K. Airflow and nanoparticle deposition in rat nose under various breathing and sniffing conditions—a computational evaluation of the unsteady and turbulent effect. Journal of Aerosol Science 2010; 41:1030-1043.
162. Mackley MR, Neves Saraiva RMC. The quantitative description of fluid mixing using lagrangian- and concentration-based numerical approaches. Chemical Engineering Science 1999; 54:159-170.
163. Lee JS. The mixing and axial transport of smoke in oscillatory tube flows. Annals of Biomedical Engineering 1984; 12:371-383.
164. Ultman J. Gas mixing in the pulmonary airways. Annals of Biomedical Engineering 1981; 9:513-527.
165. Dean WR, Hurst JM. Note on the motion of fluid in a curved pipe. Mathematika 1959; 6:77-85.
166. Alzahrany M, Banerjee A, Salzman G. Flow transport and gas mixing during invasive high frequency oscillatory ventilation. Medical Engineering & Physics 2014; 36:647 - 658.
167. Nicoud F, Ducros F. Subgrid-scale stress modelling based on the square of the velocity gradient tensor. Flow, Turbulence, and Combustion 1999; 62:183-200.
168. Otis AB, McKerrow CB, Bartlett RA, Mead J, McIlroy MB, Selverstone NJ, et al. Mechanical factors in distribution of pulmonary ventilation. Journal of Applied Physiology 1956; 8:427-443.

169. Elad D, Shochat A, Shiner RJ. Computational model of oscillatory airflow in a bronchial bifurcation. Respiration Physiology 1998; 112:95-111.
170. Barbini P, Brighenti C, Cevenini G, Gnudi G. A dynamic morphometric model of the normal lung for studying expiratory flow limitation in mechanical ventilation. Annals of Biomedical Engineering 2005; 33:518-530.
171. High KC, Ultman JS, Karl SR. Mechanically induced pendelluft flow in a model airway bifurcation during high frequency oscillation. Journal of biomechanical engineering 1991; 113:342-347.
172. Grimby G, Takishima T, Graham W, Macklem P, Mead J. Frequency dependence of flow resistance in patients with obstructive lung disease. Journal of clinical Investigation 1968; 47:1455-1465.
173. Lee WJ, M. Kawahashi, H. Hirahara. Experimental analysis of pendelluft flow generated by hfov in a human airway model. Physiological measurement 2006; 27:661-74.
174. Cohen BS, Sussman RG, Lippmann M. Ultrafine particle deposition in a human tracheobronchial cast. Aerosol Science and Technology 1990; 12:1082-1091.
175. Ultman JS, Shaw RG, Fabiano DC, Cooke KA. Pendelluft and mixing in a single bifurcation lung model during high-frequency oscillation. Journal of Applied PhysiologyPublished 1988; 65:146-155.
176. Andrey V, Murphy R. Pendelluft in chronic obstructive lung disease measured with lung sounds. Pulmonary Medicine 2012; 2012:1-6.
177. Miyawaki S, Tawhai M, Hoffman E, Lin C-L. Effect of carrier gas properties on aerosol distribution in a ct-based human airway numerical model. Annals of Biomedical Engineering 2012; 40:1495-1507.
178. Comerford A, Förster C, Wall WA. Structured tree impedance outflow boundary conditions for 3d lung simulations. Journal of Biomechanical Engineering 2010; 132:081002-081002.
179. Guerin C, Thomas Fassier, Bayle F, Lemasson S, Richard J-C. Inhaled bronchodilator administration during mechanical ventilation: How to optimize it, and for which clinical benefit? Journal of Aerosol Medicine and Pulmonary Drug Delivery 2008; 21:85-96.
180. Singh J, Mehta S, Kacmarek R. Pro/con clinical debate: Is high-frequency oscillatory ventilation useful in the management of adult patients with respiratory failure? Critical Care 2002; 6:1-3.
181. Cheifetz IM, MacIntyre NR. Respiratory controversies in the critical care setting. Respiratory Care 2007; 52:636-644.
182. Hofmann W. Modelling inhaled particle deposition in the human lung—a review. Journal of Aerosol Science 2011; 42:693-724.
183. Makris E, Pilou M, Neofytou P, Tsangaris S, Housiadas C. Particle transport and deposition under high-frequency oscillatory ventilation and normal breathing. Aerosol Science and Technology 2013; 48:150-162.
184. Alzahrany M, Banerjee A, Salzman G. The role of coupled resistance-compliance in upper tracheobronchial airways under high frequency oscillatory ventilation Medical Engineering & Physics 2014; Accepted.
185. "Ansys cfx 13.0 solver theory guide". 2010: ANSYS INC.

186. Finlay W, "The mechanics of inhaled pharmaceutical aerosols. ". 2001: Academic Press.
187. Brouns M, Numerical and experimental study of flows and deposition of aerosols in the upper human airways., in Department of Mechanical Engineering. 2007, Vrije Universiteit Brussel: Belgium. p. 1-172.
188. Vivek A, Khairy E, Chris L, Sylvia V, Numerical study of particle deposition in the human upper airways with emphasis on hot spot formation and comparison of les and rans models, in V European Conference on Computational Fluid Dynamics ECCOMAS CFD, J.C.F.P.a.A. Sequeira, Editor. 2010: Lisbon, Portugal.
189. Wang Q, Squires D, Chen M, Mclaughlin B. On the role of the left force in turbulence simulations of particle deposition. International Journal of Multiphase Flow 1997; 23:749-763.
190. Narayanan C, Lakehal D, Botto L, Soldati A. Mechanisms of particle deposition in a fully developed turbulent open channel flow. Physics of Fluids (1994-present) 2003; 15:763-775.
191. Zheng L, Kleinstreuer C, Zhang Z. Simulation of airflow fields and microparticle deposition in realistic human lung airway models. Part ii: Particle transport and deposition. European Journal of Mechanics B/Fluids 2007; 26:650-668.
192. Li Z, Kleinstreuer C, Zhang Z. Particle deposition in the human tracheobronchial airways due to transient inspiratory flow patterns. Journal of Aerosol Science 2007; 38:625-644.
193. Li Z. Particle deposition in oral-tracheal airway models with very low inhalation profiles. Journal of Bionic Engineering 2012; 9:252-261.
194. Luo HY, Liu Y, Yang XL. Particle deposition in obstructed airways. Journal of Biomechanics 2007; 40:3096-3104.
195. Morsi SA, Alexander AJ. An investigation of particle trajectories in two-phase flow systems. Journal of Fluid Mechanics 1972; 55:193-208.
196. Crowe CT, "Multiphase flow handbook". illustrated ed, ed. C.T. Crowe. 2006: CRC Press. 1156.
197. Longest PW, Kleinstreuer C, Buchanan JR. Efficient computation of micro-particle dynamics including wall effects. Computers & Fluids 2004; 33:577-601.
198. Cherukat P, McLaughlin JB. The inertial lift on a rigid sphere in a linear shear flow field near a flat wall. Journal of Fluid Mechanics 1994; 263:1-18.
199. Li A, Ahmadi G. Dispersion and deposition of spherical particles from point sources in a turbulent channel flow. Aerosol Science & Technology 1992; 16:209-226.
200. Zhang Z, Kleinstreuer C, Kim C.S. Gas–solid two-phase flow in a triple bifurcation lung airway model. International Journal of Multiphase Flow 2002; 28:1021-1046.
201. Kim CS, Garcia L. Particle deposition in cyclic bifurcating tube flow. Aerosol Science and Technology 1991; 14:302-315.
202. Kim CS, Iglesias AJ. Deposition of inhaled particles in bifurcating airway models: I. Inspiratory deposition. Journal of Aerosol Medicine 1989; 2:1-14.

203. Longest PW, Tian G, Walenga R, Hindle M. Comparing mdi and dpi aerosol deposition using in vitro experiments and a new stochastic individual path (sip) model of the conducting airways. Pharmaceutical Research 2012; 29:1670-1688.
204. Zhang Z, Kleinstreuer C, Donohue JF, Kim CS. Comparison of micro- and nano-size particle depositions in a human upper airway model. Journal of Aerosol Science 2005; 36:211-233.
205. Walters DK, Luke WH. Computational fluid dynamics simulations of particle deposition in large-scale, multigenerational lung models. Journal of Biomechanical Engineering 2010; 133:011003-011003.
206. Balashazy I, Hofmann W, T. H. Computation of local enhancement factors for the quantification of particle deposition patterens in airway bifurcations. Journal of Aerosol Science 1999; 30:185-203.
207. Schroter RC, Sudlow MF. Flow patterns in models of the human bronchial airways. Respiration Physiology 1969; 7:341-355.
208. Fink JB, Barraza P, Bisgaard J. Aerosol delivery during mechanical ventilation with high frequency oscillation: An in vitro evaluation. Chest 2001; 120:277S.
209. Longest PW, Azimi M, Golshahi L, Hindle M. Improving aerosol drug delivery during invasive mechanical ventilation with redesigned components. Respiratory Care 2013.
210. Jin HH, Fan JR, Zeng MJ, Cen KF. Large eddy simulation of inhaled particle deposition within the human upper respiratory tract. Journal of Aerosol Science 2007; 38:257-268.
211. Zhang Y, Finlay WH. Measurement of the effect of cartilaginous rings on particle deposition in a proximal lung bifurcation model. Aerosol Science and Technology 2005; 39:394-399.
212. Waleed A, Comparison of albuterol delivery between high frequency oscillatory ventilation and conventional mechanical ventilation in a simulated adult lung model using different compliance levels, in Department of Respiratory Therapy. 2010, Georgia State University: Atlanta. p. 44.
213. Balásházy I, Hofmann W, Heistracher T. Local particle deposition patterns may play a key role in the development of lung cancer. Journal of Applied Physiology 2003; 94:1719-1725.
214. Sbirlea-Apiou G, Lemaire M, Katz I, Conway J, Fleming J, Martonen T. Simulation of the regional manifestation of asthma. Journal of Pharmaceutical Sciences 2004; 93:1205-1216.
215. Gainnier M, Forel J-M. Clinical review: Use of helium-oxygen in critically ill patients. Critical Care 2006; 10:241.
216. Peterson JB, Prisk GK, Darquenne C. Aerosol deposition in the human lung periphery is increased by reduced-density gas breathing. Journal of Aerosol Medicine and Pulmonary Drug Delivery 2008; 21:159-168.
217. Orsini AJ, Stefano JL, Leef KH, Jasani M, Ginn A, Tice L, et al. Heliox improves pulmonary mechanics in a pediatric porcine model of induced severe bronchospasm and independent lung mechanical ventilation. Critical Care 1999; 3:65 - 70.

218. Kim IK, Saville AL, Sikes KL, Corcoran TE. Heliox-driven albuterol nebulization for asthma exacerbations: An overview. Respiratory Care 2006; 51:613-618.
219. Corcoran TE, Gamard S. Development of aerosol drug delivery with helium oxygen gas mixtures. Journal of Aerosol Medicine 2004; 17:299-309.
220. Sandeau J, Katz I, Fodil R, Louis B, Apiou-Sbirlea G, Caillibotte G, et al. Cfd simulation of particle deposition in a reconstructed human oral extrathoracic airway for air and helium–oxygen mixtures. Journal of Aerosol Science 2010; 41:281-294.
221. Ari A, Harwood R, Sheard M, Dailey P, Fink JB. In vitro comparison of heliox and oxygen in aerosol delivery using pediatric high flow nasal cannula. Pediatric Pulmonology 2011; 46:795-801.
222. Alzahrany M, Banerjee A. Aerosolized drug delivery in specific-patient lung model during invasive high frequency oscillatory ventilation. Journal of Aerosol Science 2014; submitted.
223. Katz A, Gentile M, Craig D, Quick G, Meliones J, Cheifetz I. Heliox improves gas exchange during high-frequency ventilation in a pediatric model of acute lung injury. American Journal of Respiratory and Critical Care Medicine 2001; 164:260-264.
224. Zeynalov B, Hiroma T, Nakamura T. Effects of heliox as carrier gas on ventilation and oxygenation in an animal model of piston-type hfov: A crossover experimental study. BioMedical Engineering OnLine 2010; 9:1-5.
225. Jan DL, Shapiro AH, Kamm RD. Some features of oscillatory flow in a model bifurcation. Journal of Applied Physiology 1989; 67:147-159.
226. Tanaka G, Oka K, Tanishita K. Secondary flow augmentation during intermittent oscillatory flow in model human central airways. JSME International Journal Series C Mechanical Systems, Machine Elements and Manufacturing 2001; 44:1041-1050.
227. Soodt T, Pott D, Klaas M, Schröder W. Analysis of basic flow regimes in a human airway model by stereo-scanning piv. Experiments in Fluids 2013; 54:1-10.
228. Nerem RM, Seed WA, Wood NB. An experimental study of the velocity distribution and transition to turbulence in the aorta. Journal of Fluid Mechanics 1972; 52:137-160.
229. Diehl J-L, Peigne V, Guerot E, Faisy C, Lecourt L, Mercat A. Helium in the adult critical care setting. Annals of Intensive Care 2011; 1:24.
230. Briant JK, Lippmann M. Particle transport through a hollow canine airway cast by high-frequency oscillatory ventilation. Experimental Lung Research 1992; 18:385-407.
231. Goode ML, Fink JB, Dhand R, Tobin MJ. Improvement in aerosol delivery with helium–oxygen mixtures during mechanical ventilation. American Journal of Respiratory and Critical Care Medicine 2001; 163:109-114.
232. Ghahramani E, Abouali O, Emdad H, Ahmadi G. Numerical analysis of stochastic dispersion of micro-particles in turbulent flows in a realistic model of human nasal/upper airway. Journal of Aerosol Science 2014; 67:188-206.

233. Kim W. Lung mucus: A clinician's view. European Respiratory Journal 1997; 10:1914-1917.
234. Benjamin M, Christian F, Dominique P, Jacques M, Patrice F. Toward the modeling of mucus draining from the human lung: Role of the geometry of the airway tree. Physical Biology 2011; 8:056006.
235. Evrensel CA, Krumpe PE, Khan MRU, Elli S. Viscous airflow through a rigid tube with a compliant lining: A simple model for the air-mucus interaction in pulmonary airways. Journal of Biomechanical Engineering 1993; 115:262-270.
236. Labiris NR, Dolovich MB. Pulmonary drug delivery. Part i: Physiological factors affecting therapeutic effectiveness of aerosolized medications. British Journal of Clinical Pharmacology 2003; 56:588-599.
237. Longest PW, Xi J. Condenstional growth may contribute to the enhanced deposition of cigarette smoke particles in upper respiratory tract. Aerosol Science & Technology 2008; 38:111-130.
238. Longest PW, Golshahi L, Hindle M. Improving pharmaceutical aerosol delivery during noninvasive ventilation: Effects of streamlined components. Annals of Biomedical Engineering 2013; 41:1217-1232.

APPENDIX A

FINAL CT-SCAN BASED MODEL

Table A.1 and A.2 present detailed descriptions of the model outlets' dimensions, generation, and the anatomical parts the outlet belongs to. The outlet numbers provided in Table A.1 and A.2 correspond to the labels shown in Figure 2.17 in chapter 2. The generation in the table represents the location of the outlet inside the tracheobronchial tree, with a higher generation number indicating a deeper site. The diameter of the airway is based on the hydraulic diameter defined as:

$$D_h = \frac{4A}{WP} \qquad \text{(A.1)}$$

Where A is the cross-sectional area and WP is the wetted perimeter of a plane cut perpendicular to the centerline of the airway.

Table A.1 Detailed description of the model outlets in left lung.

Anatomical part	Outlet No.	Generation	Diameter (mm)
Trachea	-	G0	14.82
LUL: Anterior	1	G5	2.01
	2	G5	2.3
	3	G5	2.2
	4	G5	2.98
LUL: Posterior	5	G6	2.65
	6	G6	1.96
	7	G6	1.52
	8	G6	2.74
LUL: Lingula-Superior	9	G4	1.68
	10	G4	2.05
LUL: Lingula-Inferior	11	G4	2.42
	12	G4	2.27
LLL: Superior	13	G4	1.27
	14	G4	1.16
	15	G4	2.34
LLL: Posterior basal	16	G6	2.85
	17	G6	2.37
	18	G6	2.28
	19	G6	3.2
LLL: Anterior Basal	20	G7	2.36
	21	G7	2.07
	22	G7	2.35
	23	G7	2.35
	24	G7	1.59
	25	G7	1.61
LLL: Lateral basal	26	G6	2.56
	27	G6	2.5

Table A.2 Detailed description of the model outlets in right lung.

Anatomical part	Outlet No.	Generation	Diameter (mm)
RUL: anterior	28	G5	2.35
	29	G5	1.44
RUL: Posterior	30	G6	3.88
	31	G6	3.02
	32	G5	4.7
RUL: Apical	33	G5	2.59
	34	G5	5.01
	35	G4	3.77
	36	G5	2.02
	37	G5	2.72
RML: Lateral	38	G4	1.75
RML: Medial	39	G5	0.97
	40	G5	1.86
RLL: Meddle basal	41	G6	3.09
	42	G7	2.72
	43	G7	2.75
	44	G6	3
	45	G6	1.78
RLL: Posterior basal	46	G6	3.92
	47	G7	2.89
	48	G7	3.25
RLL: Anterior basal	49	G6	2.79
	50	G6	1.85
	51	G6	3.01
RLL: Superior	52	G6	3.12
	53	G6	1.81

APPENDIX B

SINGLE IDEALIZED GEOMETRY CREATION

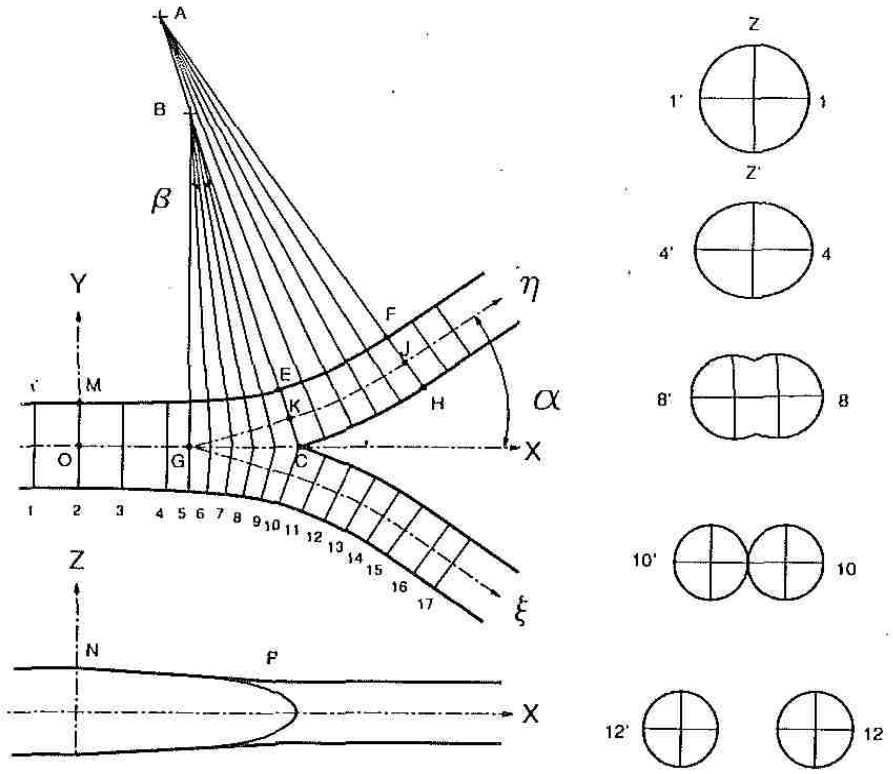

Figure B.1 Cross-sections of the single bifurcation in different directions [88]. Adopted with permission from ASME publishing.

The single bifurcation used for the validation purpose in current dissertation was created following the method by Zhao and Lieber [88]. The equations that define all points, lines and curves in the above illustration are as follows:

Point *A*	$(L-(R+0.5d)\sin\beta,\ (R+0.5d)\cos\beta,\ 0)$	(B.1)
Point *B*	$(L/2,\ L/2\tan\beta,\ 0)$	
Point *C*	$(L,\ 0,\ 0)$	
Point *G*	$(L/2,\ 0,\ 0)$	
Line *ME*	$y=a_1x^2+b_1x^8+0.5D$	(B.2)

$$a_1 = \frac{8d\cos\beta - (L - d\sin\beta)\tan\beta - 4D}{6(L - d\sin\beta)^2} \tag{B.3}$$

$$b_1 = \frac{(L - d\sin\beta)\tan\beta - 2d\cos\beta + 4D}{6(L - d\sin\beta)^8} \tag{B.4}$$

Line *EF* $$y = (R + 0.5D)\cos\beta - \{(R - 0.5d)^2 - (x - L + (R + 0.5d)\sin\beta\}^2 \tag{B.5}$$

Line *GK* $$y = a(x - 0.5L)^{\lambda} \tag{B.6}$$

$$a = \frac{0.5d\cos\beta}{(0.5L - 0.5d\sin\beta)^{\lambda}} \tag{B.7}$$

$$\lambda = \frac{\tan\beta(L - d\sin\beta)}{d\cos\beta} \tag{B.8}$$

Line *KJ* $$y = (R + 0.5D)\cos\beta - \{R^2 - (x - L + (R + 0.5d)\sin\beta)^2\}^{1/2} \tag{B.9}$$

Line *CH* $$y = (R + 0.5D)\cos\beta - \{(R + 0.5d)^2 - (x - L + (R + 0.5d)\sin\beta)^2\}^{1/2} \tag{B.10}$$

Line *PN* $$Z = \frac{0.5(d - D)x}{L - 0.5d\sin\beta} + 0.5D \tag{B.11}$$

Note: Point *P* and *K* share same x coordinate.

The flow divider is described as follows:

$$\begin{gathered} x = (1 + \tan\theta / \tan\beta)/2 \\ y = 0 \\ Z = b_2(1 - \delta^2 / a_2^2)^{1/2} \end{gathered} \tag{B.12}$$

$$a_2 = \psi_2 - \psi_1 \tag{B.13}$$

$$b_2 = \frac{0.5(d - D)x}{L - 0.5d\sin\beta}(\psi_2\sin\theta + L/2) + 0.5D \tag{B.14}$$

$$\delta = \frac{L}{2\tan\beta\sin\theta} - \psi_2 \tag{B.15}$$

The variables ψ_1 and ψ_2 are found be solving the following equations:

$$L/2\tan\beta = \psi_1\cos\theta + a_1(L/2 + \psi_1\sin\theta)^2 + b_1(L/2 + \psi_1\sin\theta)^8 + 0.5D \tag{B.16}$$

$$L/2\tan\beta = \psi_2\cos\theta + a(\psi_2\sin\theta)^{\lambda} \tag{B.17}$$

$$D = 3.81\,cm$$
$$L = 2.5D$$
$$2\alpha = 70^o$$
$$\beta = 18^o$$
$$2d^2/D^2 = 1$$
$$R = 7d$$

The MATLAB code used to solve the described equations:

```
Function []=geometry()
al=35;
be=18;
D=3.81;
d=D/sqrt(2);
L=2.5*D;
R=7*d;
a1=(8*d*cosd(be)-(L-d*sind(be))*tand(be)-4*D)/(6*(L-d*sind(be))^2);
b1=((L-d*sind(be))*tand(be)-2*d*cosd(be)+D)/(6*(L-d*sind(be))^8);
la=tand(be)*(L-d*sind(be))/(d*cosd(be));
a=0.5*d*cosd(be)/(0.5*L-0.5*d*sind(be))^la;
Ax=L-(R+0.5*d)*sind(be);
Mx=0;
Nx=0;
Cx=L;
Gx=L/2;
Ex=Cx-d*sind(be);
Kx=Cx-d/2*sind(be);
Px=Kx;
Jx=Kx+2*R*sind(0.5*(al-be))*cosd(be+0.5*(al-be));
Fx=Jx-0.5*d*sind(al);
Hx=Jx+0.5*d*sind(al);
dx=0.01;
dt=0.1;
%line ME
xme=(Mx:dx:Ex)';
```

```
yme=a1*xme.^2+b1*xme.^8+0.5*D;
zme=zeros(size(xme));
%line EF
xef=(Ex:dx:Fx)';
yef=(R+0.5*d)*cosd(be)-((R-0.5*d)^2-(xef-L+(R+0.5*d)*sind(be)).^2).^(1/2);
zef=zeros(size(xef));
%line GK
xgk=(Gx:dx:Kx)';
ygk=a*(xgk-0.5*L).^la;
zgk=zeros(size(xgk));
%line KJ
xkj=(Kx:dx:Jx)';
ykj=(R+0.5*d)*cosd(be)-(R^2-(xkj-L+(R+0.5*d)*sind(be)).^2).^(1/2);
zkj=zeros(size(xkj));
%line CH
xch=(Cx:dx:Hx)';
ych=(R+0.5*d)*cosd(be)-((R+0.5*d)^2-(xch-L+(R+0.5*d)*sind(be)).^2).^(1/2);
zch=zeros(size(xch));
%line NP
xng=(Nx:dx:Gx)';
xnp=[xng;xgk];
ynp=[zeros(size(xng));ygk];
znp=0.5*(d-D)*xnp/(L-0.5*d*sind(be))+0.5*D;
plot3(xme,yme,zme,'.','Color',[rand(1) rand(1) rand(1)]);
hold on
plot3(xef,yef,zef,'.','Color',[rand(1) rand(1) rand(1)]);
plot3(xgk,ygk,zgk,'.','Color',[rand(1) rand(1) rand(1)]);
plot3(xkj,ykj,zkj,'.','Color',[rand(1) rand(1) rand(1)]);
plot3(xch,ych,zch,'.','Color',[rand(1) rand(1) rand(1)]);
plot3(xnp,ynp,znp,'.','Color',[rand(1) rand(1) rand(1)]);
xlim([-15,15]);
ylim([-15,15]);
zlim([-15,15]);
plot3(xme,-yme,zme,'.','Color',[rand(1) rand(1) rand(1)]);
plot3(xef,-yef,zef,'.','Color',[rand(1) rand(1) rand(1)]);
plot3(xgk,-ygk,zgk,'.','Color',[rand(1) rand(1) rand(1)]);
plot3(xkj,-ykj,zkj,'.','Color',[rand(1) rand(1) rand(1)]);
plot3(xch,-ych,zch,'.','Color',[rand(1) rand(1) rand(1)]);
plot3(xnp,ynp,-znp,'.','Color',[rand(1) rand(1) rand(1)]);
plot3(xnp,-ynp,-znp,'.','Color',[rand(1) rand(1) rand(1)]);
plot3(xnp,-ynp,znp,'.','Color',[rand(1) rand(1) rand(1)]);
hold off
figure;
plot(xme,yme,'.','Color',[rand(1) rand(1) rand(1)]);
hold on
plot(xef,yef,'.','Color',[rand(1) rand(1) rand(1)]);
plot(xgk,ygk,'.','Color',[rand(1) rand(1) rand(1)]);
plot(xkj,ykj,'.','Color',[rand(1) rand(1) rand(1)]);
plot(xch,ych,'.','Color',[rand(1) rand(1) rand(1)]);
xlim([0,15]);
ylim([0,15]);
hold off
xmef=[xme;xef];
ymef=[yme;yef];
```

```
zmef=[zme;zef];
file=fopen('curveMEF.txt','wt');
for i=1:length(xmef)
   fprintf(file,'%1.8f %1.8f %1.8f\n',xmef(i),ymef(i),zmef(i));
end
fclose(file);
xgkj=[xgk;xkj];
ygkj=[ygk;ykj];
zgkj=[zgk;zkj];
file=fopen('curveGKJ.txt','wt');
for i=1:length(xgkj)
   fprintf(file,'%1.8f %1.8f %1.8f\n',xgkj(i),ygkj(i),zgkj(i));
end
fclose(file);
file=fopen('curveCH.txt','wt');
for i=1:length(xch)
   fprintf(file,'%1.8f %1.8f %1.8f\n',xch(i),ych(i),zch(i));
end
fclose(file);
xnpkj=[xnp;xkj];
ynpkj=[ynp;ykj];
znpkj=[znp;zkj+d/2];
file=fopen('curveNPKJ1.txt','wt');
for i=1:length(xnpkj)
   fprintf(file,'%1.8f %1.8f %1.8f\n',xnpkj(i),ynpkj(i),znpkj(i));
end
fclose(file);
xnpkj=[xnp;xkj];
ynpkj=[-ynp;-ykj];
znpkj=[znp;zkj+d/2];
file=fopen('curveNPKJ2.txt','wt');
for i=1:length(xnpkj)
   fprintf(file,'%1.8f %1.8f %1.8f\n',xnpkj(i),ynpkj(i),znpkj(i));
end
fclose(file);
xnpkj=[xnp;xkj];
ynpkj=[ynp;ykj];
znpkj=[-znp;-(zkj+d/2)];
file=fopen('curveNPKJ3.txt','wt');
for i=1:length(xnpkj)
   fprintf(file,'%1.8f %1.8f %1.8f\n',xnpkj(i),ynpkj(i),znpkj(i));
end
fclose(file);
xnpkj=[xnp;xkj];
ynpkj=[-ynp;-ykj];
znpkj=[-znp;-(zkj+d/2)];
file=fopen('curveNPKJ4.txt','wt');
for i=1:length(xnpkj)
   fprintf(file,'%1.8f %1.8f %1.8f\n',xnpkj(i),ynpkj(i),znpkj(i));
end
fclose(file);
function []=pr(xl,dx,th,yl,wh)
al=35;
be=18;
```

```
D=3.81;
d=D/sqrt(2);
L=2.5*D;
R=7*d;
a1=(8*d*cosd(be)-(L-d*sind(be))*tand(be)-4*D)/(6*(L-d*sind(be))^2);
b1=((L-d*sind(be))*tand(be)-2*d*cosd(be)+D)/(6*(L-d*sind(be))^8);
la=tand(be)*(L-d*sind(be))/(d*cosd(be));
a=0.5*d*cosd(be)/(0.5*L-0.5*d*sind(be))^la;
ps1=(xl(1):dx:xl(2))';
ps2=(xl(1):dx:xl(2))';
y=L/2*tand(be)-ps1.*cosd(th)-a1.*(L/2+ps1.*sind(th)).^2-b1.*(L/2+ps1.*sind(th)).^8-0.5*D;
%w=- cosd(th) - 2*a1*sind(th)*(L/2 + ps1*sind(th)) - 8*b1*sind(th)*(L/2 + ps1*sind(th)).^7;
z=L/2*tand(be)-ps2.*cosd(th)-a.*(ps2.*sind(th)).^(la);
w=- cosd(th) - a*la*sind(th)*(ps2*sind(th)).^(la - 1);
if(wh==0)
   plot(ps1,z);
elseif(wh==1)
   plot(ps1,w);
elseif(wh==2)
   plot(ps1,z,ps1,w);
end
if(yl)
   ylim([-.1,.1]);
end
function [y]=ps1eq(th,ps1)
be=18;
D=3.81;
d=D/sqrt(2);
L=2.5*D;
a1=(8*d*cosd(be)-(L-d*sind(be))*tand(be)-4*D)/(6*(L-d*sind(be))^2);
b1=((L-d*sind(be))*tand(be)-2*d*cosd(be)+D)/(6*(L-d*sind(be))^8);
y=L/2*tand(be)-ps1.*cosd(th)-a1.*(L/2+ps1.*sind(th)).^2-b1.*(L/2+ps1.*sind(th)).^8-0.5*D;
function [y]=ps2eq(th,ps2)
be=18;
D=3.81;
d=D/sqrt(2);
L=2.5*D;
la=tand(be)*(L-d*sind(be))/(d*cosd(be));
a=0.5*d*cosd(be)/(0.5*L-0.5*d*sind(be))^la;
y=L/2*tand(be)-ps2.*cosd(th)-a.*(ps2.*sind(th)).^(la);
```

The FORTRAN subroutine code used to impose Womersley velocity profile at the single bifurcation model inlet:

```
SUBROUTINE WOMTEST (
    &  NLOC, NRET, NARG, RET, ARGS, CRESLT, CZ,DZ,IZ,LZ,RZ )
     IMPLICIT NONE
CD User routine: template for user CEL function
CC --------------------
CC       Input
```

```
CC --------------------
CC  NLOC   - size of current locale
CC  NRET   - number of components in result
CC  NARG   - number of arguments in call
CC  ARGS() - (NLOC,NARG) argument values
CC --------------------
CC      Modified
CC --------------------
CC  Stacks possibly.
CC --------------------
CC       Output
CC --------------------
CC  RET()  - (NLOC,NRET) return values
CC  CRESLT - 'GOOD' for success
CC --------------------
CC      Details
CC --------------------
C ------------------------------
C     Preprocessor includes
C ------------------------------
C       Global Parameters
C ------------------------------
C ------------------------------
C       Argument list
C ------------------------------
      INTEGER NLOC,NARG,NRET
      CHARACTER CRESLT*(*)
      REAL ARGS(NLOC,NARG), RET(NLOC,NRET)
      INTEGER IZ(*)
      CHARACTER CZ(*)*(1)
      DOUBLE PRECISION DZ(*)
      LOGICAL LZ(*)
      REAL RZ(*)
C ------------------------------
C       External routines
C ------------------------------
C ------------------------------
C       Local Parameters
C ------------------------------
      COMPLEX I
      PARAMETER(I=(0,1))
C ------------------------------
C       Local Variables
C ------------------------------
      INTEGER ILOC
      REAL AL(1:NLOC,1), R(1:NLOC,1), T(1:NLOC,1),
     &  A(1:NLOC,1), W(1:NLOC,1), P(1:NLOC,1)
      COMPLEX B, C
C ---------------------------
C    Executable Statements
C ---------------------------
      R(1:NLOC,1) = ARGS(1:NLOC,1)
      T(1:NLOC,1) = ARGS(1:NLOC,2)
      A(1:NLOC,1) = ARGS(1:NLOC,3)
```

```
      W(1:NLOC,1) = ARGS(1:NLOC,4)
      P(1:NLOC,1) = ARGS(1:NLOC,5)
      AL(1:NLOC,1) = ARGS(1:NLOC,6)
C Initialise RET(1:NLOC*NRET) to zero.
      DO ILOC = 1, NLOC
        CALL CBESSJ(COMPLEX(AL(ILOC,1)*
     &    R(ILOC,1)/0.0381,0.)*(I**(3./2.)),0,B)
        CALL CBESSJ(COMPLEX(AL(ILOC,1),0.)*(I**(3./2.)),0,C)
        B=(COMPLEX(A(ILOC,1)/(P(ILOC,1)*W(ILOC,1)),0.)/I)
     &   *(COMPLEX(1.0,0.)-B/C)*EXP(I*COMPLEX(W(ILOC,1)
     &   *(T(ILOC,1)+18.6603434349),0.))
        RET(ILOC,1)=REAL(B)
      ENDDO
      WRITE(*,*)EXP(I*COMPLEX(W(1,1)
     &   *(T(1,1)+18.6603434349),0.))
C
C Set success flag.
      CRESLT = 'GOOD'
C
C=======================================================================
      END SUBROUTINE WOMTEST
C
       real*8 Function Fact(K)
       integer i
       real*8  f
         F=1.d0
         do i=2, k
           f=f*dfloat(i)
         end do
         Fact=f
       return
       End Function Fact
*          FUNCTION  GAMMA(X)           *
* ------------------------------------- *
* Returns the value of Gamma(x) in double *
* precision as EXP(LN(GAMMA(X))) for X>0. *
      real*8 Function Gamma(xx)
      parameter(ONE=1.d0,FPF=5.5d0,HALF=0.5d0)
        real*8 xx
        real*8 cof(6)
        real*8 stp,x,tmp,ser
        integer j
        cof(1)=76.18009173d0
        cof(2)=-86.50532033d0
        cof(3)=24.01409822d0
        cof(4)=-1.231739516d0
        cof(5)=0.120858003d-2
        cof(6)=-0.536382d-5
        stp=2.50662827465d0
        x=xx-ONE
        tmp=x+FPF
        tmp=(x+HALF)*LOG(tmp)-tmp
        ser=ONE
        do j=1, 6
```

```
        x=x+ONE
        ser=ser+cof(j)/x
       end do
       Gamma = EXP(tmp+LOG(stp*ser))
      return
      End function gamma
      Subroutine CBESSJ(z, nu, z1)
C!-----------------------------------------------------
C!                    inf.     (-z^2/4)^k
C!   Jnu(z) = (z/2)^nu x Sum  ------------------
C!                    k=0  k! x Gamma(nu+k+1)
C!  (nu must be >= 0).
C!-----------------------------------------------------
       Parameter(MAXK=20,ZERO=0.d0)
       Complex z,z1
       Integer k
       Complex sum,tmp
       Real*8 Fact, Gamma
       sum = CMPLX(ZERO,ZERO)
       do k=0, MAXK
         !calculate (-z**2/4)**k
      tmp = (-z*z/4.d0)**k
         !divide by k!
      tmp = tmp / Fact(k)
         !divide by Gamma(nu+k+1)
         tmp = tmp / Gamma(dfloat(nu+k+1))
         !actualize sum
      sum = sum + tmp
       end do
       !calculate (z/2)**nu
       tmp = (z/2)**nu
       !multiply (z/2)**nu by sum
       z1 = tmp*sum
      return
      End
C!end of file wom.F
```

APPENDIX C

MATLAB SCRIPT USED FOR VENTILATION WAVEFORMS CREATION

```
function [Vmax,Qmax,Qmin]=wave2(pvq,n,R,C,Tp,nmcycles,sc)
%pvq-control type ('p','v',or 'q')
%n-waveform function number
%R-resistance (4.333333333)
%C-compliance (0.126666667)
%Tp-total breathing cycle time
%nmcycles-number of cycles to produce
%sc-scale factor (needs to be iteratively adjusted until desired tidal
%     volume is reached)
global TI
global T
global trans
T=Tp;
trans=0.005;%time to transition from inspiration to expiration
TI=0.5*T-0.5*trans;
T2=0.5*T;
Ain=pi/4*(8*10^(-3))^2;%area of the inlet
dt=0.0002;
t1=(0:dt:TI);%inspiration time (or length of time to apply the specified control function)
ttrans=(TI+dt:dt:T2);
t2=(T2+dt:dt:T);%expiration time
t=[t1,ttrans,t2];
disp([length(t1),length(ttrans),length(t2),length(t)])
tpart=(0.3+dt:dt:4*TI);
P=zeros(size(t));
V=zeros(size(t));
Q=zeros(size(t));

if(pvq=='p')%pressure controlled
   %P(1:length(t1))=PC(t1,sc,n);%set the pressure for inspiration
   V(1:length(t1))=runkut(V(1),t1,@DE,R,C,@PC,sc,n);%find volume for inspiration by
Runga-Kutta
   Q(1:length(t1))=DE(t1,V(1:length(t1)),R,C,@PC,sc,n);%find flow rate for inspiration
by differential equation
   Q(length(t1)+1:length(t1)+length(ttrans))=Q(length(t1))*rsig(ttrans,TI);%smoothly
transition the flowrate to zero
   if(mod(length(t),2))
     extra=-1
   end
    %extra=0
   Q(length(t1)+length(ttrans)+1:length(t))=-
fliplr(Q(1:length(t1)+length(ttrans)+extra));%set expiration flow as the inverse of
inspiration flow
   V(1)=0;%find volume by integration
   for i=2:length(t)
      V(i)=V(i-1)+(Q(i)+Q(i-1))*(t(i)-t(i-1))/2;
   end
   P=Q*R+V/C;%find pressure for cycle
elseif(pvq=='v')%volume controlled
```

```
   V(1:length(t1))=VC(t1,sc,n);%set volume for inspiration (needs to be modified later to
include sigmoid for flow)
   for i=1:length(t1)-1%find flow by finite difference and apply sigmoid to it
      Q(i)=((V(i+1)-V(i))/(t1(i+1)-t1(i)))*sig(t1(i));
   end
   Q(length(t1))=(V(length(t1))-V(length(t1)-1))/(t1(end)-t1(end-1));
   Q(length(t1)+1:length(t1)+length(ttrans))=Q(length(t1))*rsig(ttrans,TI);%smoothly
transition the flowrate to zero
   if(mod(length(t),2))
     extra=-1
   end
   Q(length(t1)+length(ttrans)+1:length(t))=-
fliplr(Q(1:length(t1)+length(ttrans)+extra));%set expiration flow as the inverse of
inspiration flow
   V(1)=0;%find volume by integration
   for i=2:length(t)
      V(i)=V(i-1)+(Q(i)+Q(i-1))*(t(i)-t(i-1))/2;
   end
   P=Q*R+V/C;%find pressure for cycle
elseif(pvq=='q')%flow controlled
   Q(1:length(t1))=QC(t1,sc,n);%find flow rate for inspiration
   Q(length(t1)+1:length(t1)+length(ttrans))=Q(length(t1))*rsig(ttrans,TI);%smoothly
transition the flowrate to zero
   if(mod(length(t),2))
     extra=-1
   end
   Q(length(t1)+length(ttrans)+1:length(t))=-
fliplr(Q(1:length(t1)+length(ttrans)+extra));%set expiration flow as the inverse of
inspiration flow
   V(1)=0;%find volume by integration
   for i=2:length(t)
      V(i)=V(i-1)+(Q(i)+Q(i-1))*(t(i)-t(i-1))/2;
   end
   P=Q*R+V/C;%find pressure for cycle
else
   error('invalid waveform control type');
end

V=V*1000;
Q=Q*60;

Vmax=max(V);
Qmax=max(Q);
Qmin=min(Q);

vfrr=153846153.846154;

np=ceil(Q*0.000016666666667*vfrr*dt);
Np=V*10^(-6)*vfrr*.5;
```

```
disp(sum(np(1:ceil(length(np)*1.042/4))));
disp(ceil(length(np)*1.042/4));

po='b';
subplot(3,1,1);
plot(t,P,po);
title('Pressure');
xlabel('time(s)');
ylabel('Pressure(cm H_2O)');
subplot(3,1,2);
plot(t,V,po);
title('Volume');
xlabel('time(s)');
ylabel('Volume(mL)');
subplot(3,1,3);
plot(t,Q,po);
title('Flow');
xlabel('time(s)');
ylabel('Flow(L/min)');

K=Q/60/1000/Ain;

%figure;
%plot(t,Np,'b.');

filename=strcat(pvq,num2str(n),'.csv');
file=fopen(filename,'wt');
fprintf(file,'[name]\ninlet\n\n[Spatial Fields]\nt\n\n[Data]\nt [s],Velocity [m s^-1]\n');
for j=1:nmcycles
  for i=1:length(t)
     fprintf(file,'%1.6E,%1.6E\n',t(i)+(j-1)*T,K(i));
  end
end
fclose(file);

filename=strcat('N',pvq,num2str(n),'.csv');
file=fopen(filename,'wt');
fprintf(file,'[name]\nRealPartNum\n\n[Spatial Fields]\nt\n\n[Data]\nt [s],NPR []\n');
for i=1:length(t1)
   fprintf(file,'%1.6E,%1.6E\n',t(i),Np(i));
end
fclose(file);

function [z]=PC(t,sc,n)
global T

if(n==1)
   z=sc*ones(size(t)).*sig(t);
```

```
elseif(n==2)
   z=sc*(1-exp(-4*t/.0335));
   elseif(n==3)
   z=sc*sin(2/T*pi*t);
end

function [z]=VC(t,sc,n)
global TI
if(n==1)
   z=sc*t;
elseif(n==2)
   z=sc*(1/2-1/2*cos(pi*t/TI));
end

function [z]=QC(t,sc,n)
global T
if(n==1)
   z=sc*(2*t);
elseif(n==2)
   z=sc*(2-2*t).*sig(t);
elseif(n==3)
   z=sc*sin(2/T*pi*t);
end

%sigmoid function (for a smooth start up)
function [z]=sig(t)
td=0.0025;
z=(1/2-1/2*cos(t*pi/td)).*(1-heaviside(t-td))+1*heaviside(t-td);
%sigmoid function (for a smooth transition to expiration)
function [z]=rsig(t,s)
global trans
z=cos((t-s)*pi/trans);

function [z]=Pout(t,p)
global TI
z=p*rsig(t,TI);

%differential equation
function [Vdot]=DE(t,V,R,C,Pr,varargin)
Vdot=Pr(t,varargin {:})/R-V/(C*R);

function [w]=runkut(y0,t,f,varargin {:})
w=zeros(size(t));
w(1)=y0;
for i=1:length(w)-1
   dt=(t(i+1)-t(i));
   k1=dt*f(t(i),w(i),varargin);
   k2=dt*f(t(i)+dt/2,w(i)+k1/2,varargin{:});
   k3=dt*f(t(i)+dt/2,w(i)+k2/2,varargin{:});
```

```
    k4=dt*f(t(i)+dt,w(i)+k3,varargin{:});
    w(i+1)=w(i)+1/6*(k1+2*k2+2*k3+k4);
end
```

APPENDIX D

FORTRAN SUBROUTINES USED FOR PARTICLE TRACKING

i. Particle injection code

```
#include "cfx5ext.h"
dllexport(pinject)
      SUBROUTINE PINJECT (
     &  NLOC, NRET, NARG, RET, ARGS, CRESLT, CZ,DZ,IZ,LZ,RZ )
      IMPLICIT NONE
#include "parallel_partitioning.h"
      INTEGER NLOC,NARG,NRET
      CHARACTER CRESLT*(*)
      REAL ARGS(NLOC,NARG), RET(NLOC,NRET)
      INTEGER IZ(*)
      CHARACTER CZ(*)*(1)
      DOUBLE PRECISION DZ(*)
      LOGICAL LZ(*)
      REAL RZ(*)
C -----------------------------
C       Local Variables
C -----------------------------
      INTEGER I,NPI,TOLD,TNEW
      LOGICAL FLAG
      REAL RLAST
      SAVE NPI,TOLD,RLAST,FLAG
      DATA FLAG/.TRUE./
C ---------------------------
C    Executable Statements
C ---------------------------
      IF(FLAG)THEN
        NPI=INT(ARGS(1,1)+0.001)
        FLAG=.FALSE.
      END IF
      RET(1,1)=0.0
      TNEW=INT(ARGS(1,2)+0.1)
      IF(TNEW.EQ.1)THEN
        TOLD=1
        RLAST=0.0
      END IF
      IF(TOLD.NE.TNEW)THEN
        I=INT(ARGS(1,1))-NPI
        IF((ARGS(1,1)-NPI).LT.1)THEN
          RLAST=0.0
        ELSE
          RLAST=REAL(I)-0.45
          NPI=NPI+I
          TOLD=TNEW
        END IF
      ELSE
        RET(1,1)=RLAST
      END IF
Set success flag.
      CRESLT = 'GOOD'
      END SUBROUTINE PINJECT
```

C!end of file Pinject.F

ii. Particle tracking code

```
#include "cfx5ext.h"
dllexport(ptrack)
C  CFX subroutine
      SUBROUTINE PTRACK(NLOC,NRET,NARG,RET,ARGS,CRESLT,
     &                  CZ,DZ,IZ,LZ,RZ)
      IMPLICIT NONE
c     inputs
      INTEGER NLOC,NARG,NRET,I,J
      REAL ARGS(NLOC,NARG), RET(NLOC,NRET)
      CHARACTER CRESLT*(*)
      INTEGER IZ(*)
      CHARACTER CZ(*)*(1)
      DOUBLE PRECISION DZ(*)
      LOGICAL LZ(*)
      REAL RZ(*)
#include "parallel_partitioning.h"
C     ARGS(1:NLOC,1)     -Air.Density
C     ARGS(1:NLOC,2)     -Air.Dynamic Viscosity
C     ARGS(1:NLOC,3:5)   -Air.Velocity
C     ARGS(1:NLOC,6)     -MyDrg.Mean Particle Diameter
C     ARGS(1:NLOC,7)     -MyDrg.Particle Integration Timestep
C     ARGS(1:NLOC,8:10)  -MyDrg.Velocity
C     ARGS(1:NLOC,11)    -Wall Distance
C     ARGS(1:NLOC,12:14) -wall normal
C     ARGS(1:NLOC,15:17) -MyDrg.Particle Position
C     ARGS(1:NLOC,18)    -MyDrg.Particle Time
C     locals
      REAL CCF,A,B,TMP,LA,KB,FS(1:NLOC,3)
      REAL FD(1:NLOC,3), FB(1:NLOC,3)
      CHARACTER FILENM*8!3!----------------------------------------------------------------------------
      INTEGER GETPID,SEED!-----------------------------------------------------------------------------
      SAVE TMP,LA,KB,SEED
      DATA TMP/298.15/
      DATA LA/65.0E-9/
      DATA KB/1.38E-23/
      DATA SEED/15846/
!     CALL NORM([ARGS(1,12),ARGS(1,13),ARGS(1,14)])
      CALL FSAFF(ARGS(1,1),ARGS(1,6),ARGS(1,11),
     &         [ARGS(1,12),ARGS(1,13),ARGS(1,14)],
     &         [ARGS(1,3),ARGS(1,4),ARGS(1,5)],
     &         [ARGS(1,8),ARGS(1,9),ARGS(1,10)],FS(1,:))
      A=CCF(ARGS(1,6),LA)
      CALL FDRAG(ARGS(1,1),ARGS(1,6),ARGS(1,2),A,
     &         [ARGS(1,3),ARGS(1,4),ARGS(1,5)],
     &         [ARGS(1,8),ARGS(1,9),ARGS(1,10)],FD(1,:))
      CALL FBROWN(TMP,ARGS(1,7),A,ARGS(1,2),
     &              ARGS(1,6),KB,SEED,FB(1,:))
      RET=(FS+FD+FB)
```

```
C
!      open(8,FILE="NLOC.TXT",POSITION="APPEND")
!      WRITE(8,*)'ARGS            ',(',',ARGS(1,J),J=1,NARG)
!      WRITE(8,*)'LIFT FORCE      ',(',',FS(1,J),J=1,3)
!      WRITE(8,*)'DRAG FORCE      ',(',',FD(1,J),J=1,3)
!      WRITE(8,*)'BROWNIAN FORCE  ',(',',FB(1,J),J=1,3)
!      CLOSE(8)
C
C      WRITE(FILENM,'(i8)')GETPID()!----------------------------------------------
C      OPEN(9,FILE=FILENM,POSITION="APPEND")
C      WRITE(9,*)ARGS(1,6),ARGS(1,18),ARGS(1,15)
C     &        ,ARGS(1,16),ARGS(1,17),ARGS(1,11)
C      CLOSE(9)
      END SUBROUTINE PTRACK
C-------------------------------------------------------------------------
C  PARTICLE FORCE SUBROUTINES
C     SHEAR INDUCED SAFFMAN LIFT FORCE IS PUT INTO FS
      SUBROUTINE FSAFF(RF,DP,HP,N,U,V,FS)
      IMPLICIT NONE
C     inputs-fluid density, particle diameter, particle wall distance,
C           wall normal vector, fluid velocity, particle velocity, (output) saffman lift force
      REAL RF, DP, HP, N(3), U(3), V(3), FS(3)
C     locals
      REAL KA, LA, GA, US, THAT(3), FDOT, G, A, B
      INTEGER I
      CALL FINDTHAT(V,N,THAT)
      US=FDOT(V,THAT)-FDOT(U,THAT)
      IF(US*HP .NE. 0.0)THEN
        GA=FDOT(U,THAT)/HP
        KA=DP/(2.0*HP)
        B=GA*DP/2.0
        IF(ABS(US).LT.ABS(B))THEN
          LA=SIGN(1.0,B*US)
        ELSE
          LA=B/US
        END IF
        A=-RF*(DP/2.0)**2.0*(US**2.0*G(KA,LA))
        DO I=1,3
          FS(I)=A*N(I)
        END DO
      ELSE
        FS(1)=0.0
        FS(2)=0.0
        FS(3)=0.0
      ENDIF
      END SUBROUTINE FSAFF
C     DRAG FORCE WITH CUNNINGHAM CORRECTION FACTOR IS PUT INTO FD
      SUBROUTINE FDRAG(RF,DP,MU,CCF,U,V,FD)
      IMPLICIT NONE
C     inputs-fluid density, particle density, particle diameter, fluid viscosity, cunningham correction factor,
C           fluid velocity, particle velocity, (output) drag force
      REAL RF, DP, MU, CCF, U(3), V(3), FD(3)
C     locals
      REAL A, RE, MAG, CD
```

```
      INTEGER I
      RE=RF*MAG(U-V)*DP/MU
      A=0.39269908*CD(RE)*RE*DP*MU/CCF!PI/8
      DO I=1,3
        FD(I)=A*(U(I)-V(I))
      END DO
      END SUBROUTINE FDRAG
C     BROWNIAN MOTION FORCE IS PUT INTO FB
      SUBROUTINE FBROWN(T,DT,CCF,MU,DP,KB,SEED,FB)
      IMPLICIT NONE
C     inputs-fluid temperature, particle integration time step, cunningham correction factor,
C           fluid viscosity, particle diameter, Boltzman constant,(output) brownian motion force
      REAL T,DT,CCF,MU,DP,KB,FB(3)
      INTEGER SEED
C     local
      REAL D,ZE,A
      INTEGER I
      D=(KB/(9.424777961))*(T/DP)*(CCF/MU)!3*PI
      A=SQRT(2.0/D*KB*T**2.0*KB/DT)
      DO I=1,3
        CALL GET_RANDOM_NORM(ZE,1,0.0,1.0,-3.0,3.0,SEED)
        FB(I)=ZE*A
      END DO
      END SUBROUTINE FBROWN
C-------------------------------------------------------------------------------
C  SUBROUTINES FOR PARTICLE FORCE CALCULATIONS
C     CUNNINGHAM CORRECTION FACTOR SUBROUTINE
      REAL FUNCTION CCF(DP,LA)
      IMPLICIT NONE
C     inputs-diameter of the particle, mean free path
      REAL DP,LA
      CCF=1.0+LA/DP*(2.34+1.05*EXP(-0.39*DP/LA))
      END FUNCTION CCF
C     DRAG FACTOR SUBROUTINE
      REAL FUNCTION CD(RN)
      IMPLICIT NONE
C     inputs-particle reynolds number
      REAL RN
      IF(RN.LE.0.0)THEN
          CD=0.0
      ELSEIF(RN.LE.0.1)THEN
          CD=24.0/RN
      ELSEIF(RN.LE.1.0)THEN
          CD=22.73/RN+0.0903/RN**2.0+3.69
      ELSEIF(RN.LE.10.0)THEN
          CD=29.1667/RN-3.8889/RN**2.0+1.222
      ELSEIF(RN.LE.100.0)THEN
          CD=46.5/RN-116.67/RN**2.0+0.6167
      ELSEIF(RN.LE.1000.0)THEN
          CD=98.33/RN-2778.0/RN**2.0+0.3644
      ELSEIF(RN.LE.5000.0)THEN
          CD=148.62/RN-4.75E4/RN**2.0+0.357
      ELSEIF(RN.LE.10000.0)THEN
          CD=-490.546/RN+57.87E4/RN**2.0+0.46
```

```
      ELSEIF(RN.GT.10000.0)THEN
          CD=-1662.5/RN+5.4167E6/RN**2.0+0.5191
      ENDIF
      END FUNCTION CD
C     INTEGRAL CURVE FIT FOR SAFFMAN LIFT FORCE
      REAL FUNCTION G(KA,LA)
      IMPLICIT NONE
      REAL KA, LA
      G=(1.7631+0.3561*KA-1.1837*KA**2.0+0.845163*KA**3.0)
      G=G-(3.24139/KA+2.6760+0.8248*KA-0.4616*KA**2.0)*LA
      G=G+(1.8081+0.8796*KA-1.9009*KA**2.0+0.98149*KA**3.0)*LA**2.0
      END FUNCTION G
C     FIND THE DIRECTION VECTOR OF THE WALL TANGENT PARTICLE VELOCITY
      SUBROUTINE FINDTHAT(V,N,T)
      IMPLICIT NONE
C     inputs-particle velocity vector, wall normal vector, (outputs) wall tangent particle velocity vector
      REAL N(3), V(3), T(3), A(3), W
      CALL CRS(N,V,A)
      CALL CRS(A,N,T)
      CALL NORM(T)
      END SUBROUTINE FINDTHAT
C-------------------------------------------------------------------------------
C   VECTOR OPERATION SUBROUTINES
C     CROSS PRODUCT
      SUBROUTINE CRS(A,B,C)
      IMPLICIT NONE
      REAL A(3), B(3), C(3)
      C(1)=A(2)*B(3)-A(3)*B(2)
      C(2)=A(3)*B(1)-A(1)*B(3)
      C(3)=A(1)*B(2)-A(2)*B(1)
      END SUBROUTINE CRS
C     DOT PRODUCT
      SUBROUTINE DOT(A,B,C)
      REAL A(3), B(3), C
      INTEGER I
      DO I=1, 3
        C=C+A(I)*B(I)
      END DO
      END SUBROUTINE DOT
C     DOT PRODUCT
      REAL FUNCTION FDOT(A,B)
      IMPLICIT NONE
      REAL A(3), B(3)
      INTEGER I
      DO I=1, 3
        FDOT=FDOT+A(I)*B(I)
      END DO
      END FUNCTION FDOT
C     NORMALIZES THE VECTOR A
      SUBROUTINE NORM(A)
      IMPLICIT NONE
      REAL A(3),MAG
      IF(MAG(A) .NE. 0.0)THEN
      A=A/MAG(A)
```

```
      ENDIF
      END SUBROUTINE NORM
C     RETURNS THE MAGNITUDE OF THE VECTOR A
      REAL FUNCTION MAG(A)
      IMPLICIT NONE
      REAL A(3)
      MAG=SQRT(A(1)**2.0+A(2)**2.0+A(3)**2.0)
      END FUNCTION MAG
```

iii. Particle deposition code

```
#include "cfx5ext.h"
dllexport(pdep)
     SUBROUTINE PDEP(NLOC,NRET,NARG,RET,ARG,CRESLT,
     &                CZ,DZ,IZ,LZ,RZ)

#include "cfd_sysdep.h"
#include "cfd_constants.h"
C ------------------------------
C       Argument list
C ------------------------------
      INTEGER          NARG, NRET, NLOC
      REAL             ARG(NLOC,NARG), RET(NLOC,NRET)
      CHARACTER*(4)     CRESLT
      INTEGER IZ(*)
      CHARACTER CZ(*)*(1)
      DOUBLE PRECISION DZ(*)
      LOGICAL LZ(*)
      REAL RZ(*)
C     Return variables:
C     Perpendicular Coefficient of Restitution (dummy)     : RET(1,1)
C     Argument variables
C     Particle Diameter                    : ARG(1,1)
C     Particle time                       : ARG(1,2)
C     Particle Position                    : ARG(1,3:5)
      CHARACTER FILENM*20
      INTEGER GETPID
      WRITE(FILENM,*)'DEP',GETPID()!-------------------------------------------
      OPEN(9,FILE=FILENM,POSITION="APPEND")
      WRITE(9,*)ARG(1,1),ARG(1,2),ARG(1,3),ARG(1,4),ARG(1,5)
      CLOSE(9)
      RET(1,1)=0.0
      END SUBROUTINE PDEP
```

BIOGRAPHY

Mohammed S. Alzahrany was born on June 18, 1977 in Al-Bahah, Saudi Arabia. The author graduated from High School in June of 1996. The following fall, he entered King Abdul-Aziz University in Jeddah, Saudi Arabia. The author received a Bachelor of Science degree in Mechanical Engineering (June 2000) and a Master of Science degree in Mechanical Engineering (July 2007) from King Saud University in Riyadh. He enrolled as a doctoral student under the direction of Dr. Arindam Banerjee in August 2012 in the Department of Mechanical Engineering and Mechanics at Lehigh University in Bethlehem, PA. His dissertation research mainly focused on pulmonary gas transport and drug delivery in a patient specific lung model during invasive high frequency oscillatory ventilation.

LIST OF PUBLICATIONS

JP.1 Alzahrany, M., Banerjee, A. and Salzman, G. Flow transport and gas mixing during invasive high frequency oscillatory ventilation. *Medical Engineering & Physics, 2014 36*(6), 647 - 658.

JP.2 Alzahrany, M., Banerjee, A. and Salzman, G. The role of coupled Resistance-Compliance in upper tracheobronchial airways under high frequency oscillatory ventilation *Medical Engineering & Physics, published online, September 2014*.

JP.3 Alzahrany, M. and Banerjee, A. Aerosolized Drug Delivery in Specific-Patient Lung Model during Invasive High Frequency Oscillatory Ventilation. *Journal of Aerosol Science, in review. September 2014.*

JP.4 Alzahrany, M. and Banerjee, A. Effect of Carrier Gas on Transport and Aerosol-Drug Delivery by Invasive High Frequency Oscillatory Ventilation. *Journal of Aerosol Science, to be submitted.*

JP.5 Timothy V. R., Alzahrany M., Banerjee A. and Salzman G. Fluid Flow and Particle Transport In Mechanically Ventilated Airways. Part I. Fluid Flow Structures. *Medical & Biological Engineering & Computing, in review. June 2014.*

JP.6 Alzahrany M., Timothy V. R., Banerjee A. and Salzman G. Fluid Flow and Particle Transport In Mechanically Ventilated Airways. Part II. Particle Transport. *Medical & Biological Engineering & Computing, in review. June 2014*

CA.1 Mohammed Alzahrany and Arindam Banerjee. Effects of pressure controlled waveforms on flow transport and gas mixing in patient specific lung model during invasive *HFOV*. In proceeding of: 65th Annual Meeting of the APS Division of Fluid Dynamics, At San Diego, California, Vol: 57.

CA.2 Mohammed Alzahrany and Arindam Banerjee. Effect of time-dependent pressure boundary conditions on flow transport in a patient specific lung model during invasive high frequency oscillatory ventilation. In proceeding of: 66th Annual Meeting of the APS Division of Fluid Dynamics, At Pittsburgh, PA, Vol: 58.